Fermilab Library
0 1160 0020783 1

E733

A SEARCH FOR WEAKLY INTERACTING MASSIVE PARTICLES IN THE FERMILAB TEVATRON WIDE BAND NEUTRINO BEAM

By

Elisabeth J. Gallas

Michigan State University

A SEARCH FOR WEAKLY INTERACTING MASSIVE PARTICLES IN THE FERMILAB TEVATRON WIDE BAND NEUTRINO BEAM

By

Elizabeth J. Gallas

A DISSERTATION

Submitted to
Michigan State University
in partial fulfillment of the requirements
for the degree of

DOCTOR OF PHILOSOPHY

Department of Physics and Astronomy

1993

AAC5207

ABSTRACT

A SEARCH FOR WEAKLY
INTERACTING MASSIVE PARTICLES
IN THE FERMILAB TEVATRON
WIDE BAND NEUTRINO BEAM

By

Elizabeth J. Gallas

A time-of-flight technique has been used to search for new weakly interacting massive neutral particles by exploiting the time structure of the Wide Band Neutrino beam at the Fermilab Tevatron. Event times were measured relative to the accelerator RF clock using high timing resolution scintillation counters in the 100 metric ton fiducial volume of the E733 target/calorimeter during the 1987 fixed target run. The experimental signature of a new particle candidate is an event with a measured event time inconsistent with the expected time structure of the neutrino beam. No such candidates were found. This null result has been used to set limits at the 90% confidence level on a) heavy neutrino production from the decay of heavy quark states, b) massive objects directly produced in 800 GeV/c pN interactions that are noninteracting but unstable with mean lifetimes between 10^{-8} and $10^{-4}s$ and c) directly produced massive objects that are stable but weakly interacting with interaction cross sections between 10^{-29} and $10^{-31} cm^2/nucleon$.

ACKNOWLEDGEMENTS

I would first like to thank all the individuals and institutions involved in the successful running of this experiment listed in Appendix A. Particular thanks to Chip Brock, Dixon Bogert, Stu Fuess, and Linda Stutte, for their helpful input.

I am much obliged to the hunchbacks, Bill Cobau, Robert Hatcher, and George Perkins, who have all kindly filled me in on ALL the details of the running of this experiment. Nothing would be accomplished without those who actually work out the detailed details in detail.

Thanks to the Michigan State University Physics and Astronomy faculty and staff, in particular, Dr. Kovacs and Stephanie Holland, for their advice, assistance, and good humor. To ALL in the Elementary Particle Physics Group at MSU, without exception, your support and encouragement has been much appreciated.

I would also like to offer thanks to Dr. Mikie Tartaglia for his major role in the design, construction, installation, and monitoring of the time-of-flight counters, his help with the data analysis, and his endless patience for my unending questions.

Extra special thanks to Harry Weerts, my advisor, for his constant support, guidance, and perseverance throughout this analysis. Now that you have survived to see me graduate, you deserve a life where everyone does what you want.

Last, but not least, thanks to John Womersley, for his advice, support, charm, and love of words.

Contents

List of Tables xi

List of Figures xxii

Introduction 1

1 Theory 3

1.1 Motivation for a Massive Neutral Particle Search 3

1.2 The Standard Model 6

1.3 Phenomenology of Particle Production 13

1.3.1 Production of Massive Particles in pN interactions 13

1.3.2 Scaling variables for Production 15

1.3.3 Decays 16

1.3.4 *"A dependence"* of Production Cross Sections 16

1.4 Extensions of the Standard Model 18

1.4.1 Neutrino Mixing and Neutrino Oscillations 18

1.4.2 Supersymmetry 21

R-invariance 22

Low Energy Supersymmetric Theories 23

2 The Beamlines 24

2.1 The Time-of-Flight (TOF) Search Technique 24

2.2 The Wide Band Neutrino Beamline 27

2.2.1 Overview 27
2.2.2 Constituents and Spectra 27
2.2.3 Beamline Elements 32
2.2.4 Monitoring and Logic Gates 34
2.2.5 Time sub-structure of the beam 38
2.3 The Testbeam Beamline 43
2.3.1 Production of the Calibration Beam 43
2.3.2 Monitoring and Logic Gates 43
2.3.3 Purpose 45

3 The E733 Detector **46**
3.1 Introduction 46
3.2 The Apparatus 47
3.2.1 Overview 47
3.2.2 Front Veto Walls 49
3.2.3 Liquid Scintillator Tanks 50
3.2.4 Proportional Wire Tubes and the Event Trigger 50
3.2.5 Muon Spectrometer 55
3.2.6 Flash Chambers and Energy Measurement 56
3.2.7 TOF counters 59
Construction and Installation 59
Trigger and Electronics 62

4 Event Classification and Reconstruction **66**
4.1 Introduction 66
4.2 Neutrino Event Classification 66
4.3 Pattern Recognition and Tracking 67
4.4 The E733 Detector Event Display 69

4.5 The TOF Fiducial Volume 73
4.6 RF Clock Trouble Periods 74
4.7 The Final Event Sample 76
4.8 Preliminary TOF Analysis 78
4.8.1 TOF Counter Alignment 78
4.8.2 Times Relative to the RF Clock Phase 79
4.8.3 The RF Clock Phase Drift 80
4.8.4 Pulse Height Corrections 82

5 Event Time Measurement **89**
5.1 Overview 89
5.2 The TOF Event Sample 90
5.3 The Speed of Light in Scintillator. 91
5.4 Random Event Scan 92
5.5 CC-like Event Times 93
5.5.1 Time Measurement Criteria 94
5.5.2 Pulse Height Corrections to the Time 97
5.5.3 Event Timing Anomalies 103
5.5.4 The CC-like Event Time Distribution 109
5.6 NC-like Event Times 113
5.6.1 Corrections to the Time Measurements 113
5.6.2 Time Measurement Criteria 121
5.6.3 Event Timing Anomalies 121
5.6.4 The NC-like Event Time Distribution 123
5.6.5 Shower Timing Efficiency 131

6 Model Independent Predictions **132**
6.1 General Considerations in Models of New Particle Production . . . 132

6.2 Direct Production of WIMPs 135

6.3 Acceptance and Detection Efficiency 136

6.4 Detection 145

6.4.1 Noninteracting Unstable Particles 145

6.4.2 Stable Weakly Interacting Particles 152

Constant Interaction Cross Section 152

Interaction Cross Section Proportional to Energy 155

7 Limits on Heavy Neutrino Production 157

7.1 A Massive Neutrino Model 158

7.2 Heavy Neutrino Production from the Decay of Heavy Quarks 160

7.2.1 Charmed Particle Production and Decay 163

Cross section uncertainty and A dependence 169

7.2.2 Acceptance and Efficiency 170

7.2.3 ν_H Detection 180

8 Supersymmetry 193

8.1 Gluino Production and Decay 194

8.2 Acceptance and Efficiency 198

8.3 Photino Interactions in the Detector 204

8.4 Results 208

8.5 Conclusions 214

Conclusion 215

A The FMMF Collaboration 216

B Time of Flight Calculation 217

C Calculations from Time-of-Flight Counters **219**

C.1 The Speed of Light in Scintillator 220

C.2 Timing Events with Isolated Tracks 221

D Trigger, Timing, and RF Electronics **222**

E Acceptance Tables **225**

Bibliography **237**

List of Tables

1.1 Supersymmetric particle naming conventions, symbols and spin. . . . 22

2.1 Secondary Production Efficiencies and Focusing Efficiencies 30

2.2 Neutrino Decay Modes and Associated Efficiencies 31

2.3 Expected number of neutrinos per proton on target entering the detector from the decay of $\pi^{\pm}$, $K^{\pm}$, and K_L^0 40

2.4 Expected neutrino interactions from each source. 41

3.1 Table of calorimeter parameters. 49

3.2 E733 trigger conditions. 54

4.1 Calorimeter segmentation parameters. 68

4.2 The E733 TOF Data Set. 76

4.3 Scan classification of "no vertex found" events. 77

4.4 Good and Bad Pulse Height Runs. 84

5.1 Classification of events in the TOF event sample. 90

5.2 The clean track counter requirements. 96

5.3 Time measurements eliminated from the CC-like event sample. . . . 105

5.4 The shower timing consistency requirements. 121

5.5 Number of events above background calculated using 9 different TOF search windows for 3 data subsets. 130

6.1 Comparison of NA3 and E733 Experiment Characteristics 150

7.1 Sources of $D^{\pm}$ and $D_S^{\pm}$ in the neutrino beamline. 168

7.2 Guide to location of acceptance tables for ν_H production. 171

7.3 Geometric and time-of-flight acceptances for ν_H produced in the 3 body decay of the $D^{\pm}$ meson produced at the target 176

7.4 Branching ratios into specific final states for low-mass neutral heavy leptons, in percent for ν_H mixing primarily with ν_μ. 181

E.1 Geometric, time-of-flight and trigger acceptances for particles directly produced by 800 GeV/c protons at the primary target. The muon track timing TOF window is used to obtain these time-of-flight acceptances. 225

E.2 Geometric, time-of-flight and trigger acceptances for particles directly produced by 800 GeV/c protons at the beam dump. The muon track timing TOF window is used to obtain these time-of-flight acceptances. 226

E.3 Geometric, time-of-flight and trigger acceptances for heavy neutrinos produced from the decay of $D_S^{\pm}$ produced by 800 GeV/c protons at the primary target and the beam dump. The muon track timing TOF window is used to obtain these time-of-flight acceptances. 227

E.4 Geometric, time-of-flight and trigger acceptances for heavy neutrinos produced from the decay of $D^{\pm}$ produced by 800 GeV/c protons at the primary target and the beam dump. The muon track timing TOF window is used to obtain these time-of-flight acceptances. 228

E.5 Geometric, time-of-flight and trigger acceptances for heavy neutrinos produced from the decay of $D^{\pm}$ produced by the secondary π^- and π^+ flux on the beam dump. The muon track timing TOF window is used to obtain these time-of-flight acceptances. 229

E.6 Geometric, time-of-flight and trigger acceptances for heavy neutrinos produced from the decay of $D^{\pm}$ produced by the secondary K^- and K^+ flux on the beam dump. The muon track timing TOF window is used to obtain these time-of-flight acceptances. 230

E.7 Geometric, time-of-flight and trigger acceptances for heavy neutrinos produced from the decay of $D^{\pm}$ produced by the secondary p^- and p^+ flux on the beam dump. The muon track timing TOF window is used to obtain these time-of-flight acceptances. 231

E.8 Geometric, time-of-flight and trigger acceptances for photinos produced from the decay of gluinos produced by 800 GeV/c protons on the primary target and the beam dump. The shower timing TOF window is used to obtain the time-of-flight acceptances. 232

List of Figures

1.1 The Minimal Standard Model includes three generation of a) quarks and b) leptons. The superscripts indicate the fractional electric charge. 6

1.2 Feynman Diagrams for heavy quark production in hadron-nucleon interactions via a) Drell Yan and b) Gluon Fusion processes. 14

2.1 Schematic of the Wide Band Neutrino Beamline. 28

2.2 Energy Spectrum of Secondary $\pi^{\pm}$, $K^{\pm}$, $p\pm$, and K_L^0 as they exit the Quad Triplet Train 29

2.3 The predicted neutrino energy distribution (dashed line) compared to that seen (solid line) in the E733 detector. The predicted spectrum is weighted by energy to account for the known linear dependence of the neutrino interaction cross section. The data sample consists of all charged current neutrino interactions with a reconstructed primary vertex in the TOF fiducial volume. 32

2.4 Schematic: Beam monitor signal and various logic gates. 35

2.5 K_L^0 Time-of-Flight Distribution 39

2.6 Schematic of the N-Center and NH Beamlines (figure courtesy of G.J.Perkins). 44

3.1 A Schematic of the Lab C (E733) neutrino detector. 48

3.2 Proportional Tube plane readout electronics. a) Overview, b) Electronics detail. 52

3.3 Drift Chamber construction unit (courtesy of G.J.Perkins). 56

3.4 Schematic of a time-of-flight counter. 59

3.5 Cross section of a TOF counter mounted into a UniStrut rail. 61

3.6 Schematic of the time-of-flight counter plane configuration. 63

4.1 The charged and neutral current interactions in neutrino-nucleon deep inelastic scattering. 67

4.2 A typical charged current event in the E733 detector. 70

4.3 A typical neutral current event in the E733 detector. 71

4.4 The cross section of the TOF fiducial volume extends to include the area within 100 clock counts from the edge of the calorimeter in all flash chamber views. 74

4.5 Four scatterplots, like these, were used to obtain alignment constants for each TOF counter. 78

4.6 Average of event time distribution of each split tape, plotted versus the original data tape number, for both neutrino CC events and testbeam muon events (figure courtesy of M. Tartaglia). 81

4.7 RF phase correction as a function of run number. 82

4.8 Typical raw pulse height distribution for a counter hit by isolated tracks in CC neutrino interactions. 83

4.9 The average raw pulse height as a function of run number. 84

4.10 The average raw pulse height as a function of PMT number. 85

4.11 The average corrected pulse height as a function of run number. . . 87

4.12 The average corrected pulse height as a function of PMT number. . 88

5.1 A schematic of a time-of-flight counter struck by a single minimum ionizing particle. 94

5.2 The distribution of counter times in *all* track hit 4-HIT counters in CC-like events a) unshifted and b) shifted into a single period of the RF clock. The time distribution for counters passing the *clean track* criteria are shown in c). 98

5.3 For CC-like neutrino events: a) Scatterplot of PMT time versus PMT pulse height for all counters passing the clean track criteria. b) The average PMT time as a function of PMT pulse height for the same set of counters. 101

5.4 For testbeam muon events: a) Scatterplot of PMT time versus PMT pulse height for all counters passing the clean track criteria. b) The average PMT time as a function of PMT pulse height for the same set of counters. 102

5.5 The distribution of pulse height corrected counter times in track hit 4-HIT counters passing the clean track criteria in CC-like events. . . 103

5.6 The CC-like event time distribution obtained by using all counters passing the clean track criteria in CC-like events. 103

5.7 A typical cosmic rays muon event identified in the CC-like event scan. 106

5.8 An 'out of time' event identified in the CC-like event scan. 107

5.9 A typical event which utilizes a time measurement from a TOF counter that is not struck by a muon. In this event, the pattern recognition program found a track emerging from the vertex passing through counter number 16 (in the X flash chamber view, this is the topmost TOF counter in the last downstream TOF plane). Clearly, no such track exists. 108

5.10 The final CC-like event time distribution. 109

5.11 The event timing efficiency as a function of the angle of the muon with the beam axis. 110

5.12 The final CC-like event time distribution for a) single counter timed events and b) multiple counter timed events. 111

5.13 The event timing efficiency as a function of the angle of the muon with the beam axis for a) single counter timed events and b) multiple counter timed events. 112

5.14 A schematic of the energy deposition of a hadronic shower in a TOF counter. 113

5.15 Counter time measurements: a) uncorrected, b) shower width corrected, c) pulse height corrected. 115

5.16 The average uncorrected time as a function of the measured shower width in counters with overflow pulse heights in CC-like events. . . . 117

5.17 The average width corrected time (also corrected for shower angle) as a function of the variable V, the vertical distance from the vertex to the center of the TOF counter. 117

5.18 The average uncorrected time as a function of the measured shower width and the variable V for shower hit counters with overflow pulse heights. 118

5.19 The average width and V corrected counter time as a function of the number of X cluster hits in the flash chambers just upstream of the TOF counter in CC-like events. 119

5.20 The average uncorrected time as a function of the pulse height in non-clean track hit counters in CC-like events. 120

5.21 The distribution of corrected counter time measurements in 4-HIT counters a) before and b) after shower time consistency requirements are imposed in NC-like events. 122

5.22 The event time distribution obtained using shower timing a) NC-like and b) CC-like events. 124

5.23 A typical cosmic rays muon event identified in the NC-like event scan. 125

5.24 The event time distribution for NC-like events. 126

5.25 Number of NC-like events above background as a function of time. . . 127

5.26 Shower time distributions: a) NC-like single counter timed events, b) NC-like multiple counter timed events, c) CC-like single counter timed events, d) CC-like multiple counter timed events. 128

5.27 The multiple counter event timing efficiency as a function of shower energy in NC-like events. 131

6.1 Geometric Acceptance as a function of WIMP mass for production at the a) target and b) beam dump. 138

6.2 Time-of-flight acceptance as a function of WIMP mass for geometrically accepted particles produced at the a) target and b) beam dump. The solid line is ε_{TOF} using the clean track time search window and the dotted line is ε_{TOF} using the narrower shower time search window. 139

6.3 Energy Spectra for a WIMP mass of a) 1, b) 6, and c) 11 GeV/c^2 , produced by 800 GeV/c protons on the target. The unhatched area is the produced spectrum, the hatched area is the energy distribution of geometrically accepted particles and the cross hatched area shows the spectrum of time-of-flight accepted particles. 140

6.4 The maximum possible energy a WIMP can have such that it falls within the track timing search window as a function of WIMP mass. The solid line is for production at the target ($D = 1599m$) and the dotted line for production at the beam dump ($D = 1057m$). 141

6.5 The variation in the a) geometric, b) time-of-flight and c) total (geometric $\times$ time-of-flight $\times$ trigger) acceptance as a function of n and b for a WIMP mass of 13 GeV/c^2 143

6.6 The probability that a WIMP will decay in the detector fiducial volume as a function of lifetime τ. This probability was evaluated for a WIMP mass = 10 GeV/c^2 , WIMP energy = 100 GeV . The target to detector distance D = 1599 meters and the fiducial volume depth Δ = 10 meters. 146

6.7 For noninteracting unstable particles, the solid contours indicate equal 90% CL upper limits on production cross section times branching ratio (pb/nucleon) as indicated as a function of mass and lifetime for inclusive CC-like final states. Solid curves represent the E733 results in which the A dependence is assumed to be the same as the total inelastic cross section ($A^{0.72}$). If a linear dependence is assumed, the σB sensitivity *increases* by a factor of > 2.2. Dashed curved represent the NA3 results for identical σB and specific final state $\mu+\pi$ or $\mu+\mu$. The NA3 curves assume a linear dependence of the cross section. If $A^{0.72}$ dependence is assumed, their cross section sensitivity *decreases* by a factor of 4.3. 147

6.8 For noninteracting unstable particles, the solid contours indicate equal 90% CL upper limits on production cross section times branching ratio (pb/nucleon) as indicated as a function of mass and lifetime for inclusive NC-like final states. Solid curves represent the E733 results in which the A dependence is assumed to be the same as the total inelastic cross section ($A^{0.72}$). If a linear dependence is assumed, the σB sensitivity *increases* by a factor of > 2.2. Dashed curved represent the NA3 results for identical σB and specific final state a) $\pi^{\pm}e^{\mp}$ or b) $\pi^{\pm}\pi^{\mp}+X$ (inclusive). The NA3 curves assume a linear dependence of the cross section. If $A^{0.72}$ dependence is assumed, their cross section sensitivity *decreases* by a factor of 4.3. 148

6.9 The probability that a WIMP will interact in the detector fiducial volume as a function of interaction cross section σ_0. 152

6.10 For stable particles with a constant interaction cross section: the solid contours indicate equal 90% CL upper limits on production cross section times branching ratio (pb/nucleon) as indicated as a function of mass and interaction cross section σ_0 for final states a) with a muon b) without a muon. A dependence is assumed to be the same as the total inelastic cross section ($A^{0.72}$). If a linear dependence is assumed, the σB sensitivity *increases* by a factor of > 2.2. 154

6.11 For stable particles with interaction cross section proportional to the WIMP energy: the solid contours indicate equal 90% CL upper limits on production cross section times branching ratio (pb/nucleon) as indicated as a function of mass and interaction constant $\sigma_0 = \sigma_{int}/E$ for final states a) with a muon b) without a muon. A dependence is assumed to be the same as the total inelastic cross section ($A^{0.72}$) in pN interactions. If a linear dependence is assumed, the σB sensitivity *increases* by a factor of > 2.2. 156

7.1 Feynman Diagrams demonstrating the a) 2 body and b) 3 body decay of a charged D meson into a final state with a massive neutrino. . . . 161

7.2 The branching ratio for a $D^{\pm}$ meson to decay to a massive neutrino as a function of $|U_{\mu H}|^2$ for ν_H masses of a) 0.5, b) 1.1 and c) 1.7 GeV/c^2 .162

7.3 Integrated cross sections for the production of charmed quarks in πN (solid lines) and pN (dashed lines) collisions extracted from a paper by Ellis and Quigg. 166

7.4 Expected $D^{\pm}$ cross section as a function of beam energy in πN (solid lines) and pN (dashed lines) interactions. 167

7.5 The number of a) $D^{\pm}$ and b) $D_S^{\pm}$ particles produced in the beamline as a function of beam type i. 169

7.6 The geometric acceptance for heavy neutrinos produced in the 2 body decay of a) $D^{\pm}$ and b) $D_S^{\pm}$ as a function of heavy neutrino mass and beam particle type. 172

7.7 The time-of-flight acceptance for geometrically accepted heavy neutrinos produced in the 2 body decay of a) $D^{\pm}$ and b) $D_S^{\pm}$ as a function of heavy neutrino mass and beam particle type. 174

7.8 The acceptance (combined geometric,time-of-flight and trigger acceptance) for heavy neutrinos produced in the 2 body decay of a) $D^{\pm}$ and b) $D_S^{\pm}$ as a function of heavy neutrino mass and beam particle type. . 175

7.9 Value of the geometric acceptance as a function of ν_H mass for a) a fixed value of n and b varying by $\pm 1\sigma$ of the measured value and b) a fixed value of b and n varying by $\pm 1\sigma$ of the measured value in E743. 178

7.10 Value of the combination of geometric and time-of-flight acceptance as a function of ν_H mass for a) a fixed value of n and b varying by $\pm 1\sigma$ of the measured value and b) a fixed value of b and n varying by $\pm 1\sigma$ of the measured value in E743. 179

7.11 The ν_H lifetime as a function of $|U_{\mu H}|^2$ for heavy lepton masses 0.5, 1.1 and 1.7 GeV/c^2 183

7.12 Two curves show the probability of decay in the detector as a function of mixing parameter $|U_{\mu H}|^2$ for a heavy lepton with energy 10 and 30 GeV/c^2 , respectively. The hypothetical ν_H was produced from a heavy quark decay at the target (D = 1599 m) with a mass of 1.1 GeV/c^2 183

7.13 For massive neutrinos produced from the decay of the $D^{\pm}$ meson with a mass of 0.9 GeV/c^2 , the expected total number of events (top curve) and the contribution to the total from each beam source (as annotated) is shown as a function of the mixing parameter squared. . 185

7.14 Expected ν_H events as a function of heavy neutrino mass and mixing parameter squared from the decay of the $D^{\pm}$ meson. 186

7.15 Expected ν_H events as a function of heavy neutrino mass and mixing parameter squared from the decay of the $D_S^{\pm}$ meson. 187

7.16 The region excluded at the 90% confidence level by the present experiment as a function of heavy neutrino mass and mixing parameter squared. 189

7.17 Limits at the 90% confidence level on $|U_{\mu H}|^2$ as a function of the neutrino mass: a) limits obtained in the CHARM beam dump experiment; b) limits obtained in the CHARM wide-band neutrino beam; c) limits obtained studying the decay $\pi \rightarrow \nu\mu$ at SIN; d) limits from the study of the decay $K \rightarrow \nu\mu$ at KEK; e) limits from the study of the decay $K \rightarrow \nu\mu\nu^*$ at LBL; f) limits obtained in the BEBC beam dump g) limits obtained from the MARK II experiment 190

8.1 The leading order Feynman diagrams for gluino production in pp interactions via a) gluon fusion and b) $q\bar{q}$ annihilations. 195

8.2 The predicted cross section for pp (or $p\bar{p}$) $\rightarrow \tilde{g} + \tilde{q}(\bar{\tilde{q}})$ for a number of center-of-mass energies from P.R.Harrison and C.H.Llewellyn Smith. 196

8.3 The predicted photino energy distribution in the center of mass of the decaying gluino for a gluino mass of 6 GeV/c^2 ($M_{\tilde{\gamma}} = 1$ GeV/c^2). . 199

8.4 Expected energy distributions for geometrically accepted a) photinos and b) neutrinos. Each of the three curves in a) represent the photino spectrum corresponding to gluino masses of 1, 6, and 11 GeV/c^2 ($M_{\tilde{\gamma}} = M_{\tilde{g}}$). 200

8.5 The a) geometric b) time-of-flight and c) trigger acceptance as a function of gluino mass for production at the primary target (solid line) and beam dump (dashed line). 201

8.6 The overall acceptance (the combined geometric, time-of-flight and trigger acceptance) as a function of gluino mass for production at the primary target (solid line) and beam dump (dashed line). 202

8.7 Feynman diagrams for photino interaction in normal matter. 203

8.8 The minimum photino energy required to produce a gluino as a function of the gluino mass (solid curve). Also shown is the maximum energy for time-of-flight acceptance for production at the primary target (dotted line). 205

8.9 For $M_{\tilde{q}}$ of a) 1, b) 10 and c) 100 GeV/c^2 , the photino interaction cross section as a function of photino energy for three photino (gluino) masses (solid, dotted and dashed curves correspond to $M_{\tilde{g}} = 1, 6$ and 11 GeV/c^2 respectively). 207

8.10 Regions of the light gluino window excluded by other experiments at the 90% confidence level adapted from Antoniadis et al. 209

8.11 The previous figure, adapted from Antoniadis et al., is expanded here to show the region of sensitivity of the present experiment. 212

C.1 A Schematic of a time-of-flight counter struck by a single minimum ionizing particle. 219

D.1 Time-of-flight trigger and timing logic circuitry. 223

D.2 Time-of-flight RF clock electronics. 224

INTRODUCTION

A search for weakly interacting massive particles (WIMPs) has been performed in the Tevatron Wide Band Neutrino beamline using a time-of-flight technique exploiting the time structure of the beam. High timing resolution scintillation counters were used to obtain event times relative to the phase of the accelerator RF clock. Events with event times outside of the predicted time structure of the beam were considered as new particle candidates. Zero candidates remained after the analysis. These results have been used to set limits on the existence of neutral weakly interacting massive particles. The details of this analysis are described herein.

We begin by summarizing the Minimal Standard Model (MSM) of Elementary Particle Physics, presenting the theoretical motivation for looking for evidence of new physics beyond the MSM, and describing the framework of a few particular extensions of the MSM where new weakly interacting particles might arise.

The geometry and composition of the neutrino beamline and the characteristics of the neutrino beam are described in Chapter 2, along with a summary of the time-of-flight technique utilized in this experiment to search for new particles. In addition, we describe the charged particle beamline (the *testbeam*) used to transport charged hadrons and muons to the detector for calibration purposes.

The E733 detector is described in Chapter 3, focusing specifically on the properties of the timing apparatus built for this new particle search. Pattern recognition and preliminary timing analysis are set forth in Chapter 4, followed by the full details

of measuring event times relative to the accelerator RF clock described in Chapter 5.

The absence of events outside the measured time structure of the neutrino beam is used to attempt to extend limits on the existence of new particles in Chapters 6, 7 and 8. Specifically, models for the production of directly produced particles, heavy neutrinos, and supersymmetric particles are evaluated. Each model proposed is synthesized by a full computer simulation in order to gauge the sensitivity of the detector to each particular model.

Chapter 1

Theory

1.1 Motivation for a Massive Neutral Particle Search

Historically, searches for new particles have experienced continued interest in the particle physics community. The discovery of such objects can be revealing, leading to "quantum" leaps in our understanding of nature or to sighs of relief as theoretical predictions are confirmed. This tradition of interest continues, exemplified by the recent interest in the possible existence of a 17 keV neutrino [1].

The Standard Model of Elementary Particle Physics is a quantum gauge theory which successfully describes the known elementary particles and their interactions. Yet, there are lingering questions, such as:

- the Dark Matter problem – the visible mass density of the universe is only about 10% of what is necessary to explain the observed expansion rate of the universe and
- the Solar Neutrino paradox – the observed number of neutrinos from the sun is inconsistent with solar model predictions.

Such discrepancies remind us that there are mechanisms in nature, either new particles or other extensions to the theory, that are not included in the Standard Model.

It is generally agreed that the Standard Model as it stands is incomplete as an ultimate theory of matter because:

- it contains a large number of arbitrary parameters such as particle masses and couplings
- it requires additional components that include explanations for inconsistencies such as those stated above
- the gravitational interaction is thus far missing in the theory.

Arguments have been made in favor of particular extensions of the Standard Model that include *weakly interacting massive particles* called WIMPs which have properties such that they provide solutions to the above paradoxes. The acronym WIMPs was coined by Turner [2] to refer collectively to a number of hypothetical states such as axions, light neutrinos, photinos, Higgs fermions, scalar neutrinos, heavy neutrinos etc. They are grouped together because their weakly interacting properties make them good dark matter candidates, among other things. In this document, the use of the acronym "WIMP" is meant to imply the following general properties:

- *Weakly interacting* implies a non-strongly interacting particle that is not necessarily weakly interacting in the sense of the weak force ($W^{\pm}$ or Z^0 exchange).
- *Massive* implies a non-zero rest mass. References made herein to the *light* or *massless* neutrinos indicate those mass eigenstates which couple dominantly to the weak eigenstates ν_e, ν_μ, and ν_τ.
- *Electric charge* properties are not implied; however, in the context of this analysis, a zero electric charge is assumed unless otherwise stated.

The combined results of solar neutrino experiments and e^+e^- collider experiments have ruled out a wide class of dark matter candidates such as weak isodoublet neutrinos and supersymmetric particle candidates with masses less than $\approx 30\mathrm{GeV}/c^2$ [3, 4]. However, all possible states with WIMPy properties have not been ruled out. Such particles will not be seen unless they are explicitly searched for, as in the present analysis.

1.2 The Standard Model

The Standard Model of elementary particle physics is currently unequaled in its ability to describe the observed interactions between elementary particles.

The Minimal Standard Model (referred to henceforth as SM or the Standard Model) contains the minimum number of necessary particles and interactions for a self consistent theory. It includes a set of gauge bosons associated with each interaction type, namely

- one massless photon (γ) that mediates the electromagnetic interaction,
- eight massless gluons (g) exchanged in strong interactions and
- the massive $W^{\pm}$ and Z^0 bosons mediating the weak interaction.

Also included is one neutral scalar Higgs boson (H^0) and three generations of quarks and leptons shown in Figure 1.1. For each quark and lepton, there is a corresponding antiparticle with the same mass but opposite charge.

$$\text{a)} \begin{pmatrix} u^{+2/3} \\ d^{-1/3} \end{pmatrix} \begin{pmatrix} c^{+2/3} \\ s^{-1/3} \end{pmatrix} \begin{pmatrix} t^{+2/3} \\ b^{-1/3} \end{pmatrix} \qquad \text{b)} \begin{pmatrix} e^{-1} \\ \nu_e^0 \end{pmatrix} \begin{pmatrix} \mu^{-1} \\ \nu_\mu^0 \end{pmatrix} \begin{pmatrix} \tau^{-1} \\ \nu_\tau^0 \end{pmatrix}$$

Figure 1.1: The Minimal Standard Model includes three generation of a) quarks and b) leptons. The superscripts indicate the fractional electric charge.

A quantum number called the *lepton number* is associated with each lepton generation of Figure 1.1b), namely L_e, L_μ, and $L_\tau = +1\ (-1)$ for each of the two leptons (antileptons) in each generation, respectively. Lepton number has been observed to be conserved in all types of interactions.

A similar assignment is made in the quark sector for quarks listed in Figure 1.1a) and their antiquarks. All quarks are assigned a *baryon number* [1] $B = +1/3$, while antiquarks have $B = -1/3$. Experimentally it has been observed that baryon number is conserved in all interactions. But unlike the lepton number, the number of quarks of a particular generation are not always conserved (as discussed in a later section).

Quarks and leptons are always created and annihilated in pairs, conserving baryon number (B) and lepton number ($L = L_e + L_\mu + L_\tau$), L_e, L_μ, L_τ) in all interactions.

The SM contains a large number of theoretically unpredictable parameters, namely the particle masses and the couplings between them. These 18 parameters include

- 6 masses for each of the quarks listed in Figure 1.1 a),
- 3 masses for each of the charged leptons of Figure 1.1 b),
- 4 quark mixing angles that specify the Kobayashi Maskawa (KM) matrix discussed below,
- the masses of the W and Higgs bosons, and
- 3 coupling constants expressing how each of the vector bosons couple to the elementary fermions:
    1. α is the *fine structure constant* expressing the coupling between the photon and charged particles. It is usually expressed as $(e^2/(4\pi) \approx 1/137$, proportional to the square of the familiar unit of electric charge e.
    2. θ_W is the Weinberg angle used to relate α to the weak coupling constant (g_{weak}).

[1] Fractional baryon number is assigned so that bound quark states have integral baryon number. Hadrons, consisting of three quarks, have $B = 1$ and mesons, consisting of a quark antiquark pair, have $B = 0$.

3. α_s is the strong coupling constant (sometimes denoted α_3).

Many of these parameters have been experimentally measured. Some fundamental particles have not yet been directly observed; namely, the top quark, the Higgs boson, and the tau neutrino. Indirect evidence of the tau neutrino has been seen in a combination of tau decay and neutrino interaction data. The Higgs and the top quark are expected to be seen as the energy of accelerators increases to a level that can produce them.

The Standard Model is a quantum gauge theory based on the gauge group $SU(3)_C \times SU(2)_L \times U(1)_Y$. It includes the Strong, Weak and Electromagnetic interactions acting between 3 generations of quarks and leptons. The Lagrangian for the exchange of the vector bosons between fermions is given in Equations 1.1-1.4.

$$\begin{aligned}
\pounds &= e\sum_f Q_f \left(\bar{f}\,\gamma^\mu\, f\right) A^\mu && (1.1)\\
&+ \frac{g_2}{\cos\theta_W}\sum_f \Big[\bar{f}\gamma^\mu\left(1-\gamma^5\right) f\left(T_f^3 - Q_f \sin^2\theta_W\right) \\
&\qquad + \bar{f}\gamma^\mu\left(1+\gamma^5\right) f\left(-Q_f\sin^2\theta_W\right)\Big] Z_\mu && (1.2)\\
&+ \frac{g_2}{\sqrt{2}}\left[\left\{\left(\,\bar{u}\;\bar{c}\;\bar{t}\,\right)\gamma^\mu\left(1-\gamma^5\right) V_{CKM}\begin{pmatrix} d\\ s\\ b\end{pmatrix}\right.\right. \\
&\qquad \left.\left. + \left(\,\bar{\nu}_e\;\bar{\nu}_\mu\;\bar{\nu}_\tau\,\right)\gamma^\mu\left(1-\gamma^5\right)\begin{pmatrix} e\\ \mu\\ \tau\end{pmatrix}\right\} W^+ + h.c.\right] && (1.3)\\
&+ \frac{g_3}{2}\sum_q \left[\,\bar{q}_\alpha\,\gamma^\mu\,\lambda^a_{\alpha\beta}\,q_\beta\,\right] G^a_\mu. && (1.4)
\end{aligned}$$

The electromagnetic interaction describes interactions between electrically charged particles mediated by the photon. From the term 1.1, note that the strength of interaction between a photon field A^μ and a fermion is proportional to the electric charge of the fermion ($Q_f\ e$). The sum over f indicates the sum over all fermions.

Since the photon is electrically neutral, the incoming and outgoing fermion carry the same electric charge and photons do not couple to each other.

Color charge is the quantum number exchanged in the strong interaction. QCD, or Quantum Chromodynamics, describes the interaction between color charged objects. Quarks (antiquarks) carry one of three colors [2] (anticolors), while gluons are members of a color octet. In the term 1.4, G^a represents the eight electrically neutral but color charged gluons exchanged in the strong interaction. The sum over q indicates a sum over all quarks (leptons do not have color charge and thus do not participate in the strong interactions). The implicit sum [3] over indices α and β indicates the sum over three colors for the incoming and outgoing quarks. Unlike photons, the gluons exchanged in the strong interaction, carry the type of charge (color) that they couple to. Therefore, gluons interact with any colored objects, including themselves. *Gluon fusion*, a process where two incident gluons couple to form a quark-antiquark state, is expected to be the dominant production mechanism for the heavy quarks (like c (charm) and b (bottom)) in high energy pN interactions discussed further in a later section.

The coupling g_3, sometimes written in terms of the strong coupling constant $\alpha_3 = g_3^2/(4\pi)$, is known to vary considerably with the momentum transfer [4] of the interaction. But in the limited range from 3 to 40 GeV, the value of α_3 is measured to be ≈ 0.15 with an accuracy of about $20 - 25\%$ [5]. This average value is used in Chapter 8 to approximate the interaction cross section of supersymmetric particles with quarks.

Other coupling strengths (leading constants in the first three terms of Equations 1.1-1.3) like the constant $g_2 = e/\sin\theta_W$, also vary with momentum transfer, but at a much slower rate.

[2] The three colors are red, blue and green.
[3] Using the standard convention, repeated indices are meant to be summed.
[4] Momentum transfer is the momentum transmitted by the vector boson.

The Equations 1.2 and 1.3 describe the emission or absorption of the massive Z^0 and $W^{\pm}$ bosons in the so-called weak interactions. The sum over f indicates the sum over all fermions with fractional electric charge Q_f and weak isospin T_f^3. Left and right handed fermions undergo weak interactions in an asymmetric manner, suggesting an inherent handedness of the weak interaction itself. Left (right) handed fermions (antifermions) form weak interaction doublets [5] while right (left) handed fermions (antifermions) act as weak isospin singlets.

In Equations 1.2 and 1.3, the terms $(1-\gamma^5)$ and $(1+\gamma^5)$ select exclusively the left and right handed components respectively. Therefore the second line of term 1.2 describes the only interaction of right handed fermions. Since the interaction coupling is proportional to the fermion electric charge ($Q_f\ e$) and the neutrino is neutrally charged, no term in this lagrangian includes an interaction of right (left) handed neutrinos (antineutrinos). No evidence for right handed neutrinos (left handed antineutrinos) has been found, thus the Standard Model contains only left handed neutrinos (right handed antineutrinos).

In general, a weak eigenstate is not necessarily equivalent to a single mass eigenstate, but rather is a linear combination of mass eigenstates. The unitary matrix that identifies the coefficients of the transformation from the mass eigenstates to the weak eigenstates is called a *mixing matrix*. The term V_{CKM} of Equation 1.3 is a 3 by 3 matrix describing this mixing in the quark sector. Thus

$$\begin{pmatrix} d' \\ s' \\ b' \end{pmatrix} = \begin{pmatrix} V_{ud} & V_{us} & V_{ub} \\ V_{cd} & V_{cs} & V_{cb} \\ V_{td} & V_{ts} & V_{tb} \end{pmatrix} \begin{pmatrix} d \\ s \\ b \end{pmatrix}, \tag{1.5}$$

where d', s' and b' represent the weak eigenstates, and d, s and b are the mass eigenstates. This matrix is constrained to be unitary. Therefore, each of the 9 coefficients is not independent. Rather, the matrix can be expressed in terms of 4 independent parameters. Choosing the parameterization of Kobayashi and Maskawa

[5] A doublet is formed by the two particles in each respective generation shown in Figure 1.1.

[6], with 4 angles θ_1, θ_2, θ_3 and δ:

$$\begin{pmatrix} d' \\ s' \\ b' \end{pmatrix} = \begin{pmatrix} c_1 & -s_1c_3 & -s_1s_3 \\ s_1c_2 & c_1c_2c_3 - s_2s_3e^{i\delta} & c_1c_2s_3 + s_2c_3e^{i\delta} \\ s_1s_2 & c_1s_2c_3 + c_2s_3e^{i\delta} & c_1s_2s_3 - c_2c_3e^{i\delta} \end{pmatrix} \begin{pmatrix} d \\ s \\ b \end{pmatrix}, \tag{1.6}$$

where the shorthand notation $c_1 = \cos\theta_1$, $s_1 = \sin\theta_1$ etc. has been used.

This parameterization was chosen for historical reasons: In the limit where $\theta_2 = 0$ and $\theta_3 = 0$, the angle θ_1 is equivalent to the *Cabibbo mixing angle* (θ_C), the single mixing angle describing the corresponding transformation for the 4 quark case [7]:

$$\begin{pmatrix} d' \\ s' \end{pmatrix} = \begin{pmatrix} \cos\theta_C & \sin\theta_C \\ -\sin\theta_C & \cos\theta_C \end{pmatrix} \begin{pmatrix} d \\ s \end{pmatrix}. \tag{1.7}$$

The magnitude of this mixing angle has phenomenological consequences for decays considered in Chapter 7. In the 3 body decay of the charmed $D^{\pm}$ meson, the charm (c) quark can decay to either a strange (s) quark with strength proportional to $\cos\theta_C$ or a down (d) quark with strength $\sin\theta_C$. The cosine of this angle has been measured to be nearly unity (0.9747), so the charm to strange transition is a *Cabibbo favored* decay. On the other hand, the charm to down transition is *Cabibbo suppressed.* For leptons, experimental evidence of this type of mixing has not been found.

Missing from the lagrangian of Equations 1.1 - 1.4 are terms describing the interaction of the fundamental particles with the scalar Higgs boson field. It is theorized that particle masses arise by way of a spontaneous symmetry breaking mechanism through the interaction of these fundamental particles with the vacuum via Higgs boson exchange [8, 9, 10] (thus the need for the Higgs particle in the Standard Model). The generation of mass by way of this *Higgs mechanism* is appealing in that

1. The breaking of gauge symmetry leads necessarily to massless photons and gluons, yet allows for the massiveness of the W and Z bosons and the fermions.

2. Renormalizability of the theory is preserved [11].

Yet unanswered questions remain. For example:

1. Why does mass increase with each generation for quarks and charged leptons ?

2. Fermion masses are free parameters. Is there some way to predict the particle masses ?

3. Why do the neutrinos appear to be massless ? Why don't we observe a right handed neutrino ?

4. All the charged fermions are Dirac particles. Is the neutrino a Dirac particle or is it a Majorana particle (where the neutrino is its own antiparticle) ?

The present experiment cannot directly address the questions above as to the basic nature of the light neutrinos. But if additional heavy neutrinos exist, the nature of the light neutrinos may determine how these heavy neutrinos manifest themselves. So conversely, a signal of heavy neutrinos may shed light on the nature of the light neutrinos. In a later section, the consequences of nonzero neutrino masses and lepton mixing are described in addition to a consideration of the possibility of the existence of additional neutrinos (including massive right handed neutrinos).

1.3 Phenomenology of Particle Production

By observing how Standard Model particles are produced, we may be able to deduce how non-SM particles might be generated experimentally and consider possible reasons why they might be seen in the present experiment and/or why they have not been seen in other experiments to date. This section describes how different aspects of particle production and decay are studied quantitatively. These results are used to computer model WIMP generation for setting limits on WIMP production in Chapters 6, 7 and 8.

In the Standard Model, quarks are bound within multiparticle states called hadrons (which contain three quarks) and mesons (which contain a quark-antiquark pair). Heavy quark states are those states which contain one or more of the heavier quarks *charm*, *bottom* and *top*. Examples of heavy quark states include the charged $D^{\pm}$ mesons which are bound states of $(c, \bar{d})$ and $(\bar{c}, d)$, respectively. Heavy quark production is of interest here for two reasons.

1. New neutral massive particles (WIMPs) may be a decay product of a heavy quark state, as we will consider in Chapter 7.

2. WIMPs may be produced directly in pN interactions as we will consider in Chapters 6 and 8. For lack of a better phenomenological model, we assume new massive particles to have production characteristics similar to that of heavy quark production.

1.3.1 Production of Massive Particles in pN interactions

In the QCD parton model, nucleons (protons and neutrons) are made up of 3 valence quarks, gluons and quark-antiquark pairs (sea quarks). A parton is any one of these constituents. The quarks carry, on average, half of the nucleon momentum with the gluons bearing the other half. The sea quarks typically carry a much smaller

momentum fraction. In pN interactions, a parton from the incoming proton interacts with one of the partons in the target nucleon. Additional quark antiquark pairs are produced that recombine with the initial state quarks to form hadrons in the final state.

According to this model, heavy quarks are produced via the Drell Yan (quark antiquark annihilation) or gluon fusion mechanisms. The leading order Feynman Diagrams for these processes is shown in Figure 1.2.

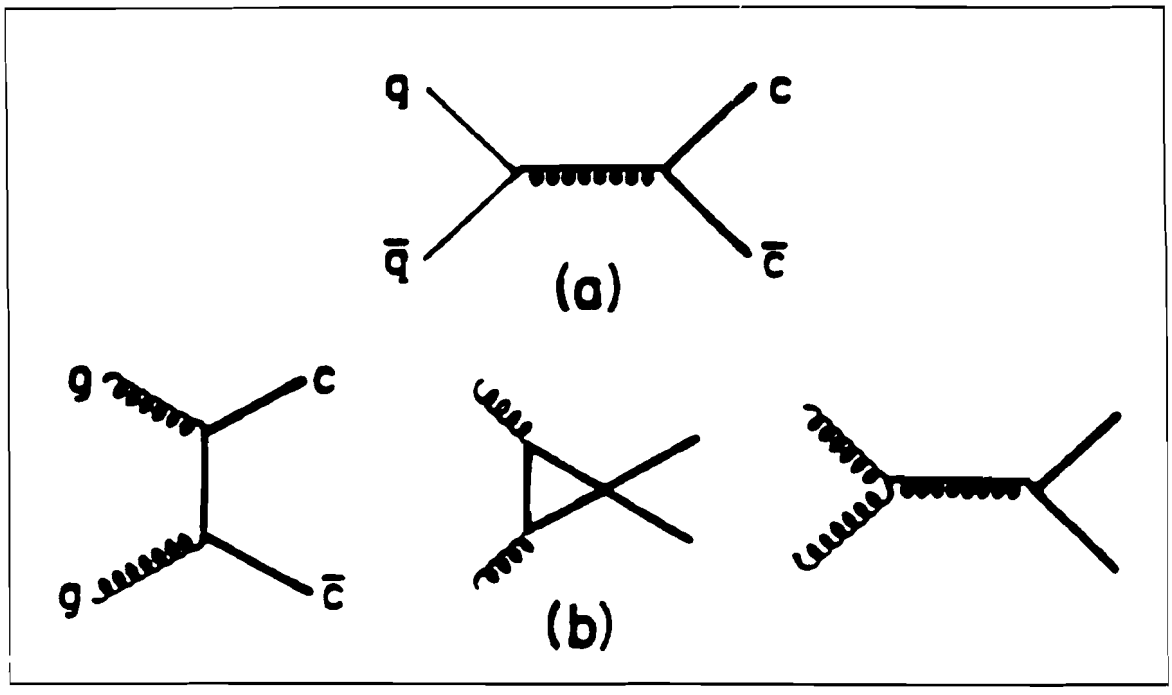

Figure 1.2: Feynman Diagrams for heavy quark production in hadron-nucleon interactions via a) Drell Yan and b) Gluon Fusion processes.

At high incided beam energy ($E > 200$GeV), gluon fusion is expected to be the dominant mechanism for heavy quark production. The cross section for the Drell Yan process is relatively less significant since the probability of finding an antiquark in a nucleon is small.

Because bottom hadroproduction data are meager, the majority of heavy quark production phenomenology has been based almost exclusively on the studies of charm particle production. Charm meson hadroproduction cross section measurements,

presented in Chapter 7, are consistent with QCD parton model predictions [12].

Chapters 6, 7, and 8 all use assumptions about the differential production rates. The following section describes how differential production is parameterized.

1.3.2 Scaling variables for Production

Many hadroproduction experiments have studied how charm particles are produced. In the center-of-mass coordinate system of the collision, the longitudinal momentum[6] is described in terms of the variable *Feynman X* (x_F), the fraction of the maximum possible longitudinal momentum ($p_{||}^{MAX}$) carried off by the inclusively produced particle:

$$x_F = \frac{p_{||}}{p_{||}^{MAX}}. \tag{1.8}$$

The maximum momentum ($p_{||}^{MAX}$) is assumed to be half of the center-of-mass energy squared ($\sqrt{s}$). Therefore,

$$x_F = \frac{2p_{||}}{\sqrt{s}}. \tag{1.9}$$

The transverse momentum[7] (p_T) has been measured to be distributed exponentially.

Production in the center-of-mass frame is parameterized using the form

$$\frac{d^2\sigma}{dx_F dp_T^2} \propto (1 - |x_F|)^n \times e^{-b(p_T^2)}, \tag{1.10}$$

where n and b are constants determined empirically for a particular process. We assume longitudinal and transverse momentum components are independent.

The motivation for using this parameterization is as follows. Using QCD fragmentation[8] arguments in the high x_F region, the inclusive cross section for any final state particle should be of the form $(1 - |x_F|)^n$ [13]. This form seems to be

[6]The longitudinal momentum is the momentum in the direction of the interacting particles.

[7]The transverse momentum is the momentum in the plane perpendicular to the direction of the interacting particles.

[8]Fragmentation is the process whereby dissociated partons always produce quark anti-quark pairs which then combine to form a collimated 'jet' of hadrons.

universally accepted (over all x_F) although occasionally experimentalists chose to fit for different values of n in the low and high x_F regions. If a final state hadron contains one of the initial valence quarks, it is more likely to be produced at high x_F, since valence quarks are more likely to have a high momentum fraction. This is called *leading production.* On the other hand, *non-leading production* refers to production of hadrons that do not contain a valence quark, which is more likely to be produced with low x_F.

Forms for the p_T dependence vary. Alternative forms include $e^{-bp_T^2}$ and e^{-bp_T} depending on the beam type and energy, x_F range, target type and experimental prejudice.

In the simulations described in the last 3 chapters, different values (or ranges) of the parameters b and n are used, depending on the type of production considered.

1.3.3 Decays

Particles produced via decay of some heavier particle have an energy and angular dependence that is model dependent. For the models considered in this thesis, we expect the decay products to have a a flat angular distribution in the center of mass of the parent particle (isotropic decay). The energy distribution of decay products is predicted on a case by case basis.

1.3.4 *"A dependence"* of Production Cross Sections

The term *"A dependence"* refers to the dependence of the cross section on the atomic weight of the target nuclei involved in an interaction. In the present experiment, the primary target is composed of beryllium oxide (A=17) and the beam dump is made of aluminum (A=27). It is important in this analysis because different types of particle production are known to have different atomic weight dependence. In particular, charm production cross sections have been measured to have a stronger A dependence than the average inelastic process cross section. In a beam dump

experiment, this results in an enhancement of the charm production probability in denser targets.

The basic mechanism for A dependence is not well understood. In the parton model, interactions occur between relatively free quarks and gluons in the nucleus. Intrinsic motion of partons in nuclei are affected by collective nuclear effects. So effective parton distributions [9] are known to change with atomic number.

The A dependence is determined by measuring α in the following formula for the invariant cross section for a particular process:

$$E\frac{d^3\sigma}{dp^3} = \sigma_0 A^{\alpha}. \tag{1.11}$$

where α is a constant and σ_0 is the invariant cross section for a hydrogen target for the same process.

The constant α for the total inelastic cross section has been measured to be 0.72 ± 0.01 [14] for protons with energies ranging from 60 to 280 GeV on six different target types (with a range in A from 7 to 238).

The constant α for charm production in pN interactions has been measured by over 30 experiments, many of which give seemingly contrary results. A thorough summary and interpretation of the results of these experiments is given by Tavernier [12]. Paraphrasing the conclusion of this study: The total charm production cross section depends more or less linearly on the atomic number A.

[9] Parton distributions express the momentum distribution of quarks or gluons in nuclei.

1.4 Extensions of the Standard Model

Though new heavy neutral particles don't fit into the Minimal Standard Model, they do fit into modest extensions of the Standard Model as described below. Limits obtained from detailed simulations for the particular models considered in this analysis are presented in the last 3 chapters.

1.4.1 Neutrino Mixing and Neutrino Oscillations

In the Standard Model, right handed neutrinos do not exist and left handed neutrinos are strictly massless. If neutrinos are indeed massless, there is no need to diagonalize the mass matrix as required in the quark sector to relate the mass eigenstates to the weak eigenstates. Hence, there is no mixing in the lepton sector as in the quark sector.

The current upper limits [15] on the mass of the mass eigenstates which couple dominantly to the weak eigenstates ν_e, ν_μ, and ν_τ are

$$\begin{aligned} m(\nu_1) &\leq 7.3 \ \text{eV/c}^2 \\ m(\nu_2) &\leq 0.27 \ \text{MeV/c}^2 \\ m(\nu_3) &\leq 35. \ \text{MeV/c}^2, \end{aligned}$$

respectively. There are no theoretical reasons to believe that these masses really vanish. Phenomenological consequences of nonzero neutrino masses can include lepton mixing analogous to the mixing observed in the quark sector and/or a quantum mechanical phenomenon called neutrino oscillations.

Consider a simple model that includes two nondegenerate neutrino mass eigenstates ν_1 and ν_2 that are related to the weak interaction eigenstates (ν_e and ν_μ) by a unitary transformation characterized by the mixing angle θ as follows:

$$\begin{pmatrix} \nu_\mu \\ \nu_e \end{pmatrix} = \begin{pmatrix} \cos\theta & \sin\theta \\ -\sin\theta & \cos\theta \end{pmatrix} \begin{pmatrix} \nu_1 \\ \nu_2 \end{pmatrix}. \tag{1.12}$$

Neutrinos are produced via the weak interaction. In this case, assuming some non-trivial mixing ($\alpha \neq 0, \pi/2, etc.$), the weak eigenstates consist of two-component waves.

As the state propagates through space, the various components evolve differently, and physical manifestations of this differing evolution may occur. To detect mixing it is essential to be able to distinguish between interactions of one component of a wave over the other. In this example, ν_μ interactions usually produce a muon in the final state, while ν_e interactions do not, so this distinction is possible.

Assume an initially pure ν_μ beam is produced with momentum p. After a time, the beam would be composed of some admixture of ν_μ and ν_e that oscillates with time (and distance). The probability of finding a ν_μ in the beam after a time t, is given by

$$P(\nu_\mu \rightarrow \nu_\mu) = 1 - sin^2 2\theta \;\; sin^2 \left[\frac{(E_2 - E_1)t}{2}\right]. \tag{1.13}$$

The momentum of each component is the same but the masses differ, so E_1 and E_2, the energy of each component, respectively, are not the same. The probability of finding a ν_e at the same time is $1 - P(\nu_\mu \rightarrow \nu_\mu)$.

Further, if we assume $p >> m_1$ and $p >> m_2$, then

$$P(\nu_\mu \rightarrow \nu_\mu) \cong 1 - sin^2 2\theta \;\; sin^2 \left[\frac{(m_2^2 - m_1^2)L}{4E}\right], \tag{1.14}$$

where E is the average beam energy, L is the distance traveled in time t, and m_1 and m_2 are the ν_1 and ν_2 masses, respectively.

For oscillations to occur, the mass eigenstates must have degenerate masses and the mixing angle must be nontrivial. To detect oscillations, the beam energy and detector configuration must be optimized so that the oscillation length

$$l = \frac{4E}{(m_2^2 - m_1^2)} \tag{1.15}$$

is comparable to the distance L for the mass difference of interest.

Consider the following possibilities:

1. If L is much shorter than the oscillation length l, then the beam will essentially be in its original state because oscillations have not yet developed.

2. If L is comparable to l, the composition of the beam will vary with L as in Equation 1.14. This is experimentally feasible for mass differences squared between 0.01 and 1000eV^2.

   (a) For mass differences smaller than 0.01, the beam energy required is too small and thus difficult to study.

   (b) For mass differences larger than 1000 eV^2, even for high beam energy, the oscillation length becomes small relative to the detector size.

3. If L is much larger than l, then the oscillation pattern will have been washed out because of the finite energy spread of the beam. Expressed quantitatively, the fractional deviation of the oscillation length is proportional to that of the energy. So oscillations become washed out after a distance $x = l/(\delta E/E)$.

To conclude this oscillation discussion: The detection of *neutrino oscillations* is not possible for large mass differences because of experimental limitations listed above in cases 2b) and 3). But evidence of *neutrino mixing* may still be present: As the mass difference becomes large, the oscillation length becomes so short that it cycles many times over the length of the detector. The oscillating term in Equation 1.14 averages to a constant, so the probability $P(\nu_\mu \rightarrow \nu_e)$ no longer varies with distance. It becomes

$$P(\nu_\mu \rightarrow \nu_e) = \frac{1}{2} sin^2 2\theta. \tag{1.16}$$

The masses of the light neutrino eigenstates are known to be small, so the present experiment is not sensitive to mixing among the known light neutrinos. But if a light neutrino mixes with a new heavy neutrino eigenstate with mass $\gtrsim$500MeV/c^2 as described in Chapter 7, the heavy state would manifest itself by arriving at the

detector later than its light counterpart. Thus, this is not a neutrino oscillation experiment but it is complementary to the search for neutrino oscillations because it can detect large mass differences even for small mixing angles as we will see in Chapter 7.

1.4.2 Supersymmetry

Supersymmetry is a symmetry that associates an integral spin particle with each half integral spin particle and vice versa. This extension of the Standard Model has received considerable attention in theoretical and experimental circles since its proposal nearly 20 years ago. It is appealing in that it provides a framework for unifying the Standard Model of strong, weak and electromagnetic interactions with the gravitational interaction. There are many excellent papers summarizing supersymmetry and its implications [16, 17, 18].

The Minimal Supersymmetric Standard Model incorporates the minimum number of new associated particles and interactions: one superpartner is associated with each Standard Model particle plus additional Higgs doublets to generate masses for the "up" and "down" type quarks and leptons.

In general, the naming conventions for the superpartners (supersymmetric partners of Standard Model particles) are

- For the gauge bosons, add the suffix *-ino*.
- For the elementary fermions (quarks and leptons), add the prefix *s*.

A superpartner has all the same quantum numbers as its SM counterpart, differing only in its spin. The symbol for a superpartner is a tilde symbol over the symbol for the Standard Model particle corresponding to it. These naming conventions and symbols are shown in Table 1.1.

Superpartner masses are the only additional model independent parameters in the theory. The squarks and sleptons are generally referred to collectively (as in

Table 1.1: Supersymmetric particle naming conventions, symbols and spin.

Associated with each Standard Model particle		is a supersymmetric partner	
l	lepton ($s = 1/2$)	$\tilde{l}$	slepton (s=0)
q	quark ($s = 1/2$)	$\tilde{q}$	squark (s=0)
γ	photon ($s = 1$)	$\tilde{\gamma}$	photino ($s = 1/2$)
g	gluon ($s = 1$)	$\tilde{g}$	gluino ($s = 1/2$)
$W^{\pm}$	W boson ($s = 1$)	$\tilde{W}^{\pm}$	Wino ($s = 1/2$)
Z^0	Z boson ($s = 1$)	$\tilde{Z}^0$	Zino ($s = 1/2$)
...	...	...	...

Table 1.1), rather than speaking of them in terms of generation, since their masses (and mass hierarchy) is not known. The couplings of SUSY particles to each other and to SM particles are expected to be the same as the familiar Standard Model couplings, with the following exception: Because cross sections in general depend on the mass of intermediating particles, the mass of the superpartners exchanged affects the overall rate of any supersymmetric process.

If this symmetry were not broken, superpartners would have the same masses (and couplings) as their SM counterparts. Therefore if supersymmetry exists in nature, it is badly broken, because of the absence of evidence of supersymmetric partners in searches to date at currently accessible mass scales.

R-invariance

Theories where supersymmetry is respected at low energies usually include a global U(1) invariance which leads to a conserved quantum number called **R-parity**. R-parity is defined as

$$R = (-1)^{3(B-L)+2S}$$

where B and L are the Baryon and Lepton number respectively and S is the particle spin. Conventional SM particles (quarks and leptons) have even R-parity, while their SUSY counterparts have odd R-parity.

As is conventional, we assume R-parity is conserved. Phenomenological consequences of this assumption are

- each interaction vertex must contain supersymmetric particles in pairs,
- the decay of a superpartner produces another superpartner, and
- the lightest superpartner (LSP) is stable.

It is generally assumed that all superpartners are unstable except for the LSP. Consequently, the LSP is the final decay product in any decay chain of heavier superpartners. Cosmological considerations restrict the LSP to be neutrally charged and non-strongly interacting [19]. It may be weakly interacting in matter, with an interaction cross section comparable to that of the neutrino.

Low Energy Supersymmetric Theories

Theories which include superpartners with masses around 100 GeV/c^2 are generally referred to as *low energy supersymmetric theories* [18]. Many such possibilities have been ruled out, however, there remains some controversy about the possibility of light gluinos with masses in the range $1\text{GeV/c}^2 < Mass_{gluino} < 5\ \text{GeV/c}^2$ [15]. This mass range is within that kinematically accessible in the present experiment: In Chapter 8, we estimate the sensitivity of the E733 detector to a specific model of supersymmetric particle production that includes gluinos with masses in this *light gluino window*.

Chapter 2

The Beamlines

2.1 The Time-of-Flight (TOF) Search Technique

The technique utilized in this experiment to search for neutral heavy particles in a beam dump was first suggested by Shrock [20].

800 GeV/c protons strike the primary production target in bunches synchronous with the accelerator RF clock. The bunches are separated by about 19 ns. The neutrino beam is primarily composed of neutrinos from conventional sources, in other words, neutrinos from the decay of pions or kaons produced by protons at the target. The beam may also contain a small fraction of neutrinos from prompt sources (from the decay of short lived heavy quark states, for example from charmed D mesons). The charged secondaries and their light decay neutrinos are highly relativistic, so they maintain the time structure of the protons on target as they traverse the over 1000 meter distance to the E733 detector. Therefore, the neutrino beam enters the E733 detector in bunches separated in time by about 19 ns. The shape of each bunch in time is expected to be approximately gaussian with an RMS deviation of less than 1 ns.

Event times relative to the phase of the RF clock are measured using high timing resolution scintillator counters operating parasitically within the detector of neutrino experiment E733 during the 1987 Tevatron fixed target run. The pattern recognition

capabilities of the calorimeter and spectrometer are used in combination with the scintillator output to reconstruct event times.

We assume the mean arrival time of all neutrino bunches relative to the RF clock is centered at $t = 0.0$ ns. Measured event times are folded into a single period of the RF clock from ≈ -9.5 to $\approx +9.5$ ns (total width = 18.83 ns). The root mean square deviation of the measured event time distribution is less than 1 ns (see Chapter 5).

Except for cosmic ray interactions, there is no known mechanism that is expected to produce an event in the E733 detector with an event time outside of the window corresponding to the arrival time of a neutrino bunch. This experiment exploits this property of the neutrino beam to search for new physics. An event time outside of the expected neutrino event time window is a distinct signature of a massive particle.

Any unknown massive neutral particle produced in the beamline that travels collinearly with the neutrino beam will arrive at the detector later than it's respective neutrino bunch because it is not traveling at the speed of light. This delay in time is called the 'time of flight' (t_{TOF}). More precisely, the t_{TOF} is the time for a massive particle to traverse a given distance minus the time a massless (speed-of-light) particle would require to travel that same distance. It is well approximated by (see Appendix B)

$$t_{tof} = \frac{D}{2c}\left(\frac{M^2}{P^2}\right), \tag{2.1}$$

where D is the distance from the point of production to the point of interaction or decay, M is the particle mass, c is the speed of light, and P is the particle momentum.

Some degree of ambiguity is associated with the t_{TOF} that is measured for a particular event because time measurements are folded into a single period of the RF clock. If the actual t_{TOF} of the massive particle is greater than the period of the accelerator clock (18.93 ns), the time that is measured is

$$t'_{TOF} = t_{TOF} - 18.93 \times m, \tag{2.2}$$

where m is an integer that shifts t_{TOF} into the time window from -9.5 to 9.5 ns. The effects of this ambiguity will be seen in Chapters 6, 7 and 8, the simulation chapters of this thesis.

In the absence of events in the signal region of the event time distribution, models of new particle production that include such events can be excluded. Such is the case in this analysis. No events were found with properties inconsistent with that of a neutrino event. This null result was used to set limits on the existence of directly produced massive particles in the last three chapters.

A high resolution time-of-flight technique has been used previously in a Fermilab neutral beam experiment to search for new massive objects [21] produced in 300 GeV/c pN collisions. The present experiment is the first implementation of this technique in a Tevatron neutrino beam line experiment utilizing a higher beam energy (800 GeV/c).

In summary, the minimum bias nature of the detector triggering system (as described in Chapter 3) and the addition of the time-of-flight apparatus to the detector makes the E733 detector uniquely sensitive to new physics. Any weakly interacting massive neutral particle that either decays or interacts in the detector leaves a distinctive signature, a t_{TOF}, which is characteristic of the mass of that particle.

2.2 The Wide Band Neutrino Beamline

2.2.1 Overview

A wide band neutrino beam is produced as a result of the following processes:

- 800 GeV/c protons on a target produce an intense spray of charged and neutral secondary particles, predominantly pions, kaons and protons
- a series of collimators and magnets immediately downstream of the target serve to focus charged secondaries into an evacuated decay pipe
- Approximately 5 % of the charged pions and 28 % of charged kaons entering the pipe decay, usually via decay modes with neutrinos in the final state
- A beam dump located downstream of the decay region serves to absorb all undecayed hadronic matter and charged leptons leaving only the weakly interacting uncharged neutrinos to enter the detector.

2.2.2 Constituents and Spectra

The neutrino beam utilized in the 1987 fixed target run in the N-Center Neutrino Beamline at Fermilab has been modeled in detail. A schematic of the beamline is shown in Figure 2.1.

Protons with momentum 800 GeV/c strike a 1 interaction length beryllium target. The differential and total cross sections for charged and neutral secondaries are predicted using a scaled production model [22] which incorporates measurements of the characteristics of charged secondaries produced by 400 GeV/c protons on beryllium targets [23]. A configuration of beam focusing elements called the The Quad Triplet Train [24] is located immediately downstream of the target. This train consists of a series of collimators and quadrupole magnets configured to optimally focus charged secondaries of momentum 300 GeV/c into the decay region. No sign

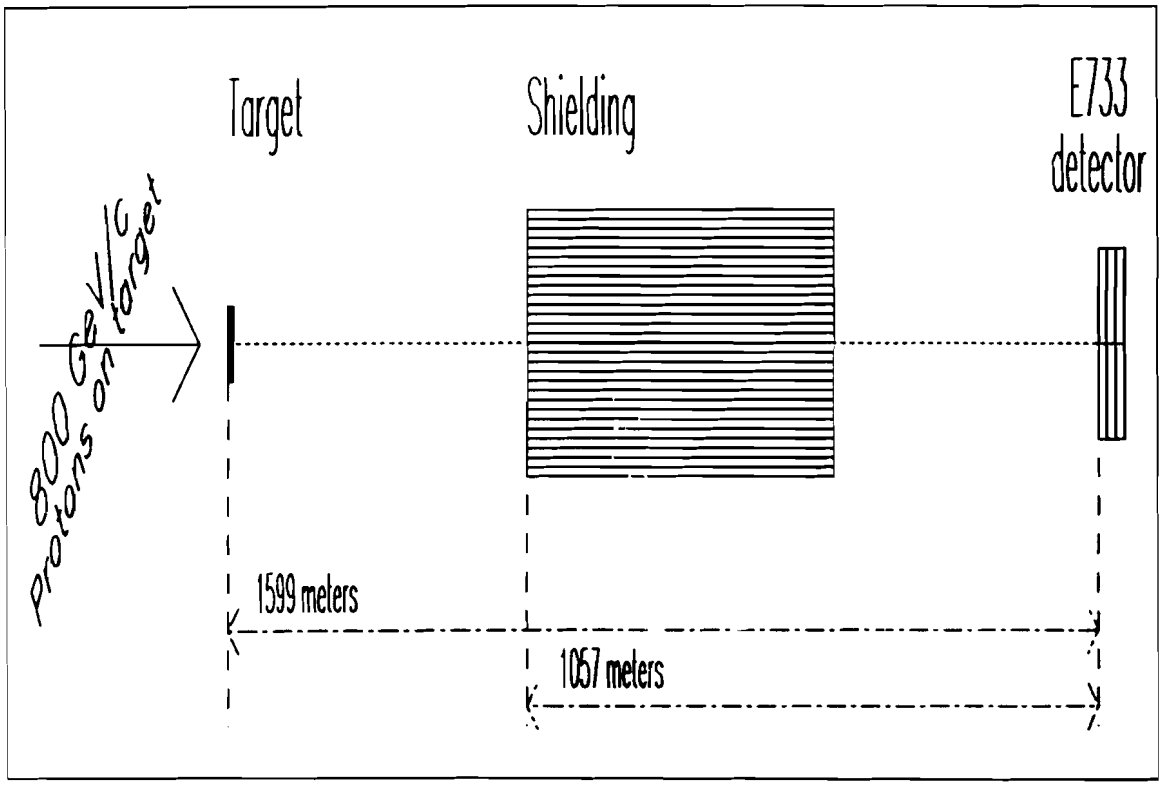

Figure 2.1: Schematic of the Wide Band Neutrino Beamline.

selection is performed by the train so the resulting flux at the detector contains both neutrinos and antineutrinos.

The traversal of particles through the train is simulated using Decay Turtle [25], a computer program designed to model charged particle transport systems. Shown in Figures 2.2 a-f are the predicted energy spectra for charged secondary pions, kaons and protons as they enter the decay region.

The proton and antiproton spectra are included here because they are of interest in the production of massive neutral particles at the beam dump demonstrated in Chapters 7, 6, and 8. The rise in the proton energy spectrum above 400 GeV/c models the expected diffractive component of the secondary proton beam. Very little data exists that measures particle production in this regime. This spectrum reflects what we believe to be reasonable based on what experimental and theoretical information is available.

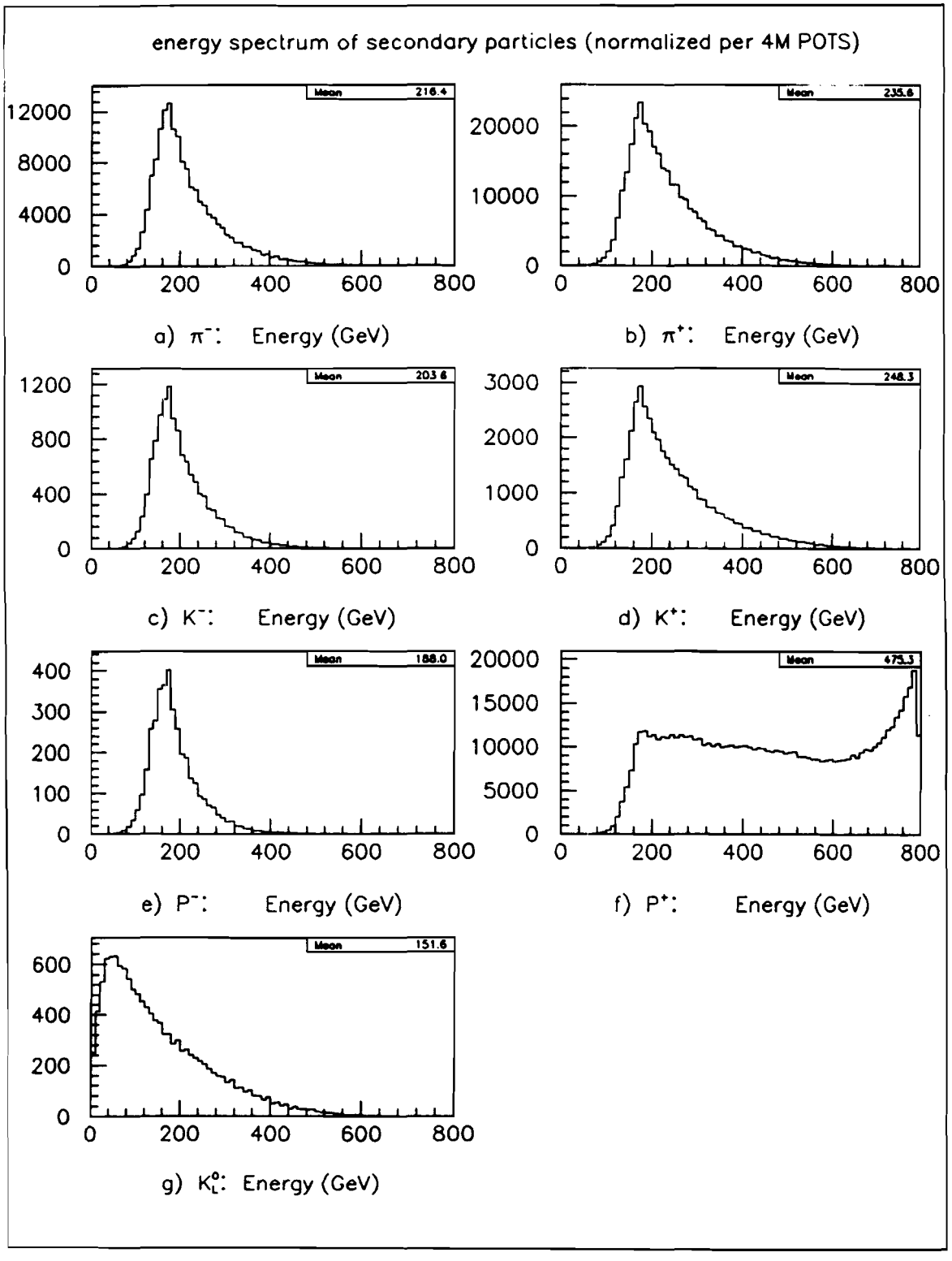

Figure 2.2: Energy Spectrum of Secondary $\pi^{\pm}$, $K^{\pm}$, $p\pm$, and K_L^0 as they exit the Quad Triplet Train

Because secondaries are transported along a straight path from the target into the decay region, neutral secondaries that have neutrino decay modes such as K_L^0 [26] must also be considered as a source of neutrinos in the beam line simulation. The expected energy spectrum of K_L^0 is shown in Figure 2.2 g.

The energy spectrum for each of the charged secondaries rises sharply from about 100 to 200 GeV/c . Low energy charged secondaries (E_ν < 100 GeV/c) are swept out of the beam as a feature of the Triplet Train. This feature has no effect on the neutral particles, thus the K_L^0 energy spectrum demonstrates no such low energy cutoff.

Shown in Table 2.1 are the factors involved in estimating the number of secondary particles entering the decay region per proton on target.

Table 2.1: Secondary Production Efficiencies and Focusing Efficiencies

Term	π^+	K^+	p^+	π^-	K^-	p^-	K_L^0
X^i_{model}	1.109	0.143	0.686	0.723	0.082	0.036	0.097
E^i_{train}	0.073	0.075	0.252	0.053	0.038	0.027	0.033

The index i is used to indicate beam particle dependence. X^i_{model} represents the number of secondaries of type i produced at the target per proton on target according to the scaled particle production model [22] mentioned previously. E^i_{train} (train efficiency) is the number of secondary particles of type i that exit the Quad Triplet Train per number produced at the target as predicted by the train simulation [25].

The decay modes considered to be significant sources of neutrinos at the detector are from the two body decay of pions and the two and three body decay of kaons. A computer simulation of the neutrino decay modes of these secondary particles is used to obtain a representation of the neutrino flux at the E733 detector. This simulation predicts the neutrino energy spectrum and the correlated radial distribution at the

detector for each neutrino type from each secondary source. This program also calculates the fraction of neutrinos entering the detector fiducial volume of those produced from each decay mode times the probability for that parent to decay. The values of this fraction, labeled F^i_j, is shown in Table 2.2 along with the decay modes and relative branching ratios Br^i_j.

Table 2.2: Neutrino Decay Modes and Associated Efficiencies

Term	$\pi^+ \to \mu\nu_\mu$	$K^+ \to \mu\nu_\mu$ $(\to \mu\nu_\mu\pi)$ $(\to e\nu_e\pi)$	$\pi^- \to \mu\bar{\nu}_\mu$	$K^- \to \mu\bar{\nu}_\mu$ $(\to \mu\bar{\nu}_\mu\pi)$ $(\to e\bar{\nu}_e\pi)$	$K^0_L \to \mu\nu_\mu\pi$ $(\to e\nu_e\pi)$
Br^i_j	1.000	0.6350 0.0320 0.0482	1.000	0.6350 0.0320 0.0482	0.270 0.386
F^i_j	0.0231	0.0632 0.0636 0.0633	0.0225	0.0544 0.0552 0.0541	0.0117 0.0119
ν^i_j/POT $(\times 10^{-4})$	18.670	4.270 0.217 0.324	8.613	1.096 0.056 0.083	0.111 0.160
$\sum_j \nu^i_j/POT$ $(\times 10^{-4})$	18.670	4.811	8.613	1.235	0.271

The index j is used to indicate decay mode dependence. Using the values for F^i_j and Br^i_j in Table 2.2 and X^i_{model} and E^i_{train} in Table 2.1, one can calculate the expected number of neutrinos from each secondary parent type (index i) and decay mode (index j) per proton on target (POT) using the formula

$$\frac{\nu^i_j}{POT} = X^i_{model} * E^i_{train} * BR^i_j * F^i_j. \tag{2.3}$$

The values of ν^i_j/POT are also shown in Table 2.2. Also shown in this table is $\sum_j \nu^i_j/POT$ representing the relative contribution to the neutrino flux from each respective source i.

Shown in Figure 2.3 is the measured energy spectrum of interacting neutrinos

within the TOF fiducial volume compared with the predicted spectrum. The predicted distribution shown is weighted by neutrino energy in order account for the known linear energy dependence of the interaction cross section. This spectrum is not corrected for energy resolution effects [27] or second order corrections to the $K_{\pm}/\pi_{\pm}$ flux ratio [28]. These spectra agree adequately for the purpose of this analysis.

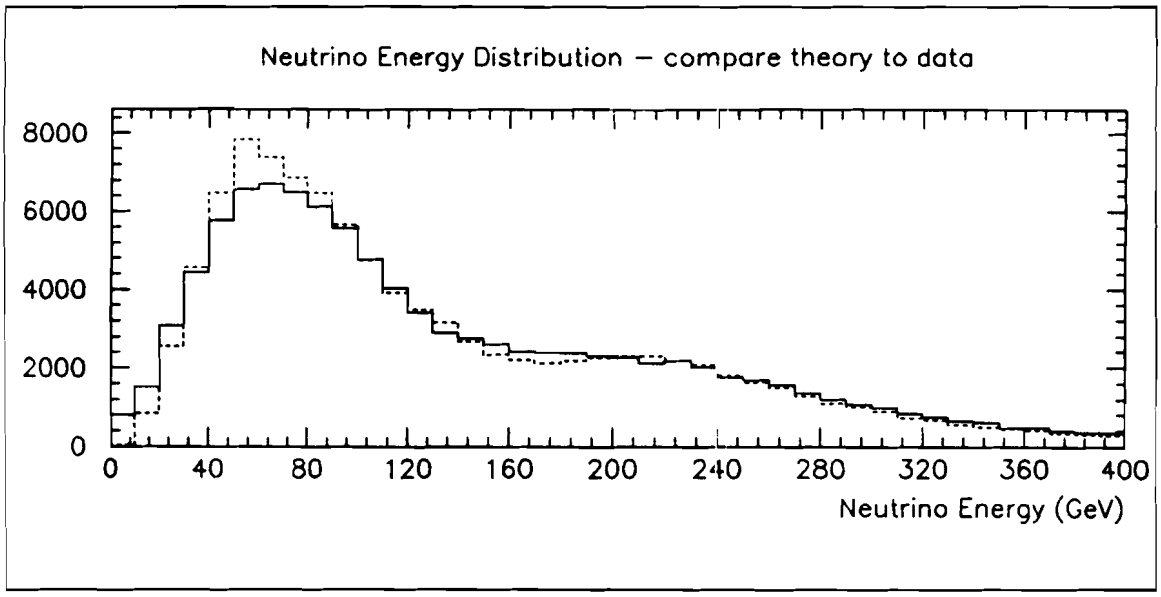

Figure 2.3: The predicted neutrino energy distribution (dashed line) compared to that seen (solid line) in the E733 detector. The predicted spectrum is weighted by energy to account for the known linear dependence of the neutrino interaction cross section. The data sample consists of all charged current neutrino interactions with a reconstructed primary vertex in the TOF fiducial volume.

2.2.3 Beamline Elements

Because of the large flux intensity and mean energy of the primary and secondary hadron beams, their absorption can produce unknown neutral massive particles in large quantities if these particles exist. Beamline elements of particular interest in searching for new particles are those elements which absorb a large fraction of the primary proton flux or the predicted secondary particle flux. Specifically, the geometry and composition of the neutrino target, the beam dump and the berm are relevant.

The primary neutrino target is located 1599 meters upstream of the detector. It is beryllium oxide (A=17) and is one nuclear interaction length long. Its cross section is many times that of the proton beam spot size. Therefore, it is expected that approximately 2/3 of all protons on target interact in the target producing secondaries, leaving approximately 1/3 (1/e) remaining 800 GeV/c primary protons undeflected through the target, the Quad Triplet Train, and the decay pipe.

Uninteracted primary protons and undecayed secondaries are eventually absorbed in the effectively infinite hadron beam dump located 1057 meters upstream of the E733 detector at the end of the decay pipe . The beam dump consists of four 5 foot long modules. The first two modules consist of a water cooled aluminum absorber $18\frac{1}{2}''$ wide $\times 26\frac{1}{2}''$ high set in steel extending to a width of $37''$ and height of $35''$. The following two modules are solid steel. Monte Carlo calculations requiring dump characteristics assume the dump composition is a uniform aluminum block (A=27) since over 99.9 % of the primary and secondary beams have a primary interaction within the first two modules.

The space (about 1050 meters) between the end of the beam dump and the face of the detector (called the "berm") contains various amounts of steel and lead inserts within dirt fill to make it more radiation hard. In addition, this space contains ion chambers, scintillation counters and muon counters for beamline monitoring and 2 other experimental halls housing neutrino detectors. In other words, the exact composition and precise amount of material in the berm is not known [29]. The beam dump and berm are collectively referred to as the *shielding*. For the purpose of anticipating event rates in the detector from weakly interacting particles, we have assumed the shielding is filled uniformly with material with a mean density equal to that of iron (density $\rho = 7.87 g/cm^3$). Using this density, the effective number of targets per unit area in the shielding (with length $L = 1057m$) is

$$N_{dump} = \rho \times N_A \times L \tag{2.4}$$

$$= 5.03 \times 10^{29} nucleons/cm^2 \tag{2.5}$$

Similarly, the mean density of the detector is $1.35 g/cm^3$ [30], so the effective number of targets per unit area in the fiducial volume is

$$N_{det} = 8.1 \times 10^{26} nucleons/cm^2. \tag{2.6}$$

2.2.4 Monitoring and Logic Gates

We begin with the assumption that new massive particle production is initiated by known particles in the beamline. Then the total integrated "live" protons on target (live POT's) during the 1987 fixed target run is a factor in estimating the number of new massive particles expected to be seen during the run. This estimation is carried out for a number of particle production models in Chapter 6. All of these models use the measured number of POTs as described below.

The number of POTs is obtained using a combination of beam monitoring information and logic gate pulses that indicate when particular beamline and detector conditions are satisfied.

Protons are extracted from the Tevatron into the fixed target beam lines for 20 seconds of the minute long accelerator cycle. During this 20 second spill, protons are fast extracted onto our primary neutrino target in three bursts or "pings", each lasting about 2 ms.

A toroid pulse monitor located just upstream of the primary production target monitors the flux of protons on target during each ping. The monitor output, a pulse train, is counted by scalars, each pulse corresponding to 10^{10} protons on target.

A schematic of the toroid pulse monitor output representing the proton intensity during a single ping as a function of time is shown in Figure 2.4 a. Figures 2.4b-e show the corresponding activity of the spill gate, beam gate, dynamic beam gate, and live beam gate logic pulses during each ping. These logic gates turn "on" and "off" when particular conditions are satisfied for the purpose of monitoring live POTs.

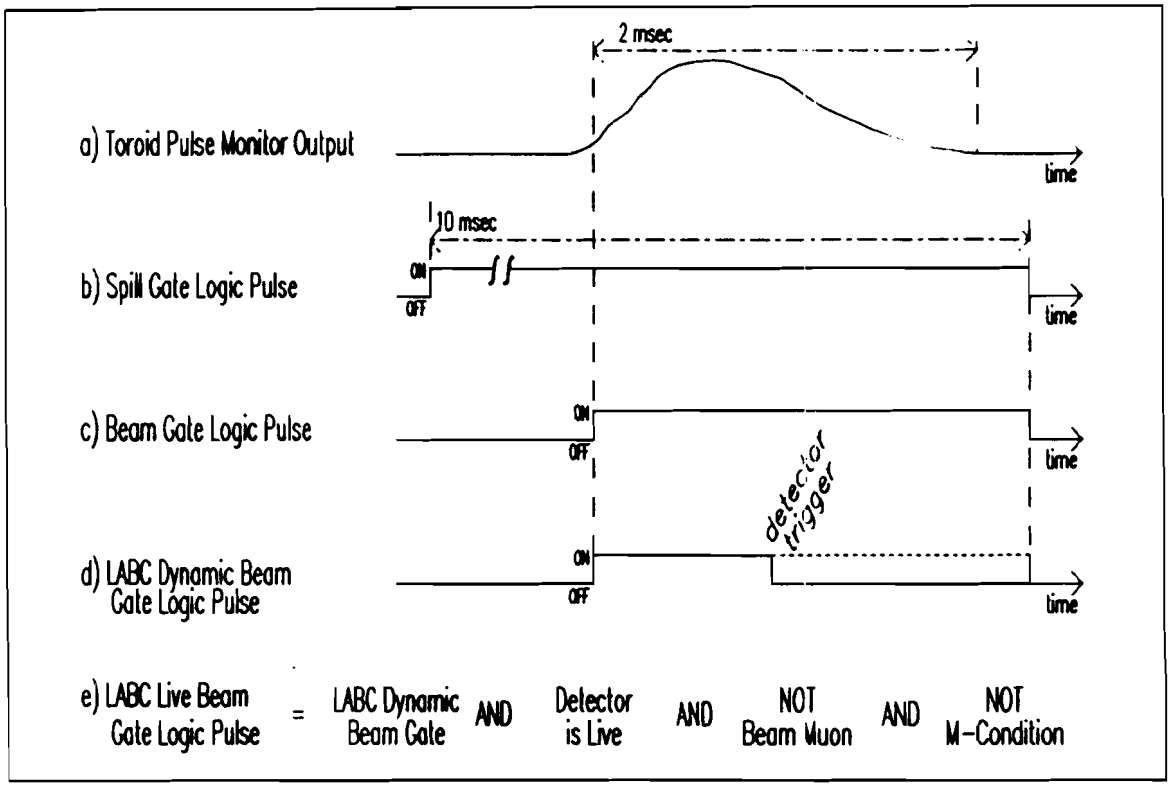

Figure 2.4: Schematic: Beam monitor signal and various logic gates.

The spill gate logic pulse is a fairly wide pulse (about 10 ms wide) meant to inclose each 2 ms ping. It turns on at some predetermined time before a 2 ms proton burst is expected as dictated by accelerator operations.

The beam gate and dynamic beam gate logic pulses both turn on when the toroid pulse monitor registers a signal above a discriminated threshold indicating a significant flux of protons on target. The beam gate pulse turns off with the spill gate, while the LAB C dynamic beam gate turns off with spill gate or when the detector is triggered whichever comes first.

The LAB C live beam gate is on when the LAB C dynamic beam gate is on and the detector is ready to take a trigger (detector is "live").

Additionally, to calculate "live POTS", a few trigger considerations need to be taken into account because they introduce detector "dead time" (time in which events could satisfy the trigger but the detector is unable to trigger because of some

coexisting condition) which translates into a "dead fraction" (a fractional reduction in the live POTs).

The first of these trigger considerations is the rejection of events induced by beam muons punching through the front face of the detector. A veto wall (acrylic scintillator plane $4' \times 8'$) located at the front face of the detector detects these stray muons caused primarily by neutrino interactions upstream of the detector. If a neutrino event occurs within approximately 1 μs of a detected beam muon, the detector will not trigger.

Another trigger consideration is the dead time caused by the delay between the pre-trigger being satisfied and a complete trigger decision being made. The detector triggering system is described in Chapter 3. Briefly, the detector employs a two step triggering system. The first level is called the pre-trigger or M-condition which looks for a coincidence signal from any 2 proportional tube planes above a minimum ionizing particle threshold. The full proportional tube response to an ionizing particle is delayed by the time for electrons to drift to the anode, the time for the signal to arrive at the trigger electronics and the time to evaluate whether trigger conditions are actually satisfied or not. The sum of these delays is a few hundred nanoseconds. After a pre-trigger was satisfied, another pre-trigger could not be generated for a fixed $1\mu s$. This condition usually occurred in coincidence with the muon punch through condition, since the energy deposited by a high energy muon traversing the calorimeter generally satisfies the trigger minimum energy criteria.

Muon punch through and/or pre-trigger delay conditions occurred less than 300 times per ping (2ms wide) introducing a dead fraction of $\approx 10 - 15\%$.

Cosmic ray muon interactions are expected at a rate of ≈ 800 Hz ($2 - 3$ events per 2 ms ping). There is no mechanism in the detector to veto cosmic rays but they typically do not satisfy the trigger requirements because:

1. The angular distribution of cosmic rays entering the detector goes roughly

like $\cos^2\theta$ where θ is the angle of the cosmic ray relative to a vertical line perpendicular to the earth's surface. Hence, a large fraction of cosmic rays enter the detector along a nearly vertical path that is not likely to pass through two or more proportional tube (PT) planes (with a horizontal separation of about half a meter). The pre-trigger condition requires a minimum amount of energy be seen in at least 2 PT planes.

2. The mean energy of cosmic ray muons (about 2 GeV) is less than the trigger minimum energy threshold (5 GeV). Their differential energy spectrum falls like E^{-2}. A cosmic ray muon that has more than 5 GeV of energy must pass through at least 2 PT planes and must also have a long enough path length in the detector such that it deposits enough energy to satisfy the trigger minimum energy threshold. Muons with sufficient energy lose energy in the E733 calorimeter at a rate $dE/dl \approx 0.25$ GeV/m so the average required path length is comparable to the length of the detector (not the height).

As described in Chapter 5, cosmic ray interactions are occasionally recorded. They are expected to be distributed flatly in time, so they are easily identified, eliminated and accounted for.

The most substantial loss of "live POTS" is caused by the dead time of the flash chambers. Once the detector has triggered and the flash chambers have fired, $4-5$ seconds is required before the refire probability of the gas in the chambers is reduced to an acceptable level. Therefore only one neutrino event can be recorded per 2 ms ping.

The total integrated protons on target was $\approx 5\times10^{17}$. The total integrated "live" protons on target (POT) during the 1987 fixed target run is

$$POT = 1.15\times10^{17}. \tag{2.7}$$

It is calculated by summing all scaled integrated counts from the toroid pulse monitor

corrected for the dead fraction introduced by the trigger conditions while the LAB C live beam gate is "on".

2.2.5 Time sub-structure of the beam

During Tevatron operation, the accelerator RF signal is continuously transmitted from the main ring control room to the E733 computer room via RG58 cable for the purpose of comparing the recorded event times to the phase of the RF clock.

The process of extracting protons from the Tevatron does not disrupt their basic time structure; protons within a ping hit the target in bunches separated in time by about 18.83 ns synchronous with the accelerator RF clock. The bunch shape is expected to be approximately gaussian with a width of less than 1 ns RMS.

Massless neutrinos from secondaries are expected to maintain this time structure in traversing the 1600 meter distance to the detector. Therefore, neutrino induced events should have measured event times within a narrow window of time at a fixed phase relative to the RF clock signal transmitted from the accelerator. The width of this window depends on the proton bunch width (about 0.6 ns RMS), the resolution of the event time apparatus (about 0.7 ns as demonstrated in Chapter 5) and the time of flight of decaying pions and kaons. The time-of-flight (TOF) Equation 2.1 is reiterated here for convenience.

$$TOF = \frac{L}{2 * c} * \frac{M^2}{P^2}. \tag{2.8}$$

This time of flight for secondaries is the time for a secondary particle of mass M and momentum P to traverse the distance L from where it was produced to where it decays minus the time it would have taken a speed of light particle to travel the same distance.

A computer simulation was performed to study the TOF of decaying secondaries in order to determine whether this factor makes a significant contribution to the

width of the event time distribution. This simulation used the energy distributions for decaying secondaries shown in Figure 2.2 and the known lifetime of these particles.

The results showed that for *charged* decaying secondaries, the TOF does not exceed 0.3 ns and the typical TOF values are less than 0.01 ns. Time differences of this order are negligible in comparison to the inherent proton bunch width and detector event time resolution. This term is therefore negligible for neutrinos from charged secondaries, which compose the majority of the neutrino beam. The shape of the neutrino event time distribution is unaffected by such time differences. This result is not surprizing since the TOF is inversely proportional to momentum and low energy charged secondaries are swept out of the beam by the magnet train.

Neutral secondaries, however do have a low energy component. The time-of-flight distribution for decaying K_L^0 is shown in Figure 2.5.

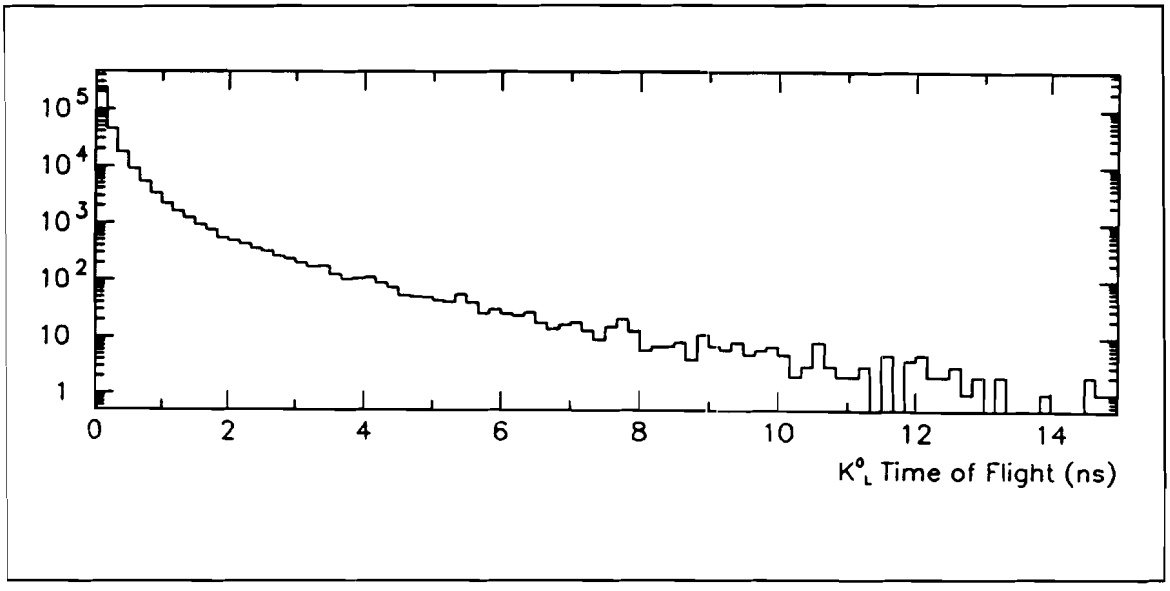

Figure 2.5: K_L^0 Time-of-Flight Distribution

The mean TOF value for decaying K_L^0 is about 0.1 ns, with a tail extending as far as 14 ns. Therefore, there exists a finite probability that a low energy K_L^0 decays into a neutrino that is seen in the detector outside of the expected event time window. In order to quantify this probability, a more detailed TOF simulation was performed

similar to, but independent of, the simulation described in Section 2.2.2. The purpose for this simulation is to estimate the fraction of neutrinos from K_L^0 expected outside of the event time window taking into account geometrical acceptance of the detector as a function of secondary energy.

Results of this simulation are shown in Table 2.3, which shows the expected neutrinos per POT from K_L^0 that enter the detector inside and outside of a 1 ns TOF window. Also shown are the corresponding numbers from charged pions and kaons. These results are consistent with $\sum_j \nu_j^i/POT$ for K_L^0 shown in Table 2.2. The

Table 2.3: Expected number of neutrinos per proton on target entering the detector from the decay of $\pi^{\pm}$, $K^{\pm}$, and K_L^0

ν/POT ($\times 10^{-4}$)	π^+	K^+	π^-	K^-	K_L^0
with TOF< 1.0 ns	26.382	5.720	13.068	1.589	0.2818
with TOF> 1.0 ns	0.000	0.000	0.000	0.000	0.0001

numbers in this table tend to be higher than those in Table 2.2 because the angular dispersion of the beam is not taken into account in this simplified simulation.

We can now estimate the number of neutrino interactions expected to be seen in the detector over the course of the run from each source, and see if the number of neutrino interactions from K_L^0 outside of a 1 ns TOF is significant. The probability that a neutrino with interaction cross section σ interacts within the detector fiducial volume is σN_{det} where N_{det} is given in Equation 2.6. The number of expected

neutrino events N_ν is

$$N_\nu = POT \left[\sum_{i=}^{\pi^\pm, K^\pm, K_L^0} \sum_{j=all}^{decaymodes} \frac{\nu_j^i}{POT} \; P_j^i \right]. \tag{2.9}$$

where POT is the number of live protons on target given in Equation 2.7 and $\frac{\nu_j^i}{POT}$ is given in Table 2.2. P_j^i, represents the average probability that the neutrino will interact in the detector. It depends on the neutrino-nucleon interaction cross section [15]:

$$\sigma_{\nu N} = 0.55 \times 10^{-38} \times E_\nu(\text{GeV}) \quad \text{cm}^2 \tag{2.10}$$

which is proportional to neutrino energy. The number of expected interactions in Equation 2.9 was calculated by a computer simulation using the expected neutrino energy and spacial distribution described in Section 2.2.2, the measured beam offset [31], and the TOF fiducial volume described in Chapter 3. The probability of interaction is weighted by the neutrino energy as in Equation 2.10.

Table 2.4 lists the number of expected interactions from each neutrino source.

Table 2.4: Expected neutrino interactions from each source.

ν source	π^+	K^+	π^-	K^-	K_L^0
expected ν interactions	20025.5	47653.3	7193.5	34532.1	825.7

Adding all contributions, the total number of expected interactions is about 110000. The actual number of interactions seen in the TOF fiducial volume is 126000, about 9% more than predicted here. Error estimates on the prediction of the absolute number of events are difficult to quantify but are unimportant for this analysis. Only the relative rates from each source are relevant. From Table 2.4, the fraction of

events from K_L^0 is 0.75% relative to the other sources. From Table 2.3, the fraction of K_L^0 neutrinos with a TOF outside of a 1 ns is 0.04% [1]. Then the total number of interactions expected from any source with a TOF greater than 1 ns is less than 0.5 events. [2]

In conclusion, the time structure of the neutrino beam entering the E733 detector mimics that of the 800 GeV/c protons on target. The TOF of decaying secondaries does not introduce a tail in the event time distribution nor does it significantly change the shape of the neutrino event time distribution.

[1] This fraction is not energy weighted. The fraction of interacting neutrinos with a TOF outside of 1 ns is expected to be even smaller: These high TOF particles have energies an order of magnitude less than the average, thus a smaller probability of interacting. Also, such low energy neutrino interactions ($E_\nu < 15$GeV) are less likely to satisfy the trigger energy requirements.

[2] $126000 \times 0.0075 \times 0.0004 = 0.38$ events during entire run. Additional corrections are expected to decrease this estimate.

2.3.3 Purpose

The primary purpose for testbeam hadrons is for detector energy calibration. The energy scale used in this analysis is described in Chapter 3 and elsewhere [27, 32]. Testbeam muons are used to gauge the momentum resolution of the muon spectrometer [30].

The interactions of testbeam muons and 'deep'[3] hadrons have an auxiliary purpose in this analysis:

- The calibration beamline is fed protons from the same (Tevatron) accelerator as the neutrino beamline and therefore has the same basic time structure. Therefore, identical phase shifts of the RF clock are observed in testbeam and neutrino events. Testbeam muon and deep hadron event timing is used to monitor any RF phase shifts throughout the run as described in Chapter 4.

- The systematics of the testbeam event time measurement are compared to that of neutrino event timing in Chapter 5.

[3] A deep hadron is a hadron that travels at least 1 interaction length beyond the first TOF

Chapter 3

The E733 Detector

3.1 Introduction

The E733 Detector was designed for studying high energy neutrino interactions in the NCenter Wide Band Neutrino Beamline [24] at Fermilab. The detector consists of a 300 metric ton target/calorimeter followed by a muon spectrometer. The large target mass is required to induce neutrinos to interact and to contain the large hadronic showers of high energy neutrino interactions. The muon spectrometer measures the momentum and charge of any high energy muons that escape through the downstream end of the calorimeter.

The E733 detector was used previously during neutrino exposures in 1982 and 1985. Many alternate descriptions of the detector are available [28, 27, 34, 32, 30, 35, 36]. The time-of-flight apparatus was introduced for the 1987 run for the purpose of making this search for new phenomena possible. It is used exclusively for this analysis.

This chapter describes the E733 detector with special emphasis on the apparatus used to measure event times relative to the RF clock.

3.2 The Apparatus

3.2.1 Overview

A schematic of the E733 detector is shown in Figure 3.1 (thanks to W.G.Cobau for help with this figure). The calorimeter consists of 38 **modules**, each with alternating layers of target material, flash chamber **(FC)** panels and proportional tube **(PT)** planes as shown. The target material is alternating layers of sand and steel shot contained within Lucite^{TM} plastic extrusions. Each layer is 3.7 meters square with a thickness of about 16 mm.

Triggering decisions are based on the energy deposition in the calorimeter as sampled by the proportional tubes. The flash chambers are passive in the triggering decision, but constitute the primary device for the measurement of neutrino interaction energy. Other elements, like the front veto wall and the scintillator timing walls aid in trigger decisions and provide timing information for the drift system in the muon spectrometer.

Also shown in the figure are the four planes of scintillator (the time-of-flight or TOF planes) for the purpose of measuring event times relative to the RF clock. They are positioned just downstream of **bay**[1] 2, 3, 4 and 5, respectively. The active region of the calorimeter extends out to an area 3.7 meters square, but the area of time-of-flight plane sensitivity is somewhat smaller (covering an area about 2.8 meters square).

Additional proportional tube planes are read out in a drift readout mode in the spectrometer (denoted *Drift Stations* in the figure), measuring the charge and momentum of outgoing muons.

[1] A bay is a set of two to five modules designated according to breaks in the support structure between sets of modules. There were a total of 8 bays in the calorimeter. Bay 1 consisted of the first 2 modules, and bays 2, 3, 4, and 5 each contained 5 modules in succession.

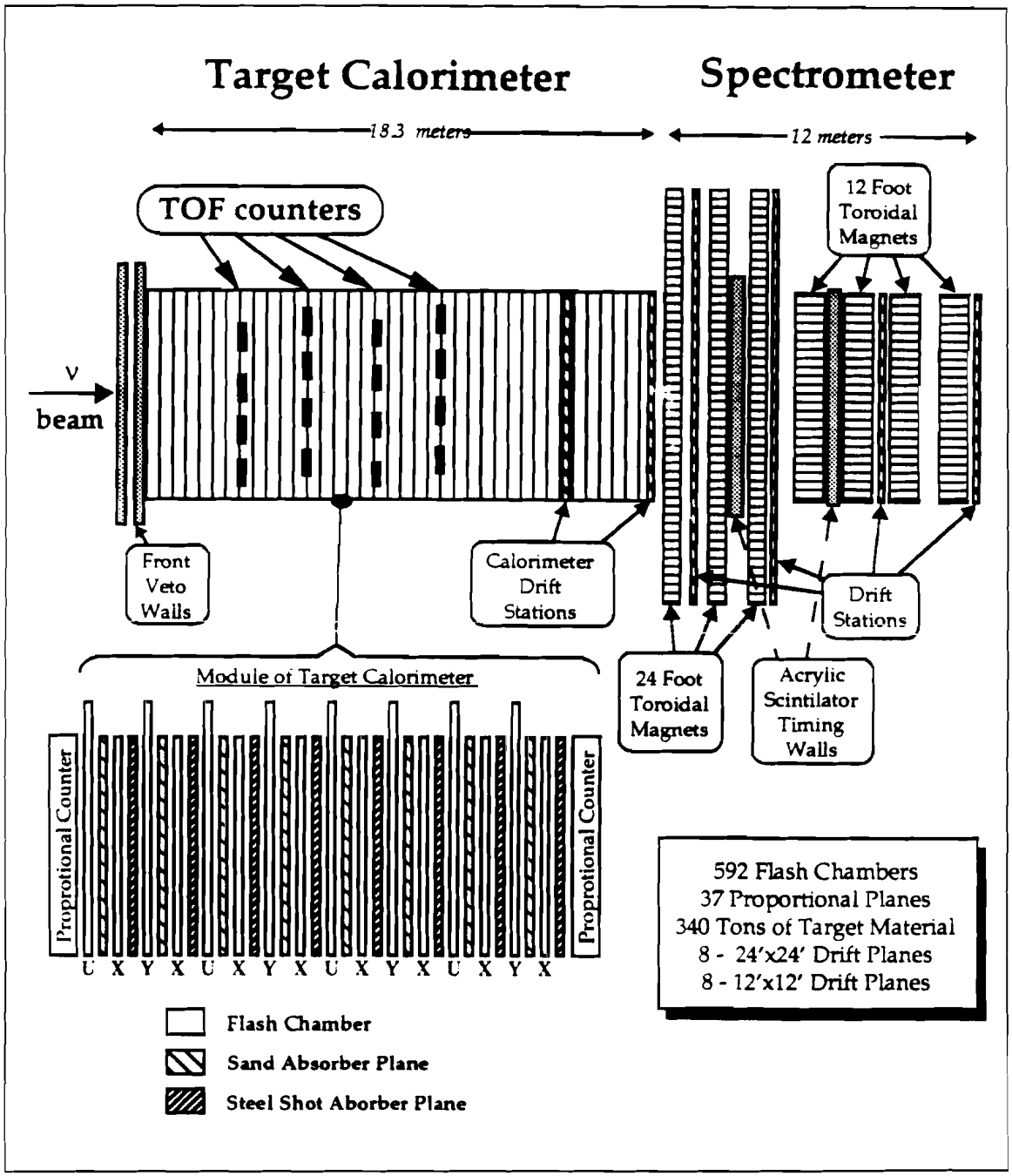

Figure 3.1: A Schematic of the Lab C (E733) neutrino detector.

The detector coordinate system, with cartesian components (w, v, z), has its origin at the center of the front face of the E733 detector. The positive z axis points downstream along the beam line, northerly in earth based coordinates. In the plane perpendicular to the z axis, the v axis points vertically upward, while the w axis points horizontally westward in earth based coordinates.

Table 3.1 summarizes some gross properties of the calorimeter. Each detector component is described more fully in the following sections.

Table 3.1: Table of calorimeter parameters.

Calorimeter parameters	
Length	18.3 m
Density	1.35 g/cm^3
Radiation Length	14 cm
Interaction Length	85 cm
proton/neutron ratio	0.964
Average A	20.2
TOF[a] Fiducial Depth	10. m
TOF Cross Sectional Area	7.6 m^2
TOF Fiducial Mass	98 metric tons

[a]the fiducial volume appropriate for this analysis is explained later

3.2.2 Front Veto Walls

The purpose of the front veto wall (shown in Figure 3.1) is to reject events caused by, or simultaneous with, the passage of charged particles through the front end of the detector. These particles include

- beam muons produced by neutrino interactions in the shielding,
- beam muons produced from the decay of secondary particles in the beamline decay region that manage to punch through the shielding and

- cosmic rays.

The front veto walls are made of sixteen acrylic scintillator panels, arranged in 2 planes to cover an effective area greater than that of the calorimeter face. No neutrino event trigger is generated when both planes simultaneously detect an incoming charged particle.

3.2.3 Liquid Scintillator Tanks

The bay boundries that did not contain time-of-flight scintillator counters were occupied by tanks of liquid scintillator (13 cm thick and 3.7 meters square) instrumented with photomultiplier tubes. These tanks were a remnant from earlier runs of the experiment. They served one purpose in the 1987 run, namely to provide the trigger logic with a coincidence signal (between two or more tanks in different bays) indicating that a cosmic ray had traversed the detector lengthwise. Such cosmic ray events are useful for alignment and for studying time dependent variations in the other detector systems.

3.2.4 Proportional Wire Tubes and the Event Trigger

The proportional tubes (PT) comprise a cardinal component of the triggering system. Their fast pattern recognition abilities enable trigger decisions to be made in 600 to 700 nanoseconds from the time the particle traverses the PT cells. This is important because the flash chamber efficiency for detecting charged particles decreases by $> 30\%$ per microsecond delay [35] after particle traversal.

Each proportional tube plane is constructed of extruded aluminum forming 144 parallel $2.54cm \times 2.54cm \times 3.4m$ cells. The cells are filled with a mixture of 90% argon and 10% methane gas. Down the axis of each cell is a $50\mu m$ diameter gold-plated tungsten wire held at high voltage. The planes are operated in proportional mode, at a voltage of about 1575 volts, providing a charge amplification (gain) of about

is about 10 cm.

neutrino interactions, and to measure the angle of high energy muons as they emerge from hadronic showers.

The 592 flash chamber planes were oriented in 3 different directions to provide a stereo view of a neutrino interaction as it develops. In a plane perpendicular to the beam axis, the U, Y, and X views had cells oriented +10, −10, and 90 degrees from the vertical, respectively. There are twice as many X chambers as U or Y.

Flash chamber planes are made of corrugated polypropylene panels 4.2 mm thick. With over 600 parallel cells per plane, they provide a transverse segmentation of 5.77 mm. The planes are filled with a spark chamber gas (90% neon, 10% helium, .1% Argon). In response to an event trigger, a high voltage pulse (5 kV in .5μs) is applied to one of the two heavy aluminum foil electrodes glued to each side of the flash chamber panel. Any residual ionization in a cell due to the passage of a charged particle is accelerated in the high electric field, inducing a plasma wave through the length of the cell.

Each cell is capacitively coupled to an AC bridged circuit at the end of the cell. A plasma wave in the flash chamber cell causes a change in the current in the circuit, inducing a sound pulse along a magnetized niobium wire ("wand") running perpendicular to all the flash chamber cells in that plane (in both directions). The acoustic pulses are converted to electronic pulses through a coil magnetically coupled to the end of the wand. The pulses are then amplified and their arrival times

cell may fire due to the passage of one particle or many particles: So the flash chamber cell is a binary object, able to distinguish between no particles and ≥ 1 particles, but unable to distinguish between 1 particle and > 1 particle. The density of hit cells in the vicinity of that cell is a better indication of the energy density, but in the center of a dense shower of energy, the flash chambers are known to saturate.

The proportional tubes, on the other hand, do not experience this saturation effect, since their pulse height output is proportional to the amount of energy deposited. Proportional tube energy measurements, combined with density of hit information and calibration beam (testbeam) and cosmic ray muon studies are used to calibrate the energy scale. The final energy resolution of the flash chambers, nominally $\sigma/E_\nu = 12-15\%$ at high energies ($E > 100$ GeV) is known to be slightly worse at lower energies. Full details of this calibration are described elsewhere [27, 32]. The energy resolution is not of major importance in this analysis.

After a cell has 'fired', a 4 or 5 second delay is required before the residual ionization is reduced to a level where 'refire' probability of that cell is small. This <u>dead time</u> limited the recording of neutrino events to one event per ping (or 3 events per accelerator cycle)[5].

The number of events recorded during a typical accelerator cycle was limited by the flash chamber dead time (4 or 5 ns). Events recorded with and without flash chamber information are called <u>flashing</u> and <u>noflashing</u> events respectively. During a typical accelerator cycle (lasting about a minute) there is time to record the following number of events:

- A flashing neutrino event is recorded during each of the 3 neutrino pings (each lasting about 2 ms in duration).
- Two flashing testbeam events are recorded during the testbeam spill (lasting about 10 seconds).

[5]See Chapter 2 for details of the accelerator cycle.

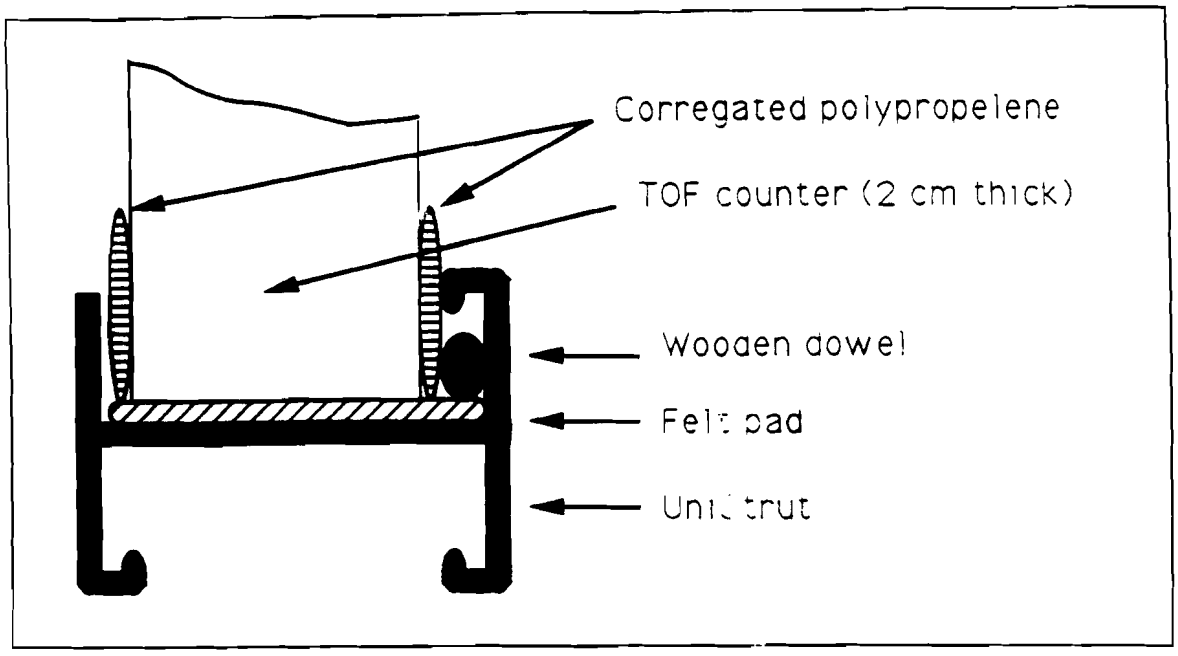

Figure 3.5: Cross section of a TOF counter mounted into a UniStrut rail.

cushioned at the bottom with felt pads. Lucite light guides were supported by triangular wooden supports to relieve stress at the glue joints.

The counters were bench tested at MSU using a 4" wide cosmic ray telescope [37]. The efficiency of the counters was measured to be greater than 97 % for cosmic ray muons. Higher efficiencies can be expected for the higher energy muons expected in high energy neutrino interactions. The difference between times measured on either side of the counter was found to have an RMS deviation of 1.0 to 1.3 ns independent of counter position and pulse height. The timing resolution of a tube, therefore, is between 0.7 and 0.9 ns. From the linear response, the speed of light in the scintillator was measured to be 15.3 cm/ns. This calculation is demonstrated in Appendix C.1.

After testing, all counters were shipped to Fermilab to be installed in the E733 detector. Sixteen of the seventeen counters made were actually used. Sets of four counters are configured as shown in Figure 3.6. Four such TOF planes planes are located at the downstream end of bays 2, 3, 4, and 5 separated by approximately 80

chambers

flash chamber planes or 5 proportional tube planes (about 2.5 meters).

The z positions of the four TOF counter planes were measured by surveyors to be z=383.7, 631.6, 884.7 and 1135.5 cm relative to the detector face at z=0. They remained stationary throughout the run. All planes (as shown in Figure 3.6) are oriented in the same direction, with the length of the scintillator running in the horizontal direction perpendicular to the beam axis (Z). They were staggered vertically to minimize gaps in coverage.

For reference, the counters are numbered from one to sixteen, starting from the upstream end, bottom to top. In the detector, each counter has two phototubes pointing in the east and west directions, respectively. Therefore, there are 16 east and 16 west phototubes. The importance of this distinction will become apparent when we begin talking about time measurements from these phototubes.

Trigger and Electronics

Signals from each of the photomultiplier tubes (PMT) were connected to the TOF electronics via varying length of RG-38 coaxial cables. The cable lengths were chosen such that simultaneous timing signals would be produced from all TOF counters struck by a particle traversing the detector in the beam direction at the speed of light. A schematic of the TOF electronics is shown in Figure D.1. and the RF clock circuitry is shown in Figure D.2 [38].

Anode signals from each of the (32) PMT's are fanned out and routed to 3 places: Two are sent to discriminators, one set at a low (L) threshold of 30 mV, the other set at a higher (H) threshold of 75 mV. The low and high threshold crossing times relative to the common START signal are digitized and stored. The third signal was pulse height analyzed (the output pulse was integrated over 200 ns and digitized). These pulse heights are the only available direct measure of the total energy deposited in the scintillator.

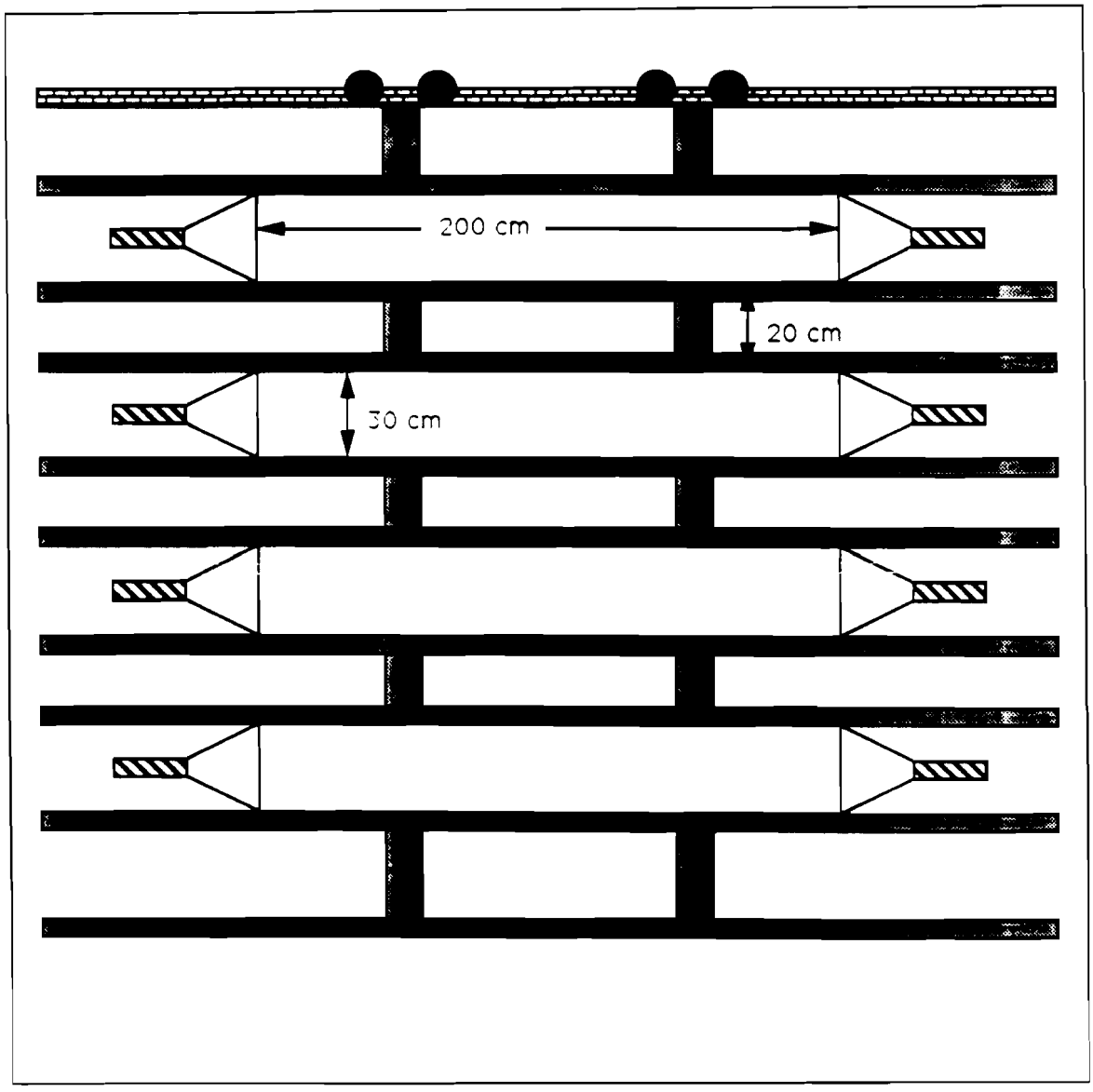

Figure 3.6: Schematic of the time-of-flight counter plane configuration.

A TOF trigger was generated when signals from 2 PMT's from either the east or west side of the detector crossed the low threshold in coincidence (within 50 ns). The common START signal occurred when the second tube went above threshold. When the common START is generated, TFC[8] units were used to digitize the times when the discriminated PMT anode signals crossed their L and H thresholds relative to the common START signal.

For each counter, these times are referred to as the east low (EL), east high (EH), west low (WL), and west high (WH) times, designated

$$t^S_{EL},\ t^S_{EH},\ t^S_{WL},\ and\ t^S_{WH}. \tag{3.1}$$

A **4-HIT counter** is a counter which has all 4 discriminator levels satisfied. In this analysis, the only time measurements used are those from 4-HIT counters.

The RF clock signal (sent along a buried cable with electronic repeaters along the way) arrives at the E733 RF circuitry as a 53.102 MHz sine wave. This signal is sent to a discriminator operating (normally) in zero-crossing mode. The discriminated output is prescaled to generate a single output pulse every 4th RF cycle in two independent circuits, whose relative phase was 180^0, to two separate TFC channels. An RF STOP signal was formed by the first of these channel inputs occurring after a fixed time delay after the START. The two TFC channels are necessary because a STOP can occur relative to the START such that the TFC channel was insensitive or nonlinear; This arrangement guarantees that one or the other channels will be linear. The time difference between the common START and the RF STOP is designated

$$t_{RF}. \tag{3.2}$$

Problems with the RF clock early in the run indicated that an additional redundancy in the RF clock circuitry would be useful. An identical RF circuit was run in parallel with the first, using the same zero-crossing discriminator output. For most

[8]TFC is a Time to FERA Converter. A FERA is a Fast Encoding Readout ADC.

of the run, the output of each individual circuit produced the same results. But on some occasions, as will be seen in Chapter 4, discrepancies existed between the RF clock circuits, due to accelerator RF problems, power glitches, or simply one unit missing a pulse. The redundancy in the RF circuitry proved to be a useful tool in finding and eliminating runs with RF clock problems.

Information from the time-of-flight counters was available much earlier than that of the proportional tubes. Therefore, the TOF system was designed to trigger itself, digitize and store all TOF signals, and then wait for a trigger signal from the detector. If an event trigger is generated, the digitized times and pulse heights are read out. If an event trigger does not occur within about 700 ns, the TOF trigger cleared itself, then waited for the next event.

Chapter 4

Event Classification and Reconstruction

4.1 Introduction

The last chapter described the E733 apparatus. This chapter

- explains the steps in the data reduction that lead to the final event sample and
- describes some off-line corrections made to the timing signals preliminary to their use in Chapter 5, where the event timing measurement is described.

4.2 Neutrino Event Classification

Neutrinos interact with nuclear matter through the exchange of charged ($W^{\pm}$) or neutral (Z^0) gauge bosons, commonly referred to as *charged current* (CC) or *neutral current* (NC) interactions, respectively. The corresponding Feynman diagrams are shown in Figure 4.1.

Both types of events have a hadron shower with a widely varying amount of energy. Additionally, charged current events have a high energy muon in the final state, while neutral current events have a neutrino which escapes the detector unseen. There are many subtle difficulties in distinguishing between charged and neutral current events [32]. But in this analysis, we are not necessarily concerned

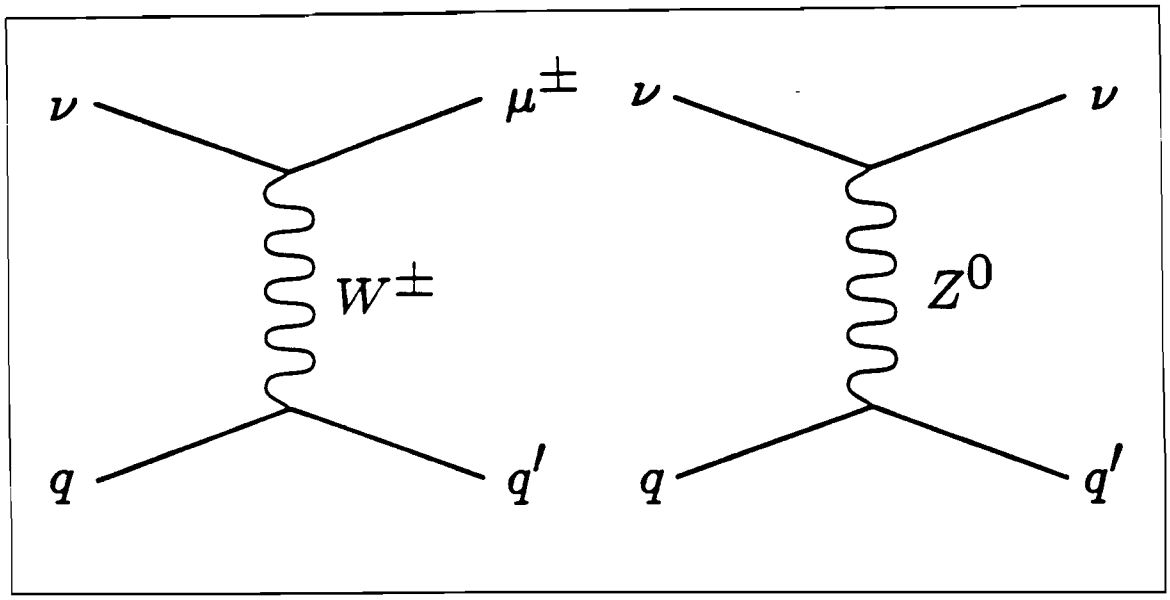

Figure 4.1: The charged and neutral current interactions in neutrino-nucleon deep inelastic scattering.

with whether an event is *really* a CC or an NC event. What is useful in the distinction between these two event types for a WIMP search is that they have a distinct difference in their topology. Namely, one type of event contains a high energy muon[1] , and the other does not.

As we will see in Chapter 5, the timing resolution for events with a high energy muon is better than the resolution for events without a muon. Therefore, we distinguish between these different WIMP final states throughout this analysis in all results obtained. Events with a high energy muon are called <u>CC-like</u>, and events without a muon are called <u>NC-like</u>.

4.3 Pattern Recognition and Tracking

Before analysis of time measurements can begin on any particular event, a decomposition of the event's topology must be performed. Accurate time measurements require that the approximate location of energy deposition in the scintillator be

[1]Implicit in this definition is that the muon is required to come from the event vertex. The muon is not a decay product that emerges from the hadronic shower.

known. Table 4.1 shows the longitudinal and transverse segmentation of the flash chambers, proportional tubes and TOF counters, respectively, for comparison. The

Table 4.1: Calorimeter segmentation parameters.

	Flash chamber	Prop tube	TOF plane
total number of planes	592	37	4
transverse segmentation	5.77 mm	10 cm	50 cm (vertical)
longitudinal segmentation	3.2 cm	46 cm	2.5 m
radiation length per unit segmentation	0.22	3.6	17.85
absorption length per unit segmentation	0.036	0.59	2.94

TOF counters cover a large proportion of the active calorimeter volume. They have a simple geometry and course segmentation.

Light requires about 13 ns to traverse the length of a counter. Since the required event timing resolution is about 1 ns, corrections to the measured times for the light transit time are essential. The finer segmentation of the flash chambers and proportional tubes can be used to locate the position of energy deposition within the counter, enabling us to make these corrections to the time as described in the Chapter 5.

The position of an event vertex is found using proportional tube and flash chamber information. A vertex position is first localized in the z-dimension by finding the first two sequential PT planes with HITBITs on. Then in the flash chambers, the lateral position and a refined z-position are found in a 3-dimensional fit utilizing each of the three FC views. The vertex finding efficiency was $> 99\%$ for events with energy $> 10\ GeV$ [27].

The MTF (Muon Track Finding) algorithm was used to find muon tracks in the calorimeter. Specifically, we are interested in finding muons that emerge directly from the primary interaction vertex. MTF begins by searching for sequential FC hits in narrow angular regions projected from the event vertex in each of the 3 views. Track segments are identified where the density of hits in these projections indicates possible tracks. Muon tracks are found by combining track segments in a 3 dimensional match. Final candidate muons are required to have a track length of at least 500 cm within the calorimeter if they exit the side of the calorimeter, and at least 1000 cm if they do not. A CC-like event is defined as an event with such a muon track. A NC-like event does not contain an identified muon track.

Another feature of interest in this analysis is the z location of the end of the hadron shower. To find the shower end: First, any FC hits thought to be associated with the muon track are eliminated in a CC-like event. Then, starting at the event vertex, FC planes are stepped through in groups of 16 chambers. The shower end, called **JEND**, is the FC plane 16 flash chambers downstream of the last set of 16 chambers with a number of hits above a low threshold (4 FC hit cells).

4.4 The E733 Detector Event Display

The E733 event display is used extensively to perform visual scans of various events in many stages of this analysis. To demonstrate how one interprets the E733 detector event display, Figures 4.2 and 4.3 show how typical charged and neutral current events appear in the detector. At the top of the page, one can find:

- the run and event number of the event displayed,
- the total number of raw flash chamber hits (FC HITS=),
- the maximum proportional tube pulse height (PHT, MAX=),
- the pulse height sum for the proportional tubes (SUM=),

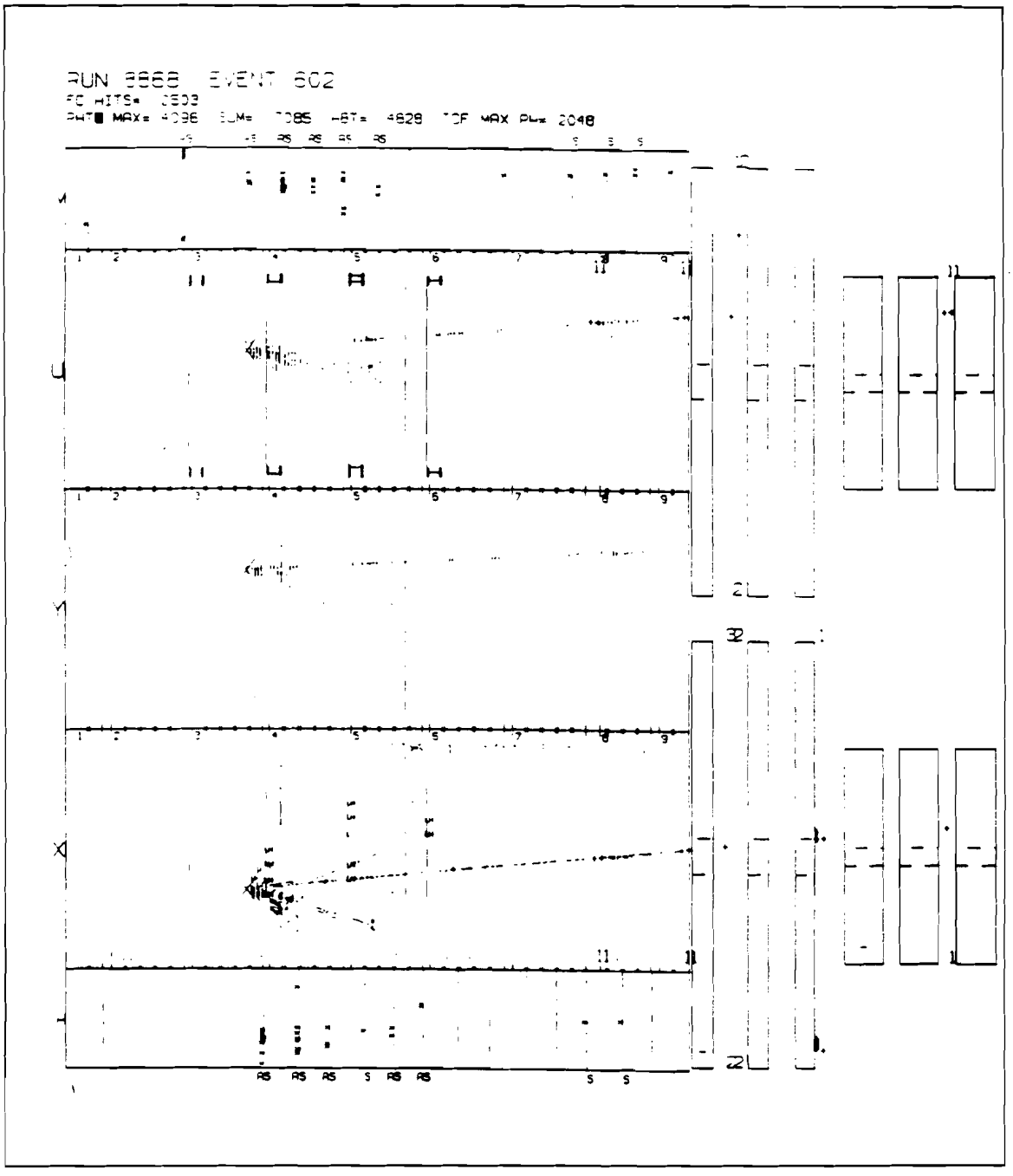

Figure 4.2: A typical charged current event in the E733 detector.

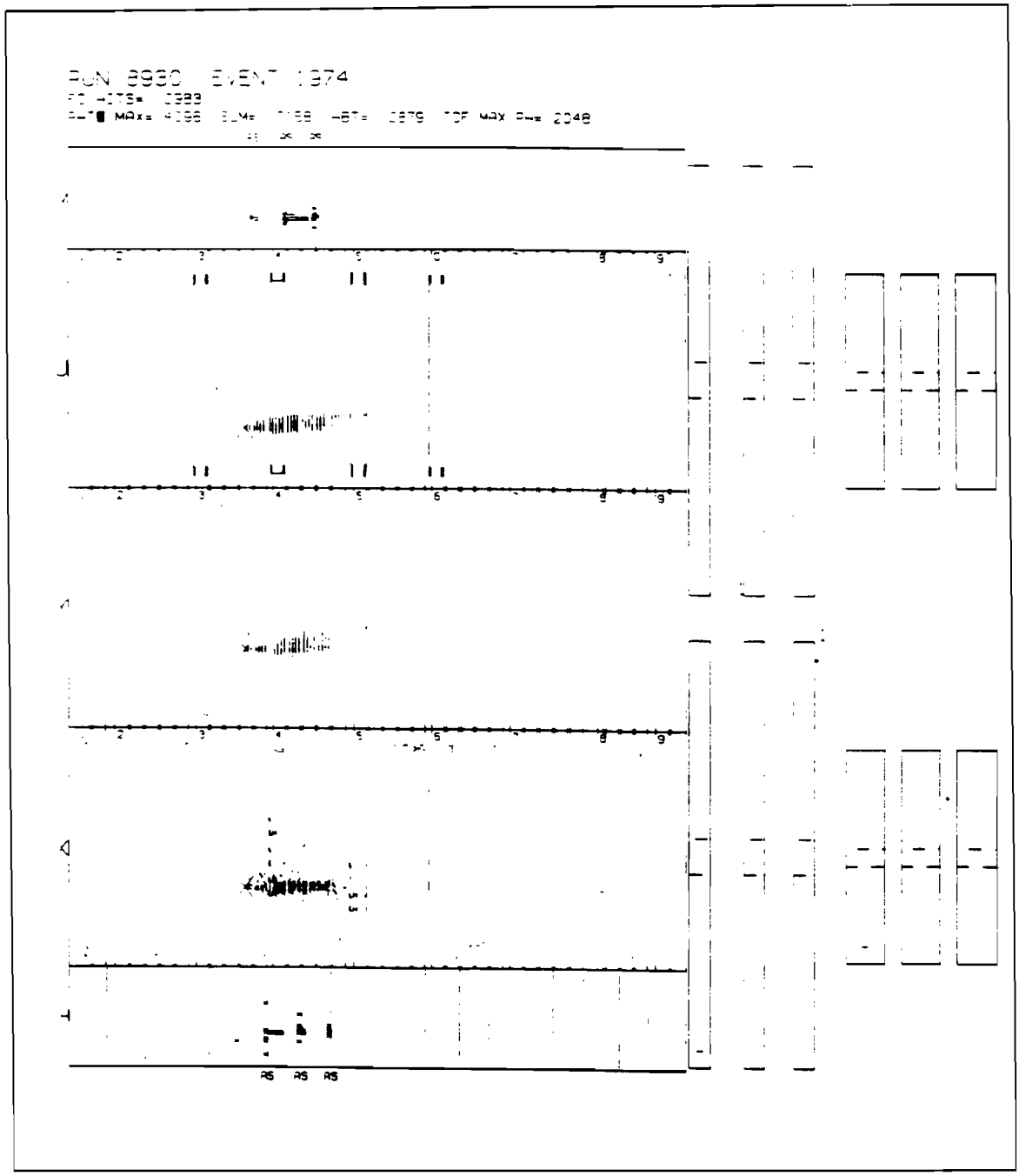

Figure 4.3: A typical neutral current event in the E733 detector.

- the pulse height sum for all HITBIT channels (HBT=), and

- the maximum TOF counter pulse height.

In this display format, the neutrino beam enters from the left. On the left side of the page, the 3 large boxes represent the 3 views of the flash chambers (labeled U, Y and X on the left side). Each dot in these boxes represents a hit flash chamber cell. Note that the density of hits in the X view is roughly twice that in the U or Y views, since there are twice as many X view planes.

The position of the reconstructed event vertex is indicated by the 'X' in each of the flash chamber views. The measured shower end is indicated by the solid vertical line in each view.

The smaller boxes above and below the larger boxes are the proportional tube vertical (V) and horizontal (W) views, respectively. A short single line at the position of the PT cell indicates the pulse height is just above a low threshold. An arrow head indicates the pulse height is over the HITBIT threshold. The bin at the head of the arrow indicates the magnitude of the pulse height. The standard LATCHes, as described earlier, are displayed for each plane, indicated by S and/or A (for SINGLE or ANALOG MULTIPLICITY) on the line just above/below the vertical/horizontal PT views.

The TOF counters are superimposed on the U and X views of the flash chambers. Each TOF plane appears as a line in the U view, a view from the top of the detector. The bar graphs just above/below each line are the east/west pulse heights for the 4 TOF counters in that TOF plane.

Each of the 16 TOF counters is a short line in the X view, the view through the side of the detector. A 'L' or 'H' appears on each counter in this view for each tube with a pulse height above the low and high threshold. 4-HIT counters have two L's and two H's. The CC-like event (Figure 4.2) has five 4-HIT counters, two of which

are hit by the muon track. The NC-like event (Figure 4.3) has two 4-HIT counters.

The muon spectrometer is displayed on the right side of the figure. The CC-like event displayed in Figure 4.2 has a high energy muon which is tracked in the spectrometer. The hits in the horizontal and vertical views of the drift system appear as '+' in the display.

4.5 The TOF Fiducial Volume

Events occurring near the calorimeter edge are problematic because

- energy loss outside the active region leads to inaccurate energy measurements,
- events may be classified incorrectly because muons may escape detection and
- pattern recognition algorithms may have unanticipated difficulties, that lead to incorrect event timing.

The depth of the TOF fiducial volume extends from the front face of the calorimeter to the z position of the last TOF plane. The cross sectional area deemed appropriate for the TOF analysis is shown in Figure 4.4. It has roughly a stop sign shape, with opposite sides parallel to the direction of the cells in each FC view. In terms of flash chamber coordinates, the fiducial volume includes the area within 100 clock counts from the edge of the detector in all flash chamber views. This TOF fiducial volume has cross sectional area larger than that subtended by the TOF scintillator, taking maximum possible advantage of the areal extent of the TOF planes, but is far from the detector edge to ensure reasonable pattern recognition abilities.

All acceptances, timing efficiencies, and event time analysis are based on this fiducial volume. An event is classified as inside the fiducial volume if the event vertex is within that volume.

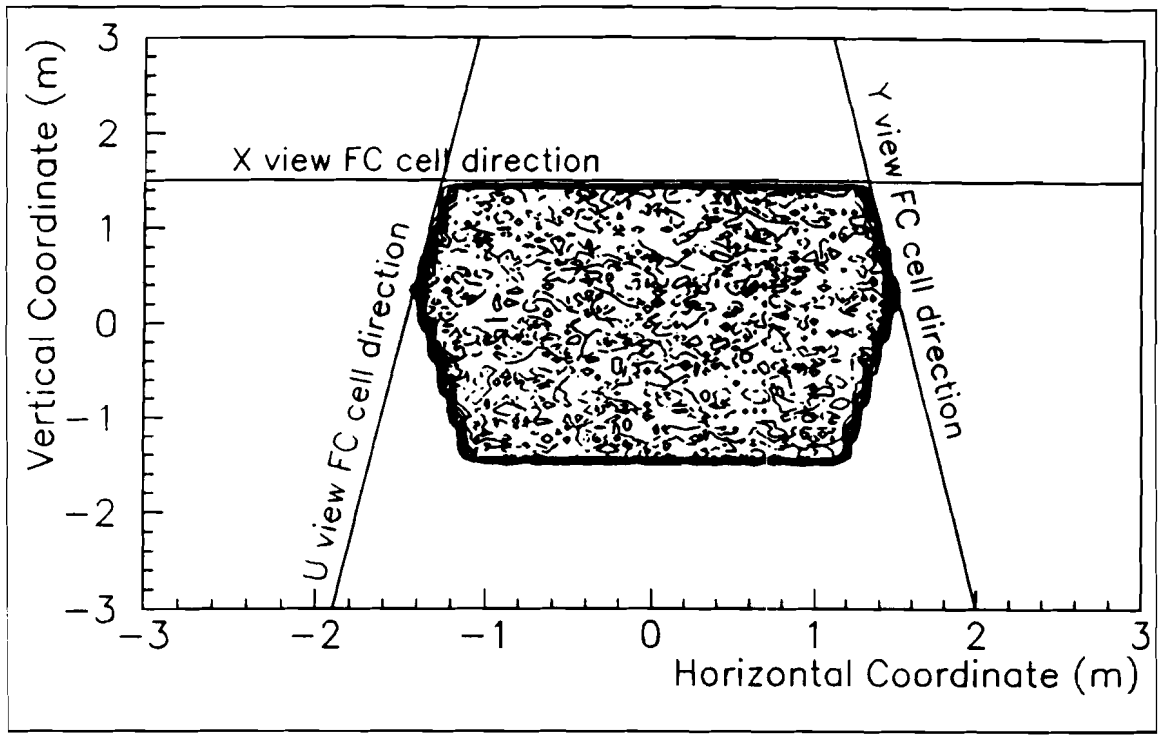

Figure 4.4: The cross section of the TOF fiducial volume extends to include the area within 100 clock counts from the edge of the calorimeter in all flash chamber views.

4.6 RF Clock Trouble Periods

There were some trouble periods during the run where the incidence of inconsistent timing measurements was frequent. Thanks to the redundancy in the RF circuitry, problem runs were more easily identified and eliminated. The number of events eliminated in the runs listed below is documented in the next section.

Early in the run, it was noticed that the zero-crossing discriminator was not generating pulses every cycle. The problem was solved by placing the discriminator in leading edge mode which fixed the problem until the unit was replaced. Runs 8700-8730 were eliminated from the data sample.

Runs 8962-8970 were eliminated during a period when the TOF TDC's were being calibrated. Calibrations were also performed during runs 9156-9182 (problems with the RF discriminator were also noticed during this time).

There were a number of periods where particular RF clock problems occurred

frequently or continuously throughout a particular run. Because these problems did not occur in isolation, all events in the following runs were eliminated from the data sample: 9646-9653, 9679-9681, 9692, 9696, 9703, 9706, 9719-9721, 9800-9810, 9843, 9879-9889, 9917-9949. These runs had multiple occurrences of problems like:

- The time t_{RF} was in the overflow range, indicating that neither of the RF TDC channels had received an RF STOP.
- The phase between the two independent circuits were continuously checked throughout the run. In a few runs, the relative phases measured by each of the redundant circuits were inconsistent, phase shifts occurred frequently, or no phase could be determined at all.
- Time measurements made during a run were distributed flatly in time, indicating no correlation with the RF phase whatsoever.

During many of the runs found to have RF clock problems, hardware failures could not be identified. Frequently these problems were coincident with RF problems logged by FNAL accelerator operations.

4.7 The Final Event Sample

The total data sample was initially split into separate subparts, one that includes all testbeam data, and another that includes all neutrino data. There are almost half a million events in the neutrino data set recorded over the course of the run. Table 4.2 shows how these events are categorized before further analysis begins.

Table 4.2: The E733 TOF Data Set.

Events	Classification
485,347	Total Events
125,640	Neutrino Events within the TOF fiducial volume
64,839	recorded during bad RF clock runs
1,260	inconsistent trigger and/or gate information
112,662	toroid pulse monitor output indicates less than 10^{10} protons on target for current spill
43,198	not recorded during the beam gate
16,954	no vertex found
85,988	vertex downstream of last TOF plane
34,806	lateral position of vertex outside of TOF fiducial volume

The E733 TOF event sample should consist of all neutrino events within the TOF fiducial volume. This number may exceed the 125,640 listed in the table because some fraction of the "no vertex found" events might be true neutrino events that eluded the pattern recognition programs. An event scan was performed on a fraction of these events, so that proper accounting could be made.

A total of 200 events were scanned by eye, looking at event pictures like those shown in Figures 4.2 and 4.3. The detailed information available on the event display enables relatively easy event evaluation. All events were classified as shown in Table 4.3. Only 3 of the 200 events (1.5%) were neutrino events that should have been included in the TOF event sample, indicating over the entire run an increase in the

Table 4.3: Scan classification of "no vertex found" events.

Events	Classification
80	no flashing events
20	cosmic ray events
27	beam muon or noise events
23	beam muons (veto wall failure)
45	neutrino interactions outside of detector
2	neutrino interactions downstream of last TOF plane
3	neutrino interactions

TOF event sample of only 253 events which is less than 0.20% of the total event sample. All events in Table 4.2 appearing above the *Subtotal* are eliminated from the TOF data set. A total of 125,640 events comprise the TOF Final Event Sample. Chapter 5 describes how event times relative to the RF clock are obtained for these events.

4.8 Preliminary TOF Analysis

4.8.1 TOF Counter Alignment

The z position of each TOF plane was measured, as described earlier. Alignment of the TOF counters in the vertical (V) and horizontal (W) views was accomplished utilizing about 80,000 flashing cosmic ray muon events recorded throughout the run. These cosmic ray muons are distributed uniformly throughout the fiducial volume.

Muons deposit energy in the calorimeter along fairly straight trajectories that can be fit as tracks using flash chamber information. These tracks were used to reconstruct the transverse coordinates (W,V) of all cosmic ray muons as they pass through each TOF plane. These coordinates are called **space points.**

For each of the 16 counters, four 2-dimensional scatterplots, like those shown in Figure 4.5, were produced. Each of the four plots is a narrow window with an

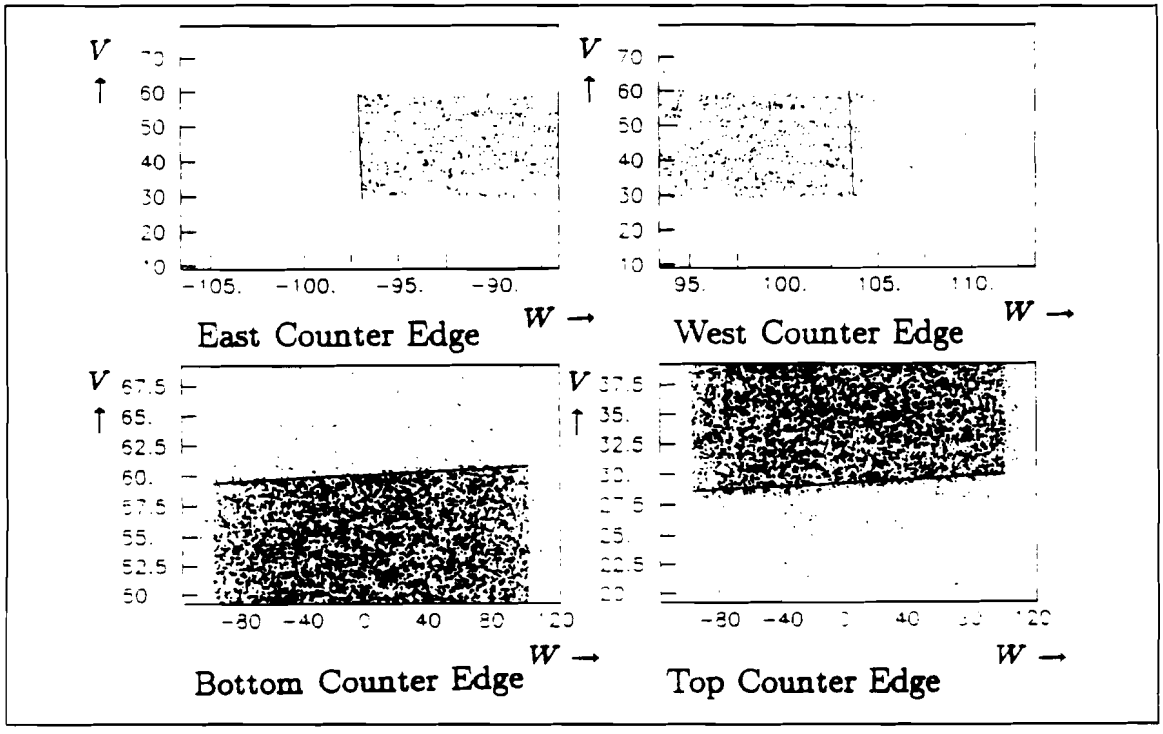

Figure 4.5: Four scatterplots, like these, were used to obtain alignment constants for each TOF counter.

area that includes one of the 4 edges of that counter. An entry was made in the

scatterplot at the (W,V) position of the space point if the nearest counter to that space point was a 4-hit counter.

We made the following assumptions to get the alignment constants:

- Each TOF plane is assumed to be vertical, holding each counter in the plane at the same z position measured by the surveyors.
- The counter edges are flat and and the corners are square. These assumptions follow from the nature of the apparatus used to cut the scintillator: The cutting tool ran parallel to a stationary edge along a straight track.
- The length and width of the scintillator is known: Each piece was measured to the tenth of a centimeter using a standard tape measure. These lengths and widths were datafied and used as constants in the alignment procedure for each individual counter.

The alignment algorithm defined a rectangular template with the known size and shape of each counter. This template was then rotated and translated simultaneously over the 4 scatterplots. Alignment constants were established when the template position maximized the number of hits within it.

The straight lines in Figure 4.5 show the final position of the template sides for this particular counter. The hit density remains relatively constant near the counter edges, indicating that the counter efficiency does not diminish as tracks strike close to the counter edge. The lack of a significant number of hits outside the east and west counter edge indicate that tracks through the light guide are not likely to affect our time measurements.

4.8.2 Times Relative to the RF Clock Phase

The times t_{EL}, t_{EH}, t_{WL}, and t_{WH}, of Equation 3.1 are the times that the east and west PMT pulses crossed the L and H thresholds relative to the common START

time of the event. The first step in calculating event times relative to the RF clock phase is to redefine these times relative to the RF STOP rather than the common START:

$$
\begin{aligned}
t_{EL}^{RF} &= t_{EL}^{S} - t_{RF} \qquad (4.1)\\
t_{EH}^{RF} &= t_{EH}^{S} - t_{RF}\\
t_{WL}^{RF} &= t_{WL}^{S} - t_{RF} \qquad and\\
t_{WH}^{RF} &= t_{WH}^{S} - t_{RF}.
\end{aligned}
$$

In performing this shift, note that the time scale has been inverted (smaller times are later than larger times). We will see this again when we plot some event time distributions.

Also note that these times are relative to the RF clock prescaled by a factor of four (as described in Chapter 3. To get times relative to the phase of the RF clock within a single period of the RF clock, we will need to shift time measurements by an integral (1-4) number of RF clock periods. This number of shifts is random from event to event, but must be constant amongst all counters measuring times for a single event. So this is not an undesirable ambiguity: it actually proves to be a useful constraint in combining individual measurements to obtain event times.

4.8.3 The RF Clock Phase Drift

Ultimately, we wish to measure the time an event occurs relative to the phase of the accelerator RF clock. We call this time the <u>event time</u>. We found that the true phase of the accelerator clock and the phase of the accelerator clock signal received at the E733 detector electronics were subject to relative variations. But these variations can be monitored and corrected for, as described in this section.

As shown in Appendix C.2, the time measured by a single counter struck by an isolated track is independent of the position of energy deposition within the counter.

Tracks strike counters in isolation in CC-like neutrino events beyond the measured shower end, and in muon testbeam events.

Studies of event times relative to the RF clock based on these isolated track hit counter measurements show both discrete jumps and slow drifts of the phase of the RF clock over the course of the run. The same changes in phase are observed in both the testbeam and neutrino data as shown in Figure 4.6 [39]. The direction of

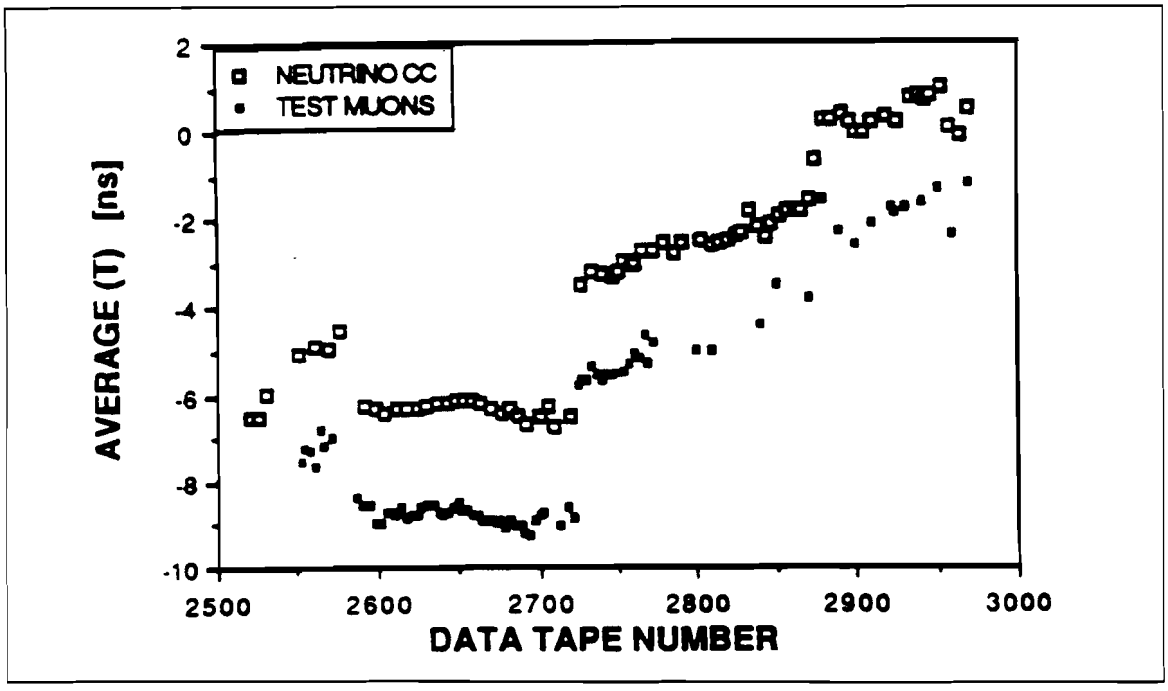

Figure 4.6: Average of event time distribution of each split tape, plotted versus the original data tape number, for both neutrino CC events and testbeam muon events (figure courtesy of M. Tartaglia).

slow drift of the RF clock is consistent with changes in the outside temperature. The discrete jumps undoubtedly reflect changes in the accelerator operation.

In order to combine neutrino event time measurements over the entire run, these shifts must be corrected for on a run by run basis. Corrections to the phase are obtained using the large sample of testbeam data available (both flashing and noflashing testbeam data are utilized). For each run with more than 9 testbeam events, the shift is the average test beam events time, otherwise the shift was assumed to be

zero [39]. The final shifts utilized as a function of run number is shown in Figure 4.7.

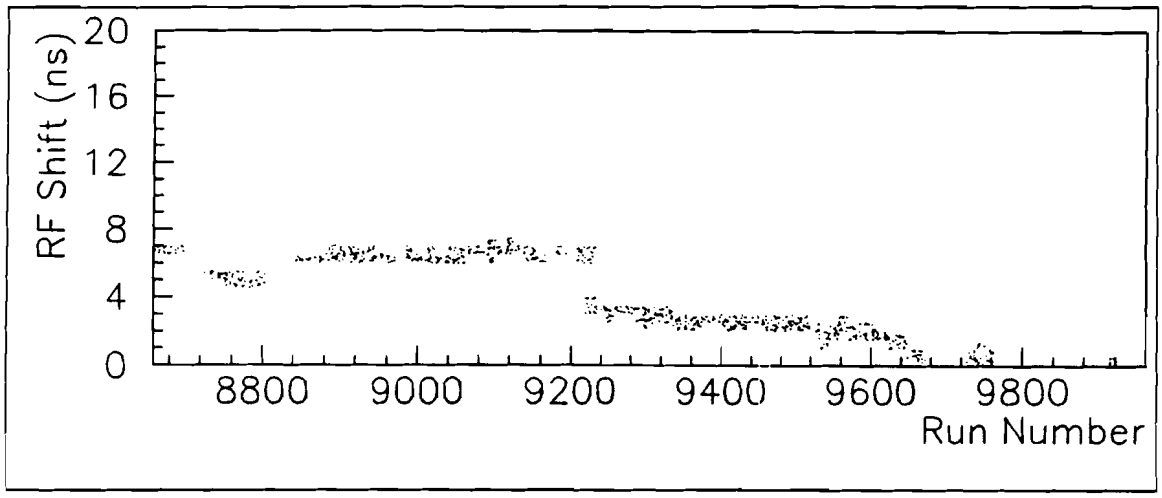

Figure 4.7: RF phase correction as a function of run number.

These phase shifts, called t_{PHASE}, were applied to all counter time measurements.

$$
\begin{aligned}
t_{EL} &= t^{S}_{EL} - t_{RF} + t_{PHASE} \\
t_{EH} &= t^{S}_{EH} - t_{RF} + t_{PHASE} \\
t_{WL} &= t^{S}_{WL} - t_{RF} + t_{PHASE} \quad \textit{and} \\
t_{WH} &= t^{S}_{WH} - t_{RF} + t_{PHASE}.
\end{aligned}
\tag{4.2}
$$

These corrected times are the times averaged to get event times in Chapter 5.

4.8.4 Pulse Height Corrections

As shown in Figure 3.4, each processed PMT output pulse yields 2 time measurements indicating when the pulse crosses a low (L) and high (H) threshold. In addition, a digitized pulse height is recorded, equal to the PMT output pulse integrated over 200 ns. This pulse height (PHT) has proven to be the best measure of the total energy deposited in the scintillator. Since the energy deposited can affect the time measurements, the pulse height information needs to be well understood. Pulse height measurements are used for timing corrections in Chapter 5.

For reference, Figure 4.8 shows a distribution of raw pulse heights for a counter struck by isolated muon tracks in CC neutrino events. The unit of energy measure-

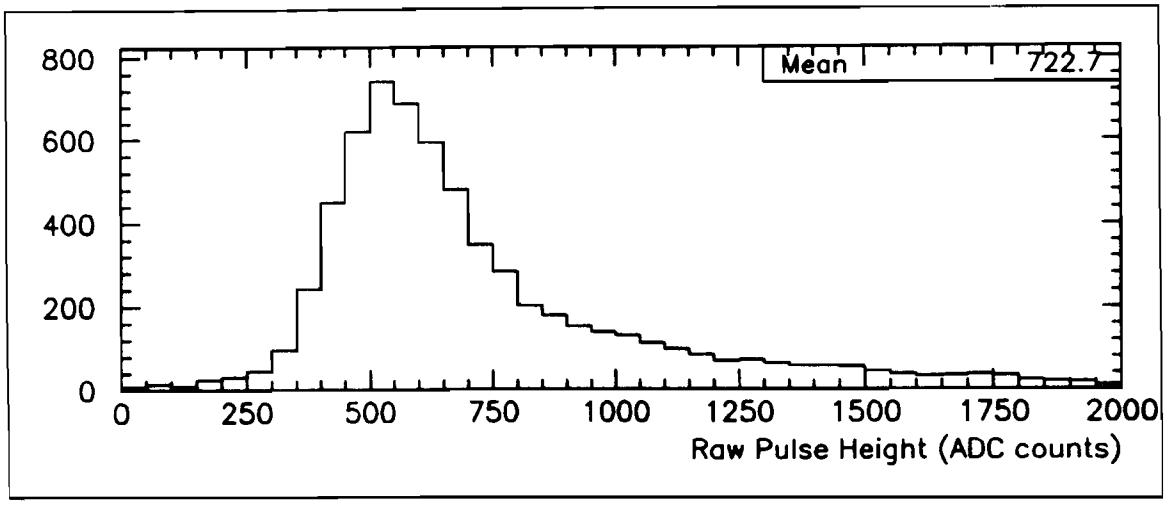

Figure 4.8: Typical raw pulse height distribution for a counter hit by isolated tracks in CC neutrino interactions.

ment by the charge integrating ADC[2] is the ADC count. The energy deposited by minimum ionizing particles in the scintillator varies widely, peaking between 500 and 600 ADC counts, and averaging at over 700 ADC counts for this particular counter. The range of the ADC unit digitizing the pulse height had a maximum of just over 2000 ADC counts. Pulse heights recorded with the maximum possible value are called **'overflow pulse heights'**. In this particular counter, a minimum ionizing particle had an overflow pulse height less than 5% of the time.

The gain of each of the 32 PMTs was different. In addition, the gain of each tube varied with time. The remainder of this section describes corrections made to the raw pulse heights to compensate for these variations.

On two occasions during the run while data were being taken, attempts were made to improve the grounding configuration of the photomultiplier tubes. During these periods, pulse height information was not recorded. After these changes were made, the overall gain of all of the tubes was modified because the ground was

[2]An ADC is an Analog to Digital Converter.

shifted. Shown in Figure 4.9 is the average raw pulse height from isolated track hit counters as a function of run number in CC neutrino events. There are 3 distinct run

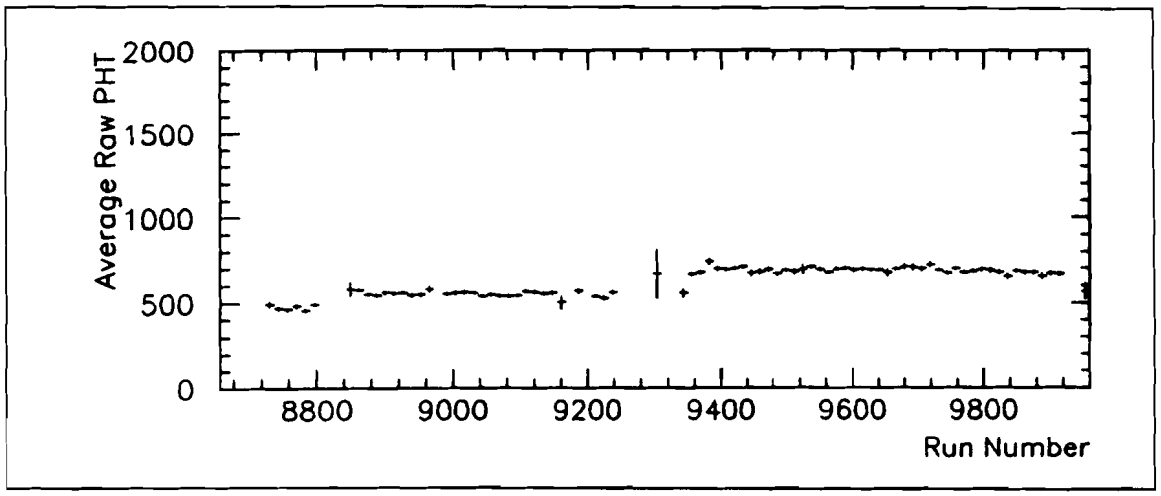

Figure 4.9: The average raw pulse height as a function of run number.

periods, separated by the ground modification work periods, where the average pulse height remains relatively constant, as shown in the figure. Table 4.4 lists the run periods when the system was worked on and when the pulse heights were believed to be stable in time. The run periods when PHT information is not available are

Table 4.4: Good and Bad Pulse Height Runs.

PHT Run Range	Run Numbers	Average Pulse Height	Fraction of Data Set
	8604 - 8711	Bad PHT runs	.4%
1.	8712 - 8817	496 ACD counts	.6%
	8818 - 8835	Bad PHT runs	6%
2.	8839 - 9244	565 ADC counts	38%
	9245 - 9298, 9300 - 9346	Bad PHT runs	5%
3.	9299, 9347 - 9951	696 ADC counts	50%

called 'Bad PHT runs', the three run ranges where PHT information is available are designated 'PHT run range 1, 2 and 3'.

In addition to this run dependence, the gain of each of the photomultiplier tubes varies. Figure 4.10 shows the average pulse height for each of the 32 tubes (2 PMT's per TOF counter) from counters struck by isolated tracks in CC neutrino events. The

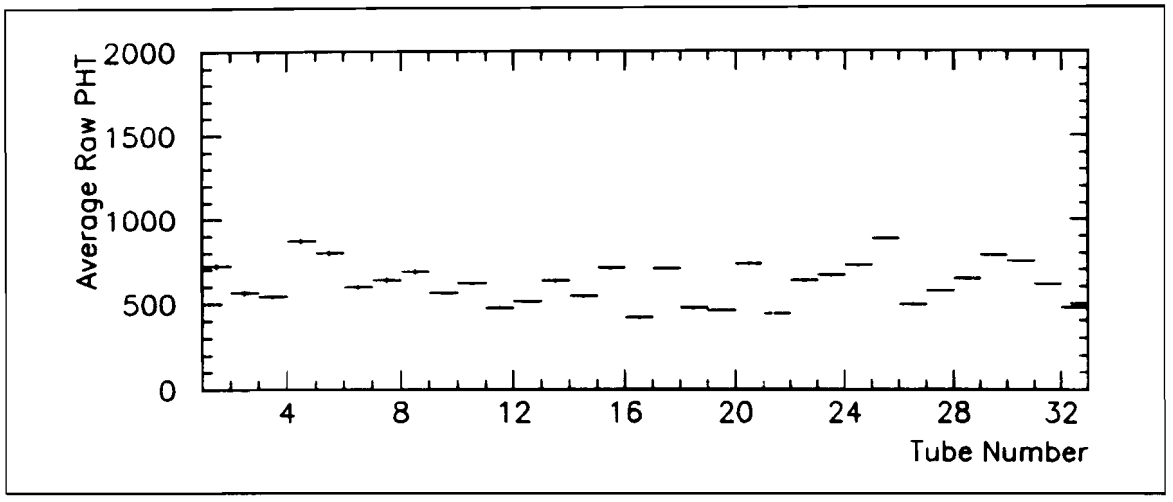

Figure 4.10: The average raw pulse height as a function of PMT number.

tubes are numbered from 1 to 32 starting in the furthest upstream bay, numbered bottom to top, east to west. The east tube of counter 1 is tube 1, the west tube is number 2, etc.

Testbeam muon data cannot be used to assess these corrections because the incoming testbeam particles always illuminate the same section of the calorimeter, generally through TOF counters 2 and/or 10. Therefore, gain corrections are obtained using track hit counters in CC-like neutrino events.

Given identical photocathode illumination, two PMT's with different relative gains will have different characteristic pulse height spectra. The gain of a PMT refers to the total amount of dynode amplification of the input signal: the higher the gain, the more the input signal is amplified.

We wish to normalize the 32 PMT pulse height spectra. We want the corrected pulse height output to be the same for all tubes given a fixed total energy deposited in that TOF counter. As the gain increases, the shape of the distribution changes

as well as the overall increase in average pulse height. Therefore, we cannot merely shift the pulse height spectrum of a tube with a lower gain by a constant.

The normalization process must involve a correction that mimics the nature of a voltage gain, by multiplying each pulse height by a constant factor. Given two pulse height distributions, the normalization proceeds as follows:

1. Choose the distribution with the highest statistics as the reference distribution.

2. Multiply the value of each entry in the other pulse height distribution by a constant and fill a new pulse height distribution with this corrected pulse height.

3. Iterate over the value of the multiplicative constant. The optimal gain correction constant is obtained when the value of χ^2 is minimized, where χ^2 is given by:

$$\chi^2 = \sum_i \left[\frac{(N_S^i - N_R^i)^2}{(2(\epsilon_S^i + \epsilon_R^i))} \right] \tag{4.3}$$

   The sum over i is the sum over all histograms bins. N_S^i and N_R^i are the number of entries in bin i of the shifted and reference pulse height distributions, respectively. The uncertainty in N_S^i and N_R^i are ϵ_S^i and ϵ_R^i, respectively.

4. The fitting program uses a MINUIT [40] function minimization routine called SIMPLEX.

We assume that the run dependent gain is independent of tube number and that it is constant within each of the three run periods. A pulse height distribution, like the one in Figure 4.8, was produced for each tube in each of the 3 run ranges.

To get the run dependent gain corrections, run range 3 was chosen as the reference distribution for each of the tubes since it has the best statistics. For each tube number, the procedure above was used to find the run dependent gain for PHT run range 1 and 2 relative to run range 3 for that tube. The final run dependent gains (for run ranges 1 and 2) is the statistical average of the gains calculated for each

tube number. The average pulse heights as a function of run number after the run dependent gain corrections are made is shown in Figure 4.11.

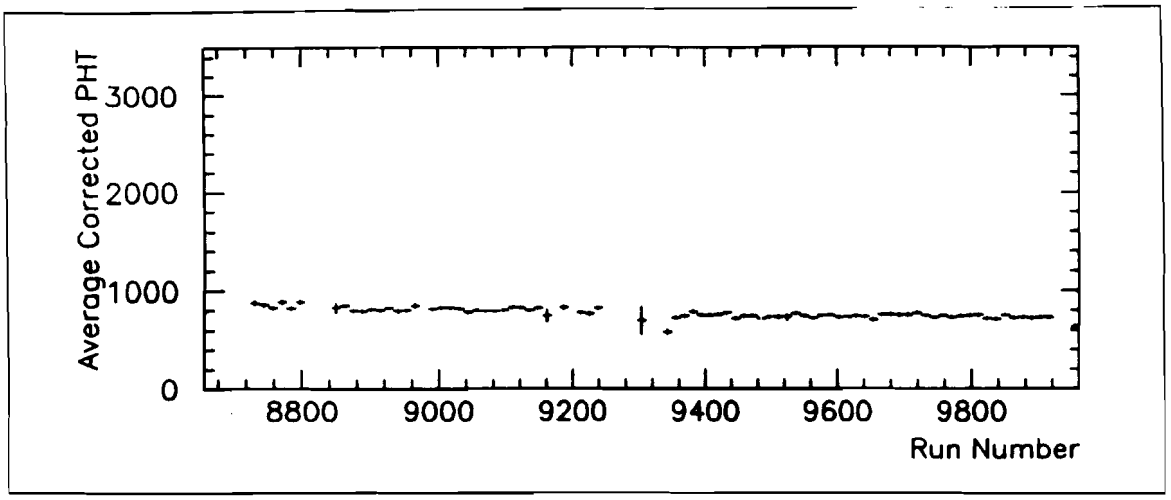

Figure 4.11: The average corrected pulse height as a function of run number.

These run dependent gains are applied to the data sample before the tube dependent gain corrections are calculated. A pulse height distribution like that in Figure 4.8 that include all 3 PHT run ranges is made for each of the 32 PMT's. To get the tube dependent gain corrections, tube number 28 (west tube of counter 14) was chosen as the reference distribution since it has the best statistics. A tube dependent gain was calculated for each tube as described in the procedure above. The average pulse heights as a function of tube number after the run and tube dependent gain corrections are shown in Figure 4.12. In the process of gain normalization, the scale of the pulse height is expanded, extending to over 3000 corrected ADC counts. This occurred because the reference distributions chosen had higher average pulse heights than the other distributions.

Overflow pulse heights are reassigned to have a value beyond the corrected PHT scale, at 3501 corrected ADC counts. The pulse heights referred to henceforth are the run and tube dependent gain corrected pulse heights.

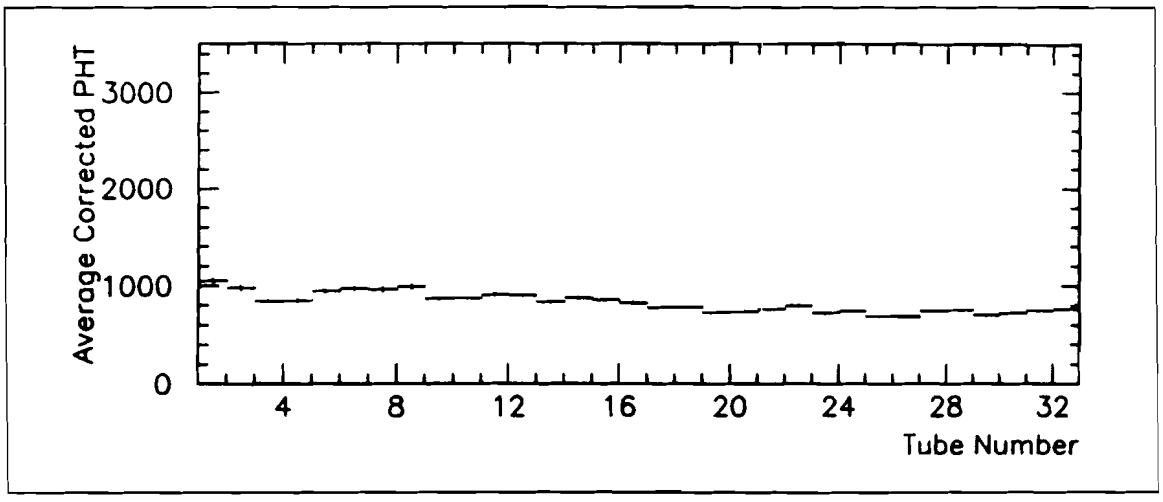

Figure 4.12: The average corrected pulse height as a function of PMT number.

Chapter 5

Event Time Measurement

5.1 Overview

The Time of Flight (TOF) counter configuration described in Chapter 3 was designed to maximize coverage within the active fiducial volume while minimizing the cost and maximizing the ease of integration of the TOF apparatus into the already existing E733 detector. Because of the relatively large size of the scintillator and the finite speed of light, each time measurement must include a correction for the time required for the scintillation light to travel from the region of energy deposition to the photomultiplier tube. Therefore, the ability to accurately measure event times depends on the ability to predict where energy is deposited in the scintillator.

The pattern recognition program identifies the final state topology, finds tracks, and locates the end of the hadronic shower (JEND). The energy deposited by a single track is much more localized than the energy deposited by multiple tracks (as in a hadron shower). We therefore separate the data sample into two parts, a CC-like part and an NC-like part[1], since each subset will have distinct timing characteristics:

1. Event timing of CC-like events is obtained using the timing information from counters struck by tracks.

2. For events with only a hadronic shower (NC-like), accurate measurement of

[1] CC-like events have a muon of sufficient length, NC-like events do not, as described in Chapter 4.

event times will rely on ability to reconstruct a map of the energy deposition in each TOF counter plane using the other detector elements, namely from the flash chambers and the proportional tubes.

5.2 The TOF Event Sample

As described in Chapter 4, the E733 TOF event sample consists of 125,640 events with event vertices within the TOF fiducial volume. Of these events, 94,675 are classified as CC-like and the remaining 30,954 events were NC-like. Although these events were all within the TOF fiducial volume, some events did not satisfy the TOF trigger so they had no TOF record, or they had a TOF record of incorrect length so they were not utilized. The number of such events in each class is summarized in Table 5.1.

Table 5.1: Classification of events in the TOF event sample.

Classification	CC-like Events	NC-like Events
No TOF record	14004	7060
Short TOF record	105	38
Long TOF record	193	61
Good TOF record	80371	23795
Total	94675	30954

The timing efficiency, ε_{timing}, is the ratio of the number of events with timing information to the total number of events. Based on the information in Table 5.1, we conclude that the maximum possible event timing efficiency is about 85% and 77% for CC-like and NC-like events, respectively.

5.3 The Speed of Light in Scintillator.

We start with the measured tube times of Equation 4.3 (t_{EL}, t_{EH}, t_{WL}, and t_{WH}) : the times, relative to the phase of the RF clock that the east and west PMT output pulses crossed a low (L) and high (H) threshold. These times are corrected for cable lengths and the RF clock drift as documented in Chapter 4.

To turn these measurements into a measurement of the event time, they must be corrected for the time required for the light to travel from the point of energy deposition to the photocathode, which depends on the speed of light in scintillator.

This speed of light was measured using data from counters hit by isolated tracks in CC-like events. We assume that the scintillator response is linear with the distance from the position of energy deposition to the photocathode. From Appendix C.1, the speed of light in the scintillator is

$$v = \frac{d}{t_E + t_W}, \tag{5.1}$$

where, in this case, the time measurement sum $t_E + t_W$ (the sum of the east and west tube times) is averaged over the event sample of isolated track hit counters. This speed was calculated independently for the low and high thresholds in an attempt to take into account the longer time required for the tube to collect enough light to cross the high threshold. The measured velocities are $v_L = 0.541c$ and $v_H = 0.513c$ for the low and high threshold levels, respectively.

The average event time in this analysis is assumed to be zero. The zero of the event time distribution was determined to be the average time that the low level discriminators crossed threshold for counters hit by isolated tracks. This time is independent of the hit position, as shown in Appendix C.2.

5.4 Random Event Scan

In order to get an idea of the level of sophistication needed in an event timing program to realize a optimum event timing efficiency, an event scan was performed on a subset of the data.

A total of 519 identified charged current events with a vertex in the TOF fiducial volume where chosen from 20 data tapes picked randomly from the entire data taking period.

All event pictures were scanned by eye, noting the location of 4-HIT counters hit by tracks and/or showers upstream and downstream of the measured shower end.

The events fell into one of the following categories:

22% of the events have at least one 4-HIT counter that appears to be hit cleanly by a single muon track *downstream* of JEND. This subset represents the sample of events with isolated track hit counters in CC-like events.

7% of the events have at least one 4-HIT counter that appears to be hit cleanly by a single muon track *upstream* of JEND.

12% of the events have at least one MTF track traversing a 4-HIT counter *upstream* of JEND. But, in the vicinity of the track hit counter, additional energy (shower debris) is present in the flash chambers in addition to what normally might be associated with "minimal ionizing particles". To obtain event times for these events, time measurements have to be corrected somehow for the wider spacial distribution of the energy in the counter due to this additional energy.

44% of these events do not have any 4-HIT counters traversed by muon tracks.

15% of the events will never have a measured event time because no 4-HIT counters were hit by anything in the neutrino interaction or the TOF trigger

was not satisfied (no TOF record exists). This category is representative of the number of events in Table 5.1 with no TOF record or an incomplete TOF record.

Based on this event scan, we conclude that in CC-like events:

- An event time efficiency of 22% can be expected if counters utilized to obtain event times are required to be downstream of the measured shower end (JEND).
- An additional 7% efficiency may be obtained by utilizing isolated track hit counters upstream of JEND.
- Another additional 12% in efficiency may be gained if measured times from track hit counters can be corrected for additional hadronic shower debris.

The detector's sensitivity to new particle production depends on the event timing efficiency as well as the timing resolution. Obviously, in sensitive devices such as the TOF counters, spurious measurements are encountered. But there are a number of tube and counter time consistency requirements that can be imposed to eliminate such measurements from the data.

Section 5.5 describes the method used to obtain the event time distribution for CC-like events. Every attempt has been made to maximize the timing efficiency while maintaining good timing resolution. The timing resolution obtained in NC-like events is somewhat poorer, as we will see in Section 5.6, but a comparable timing efficiency is maintained.

5.5 CC-like Event Times

A CC-like final state, by definition, contains a long muon track. In CC-like events, only those 4-HIT counters which are traversed by a flash chamber tracked muon are considered for use in obtaining the measurement of the event time. This section

describes how a CC-like event time is determined, and presents the distribution of event times for all timed CC-like events in the event sample.

5.5.1 Time Measurement Criteria

Of the 94,675 CC-like events, 80,371 events have at least one 4-HIT counter. 55,83 events have at least one track hit 4-HIT counter. In these 55,831 events, there 93,292 track hit 4-HIT counters (an average of 1.7 counters per event). These are the time measurements utilized to obtain event times in CC-like events.

A schematic of a TOF counter struck by a high energy muon is shown in Figure 5.1. To use the time measurements t_{EL}, t_{EH}, t_{WL}, and t_{WH} of Equation 4.3 to obtain

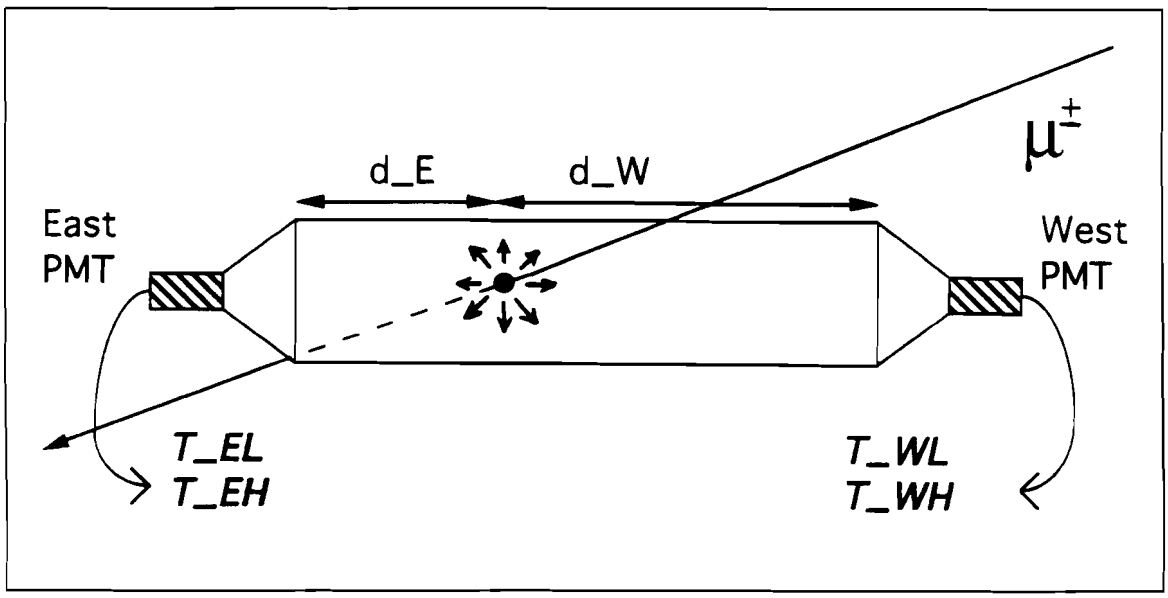

Figure 5.1: A schematic of a time-of-flight counter struck by a single minimum ionizing particle.

an event time from track hit counters, a couple of corrections to these times need to be made, as shown in Equation 5.2. These corrections are described below.

$$
\begin{aligned}
t^{\mu}_{EL} &= t_{EL} + \frac{d_E}{v_L} + \frac{z_\mu - z_\mu \cos\theta_\mu}{c\cos\theta_\mu}, \\
t^{\mu}_{EH} &= t_{EH} + \frac{d_E}{v_H} + \frac{z_\mu - z_\mu \cos\theta_\mu}{c\cos\theta_\mu},
\end{aligned}
$$

$$t^{\mu}_{WL} = t_{WL} + \frac{d_W}{v_L} + \frac{z_\mu - z_\mu \cos\theta_\mu}{c\cos\theta_\mu}, \quad and$$
$$t^{\mu}_{WH} = t_{WH} + \frac{d_W}{v_H} + \frac{z_\mu - z_\mu \cos\theta_\mu}{c\cos\theta_\mu}. \tag{5.2}$$

The second term in Equation 5.2 reflects the necessary correction to the measured time for the time required for the scintillation light to travel from the point of energy deposition to the PMT. The spacial position of charged particle traversal in a TOF counter is determined using flash chamber tracks, so the distances d_E and d_W, the distance from the point of energy deposition to the east and west PMT's (shown in Figure 5.1), are known. As described in the last section, v is the measured speed of light in scintillator.

As described previously, counter timing measurements from each counter are shifted such that they measure on average the same time when struck by a particle traveling at the speed of light in the beam direction ($+\hat{z}$). If a muon is at an angle greater than a few degrees with the beam direction, an additional correction to the measured time is needed for the additional time required for the muon to travel in the transverse direction. The third term in Equation 5.2 expresses the magnitude of this necessary correction. The muon angle, θ_μ, is measured by the flash chambers. The z_μ in Equation 5.2 is the distance in the beam direction from the event vertex to the z position of the TOF counter plane.

The four times in Equation 5.2 are averaged to obtain a counter time. The distribution of all track hit 4-HIT counter times is shown in Figure 5.2 a). The same distribution of times is shown in Figure 5.2 b) with counter times shifted[2] into a single period of the RF clock extending from about -9.5 to $9.5ns$ (a single period of the RF clock spans $18.83ns$). This shift (equal to an integral number of RF clock periods) is relatively unambiguous for truly isolated track hit counters, but the long high tails in this distribution indicate that many of the measurements in

[2]Recall that this shifting is necessary because the RF clock signal is prescaled by a factor of 4 as described in Chapter 3.

this distribution are not consistent with a single minimum ionizing particle traversal. Ideally, we expect this distribution of counter times to be more gaussian-like (though not necessarily gaussian), with a mean near $t = 0$ and an RMS deviation of about 1 ns.

In order to eliminate time measurements known to be inconsistent with a signal produced from the traversal of single tracks, a set of requirements, listed in Table 5.2, were imposed on the time measurements utilized. The first three cuts require that

Table 5.2: The clean track counter requirements.

	Requirement	Elucidation
1.	rise times $< 1.5ns$	The east and west rise times, the time differences between the low and high threshold times in the east and west tubes, are required to be less than 1.5 ns.
2.	$\lvert t_E - t_W \rvert < 3.0ns$	The average east tube event time must be consistent with the average west tube time within 3.0 ns.
3.	$\lvert t_E * - t_W * \rvert < 3.0ns$	East low and west high or east high and west low threshold times must agree within 3.0 ns.
4.	vertex $-12fc < z(TOF)$	The TOF plane utilized must be more than 12 flash chamber planes downstream of the event vertex.
5.	not PHT overflow	During good pulse height runs, if the pulse height of either PMT is in the overflow range, neither tube time measurement in that counter is utilized.
6.	$JEND < z(TOF)$	During bad pulse height runs, the TOF counters utilized must be downstream of JEND.

tube times be consistent with each other to within a factor of $1-2$ of their expected time resolution. The pulse height requirement is imposed to eliminate measurements from counters struck by more energy than is expected from a single track. In the absence of pulse height data (during bad pulse height runs) we require that counter times utilized be downstream of the measured end of the shower (JEND).

Counters that pass all of these criteria are called "clean track counters" or counters passing the "clean track criteria". The distribution of counter times passing

these requirements is shown in Figure 5.2 c).

These time distributions are inverted as described in Chapter 4: Smaller time measurements are the latest chronologically, while larger times are early. This inversion occurred when times were shifted relative to the time of the RF clock STOP signal, which always occurred later than the timing signals from the counters (see Equation 4.2). In other words, the measured times less than 0. ns are events which occur later than the mean time of arrival of the neutrino bunch.

5.5.2 Pulse Height Corrections to the Time

The distribution of clean track counter times of Figure 5.2 c) looks considerably cleaner than the one shown in Figure 5.2 b). In particular, the number of time measurements in the tails has decreased dramatically, however, the distribution is still wider than anticipated.

Thus far, we have assumed that the TOF counter timing signals from a muon track is ideal. In reality, we know that additional factors may affect the outcome of the timing measurement.

High energy muons transfer energy to any medium through various electromagnetic processes:

1. Ionization is the principal form of energy loss for muons traversing a medium. The amount of energy deposited depends on the electron density of the medium, and the charge and velocity of the incoming particle.

   For relativistic muons, such as those typical in high energy charged current neutrino interactions, the electrons emitted occasionally have enough energy to produce secondary ionization in the atoms along their path. These high energy electrons are called δ rays.

2. The electromagnetic radiation emitted by charged particles decelerated in the field of atomic nuclei is called bremsstrahlung. Such radiation produces

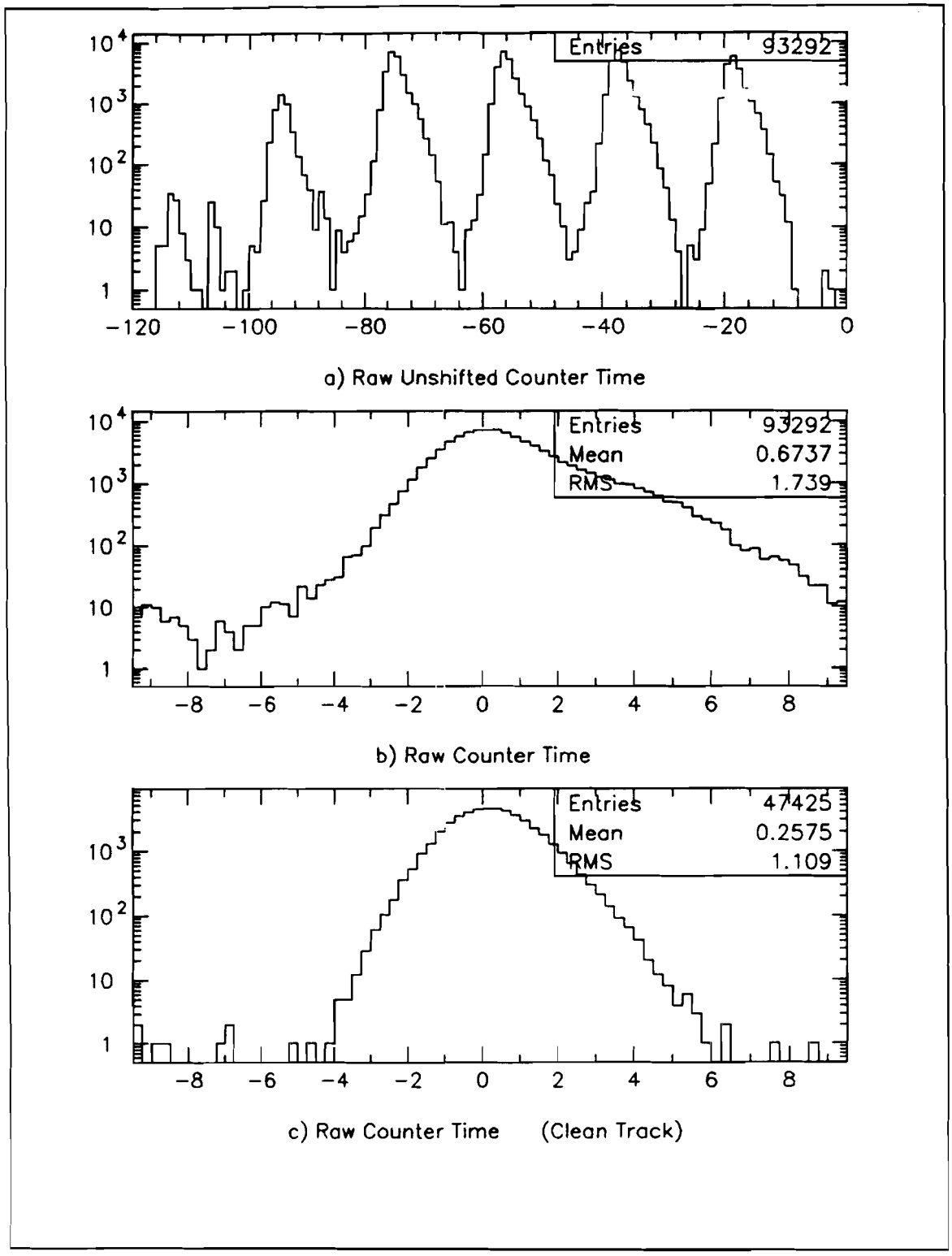

Figure 5.2: The distribution of counter times in *all* track hit 4-HIT counters in CC-like events a) unshifted and b) shifted into a single period of the RF clock. The time distribution for counters passing the *clean track* criteria are shown in c).

electron-positron pairs that deposit energy in a shower denser than a typical hadronic shower of the same energy.

δ ray emission and bremsstrahlung occur at a lower rate than basic ionization. But if either of these higher energy transfer processes occur near a TOF counter, the energy deposited in the scintillator will be greater and the energy will be distributed over a wider area.

3. Atomic excitation is another mechanism by which charged particles can transfer energy to a medium. High energy muons are not expected to produce significant atomic excitation directly, but do so secondarily via ionization processes. This is the source of the light emitted in the scintillator, which is induced by ionization.

The total energy loss of the muon in a thin absorber like a TOF scintillator counter varies according to a Landau distribution[3]. A fraction of the energy loss in the scintillator is converted to produce scintillation light. This light is emitted isotropically, and is collected by the PMTs at the ends of each TOF counter after multiple internal reflections in the scintillator and light guides. Time measurements are generated when the PMT output crosses low and high thresholds.

If more energy is deposited in the scintillator, more light will be emitted in the direction of the PMT, resulting in earlier threshold crossings, and thus earlier time measurements. Conversely, lower energy pulses result in delayed time signals.

If energy is deposited over a wider area in the scintillator, the scintillation light will not have to travel as far in the scintillator to reach the PMT. Again, earlier time measurements are a result.

The only direct measurement of the amount of energy deposited in the scintillator is the measured pulse height (described in Chapters 3 and 4). The PMT pulse height

[3]A Landau distribution has a narrow peak at low values and a long asymmetric tail at high values.

is strongly correlated with the PMT time measurement[4] as shown in Figure 5.3 a) for counters passing the clean track criteria.

Figure 5.3 b) demonstrates the correlation more clearly. Here, points on the graph indicate the average of all PMT time measurements as a function of PMT pulse height. The pulse height is a measure of the amount of energy deposited in the scintillator. As the pulse height increases, the measured time, on average, is earlier (earlier times have a higher measured time).

This correlation is used to correct the measured PMT times. In the three pulse height regions: 1) $300 < PHT < 800$, 2) $800 < PHT < 2000$, and 3) $2000 < PHT < 3500$, a linear fit for the average PMT time as a function of pulse height is obtained as shown (by 3 solid lines) in Figure 5.3. The corrected PMT time is the raw PMT time (as in Equation 5.2) shifted by an amount dictated by the linear fit of the average time found at the PMT pulse height.

A very similar correlation is found in testbeam muon event time measurements passing the same criteria as shown in Figure 5.4 a) and b). Overlaid on b) is the linear fit to the average time as a function of pulse height found in neutrino data shifted by $-2.5ns$[5]. The fit found in neutrino data deviates from the average testbeam times no more than a few nanoseconds in each pulse height range. An identical correlation is not expected because the muon energy spectrum is different in neutrino and testbeam data and testbeam muons almost always traverse the same TOF counters (numbers 2 and 10). Therefore measurement systematics of clean track timed neutrino events and muon timed testbeam events are expected to be different.

[4]The PMT time is obtained by averaging the low and high threshold time measurements.

[5]Since testbeam muons arrive at the detector from a different beamline (of longer length) the average testbeam time is different from that of neutrino events. The measured difference between average event times in testbeam and neutrino events is $-2.5ns$.

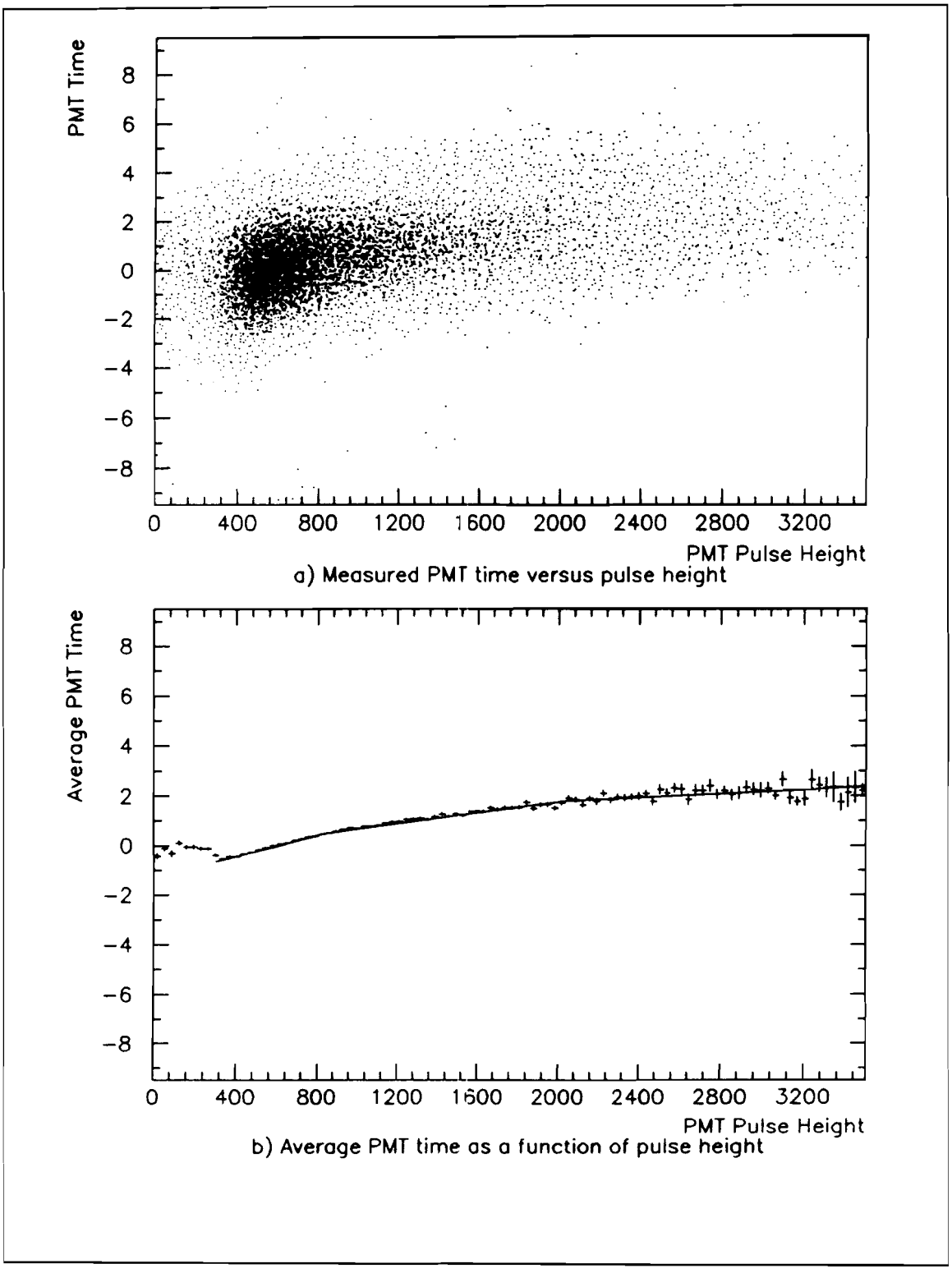

Figure 5.3: For CC-like neutrino events: a) Scatterplot of PMT time versus PMT pulse height for all counters passing the clean track criteria. b) The average PMT time as a function of PMT pulse height for the same set of counters.

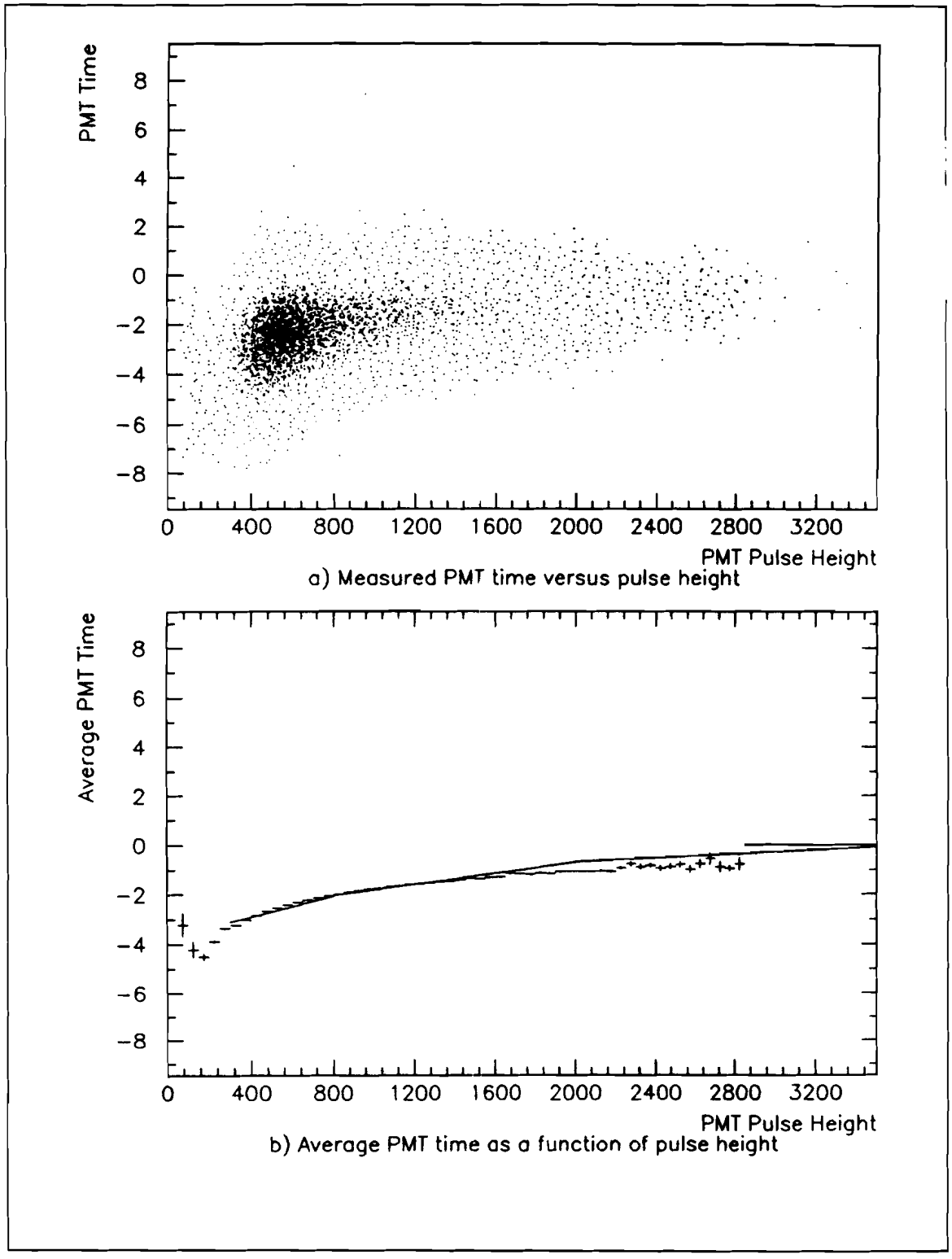

Figure 5.4: For testbeam muon events: a) Scatterplot of PMT time versus PMT pulse height for all counters passing the clean track criteria. b) The average PMT time as a function of PMT pulse height for the same set of counters.

5.5.3 Event Timing Anomalies

The pulse height corrected time distribution for all counters passing the clean track criteria is shown in Figure 5.5. The CC-like event time distribution, shown in Figure

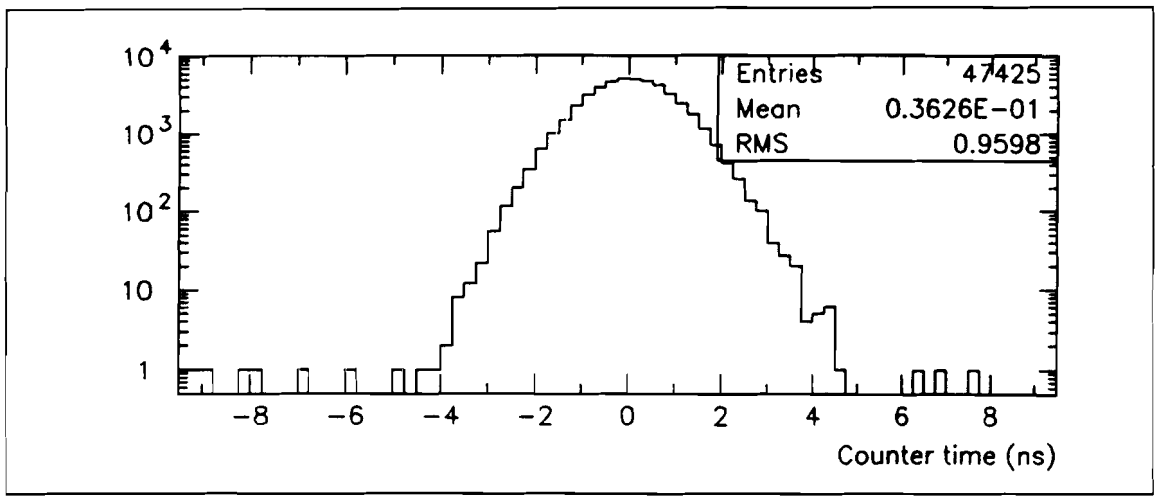

Figure 5.5: The distribution of pulse height corrected counter times in track hit 4-HIT counters passing the clean track criteria in CC-like events.

5.6, is obtained by averaging all clean track hit counter time measurements available in each event.

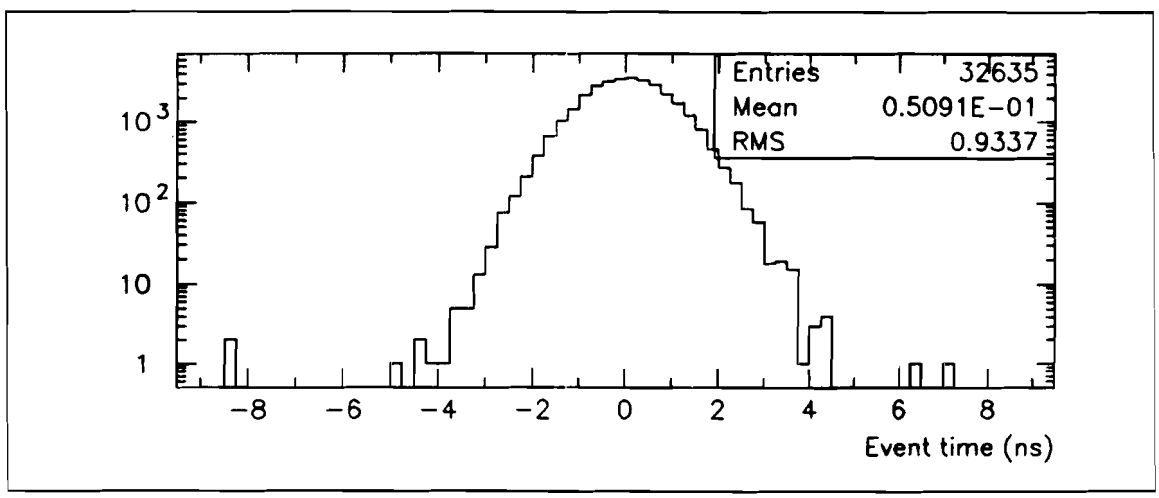

Figure 5.6: The CC-like event time distribution obtained by using all counters passing the clean track criteria in CC-like events.

A number of 'outliers' (events with measured times in the 'early' and 'late' tails

of the event time distribution) are clearly seen in Figure 5.6. There are a number of possible explanations for such event time measurements:

1. Such events may be a signature of WIMP induced interactions in the detector.

2. Cosmic ray induced events may contaminate the CC-like neutrino event sample at a small level.

3. Bicron-408 scintillator is sensitive to neutral particles as well as to charged particles. Other byproducts of generic neutrino interactions, such as slow neutrons emerging from hadronic showers, may strike TOF counters, producing late timing signals.

4. The event pattern recognition algorithm may incorrectly identify tracks or vertex positions. Such inefficiencies can affect timing results.

In order to study any unanticipated systematics of the timing analysis and identify any true WIMP candidates, all events with any clean track counter time measurement outside of 3 ns were scanned by eye. A total of 160 were scanned. A number of anomalous events were identified and eliminated from the analysis. Table 5.3 lists the justification for event or counter elimination, and the number of events in each category.

Cosmic ray events are expected to have a flat event time distribution. Based on the 6 cosmic ray events found outside of a time window from $-3 < t < 3$ ns with an average timing efficiency of 34%, we conclude that the total CC-like event sample is contaminated with cosmic rays at a less than 0.03% level[6]. Contamination at such a small level has a negligible effect on the timing efficiency.

[6]If 6 cosmic rays are found in a 13 ns time interval with an average timing efficiency of 34%, then over a time interval of 18.83 ns (one RF clock period), about 26 total cosmic rays events are expected. The total CC-like event sample contains about 95,000 events. Twenty six events in 95,000 is less than 0.03% of the sample.

Table 5.3: Time measurements eliminated from the CC-like event sample.

Number of Events	General classification
6	Cosmic ray events misidentified as CC-like neutrino events such as that shown in Figure 5.7.
1	Occasionally, a neutrino event is recorded that contains additional flash chamber hits due to residual ionization from a previous interaction. Figure 5.8 shows one such 'out of time' event. This event contained a timing irregularity because the pattern recognition program used flash chamber hit information from both events to find muon tracks. Therefore, the event was eliminated from the event sample.
13	Thirteen events were found which utilized time measurements from TOF counters that were not traversed by a high energy muon. The detail of the E733 event display makes this determination unambiguous. An example of such an event is shown in Figure 5.9, where the pattern recognition algorithm finds a muon track striking counter number 16 (the topmost counter in the last TOF plane). The event picture shows clearly that no muon traverses this region. In each of these thirteen events, either no muon is visible traversing the 4-HIT counter with the anomalous time or the muon track ranges out before hitting the counter utilized. These events were not eliminated from the event sample, just the counter measurement which was deemed incorrect.

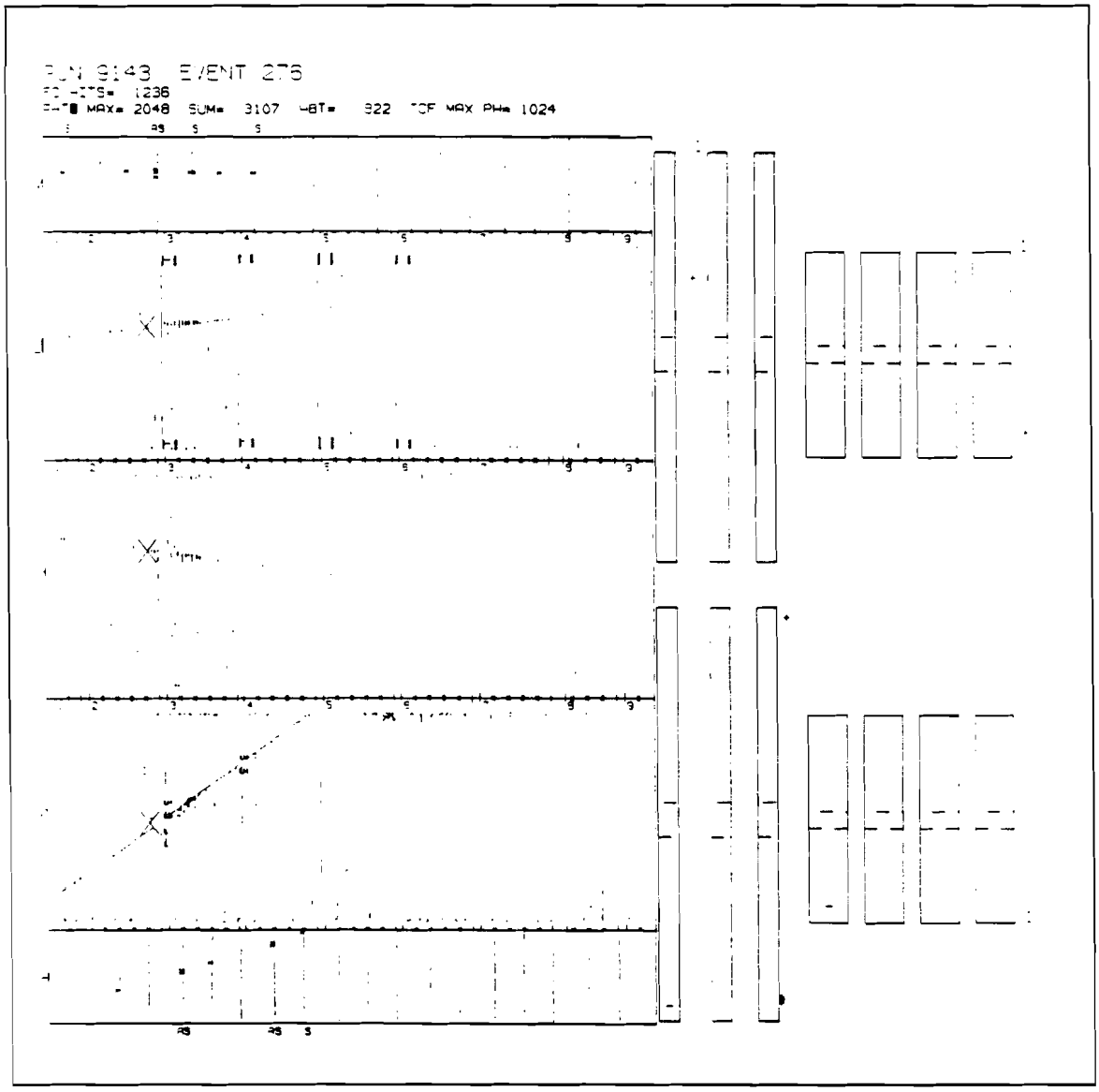

Figure 5.7: A typical cosmic rays muon event identified in the CC-like event scan.

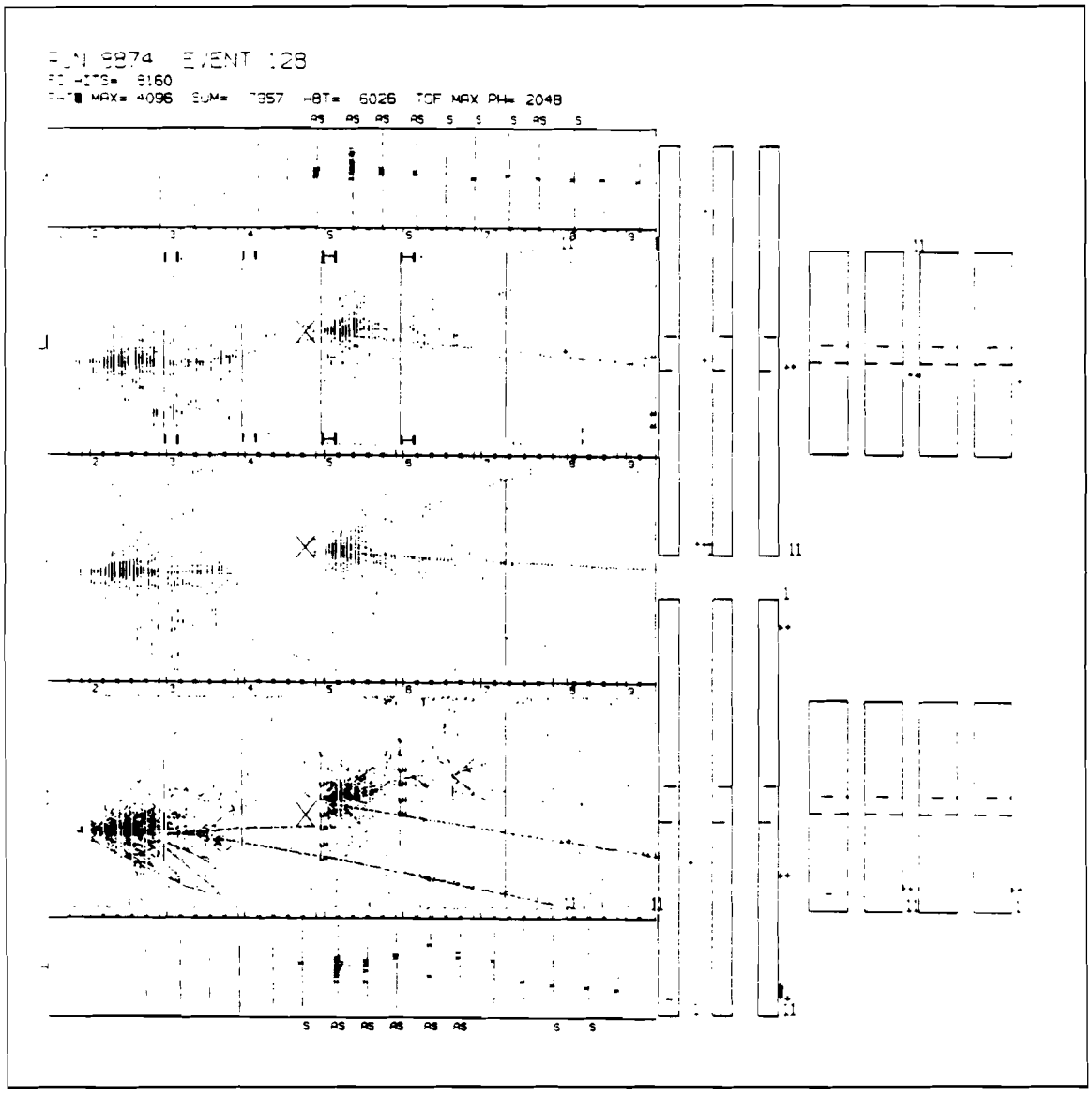

Figure 5.8: An 'out of time' event identified in the CC-like event scan.

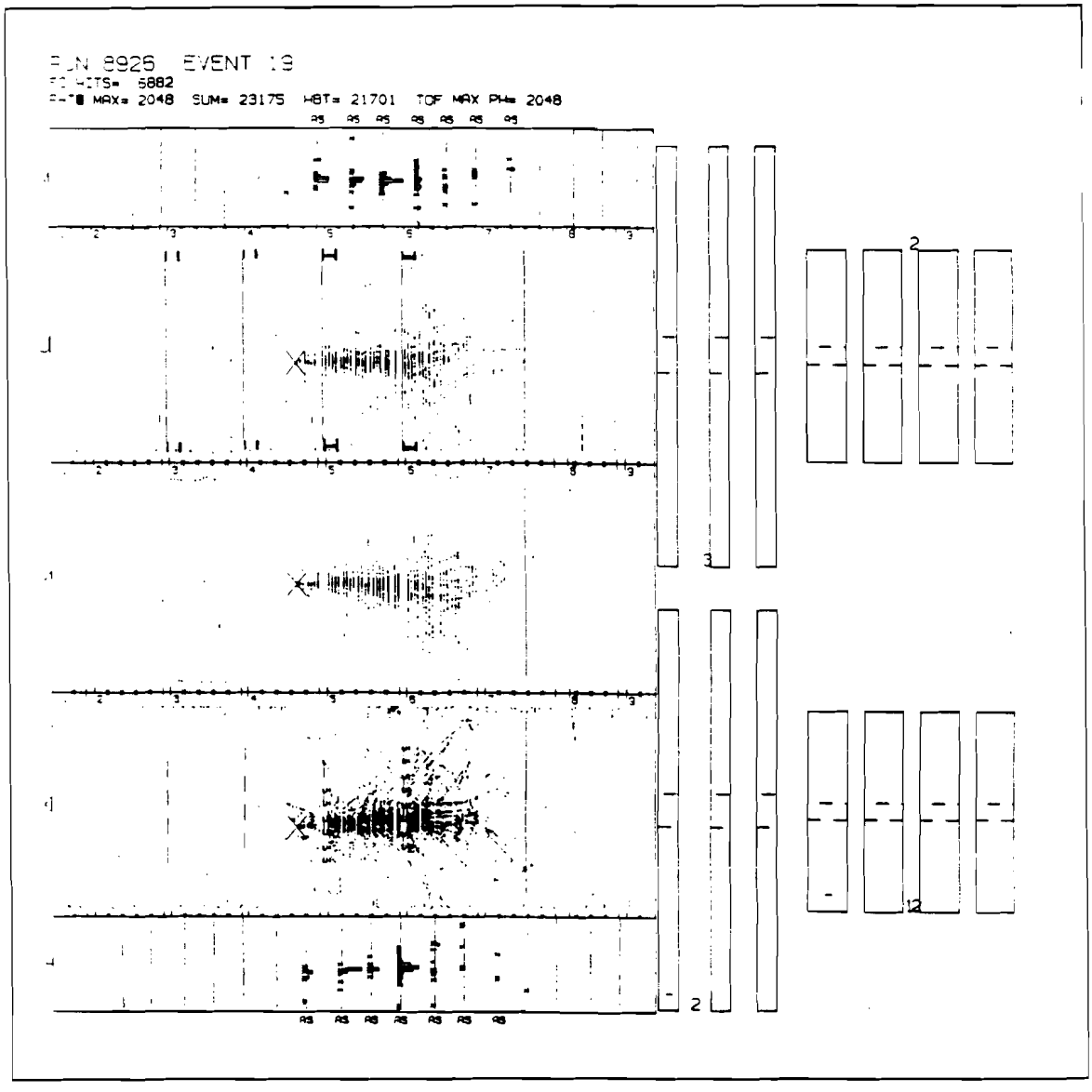

Figure 5.9: A typical event which utilizes a time measurement from a TOF counter that is not struck by a muon. In this event, the pattern recognition program found a track emerging from the vertex passing through counter number 16 (in the X flash chamber view, this is the topmost TOF counter in the last downstream TOF plane). Clearly, no such track exists.

5.5.4 The CC-like Event Time Distribution

After the events or counters discussed in the last section are eliminated from the TOF CC-like event sample, a final event time distribution is obtained as shown in Figure 5.10. Zero events are observed in the time window outside of $-4.5 < t < 4.5$

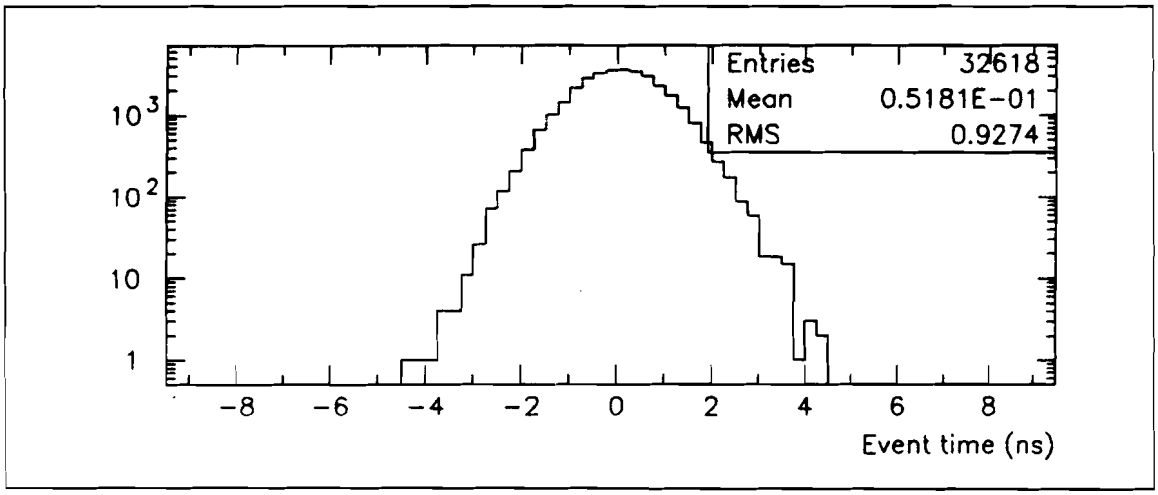

Figure 5.10: The final CC-like event time distribution.

ns.

A total of 32,618 events were timed in the CC-like event sample consisting of 94,675 events, yielding an average timing efficiency of 34.5%. This efficiency is not independent of final state characteristics: The efficiency depends the angle of the muon relative to the beam axis (θ_μ) as shown in Figure 5.11. Timing efficiency exceeds 40% at small muon angles. It decreases linearly to about 16% at 0.2 radians, remaining relatively constant at 16% for higher muon angles.

The time window outside which no events are seen (called the *search window*), and the timing efficiency as a function of θ_μ are used in Chapters 6 and 7 to set limits on new particle production. If any particle production model predicts that more than 2.3 events[7] with this final state topology should be recorded with a time-of-flight in the search window (outside $-4.5 < t < 4.5$ ns), then that model can be

[7]According to poisson statistics, if more than 2.3 events are expected, it is more than 90% probable that more than 0 event will be seen in the detector.

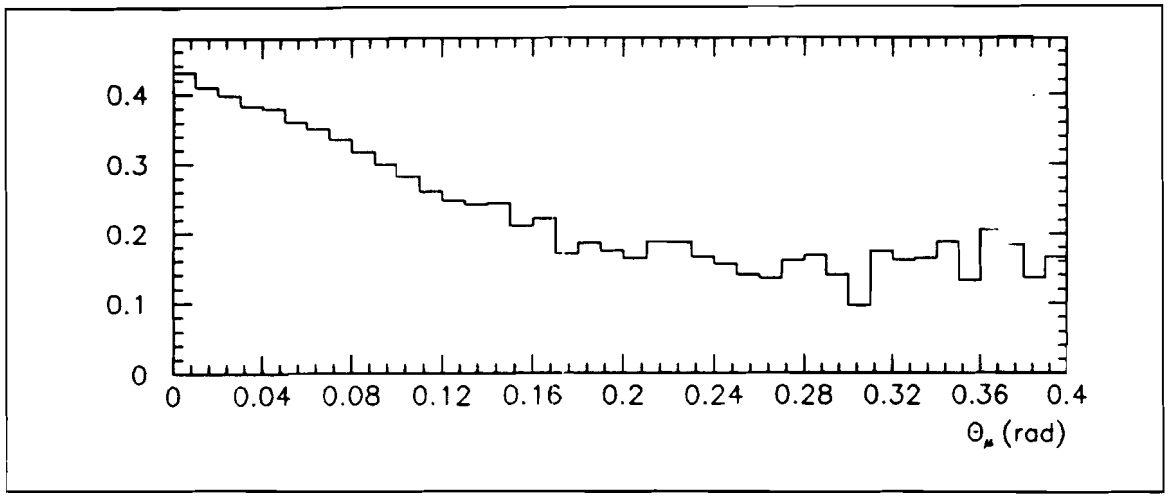

Figure 5.11: The event timing efficiency as a function of the angle of the muon with the beam axis.

excluded at the 90% confidence level.

But before using these results the CC-like timed event sample is broken up into two parts: the first part consists of all events timed using a single counter time measurement, the second part contains events timed using two or more counters. The advantage in separating the sample in this way is that the timing resolution is better in the latter sample, thus enabling us to use a wider search window for a fraction of the timing efficiency.

The CC-like event time distribution for the single and multiple counter timed events are shown in Figure 5.12 a) and b) respectively. As shown in the figure, the search windows corresponding to the single and multiple counter timed samples are $-4.5 < t < 4.5$ ns and $-3.25 < t < 3.75$ ns, respectively.

The corresponding timing efficiency for single and multiple counter timed CC-like events is shown in Figure 5.13 a) and b), respectively.

In Chapters 6 and 7, all limit results obtained for CC-like final states use these two search windows and efficiency distributions. The different CC-like event timing efficiency distributions (above) are folded in with the expected distribution of muon angles for each model, in order to properly account for the dependence of the timing

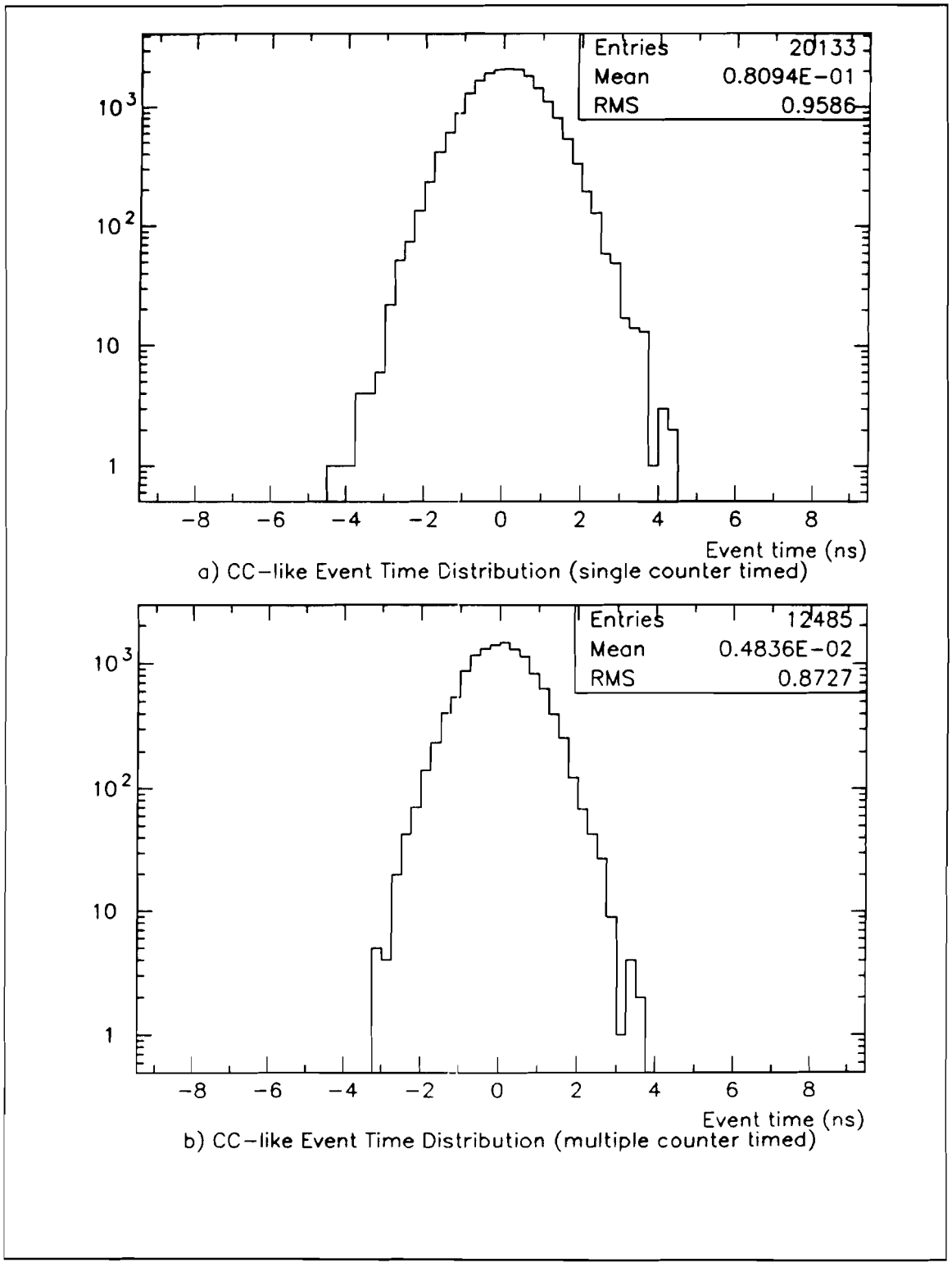

Figure 5.12: The final CC-like event time distribution for a) single counter timed events and b) multiple counter timed events.

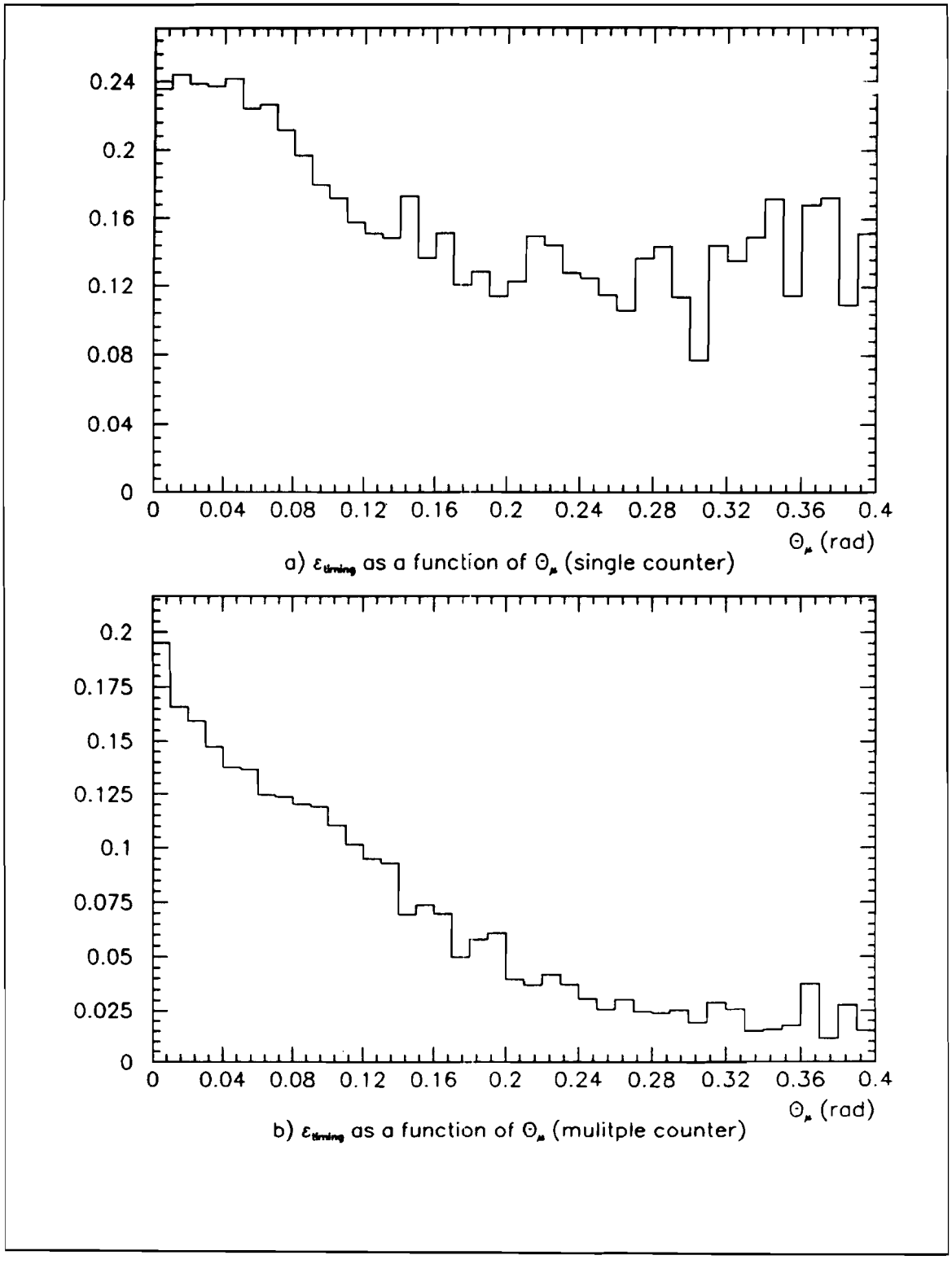

Figure 5.13: The event timing efficiency as a function of the angle of the muon with the beam axis for a) single counter timed events and b) multiple counter timed events.

efficiency on the muon angle.

5.6 NC-like Event Times

NC-like final states consist of a hadronic shower of varying energy, but no high energy muon tracks. The energy deposition of showers in TOF counters is inherently less localized than that of single tracks, therefore, we expect time measurements to be less precise, while corrections become more elaborate.

5.6.1 Corrections to the Time Measurements

CC-like events contain a shower as well as at least one muon track. The data set used to test shower timing algorithms described in the next few sections was the clean track timed CC-like event sample. These events are known to have event times between −4.5 and 4.5 ns. All corrections to measured times in NC-like events are based on studies of shower timing in timed CC-like events.

A schematic of an idealized distribution of hadronic energy in a TOF counter is shown in Figure 5.14. In principle, if the location of the 'shower edge' in each TOF

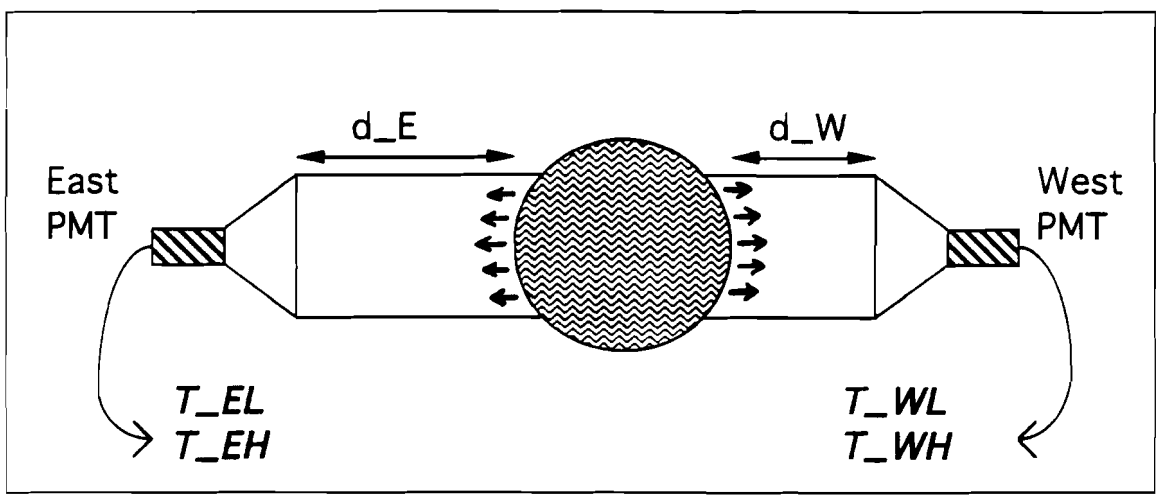

Figure 5.14: A schematic of the energy deposition of a hadronic shower in a TOF counter.

counter can be identified, then the distances d_E and d_W (the distance from the east

and west shower edges to the east and west tubes) can be determined. Then the times can be corrected, just as in Equation 5.2, to get measured event times.

Flash chamber hit information has been used to measure the location of the shower edges, and thus the *shower width*, according to the following procedure:

1. The pattern of hit flash chamber cells was studied in the 24 flash chamber planes upstream of each TOF plane. These 24 planes were split into 3 groups, each containing 8 flash chamber planes. A group of 8 FC planes, called a modulw, is 25 – 30 cm in depth. Each modulw contains four X view, two Y view and two U view flash chamber planes.

2. In each flash chamber plane, FC hits were summed in groups of 10 cell bins (64 bins per plane). Each 10 cell bin is about 6 cm wide. In each modulw, these 10 cell binned hits were summed by view. Adjacent 10 cell summed hits in each view with nonzero FC hits were grouped together to form *clusters*.

3. Associated with each *cluster* is a sum of FC hits and a spacial location in the calorimeter. These clusters are projected from the vertex onto each TOF plane in each view in each modulw.

4. These cluster projections are 2-D matched in the U and Y views at the vertical location of each TOF counter for each modulw. Shower edges are defined as the location of the outermost edge of cluster projections that coincide in all 3 modulw's upstream of that TOF plane.

5. Cluster projections in the X view are used later when consistency constraints are imposed on the timing measurements utilized. The density of hits in X view clusters is also used to correct counter times as described later.

The distribution of counter times with no corrections is shown in Figure 5.15 a). The location of the edges of the shower (obtained as described above) are used

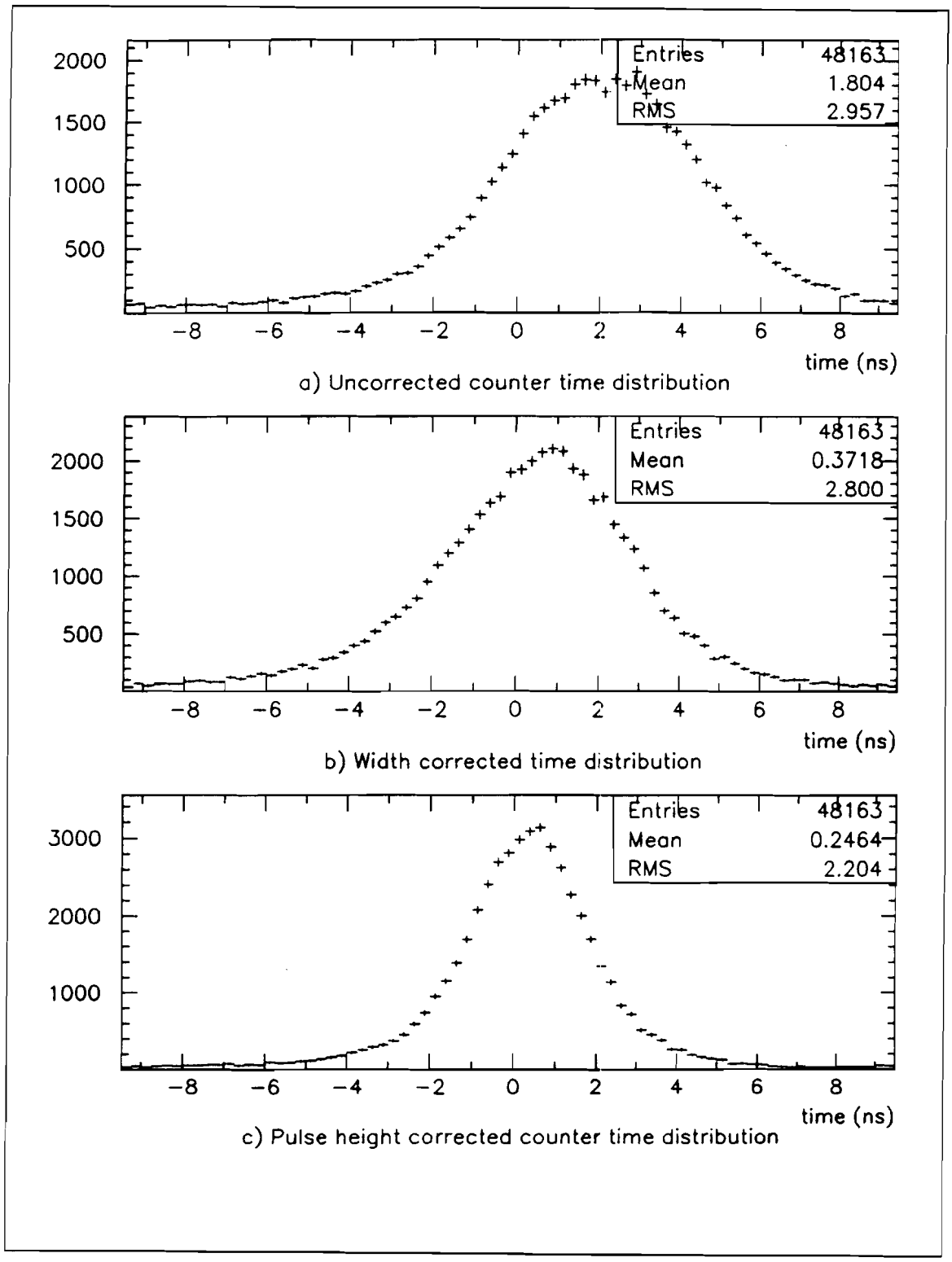

Figure 5.15: Counter time measurements: a) uncorrected, b) shower width corrected, c) pulse height corrected.

to find d_E and d_W in Figure 5.14. Then width corrected times are obtained using Equation 5.2, where the angle θ becomes the angle of the shower edge relative to the vertex with the beam direction. Figure 5.15 b) shows the width corrected counter time distribution. Only a moderate improvement in resolution is achieved in making the width correction, so other corrections were sought. A particularly promising correction used a philosophy similar to the pulse height correction described in the last section for clean track counters: The centroid of the shower was assumed to be located (in the TOF counter) at the horizontal position of the vertex. The tube times were then corrected for a 'width' proportional to the tube pulse heights. The resulting time distribution is shown in Figure 5.15 c).

This distribution is clearly narrower than the previous measured width corrected distribution, indicating that time measurements depend more on the total energy deposited in the scintillator than the actual measured width of the shower as seen by the flash chambers.

The measured width of the shower (described above) becomes a useful observable when the pulse height is in the overflow range. Figure 5.16 shows the average uncorrected time as a function of measured shower width for counters with pulse heights in the overflow range. As the shower width widens, earlier times are recorded, as expected. This indicates that for counters with overflow pulse heights, a correction correlated with the measured width should be applied.

Another event observable, called $\underline{V}$, is also correlated with the measured time in overflow pulse height counters. The variable V is defined as the vertical distance from the vertex to the center of the TOF counter. Figure 5.17 shows the average counter time as a function of V, where the average time is corrected for the angle of the shower with the beam axis (as in the third term of Equation 5.2 for muon tracks). Despite the correction for the angle of the shower, a correlation is clearly observed. This indicates that the TOF counters 'see' more energy in the forward

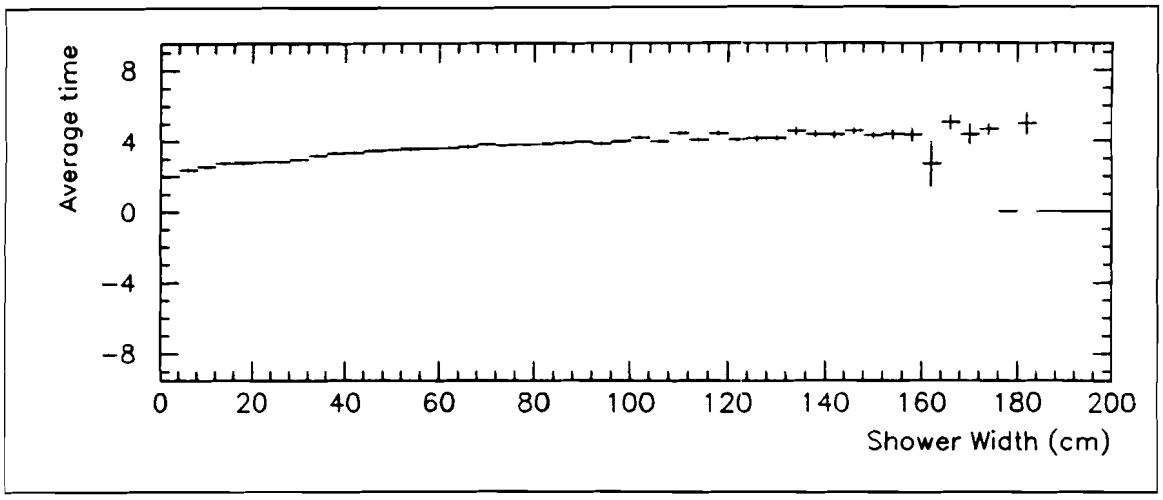

Figure 5.16: The average uncorrected time as a function of the measured shower width in counters with overflow pulse heights in CC-like events.

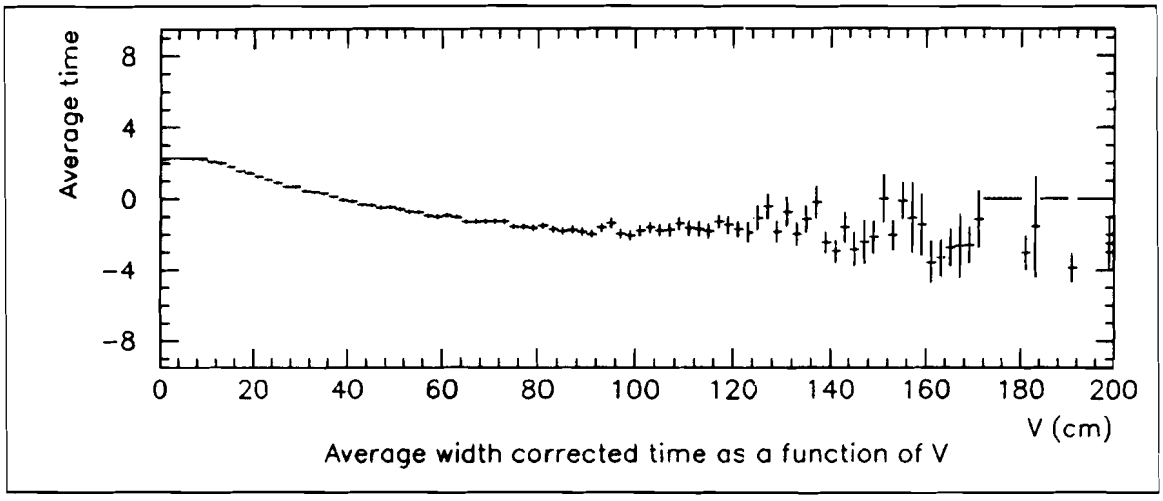

Figure 5.17: The average width corrected time (also corrected for shower angle) as a function of the variable V, the vertical distance from the vertex to the center of the TOF counter.

direction than the flash chambers indicate. Such energy could be in the form of neutral particles, like neutrons, which the TOF scintillator is sensitive to, but the flash chambers are not.

The dependence of the measured counter times with shower width and V was correlated, so corrections to the time as a function of these variables were combined. Figure 5.18 shows the average counter time as a function of shower width[8] on one

[8]Since the width dependence was constant above 100 cm, if the measured shower width was

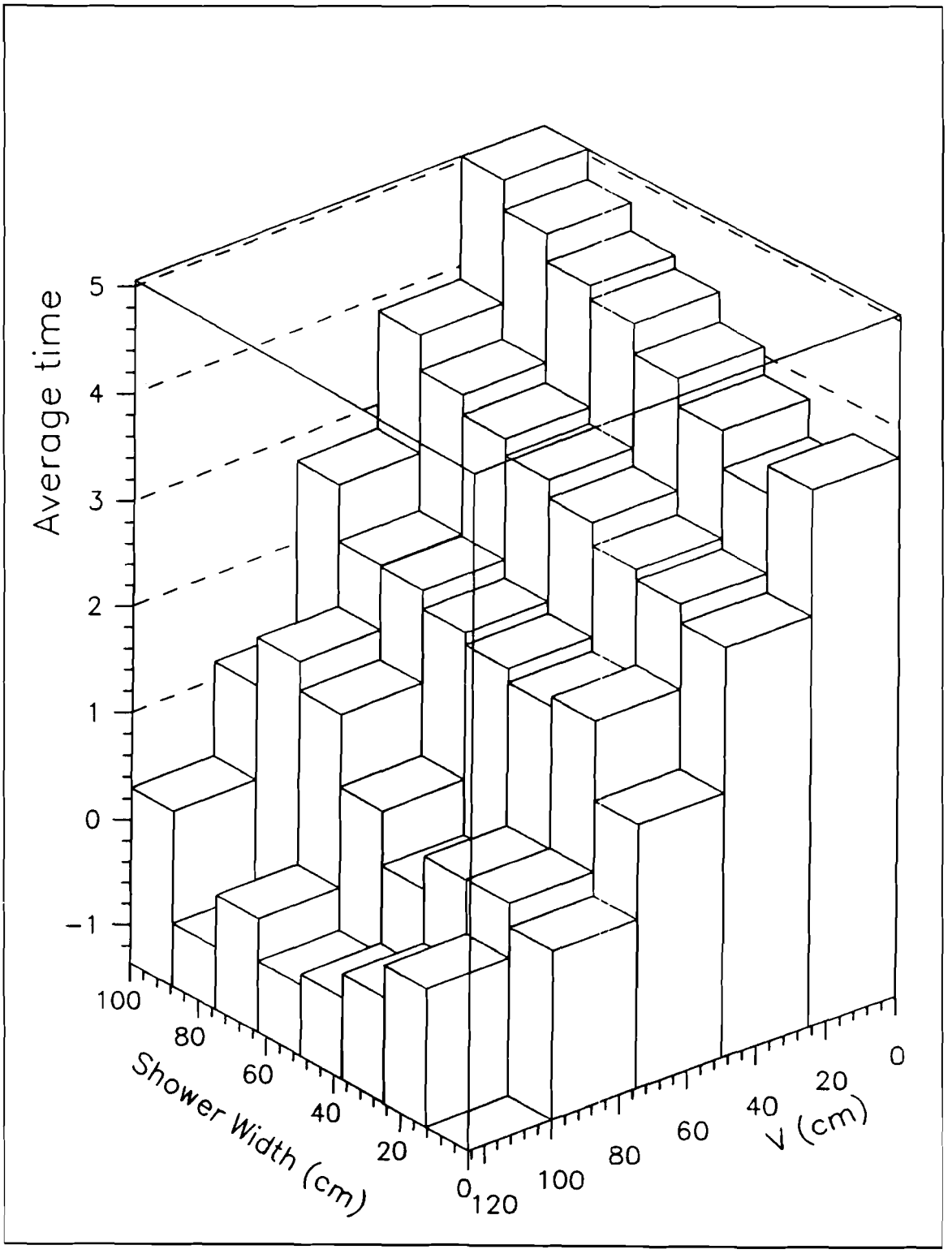

Figure 5.18: The average uncorrected time as a function of the measured shower width and the variable V for shower hit counters with overflow pulse heights.

axis, and V on the other axis for 4-HIT counters with overflow pulse heights. As expected, the earliest measured times occur for low V and high measured shower width.

If overflow pulse height counter times are shifted according to the average time shown in Figure 5.18, the shifted time is still moderately correlated with the number of X cluster hits, another measure of the energy deposition in the TOF counter. Recall that X view flash chamber cells run east to west, parallel to the long edge of TOF counters. The number of X cluster hits (mentioned above) is the sum of all hits in all X view flash chamber cells between the event vertex and the TOF counter in the modulw directly upstream of the TOF counter. The average width and V corrected counter time as a function of X cluster hits is shown in Figure 5.19. A linear fit to this correlation is shown in the figure. This fit is used as the final

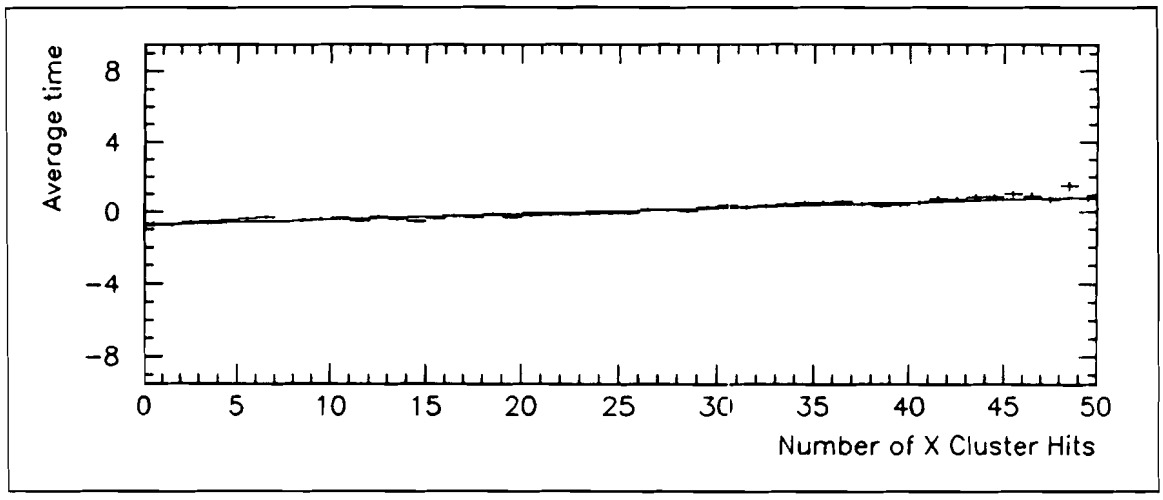

Figure 5.19: The average width and V corrected counter time as a function of the number of X cluster hits in the flash chambers just upstream of the TOF counter in CC-like events.

correction to measured times for counters with pulse heights in the overflow range.

In summary, for all counters with pulse heights in the overflow range where a measured shower width is available,

greater than 100 cm (half the length of the counter), then the measurement was included in the last bin of this plot (at width = 99 cm).

- counter times are shifted according to the average time as a function of measured width and V as in Figure 5.18 then

- times are shifted according to the linear fit shown in Figure 5.19.

When counter pulse heights are in the normal (minimum ionizing particle) range, counter times can be corrected using the pulse height, just as in the clean track hit timing analysis. The average uncorrected time as a function of pulse height in non-clean track hit counters in CC-like events is shown in Figure 5.20. The average time

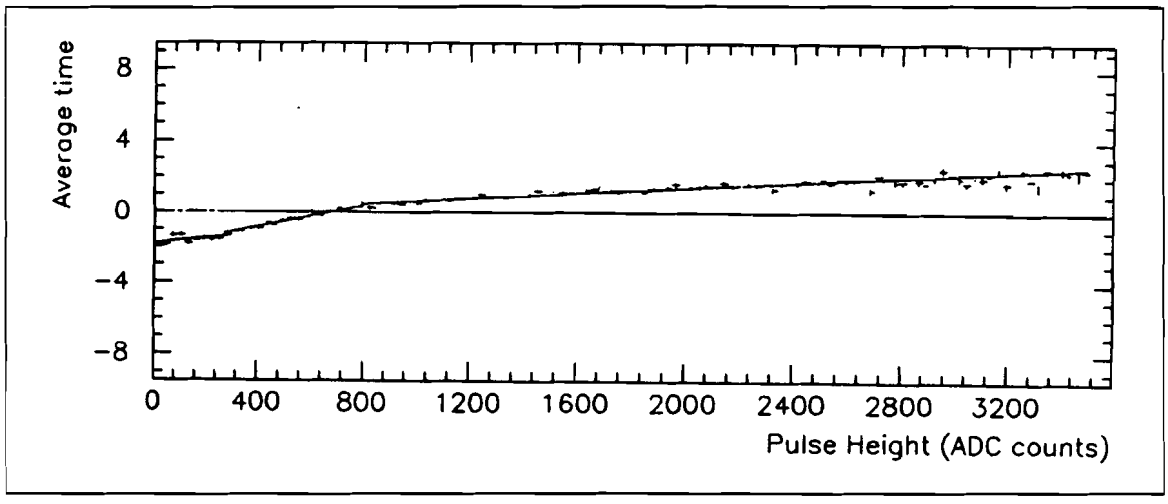

Figure 5.20: The average uncorrected time as a function of the pulse height in non-clean track hit counters in CC-like events.

as a function of pulse height was fit in three pulse height ranges: $0 < Pht < 300$, $300 < Pht < 800$, and $800 < Pht < 3500$. The linear fits are shown by the solid lines in Figure 5.20. When one PMT pulse height of a counter is in the overflow range, or both are in the overflow range and a measured width is not available, tube times are shifted by 2.01 or 3.40 ns, respectively (these constant time shifts are the average time from all counters with these characteristics). After this correction is applied, strong correlations between counter times and other measurables, like the shower width, are not observed.

5.6.2 Time Measurement Criteria

After all the corrections to the TOF counter times have been applied, the consistency requirements listed in Table 5.4 are imposed on all measurements. Time measurements passing these criteria are used to obtain event times.

Table 5.4: The shower timing consistency requirements.

	Requirement	Elucidation
1.	good PHT run	Pulse height information must be available (pulse height information is missing during some runs – about 13% of the data).
2.	vertex $< z(TOF)$	The TOF plane utilized must be downstream of the vertex (occasionally, backscattered particles can produce timing signals upstream of the vertex).
3.	X cluster hits > 0	The density of hits in X view clusters in the modulw just upstream of the TOF counter utilized must be nonzero.
4.	rise times $< 1.5ns$	The east and west rise times, the time differences between the low and high threshold times in the east and west tubes, are required to be less than 1.5 ns.
5.	$\lvert t_E - t_W \rvert < 13.0ns$	The average east and west tube times must be consistent with energy deposition within the length of the counter (scintillator light requires about 13. ns to traverse the length of the counter).
6.	RF shift consistency	The number of integral RF period shifts required to bring the time signal into a single period of the RF clock (from $-9.5 < t < 9.5$) must be the same as that of the *earliest* counter in that event.

The distribution of corrected 4-HIT counter times in NC-like events before and after the imposition of these cuts is shown in Figure 5.21 a) and b), respectively.

5.6.3 Event Timing Anomalies

The event time for NC-like events is obtained by averaging all corrected time measurements passing the shower timing criteria in each event. The distribution of NC-like event times is shown in Figure 5.22 a). The sample of clean track timed CC-like events were analyzed using the same shower timing technique. The resulting

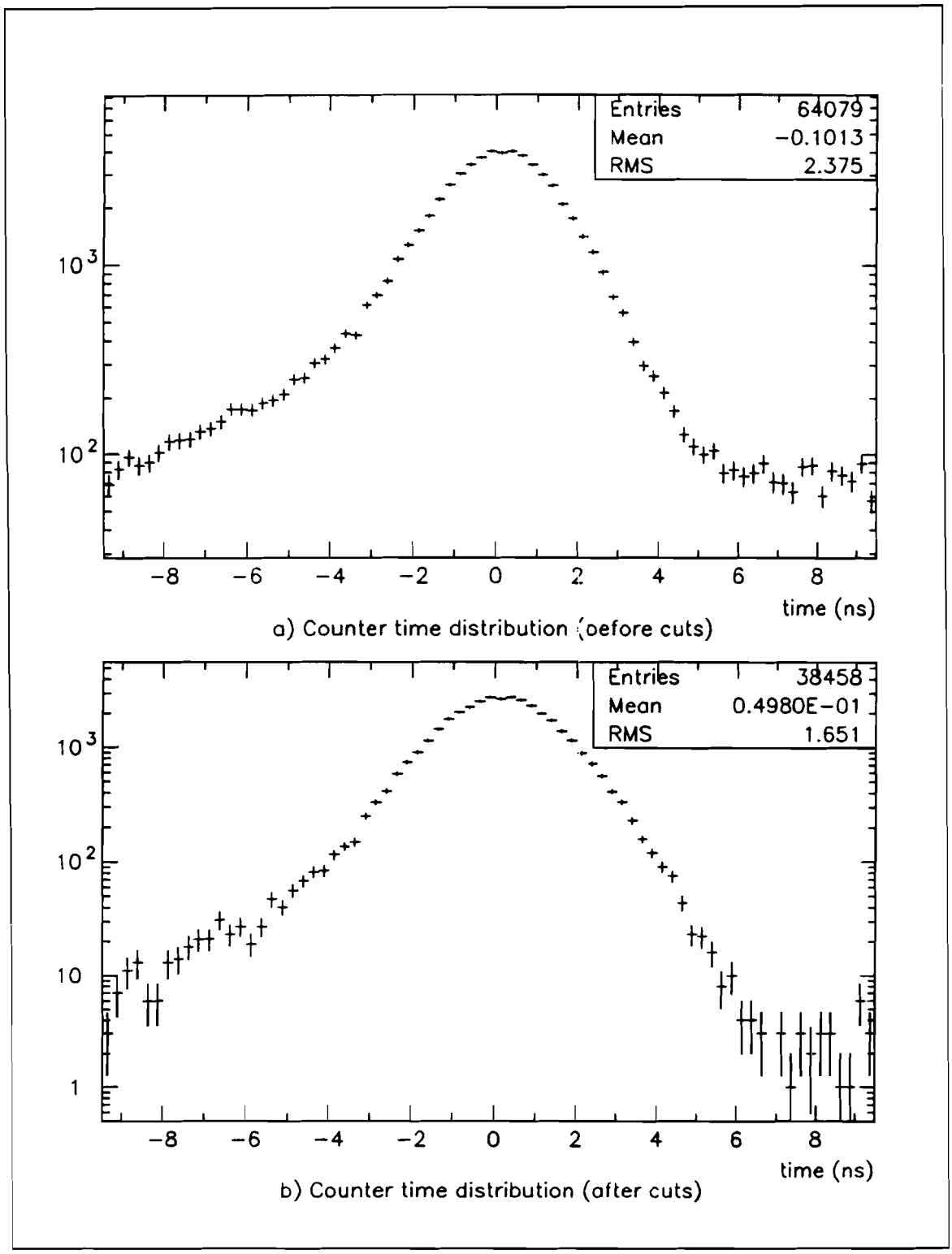

Figure 5.21: The distribution of corrected counter time measurements in 4-HIT counters a) before and b) after shower time consistency requirements are imposed in NC-like events.

CC-like event time distribution is shown in Figure 5.22 b).

A significant number of 'outliers' (events with measured times in the 'early' and 'late' tails of the event time distribution) are clearly seen in Figure 5.22. Just as in the clean track event time analysis, an event scan was performed to seek out problems with the shower timing analysis.

All events with an event time outside a time window of $-5 < t < 5$ ns were scanned by eye. A total of 154 events were scanned, 82 of which were classified as NC-like, the remaining 72 were CC-like. Twenty two cosmic ray events were found, like the one shown in Figure 5.23. All were classified as NC-like. They were distributed uniformly in time. No other obvious problems with the event timing procedure were found.

The 22 cosmic ray events were eliminated from the sample. Based on a average shower timing efficiency of 53%, the expected contamination of the NC-like event sample due to cosmic rays (identified as NC-like events by the pattern recognition program) is less than 0.3%. Contamination at this level will not affect the timing efficiency significantly.

5.6.4 The NC-like Event Time Distribution

The event time for NC-like events after the elimination of all identified cosmic ray events is shown in Figure 5.24. This time distribution is asymmetric about the mean, with a significant 'shoulder' on the late falling edge (around -4 ns). Also a number of outliers are observed in the early and late tails of the distribution. These features could be evidence of WIMPs or event timing systematics.

Though the event timing resolution is not ideal, additional information is available. Because

- the timing of showers in CC-like and NC-like events are expected to have the same timing systematics and

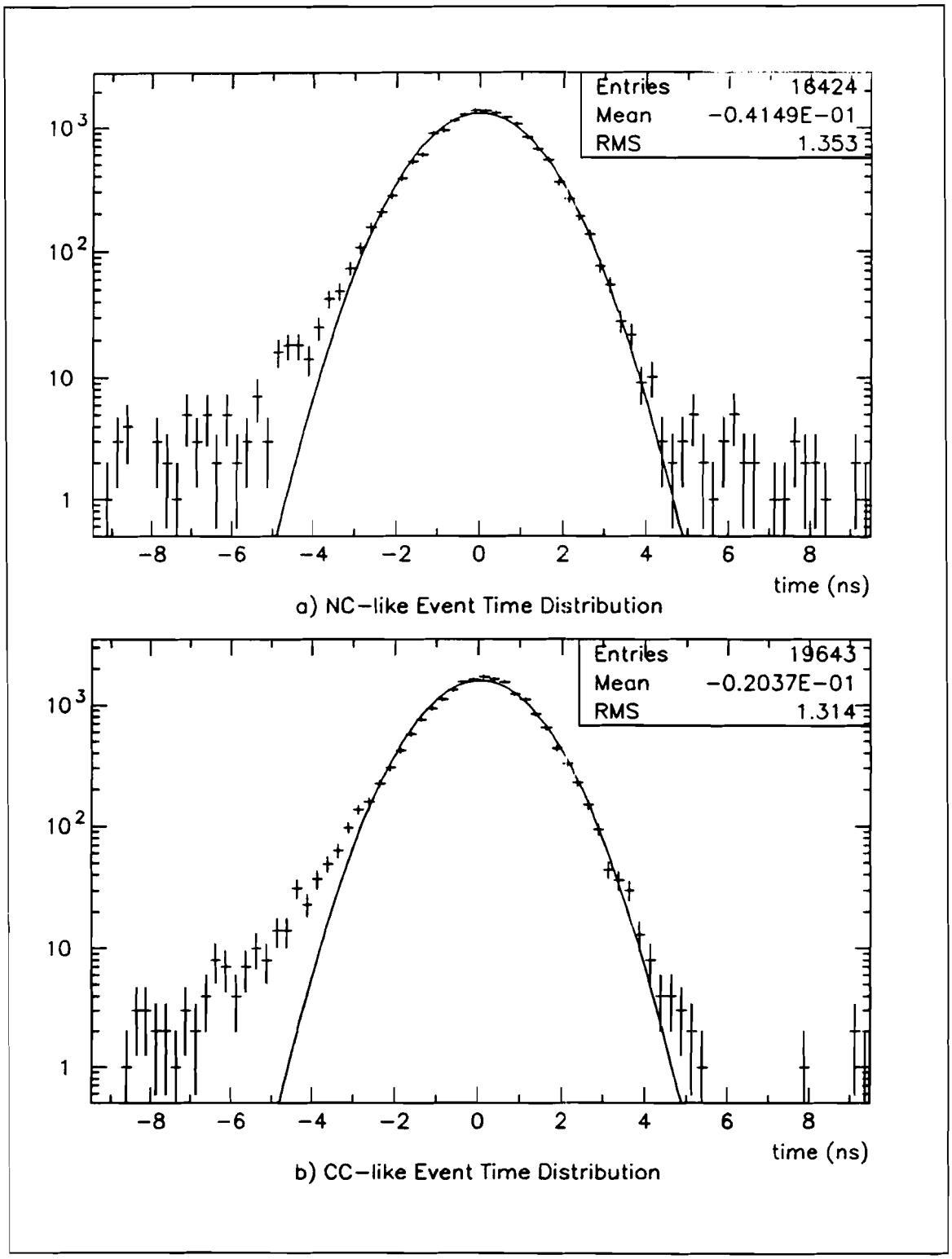

Figure 5.22: The event time distribution obtained using shower timing a) NC-like and b) CC-like events.

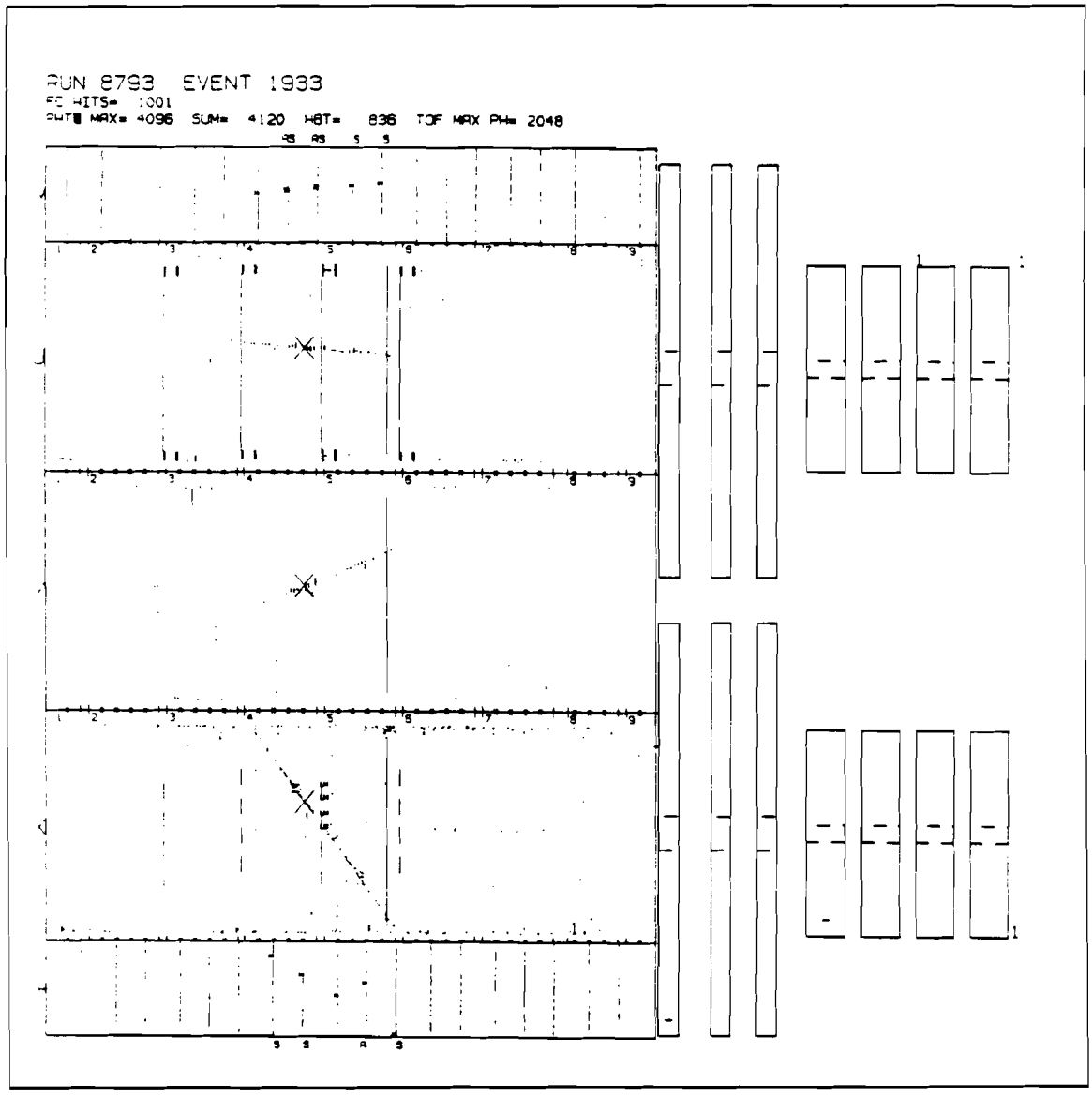

Figure 5.23: A typical cosmic rays muon event identified in the NC-like event scan.

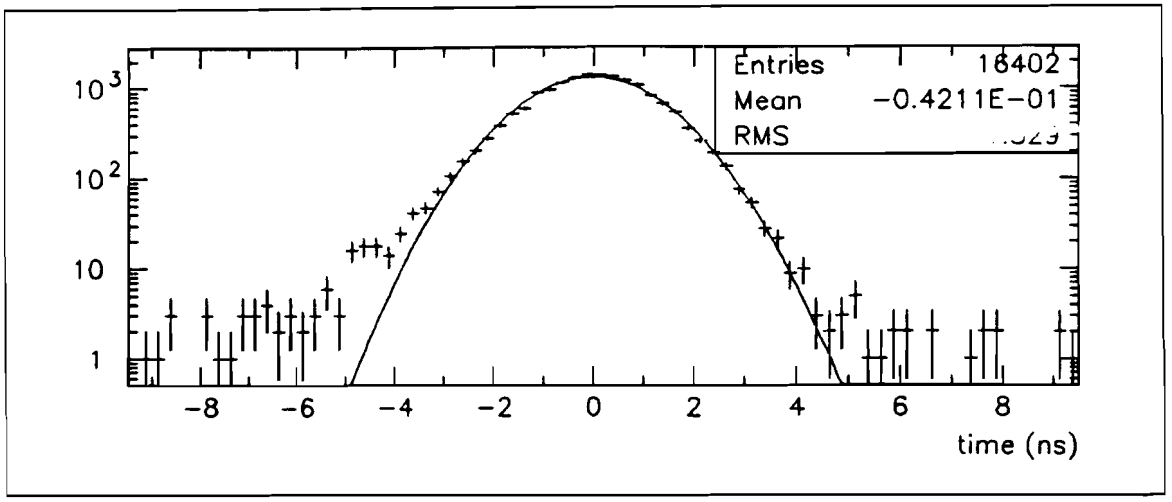

Figure 5.24: The event time distribution for NC-like events.

- since timed CC-like events are ***known*** to have event times in the time window $-4.5 < t < 4.5$ ns,

then the clean track timed CC-like event sample timed with the shower timing technique yields a time distribution that is an estimate of the background of the NC-like event time distribution. In other words, the distribution of Figure 5.22 b) is assumed to be the (yet unnormalized) background to the distribution of Figure 5.24.

Inevitably, we want to calculate the number of events in excess of the estimated background outside of a given event time window. To calculate this number of events:

1. Choose an event time window. For example, choose an event time window extending from -5.0 to 5.0 ns.

2. Find the constant necessary to normalize the number of events in the CC-like distribution to the number of events in the NC-like distribution ***inside*** that chosen event time window.

3. Normalize the entire CC-like distribution by that normalization constant.

4. Subtract the normalized CC-like distribution from the NC-like distribution.

5. Add the number of events in excess of the background outside of the chosen time window.

Figure 5.25 is the time distribution obtained after the normalization and subtraction of the background distribution (of Figure 5.22 b)) from the NC-like time distribution (Figure 5.24) using a time window extending from −5.0 to 5.0 ns. The

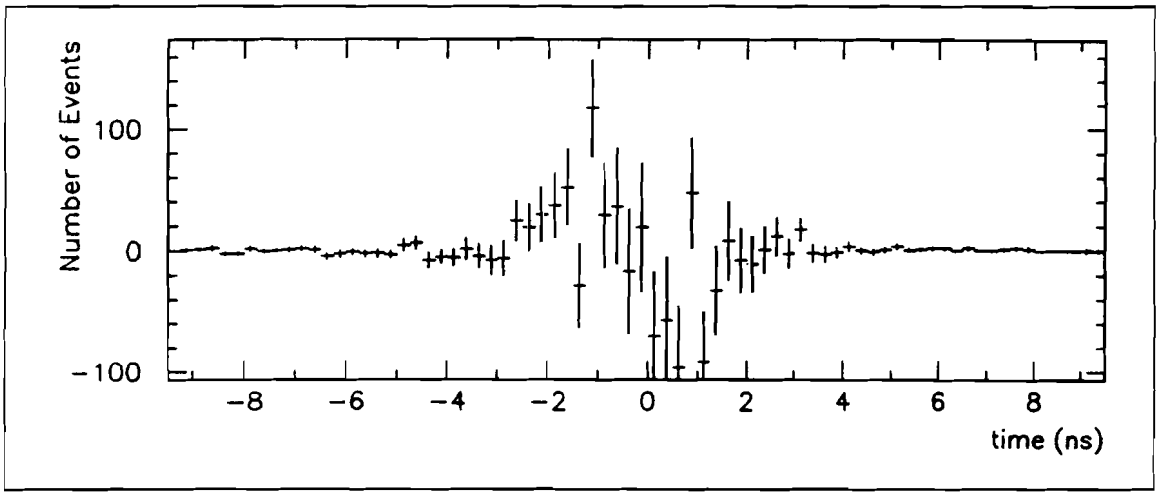

Figure 5.25: Number of NC-like events above background as a function of time.

number of events above background outside the time window after the subtraction is -0.12 ± 10.98 events.

Just as in the clean track timing case, the timing resolution is better for events that utilize more than one counter to obtain the event time. So again, the sample is broken up into two parts, the first containing events timed with a single counter time measurement and the other containing events with two or more counter times utilized. The resulting NC-like event time distributions are shown in Figure 5.26 a) and b) for the single and multiple counter timed events, respectively. The average multiple counter timing efficiency is 37%, while the single counter timing efficiency is 16% (total shower timing efficiency is 53%).

The time distributions for single and multiple counter timed CC-like events are shown in Figure 5.26 c) and d). Evidence of an asymmetry in the timing resolution is

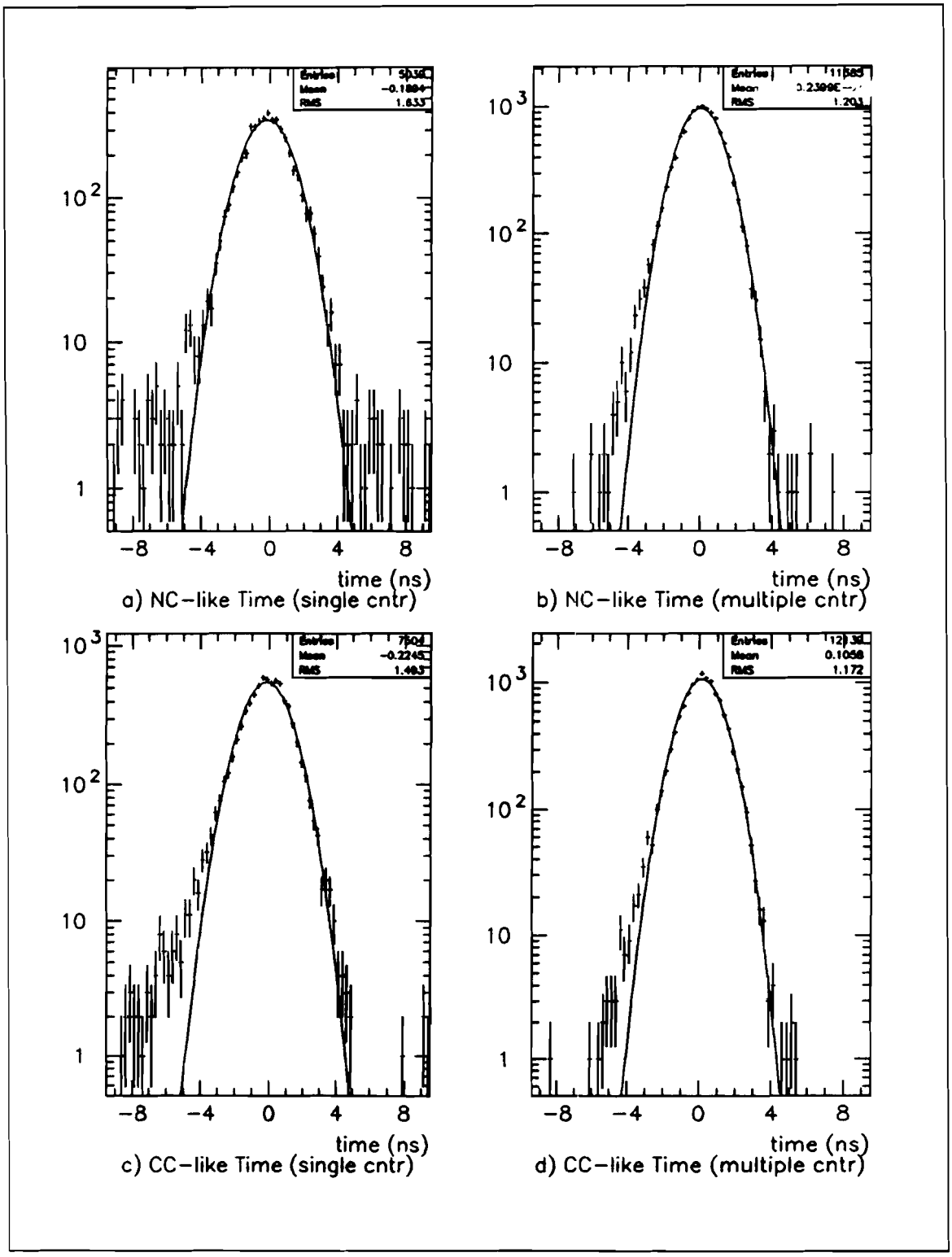

Figure 5.26: Shower time distributions: a) NC-like single counter timed events, b) NC-like multiple counter timed events, c) CC-like single counter timed events, d) CC-like multiple counter timed events.

most clearly apparent in the multiple counter timed event time distribution, where a shoulder is evident in the late time tail between -3 and -5 ns. This asymmetry may be caused by slow particles (like neutrons) striking counters after faster particles. This is not expected to affect the raw timing measurements, but it would affect the pulse height measurement. Consequentially, overcorrections to the time for the pulse height would be made, resulting in a slightly late time measurement for a small fraction of the events.

Using the method described above, the number of events above background outside a number of different time windows was calculated for

1. the entire shower timed data set,
2. the single counter timed data set, and
3. the multiple counter timed data set.

The results are shown in Table 5.5.

The number of events outside each time window is consistent with zero, but the uncertainties in the number of events become larger as the search window gets wider or where the time resolution is poorer (in this case, events timed with a single counter have poorer resolution).

To obtain limits for particle production in Chapters 6 and 8, we have used the results for the the multiple counter timed data set with a TOF search window outside $-5.0 < t < 5.0$ ns. The number of events found in the search window is -3.32 ± 4.16, so if a model predicts that more than 3.5 events should be seen in this search window[9], then that model can be excluded at the 90% confidence level.

The motivation for breaking up the timed event sample into single and multiple counter timed events in the shower timing case is different than that in the clean track

[9]For Gaussian errors, the confidence interval corresponding to a 90% confidence level is $\pm 1.64\sigma$ from the central value. Assuming the uncertainty in the number of events is gaussian, -3.32 events seen while more than 3.5 events are expected is excluded at a 90% CL.

Table 5.5: Number of events above background calculated using 9 different TOF search windows for 3 data subsets.

All Shower Timed Events	Time Window	Number of Events
	$9.50 < t < -9.50$	0.00 ± 0.00
	$7.00 < t < -7.00$	5.14 ± 6.07
	$6.00 < t < -6.00$	3.61 ± 8.40
	$5.50 < t < -5.50$	2.42 ± 9.37
	$5.00 < t < -5.00$	-0.12 ± 10.98
	$4.50 < t < -4.50$	9.71 ± 13.75
	$4.00 < t < -4.00$	-0.46 ± 17.05
	$3.50 < t < -3.50$	-10.33 ± 22.40
	$3.00 < t < -3.00$	-7.79 ± 30.35
	$2.50 < t < -2.50$	20.14 ± 43.77
Single Counter Timed Events	**Time Window**	**Number of Events**
	$9.50 < t < -9.50$	0.00 ± 0.00
	$7.00 < t < -7.00$	7.97 ± 5.66
	$6.00 < t < -6.00$	9.62 ± 7.78
	$5.50 < t < -5.50$	9.94 ± 8.63
	$5.00 < t < -5.00$	12.28 ± 9.71
	$4.50 < t < -4.50$	23.38 ± 11.91
	$4.00 < t < -4.00$	18.99 ± 14.06
	$3.50 < t < -3.50$	15.90 ± 17.76
	$3.00 < t < -3.00$	10.58 ± 22.62
	$2.50 < t < -2.50$	47.02 ± 30.96
Multiple Counter Timed Events	**Time Window**	**Number of Events**
	$9.50 < t < -9.50$	0.00 ± 0.00
	$7.00 < t < -7.00$	0.06 ± 1.39
	$6.00 < t < -6.00$	0.13 ± 1.97
	$5.50 < t < -5.50$	0.19 ± 2.41
	$5.00 < t < -5.00$	-3.32 ± 4.16
	$4.50 < t < -4.50$	-0.81 ± 5.90
	$4.00 < t < -4.00$	-1.44 ± 8.70
	$3.50 < t < -3.50$	2.20 ± 12.60
	$3.00 < t < -3.00$	23.74 ± 19.22
	$2.50 < t < -2.50$	37.95 ± 29.87

counter case. In the clean track case, the motivation was to enable utilization of a wider search window for a fraction of the time. In the shower timing case, the number of events in the search window is always consistent with zero, but by improving the timing resolution of the measurement, the uncertainty in the background decreases and enables a more sensitive search.

5.6.5 Shower Timing Efficiency

For NC-like final states, the timing efficiency depends on the measured final state energy as shown in Figure 5.27. This timing efficiency is used for obtaining limits

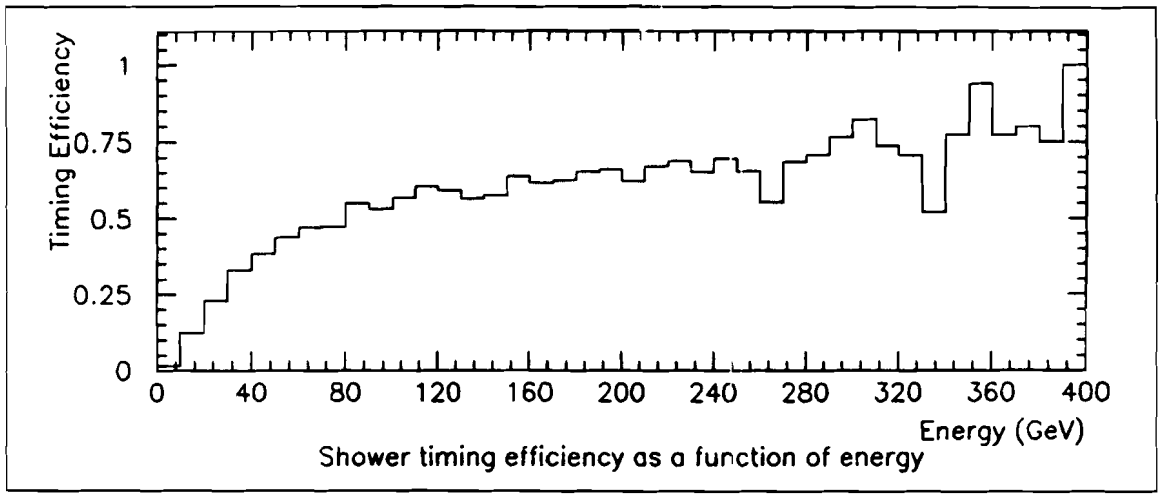

Figure 5.27: The multiple counter event timing efficiency as a function of shower energy in NC-like events.

for directly produced long lived particles and supersymmetric particle production (in Chapters 6 and 8). The "shower timing TOF search window" refers to a time *outside* of $-5 < t < 5\ ns$.

Chapter 6

Model Independent Predictions

6.1 General Considerations in Models of New Particle Production

The absence of events outside the predicted time structure of the neutrino beam can be used to extend limits on the existence of new particles. To obtain such limits, it is necessary to make assumptions about how and where new particles might be produced and how they might interact or decay in the detector.

Model calculations using generalized theoretical assumptions and a cursory detector simulation (ie a back of the envelope calculation) can indicate which of the models are more viable than others. However, ultimately the only true indication of how sensitive the detector is to a particular model is a result of Monte Carlo simulations that use detailed information about the model, the beamline, and the detector. The validity of any such prediction relies on the reasonableness of the assumptions made and a consideration of the stability of the results under the perturbation of those assumptions.

Before beginning a detailed discussion elaborating on any particular model, it is useful to consider what general features models might have that make the E733 detector sensitive to them.

The addition of the TOF apparatus to the E733 detector transformed the experiment into a beam dump-like search experiment which is free of background from

conventional *and* prompt sources of neutrino interactions in the time-of-flight search window. In order to detect WIMPs, they must be weakly interacting enough to survive traversal of the over 1000 meters of shielding (the beam dump and the berm). Thereafter they must either decay or interact within the 10 meter long fiducial volume of the detector in the time-of-flight search window. The final state must contain particles that deposit at least 5 GeV of visible energy in the detector in order to satisfy the trigger minimum energy requirement.

New particles may be produced directly by incident primary protons on the target or by the secondaries on the beam dump. Or, just as the conventional neutrinos are produced, new particles could be the decay products of secondary or tertiary particles produced at the target or the dump.

This experiment is expected to be sensitive to WIMPs in the mass range from about 0.5 to about 38.8/2 GeV/c^2 . The upper bound is half the energy available in the center of mass in 800 GeV/c protons-nucleon interactions. The lower mass bound is constrained by the time-of-flight acceptance: Recall the formula for the t_{TOF} in Equation 2.1. For WIMP energies well above the minimum energy required by the trigger, a mass of $\geq$ 0.5 GeV/c^2 is required in order for massive particles to lag behind speed of light particles far enough to enter the detector in the time-of-flight search window. This lower limit depends on the model being considered because it is inherently dependent on the distribution of energies at which the particles are produced.

Ultimately, the measure of sensitivity of the detector to a new particle production mechanism is an accurate prediction of the number of events expected to be seen in the E733 detector during the 1987 run. This prediction is based on detector geometry, detector efficiency, and the production, decay and interaction characteristics of the new particles for the model at hand.

The number of expected events (N_{EE}) expected to be seen due to new particles

in the E733 detector outside of a given time-of-flight window is the product of the following terms:

$$N_{EE} = N_{WIMPs} \times \varepsilon \times P. \tag{6.1}$$

Each of the terms in this expression is itself a product of a number of terms. To elaborate,

N_{WIMPs} is the total number of new particles expected to be produced anywhere in the neutrino beamline during the 1987 run (based on the beam flux, production cross section and beamline geometry),

ε is a product of acceptance and efficiency terms. It is the fraction of particles produced which actually pass through the detector fiducial volume in the time-of-flight search window with a total energy that could satisfy the minimum energy trigger requirements times an efficiency for obtaining an event time for this type of event.

P is the probability that the new particle survives the traversal of the beam dump and berm and then decays or interacts in the detector.

Beyond these general statements, details of the calculation are model dependent and must be treated on a case by case basis.

The Minimal Standard Model (SM) does not predict the existence of additional unseen particles other than ν_τ, the top quark, and the Higgs Boson as described in Chapter 1. However, modest extensions of the SM accommodate additional particles such as heavy neutrinos or supersymmetric (SUSY) particles. The two chapters following this one describe the sensitivity of the E733 detector to these two possibilities.

The remainder of this chapter is dedicated to the presentation of a limit on directly produced massive particles based on fundamental production, interaction and

decay assumptions without reference to any particular mechanism for production.

6.2 Direct Production of WIMPs

We assume that WIMPs are directly produced by some unspecified mechanism in 800 GeV/c proton nucleon collisions at the target or the dump.

The maximum possible WIMP mass that could be produced in such interactions is half of the available center-of-mass energy. I have chosen to evaluate the acceptances for WIMPs in the mass range from 1 to 20GeV/c^2 Production of the higher mass particles may be less likely [1] , but this can be taken into account in the production cross section.

In Equation 6.1, the number of WIMPs produced, N_{WIMPs}, with production cross section σ_{WIMP} (in 800 GeV/c pN interactions), is

$$N^i_{WIMPs} = POT \times X^i_{model} \times \frac{\sigma_{WIMP}}{\sigma_{total}}. \tag{6.2}$$

In this expression, POT is the number of integrated live protons on target as given in Equation 2.7. The index i indicates production of WIMPs at the target ($i = 1$) and the beam dump ($i = 2$). Note that only primary interactions are considered in this chapter. X^i_{model} is the fraction of particles per proton on target which have a primary interaction in the target (i=1) and beam dump (i=2). The primary target has a depth of 1 interaction length. Therefore $X^1_{model} = (1 - e^{-1}) = 0.6321$. All primary protons that do not interact in the target are absorbed in the beam dump downstream of the decay pipe so $X^2_{model} = (1 - X^1_{model}) = 0.3679$. In other words, 63% of all primary protons interact in the primary target, leaving 37% of the primary protons to interact in the beam dump.

[1] In the parton model, partons (quarks or gluons in the nucleus) have, on average, one sixth of the total momentum of the nucleon, and hence approximately one sixth of energy. A production mechanism involving two of these constituents therefore, on average, has one sixth of the total center-of-mass energy available to create new massive particles. The average 2 parton center-of-mass energy is then (38.8 GeV) $\times \frac{1}{6} \approx$ 6.5GeV. But the momentum fraction carried by any parton can be higher (though with smaller probability), so the center-of-mass energy available to produce new particles may be higher than 6.5GeV.

The fraction of primary interactions that produce WIMPs is $\frac{\sigma_{WIMP}}{\sigma_{total}}$ where σ_{total} is the total interaction cross section for 800 GeV/c protons on a nuclear target. The atomic weight (A) dependence of the total inelastic cross section is ($\propto A^{0.72}$) [14]. We assume that the A dependence of the production cross section for WIMPs σ_{WIMP} is the same. If a linear A dependence is assumed, this fraction *increases* by a factor of ($\frac{A^{1.0}}{A^{0.72}}$ =)2.2 at the target (where $A = 17$) and a factor of 2.5 at the beam dump (where $A = 27$).

6.3 Acceptance and Detection Efficiency

The term ε in Equation 6.1 is the product of a number of acceptances and efficiencies. Specifically

$$\varepsilon = \varepsilon_{geo}\varepsilon_{TOF}\varepsilon_{trig}\varepsilon_{timing} \tag{6.3}$$

where ε_{geo} is a geometric acceptance, ε_{TOF} is a time-of-flight acceptance, ε_{trig} is a detector trigger efficiency, and ε_{timing} is a timing efficiency.

Estimating these terms requires that we make some assumptions about the energy and angular spread of the produced WIMPs. In analogy to heavy quark production in proton-nucleon collisions, production in the center-of-mass frame can be parameterized by

$$\frac{d^2\sigma}{dx_F dp_T^2} \propto (1 - |x_F|)^n \times e^{-b\sqrt{(p_T^2+M^2)}}, \tag{6.4}$$

where M is the mass of the particle produced (in this case the WIMP), and n and b are constants normally determined empirically for a particular process.

The motivation for using this parameterization is described in Chapter 1. I have chosen an alternate mass dependent parameterization in the transverse momentum term so that the $< p_T >$ scales with the mass of the particle produced as expected in the QCD parton model for heavy quark production. In this way, a single parameterization applies to a wider range of particle masses. A more theoretically motivated

parameterization [41] may be

$$exp[-bp_T^2(1 - c\ln(\frac{p_T^2}{M^2}))], \tag{6.5}$$

but heavy quark production data have not been fit to this form, so the values of the constants b and c are unavailable.

We have assumed that $n = 5.0$ and $b = 3.45$ as in a similar simulation [42] of a production of supersymmetric particles in a similar mass range. These values are in the midrange of what might be expected in the direct production of massive particles. Effects of variation of these constants will be discussed later.

Using these production assumptions, the various acceptances can be estimated as described below. For easy reference, all geometric, time-of-flight and trigger acceptances for this model are listed in Tables E.1 and E.2 in Appendix E.

We find that the geometric acceptance, ϵ_{geo} (the number of particles that pass through the E733 detector fiducial volume per number produced), for particles produced by 800 GeV/c protons at the target and the beam dump according to Equation 6.4 varies as a function of mass as shown in Figure 6.1. Because the beam dump is about 500 meters closer to the detector than the target, ϵ_{geo} is notably higher for dump production.

Although the fiducial volume is not exactly circular in cross section, it is roughly true that the geometrically accepted particles are those that are projected directly forward from the production point into a cone with an opening angle of $1. - 2.$ mrad. The angle of the WIMP in the lab with the z-direction (beam direction),

$$\theta_{lab} = \arctan(\frac{p_\perp}{p_{||}}), \tag{6.6}$$

must be less than $\approx 0.5 - 1.0$ mrad. The $p_\perp$ term is dominated by the p_T^2 dependence, while the $p_{||}$ term is dominated by the x_F dependence of the differential cross section. As a result of the mass dependence in the p_T^2 term, lower mass particles are more likely to have lower p_t and thus a lower production angle. On the other hand,

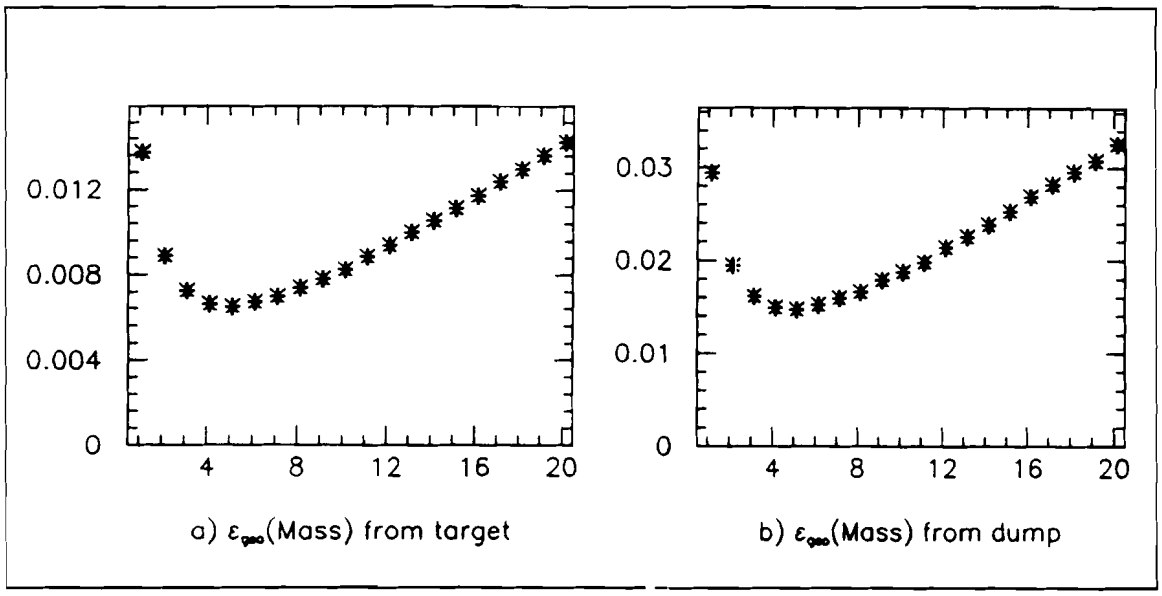

Figure 6.1: Geometric Acceptance as a function of WIMP mass for production at the a) target and b) beam dump.

due to the mass independent $(1 - x_F)^n$ term, higher mass particles tend to have a higher longitudinal momentum after the boost to the lab frame. As a result of these competing factors, a dip in the acceptance occurs at intermediate masses with higher acceptance at the low and high masses.

The time-of-flight acceptance, ε_{TOF}, is evaluated by requiring geometrically accepted particles to enter the detector in the time-of-flight search window. The width of this time window depends on the expected final state:

- If the final state contains a high energy muon (CC-like), the clean track TOF search window applies: if t_{TOF} of a particle is in the range from 3.25 to 15.08 ns, it is time-of-flight accepted.
- If no high energy muon is expected in the final state (NC-like), then the shower timing TOF window applies: if t_{TOF} of a particle is in the range from 5.00 to 13.93 ns, it is time-of-flight accepted.

The ε_{TOF} is the fraction of time-of-flight accepted particles of the geometrically accepted particles.

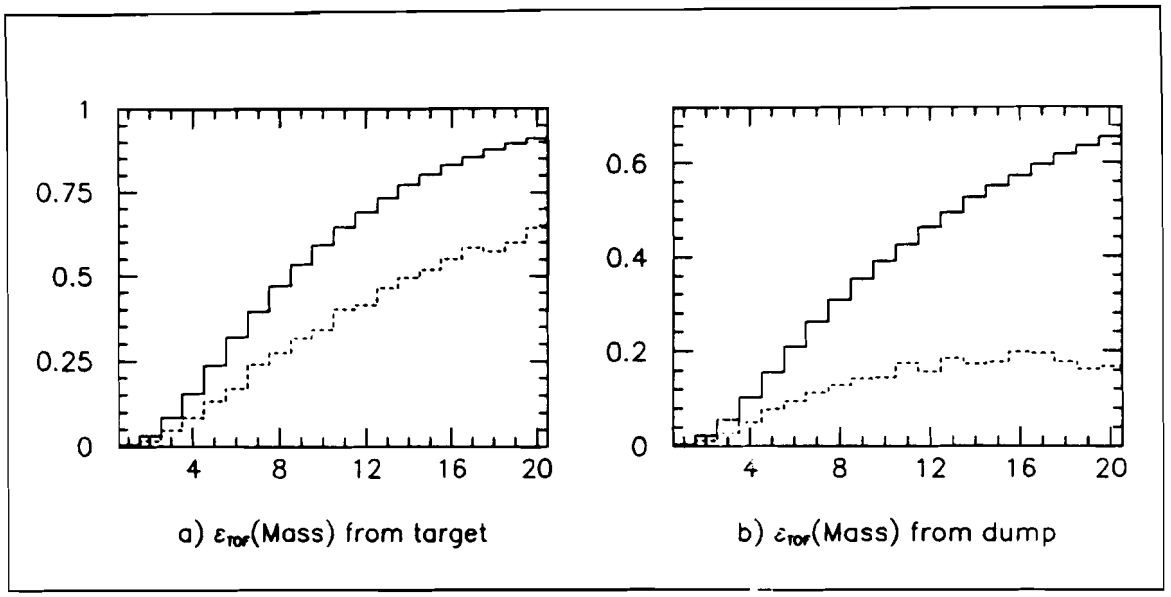

Figure 6.2: Time-of-flight acceptance as a function of WIMP mass for geometrically accepted particles produced at the a) target and b) beam dump. The solid line is ε_{TOF} using the clean track time search window and the dotted line is ε_{TOF} using the narrower shower time search window.

Figure 6.2 a) and b) shows the time-of-flight acceptance as a function of the WIMP mass for geometrically accepted particles produced at the target and dump respectively. Because the beam dump is closer to the detector than the target, ε_{TOF} is notably lower for dump production. ε_{TOF} is smaller for the narrower shower time window (in comparison to the track time window) by almost a factor of two.

The effects of the geometric and time-of-flight cuts on the produced energy spectrum are shown in Figure 6.3 a), b) and c) for WIMP masses 1 GeV/c^2, 6 GeV/c^2 and 11 GeV/c^2 respectively. The unhatched histogram represents the produced energy spectrum, the hatched histogram is the spectrum of geometrically accepted particles and the cross hatched histogram represents the spectrum of geometrically and time-of-flight accepted particles.

The discontinuities in the time-of-flight accepted energy spectrum are a result of the t_{TOF} being some integral multiple of the RF clock period plus or minus the measured width of the neutrino bucket for that WIMP mass in that energy range

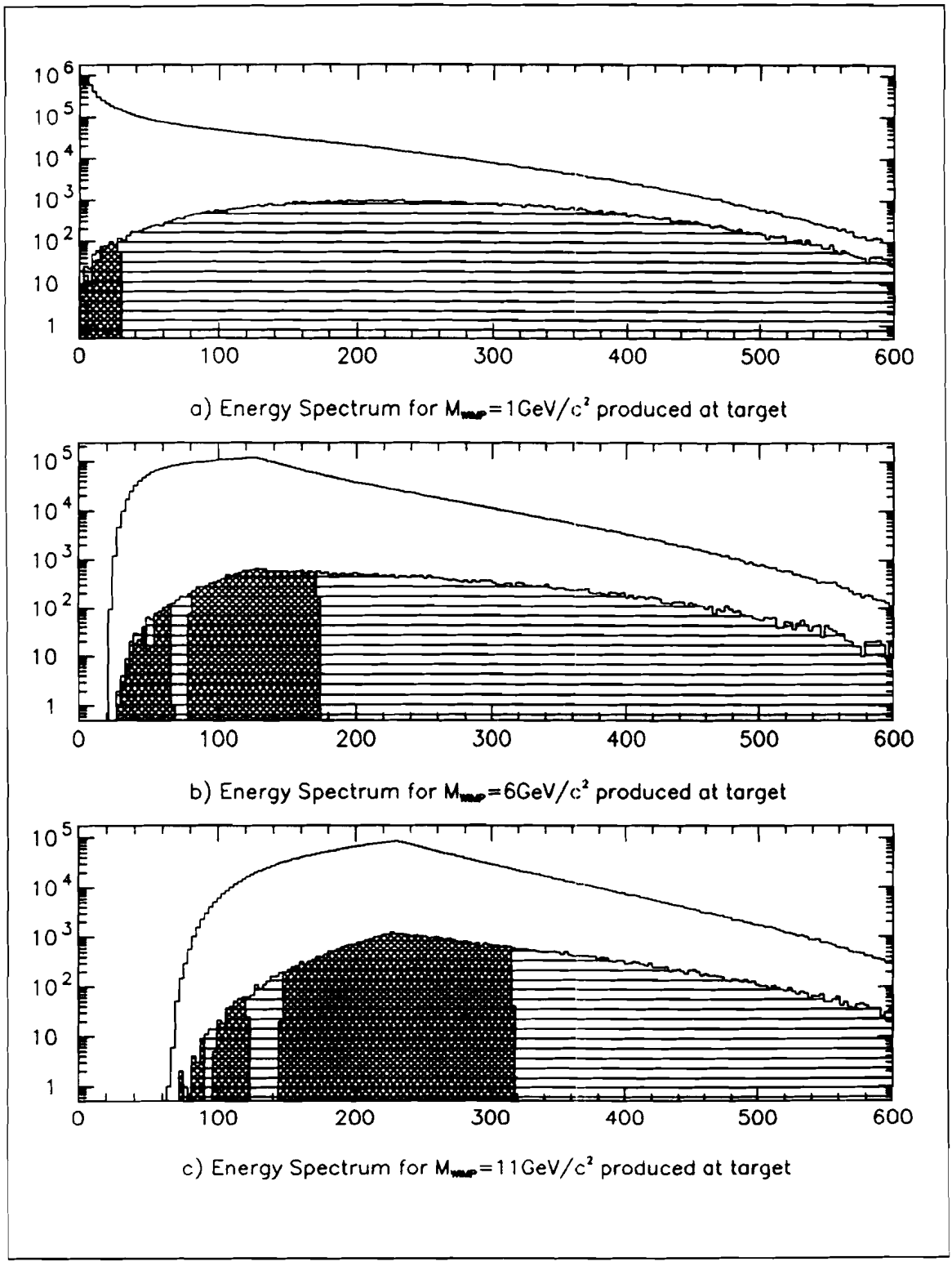

Figure 6.3: Energy Spectra for a WIMP mass of a) 1, b) 6, and c) 11 GeV/c^2 , produced by 800 GeV/c protons on the target. The unhatched area is the produced spectrum, the hatched area is the energy distribution of geometrically accepted particles and the cross hatched area shows the spectrum of time-of-flight accepted particles.

. This discontinuity does not result in a blind spot, or insensitivity of the detector, to a particular production mechanism because in general particle production occurs over a wide range of energies, rather than in a narrow range of energies that happen to satisfy this criteria. Also, production would occur at both the target and the beam dump which have characteristically different such discontinuities associated with them that do not tend to overlap.

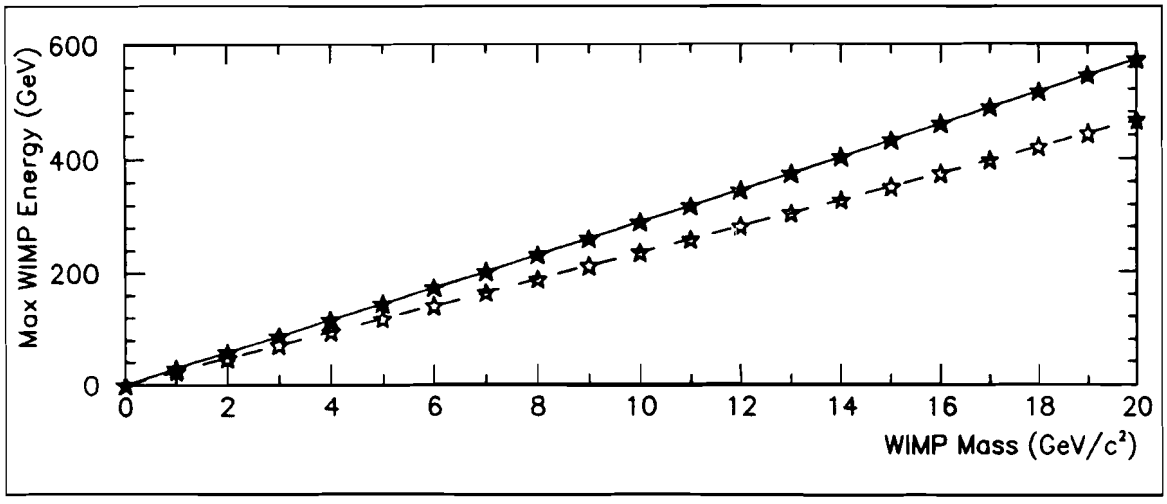

Figure 6.4: The maximum possible energy a WIMP can have such that it falls within the track timing search window as a function of WIMP mass. The solid line is for production at the target ($D = 1599m$) and the dotted line for production at the beam dump ($D = 1057m$).

The geometrically accepted particles, those with $\theta_{lab} < 1mrad$, tend to be those with the higher energies, while the time-of-flight acceptance is essentially a maximum energy cutoff. If a particle is too energetic, it does not fall out of time sufficiently to appear different from a neutrino event. This cutoff is proportional to the mass. By rearranging Equation 2.1, one can obtain an expression for the maximum momentum that a particle of a given mass M can have such that it still falls within the TOF search window. The maximum energy (corresponding to this maximum momentum) as a function of mass is plotted in Figure 6.4 for the track timing search window. The solid line is for particles produced at the target and the dotted line for production at the beam dump. This maximum energy for the shower timing search window is even

more restrictive: it is about 80 % of that for the track timing search window. This cutoff energy is a peculiarity of this time-of-flight search experiment. Its effect on the acceptance can be quite severe, reducing the sensitivity of the apparatus particularly to the production of WIMP masses below 1 or 2 GeV/c^2 .

The trigger efficiency, ε_{trig}, is the efficiency with which the detector is able to trigger on an event. It is assumed that WIMPs interacting or decaying in the detector will deposit 100 % of their energy therein, and that the trigger efficiency is the same for these events as for garden variety neutrino events of the same visible energy. This efficiency is described more fully in Chapter 3. For this analysis, it is parameterized as a step function as follows.

$$\varepsilon_{trig} = \left\{ \begin{array}{lll} 1. & for & E > 5\text{GeV} \\ 0. & for & E \leq 5\text{GeV}. \end{array} \right\}$$

This efficiency does not effect WIMPs with mass greater than 5GeV; for lower mass WIMPs, this efficiency on average is greater than 90 % for geometrically and time-of-flight accepted particles.

It is practical to ask how these acceptances change as a function of changes in the constants n and b in Equation 6.4. Figures 6.5 a) and 6.5 b) demonstrate the variation in the geometric and time-of-flight acceptance respectively as a function of n and b for a WIMP mass of 13 GeV/c^2. The ranges of n and b evaluated are justified as follows.

A survey of the literature measuring n in heavy quark production shows that values of n have been measured to vary in the range $1 \leq n \leq 10$ depending on the particle studied, the beam energy, etc. [43, 44]. The results suggest higher values of n for higher beam energies, which should be more appropriate in this case.

Values of b in heavy quark production experiments range from approximately 0.8 to 3.4 [45] for the $e^{-bp_T^2}$ parameterization. We have chosen a different parameterization (Equation 6.4) that applies over a larger mass range. In the mass range of the

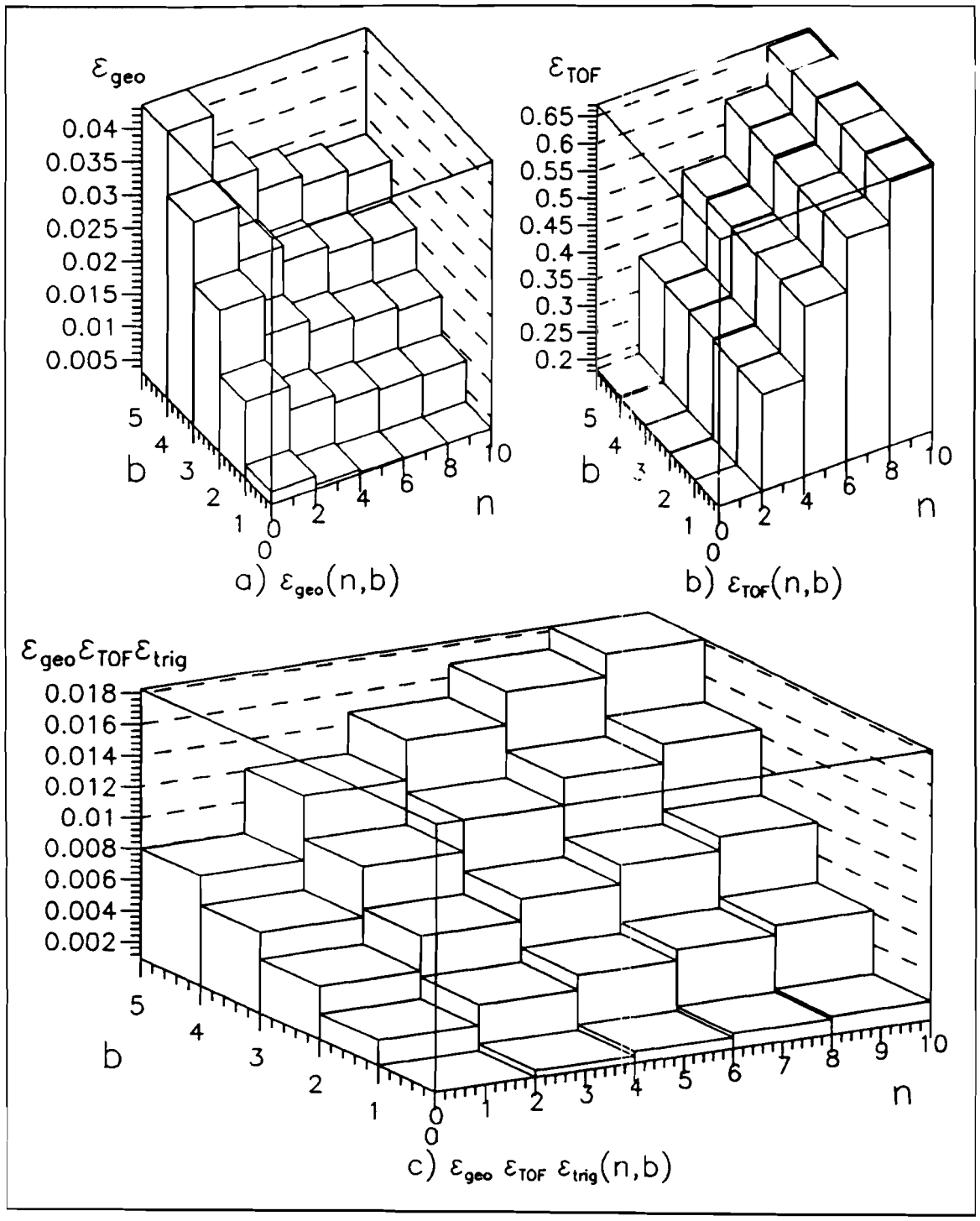

Figure 6.5: The variation in the a) geometric, b) time-of-flight and c) total (geometric × time-of-flight × trigger) acceptance as a function of n and b for a WIMP mass of 13 GeV/c^2 .

heavy quark states studied in the literature, the variation in the p_T spectrum is represented in our parameterization somewhere over the range in b from $0.5 \leq b \leq 5.0$.

Figure 6.5 c) demonstrates the variation in the total acceptance (the product of the geometric, time-of-flight, and detector trigger acceptance) as a function of n and b for a WIMP mass of 13 GeV/c^2.

In Figure 6.5 a) we see that higher geometric acceptance is seen for higher values of b (a more strongly peaked p_T distribution means more particles produced at near zero p_T). Figure 6.5 b) shows higher time-of-flight acceptance for higher values of n. In the higher n regime, a more strongly peaked x_F distribution results in less longitudinal momentum imparted on average to the produced particle.

In Figure 6.5 c) we see that the combination of these two effects results in a variation in the combined acceptance of less than a factor of 10 for a wide range in the production parameterization constants n and b. This is true for all WIMP masses in the range $1 \leq M \leq 20$ GeV/c^2. The central bin in these plots is representative of the n and b values chosen (5.0 and 3.45 respectively) to obtain the acceptances used for this analysis.

These last three plots are intended to demonstrate what happens to the overall acceptance over a wide range of values of the parameters n and b. Low values of *both* n *and* b are not anticipated based on heavy quark production data at high energies. So in summary, the overall acceptance changes with n and b, but not such that the acceptance is appreciably different from the acceptance for $n = 5.$ and $b = 3.45$ used in this analysis.

The final term in ε is the timing efficiency, ε_{timing}, the fraction of events expected to have a reliable event time measurement. We assume that interacting or decaying WIMPs deposit all available energy in the detector. This efficiency, as described in Chapter 5, depends on the final state topology:

- If the final state contains a high energy muon (CC-like), then ε_{timing} depends

on the angle of the muon relative to the beam direction. Since this angular distribution cannot be anticipated, we assume that such final states have the same timing characteristics as a charged current neutrino interaction of the same energy.

- If no high energy muon is present in the final state (NC-like), then ε_{timing} depends on the final state visible energy. We assume that such final states have the same timing characteristics as neutral current neutrino interactions with the same visible energy.

In other words, the ε_{timing} is assumed to be the same as the ε_{timing} of neutrino events (as reported in Chapter 5).

6.4 Detection

If a neutral particle enters the detector and deposits at least 5 GeV of visible energy within it, the E733 detector trigger requirements are satisfied and the event is recorded. Particles can deposit energy via decay or interaction. These two cases are treated separately in the sections following.

6.4.1 Noninteracting Unstable Particles

If we assume the WIMP is noninteracting but unstable with lifetime τ, the probability P in Equation 6.1 that it will decay in the detector is

$$P = P_s \times P_d \tag{6.7}$$

$$= exp\left(\frac{-D}{\gamma\beta c\tau}\right) \times \left[1 - exp\left(\frac{-\Delta}{\gamma\beta c\tau}\right)\right] \tag{6.8}$$

where P_s is the probability that the particle survives from the point of production to the detector (a distance D) times P_d, the probability that the WIMP decays within the detector fiducial volume (with a depth $\Delta = 10$ meters).

Shown in Figure 6.6 is this probability P as a function of lifetime τ for a WIMP produced at the target with a fixed mass and energy. A particle with a lifetime

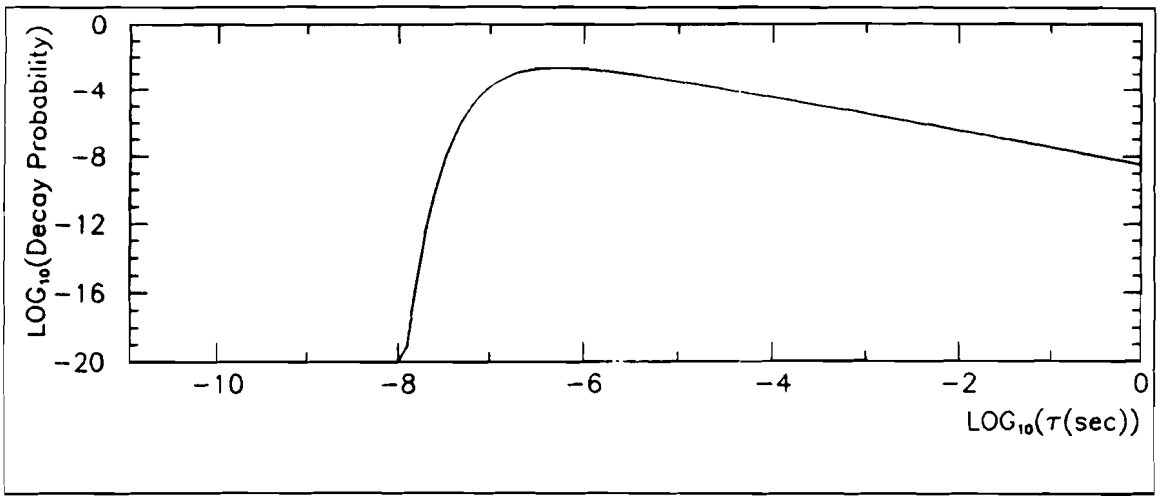

Figure 6.6: The probability that a WIMP will decay in the detector fiducial volume as a function of lifetime τ. This probability was evaluated for a WIMP mass $= 10$ GeV/c^2 , WIMP energy $= 100$ GeV . The target to detector distance $D = 1599$ meters and the fiducial volume depth $\Delta = 10$ meters.

shorter than $\approx 10^{-8} sec$ (the lifetime of a charged pion) typically decays before reaching the detector, while a particle with lifetime longer than $10^{-4} sec$ have a very small probability of decaying at all.

We have identified all of the factors in Equation 6.1 (N_{WIMPs}, ϵ, and P) for unstable noninteracting directly produced particles. So we can calculate the number of events expected to be seen in the detector over the course of the run. If a statistically significant number are expected (as described in Chapter 5), such particles can be excluded. A computer simulation based on the assumptions stated above is used to predict the acceptances and efficiencies, get the energy spectrum of accepted particles, and calculate the probability that they will decay in the detector.

For this noninteracting unstable particle model, the independent parameters are the production cross section σ, the mass M, the branching ratio B producing the indicated final state and the mean lifetime τ.

Contours of equal 90% confidence level upper limits on production cross section

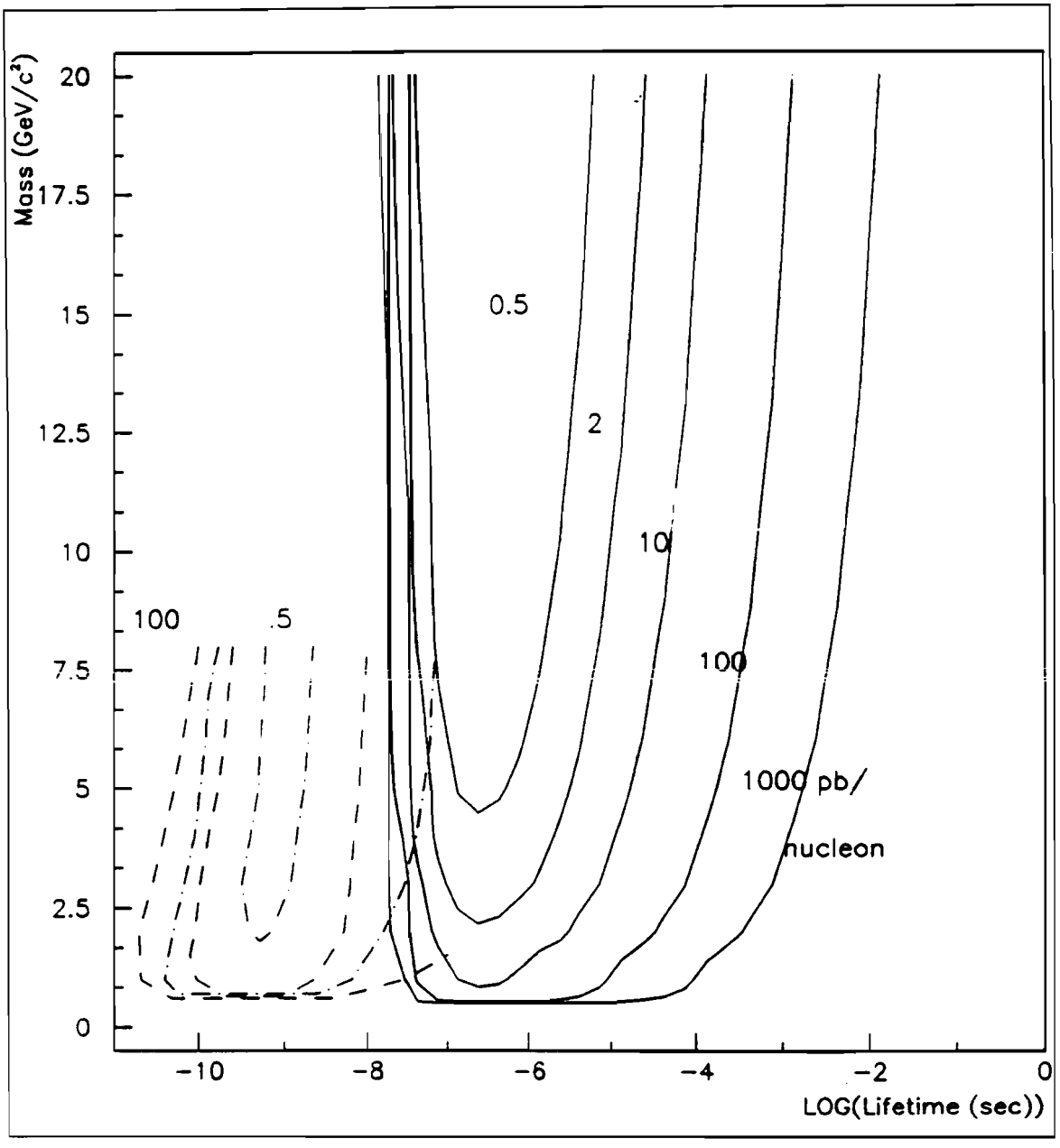

Figure 6.7: For noninteracting unstable particles, the solid contours indicate equal 90% CL upper limits on production cross section times branching ratio (pb/nucleon) as indicated as a function of mass and lifetime for inclusive CC-like final states. Solid curves represent the E733 results in which the A dependence is assumed to be the same as the total inelastic cross section ($A^{0.72}$). If a linear dependence is assumed, the σB sensitivity *increases* by a factor of > 2.2. Dashed curved represent the NA3 results for identical σB and specific final state $\mu+\pi$ or $\mu+\mu$. The NA3 curves assume a linear dependence of the cross section. If $A^{0.72}$ dependence is assumed, their cross section sensitivity *decreases* by a factor of 4.3.

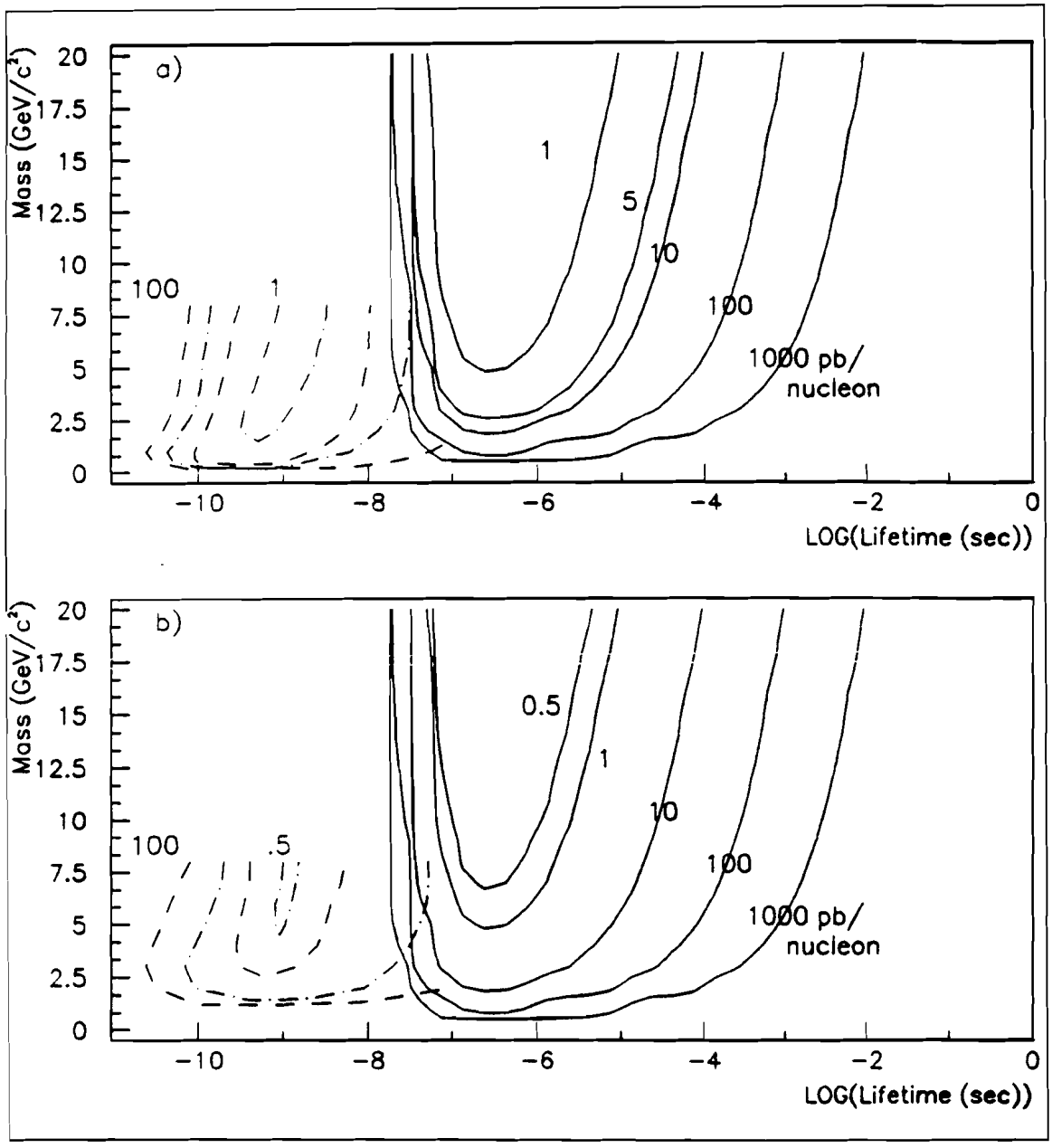

Figure 6.8: For noninteracting unstable particles, the solid contours indicate equal 90% CL upper limits on production cross section times branching ratio (pb/nucleon) as indicated as a function of mass and lifetime for inclusive NC-like final states. Solid curves represent the E733 results in which the A dependence is assumed to be the same as the total inelastic cross section ($A^{0.72}$). If a linear dependence is assumed, the σB sensitivity *increases* by a factor of > 2.2. Dashed curved represent the NA3 results for identical σB and specific final state a) $\pi^{\pm}e^{\mp}$ or b) $\pi^{\pm}\pi^{\mp} + X$ (inclusive). The NA3 curves assume a linear dependence of the cross section. If $A^{0.72}$ dependence is assumed, their cross section sensitivity *decreases* by a factor of 4.3.

times branching ratio (pb/nucleon) as a function of mass and lifetime are shown in Figure 6.7 for CC-like final states. Figure 6.8 a) and b) show similar contours for NC-like final states. Note that plots a) and b) show the same E733 results for slightly different values of σB so that direct comparison can be made to two distinct NA3 final state topologies (NA3 experimental details below).

We have assumed that the atomic weight dependence of the production cross section is the same as that of the total inelastic cross section ($\propto A^{0.72}$) [14]. If a linear dependence is assumed, the sensitivity in σB *increases* by at least a factor of 2.2. For example, assuming a linear A dependence, the 100 pb/nucleon upper limit curve becomes a 41 pb/nucleon upper limit, calculated as follows:

$$\frac{1}{2}\left(\frac{100}{2.2}+\frac{100}{2.7}\right)=41, \tag{6.9}$$

assuming an equal contribution from the target ($A = 2.2$) and the dump ($A = 2.7$). [2]

In Figures 6.7 and 6.8 a) and b), the dashed curves indicate results from the NA3 [46] experiment for identical σB and specific final state $\mu + \pi$ or $\mu + \mu$, $\pi^{\pm}e^{\mp}$, and $\pi^{\pm}\pi^{\mp} + X$ (inclusive) respectively. The NA3 collaboration assumes a linear dependence of the cross section to obtain these contours. If an $A^{0.72}$ dependence is assumed, their cross section sensitivity *decreases* by a factor of 4.3.

The NA3 experiment [46] is a short beam dump experiment performed at CERN designed to look for charged or neutral massive ($> 1\text{GeV}/c^2$) particles with lifetime in the range $10^{-11} < \tau < 10^{-8}$ s. We will focus specifically on their neutral particle search results. Summarizing the NA3 setup: A 300 GeV/cπ^- beam is incident on a 2 meter long iron beam dump with a conical tungsten plug (A=184). A 2 meter long decay region followed by a large acceptance spectrometer is located immediately

[2]For an exact calculation of the contribution from the target and the dump, each term in the sum of Equation 6.9 should be weighted by the overall acceptance in Tables E.1 and E.2 for the WIMP mass of interest.

downstream of the dump. The spectrometer records events consistent with a neutral particle decaying in the decay region to two or more charged particles.

Table 6.1 lists some general characteristics of both the E733 and NA3 experiment for comparison [3]. These two experiments are complimentary: Their range in lifetime sensitivity is very different. The long beamline makes E733 insensitive to shorter lifetimes, but when combined with the higher integrated luminosity, E733 is more sensitive to longer lifetimes despite lower acceptances.

Table 6.1: Comparison of NA3 and E733 Experiment Characteristics

Characteristic	NA3	E733
beam type	π^-	p^-
beam energy ($\sqrt{s}$)	300 GeV/c ($\approx$ 24 GeV)	800 GeV/c ($\approx$ 39 GeV)
integrated luminosity	$69pb^{-1}$	$2.88 \times 10^6 pb^{-1}$
target type (A)	W (184)	BeO (17) target Al (28) beam dump
production to decay distance	$< 4m$	$1599m$ (target) $1057m$ (beam dump)
decay volume length	$2m$	$10m$
decay volume cross section	$1.5m$ diameter	$3.12m$ diameter
geometric acceptance	$> 85\%$	$0.006 - 0.014$ (target) $0.015 - 0.030$ (beam dump)
time-of-flight acceptance	not applicable	$0.01 - 0.90$ (target) $0.001 - 0.066$ (beam dump)
final state	requires at least 2 charged particles in final state	any combination of charged or neutral hadrons, charged leptons, photons depositing a total energy > 5GeV

In summary, the present experiment excludes noninteracting unstable particles directly produced in 800 GeV/c pN interactions with

[3] NA3 acceptances estimated using production and decay assumptions and beamline geometry. These results have not been verified by the NA3 collaboration.

- mass less than 20 GeV/c^2 and
- lifetime in the range from $10^{-7.5}$ to 10^{-5} seconds and
- production cross sections greater than a few picobarns.

6.4.2 Stable Weakly Interacting Particles

Constant Interaction Cross Section

If we assume the WIMP is stable but weakly interacting with interaction cross section σ_0, the probability P in Equation 6.1 that it will interact in the detector is

$$P = P_s \times P_{int} \tag{6.10}$$

$$= exp(-\sigma_0 N_{dump}) \times [1 - exp(-\sigma_0 N_{det})] \tag{6.11}$$

where P_s is the probability that the particle survives from the point of production to the detector (traverses the shielding within which there are $N_{dump} = 5.0 \times 10^{29} nucleons/cm^2$ [4] target nucleons with which to interact per unit area) times P_{int}, the probability that the WIMP interacts within the fiducial volume (where $N_{det} = 8.1 \times 10^{26} nucleons/cm^2$ [5] is the number of target nucleons within the detector fiducial volume).

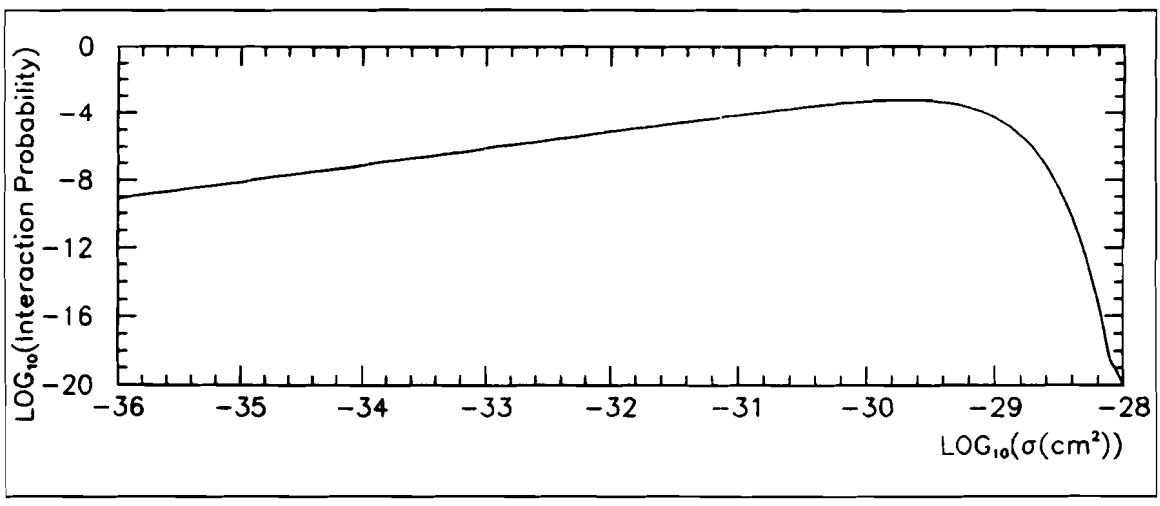

Figure 6.9: The probability that a WIMP will interact in the detector fiducial volume as a function of interaction cross section σ_0.

Shown in Figure 6.9 is this probability P plotted as a function of interaction cross section σ_0. A particle with a cross section larger than $\approx 10^{-28} cm^{-2}$ interacts before

[4] see Equation 2.5
[5] see Equation 2.6

reaching the detector, while a particle with σ_0 smaller than $\approx 10^{-33} cm^{-2}$ have a very small probability of interacting at all.

We have identified all of the factors in Equation 6.1 (N_{WIMPs}, ε, and P), for stable weakly interacting directly produced particles. We can calculate the number of events expected to be seen in the detector over the course of the run. A computer simulation utilizing the stated assumptions is used to predict the acceptances and efficiencies, get the energy spectrum of accepted particles, and calculate the probability of interaction in the detector.

For this model, the independent parameters are the production cross section σ, the mass M, the branching ratio B producing the indicated final state and the interaction cross section σ_0.

Shown in Figure 6.10 are contours of equal 90% CL upper limits on production cross section times branching ratio (pb/nucleon) as a function of mass and interaction cross section for final states a) including a muon and b) not including a muon.

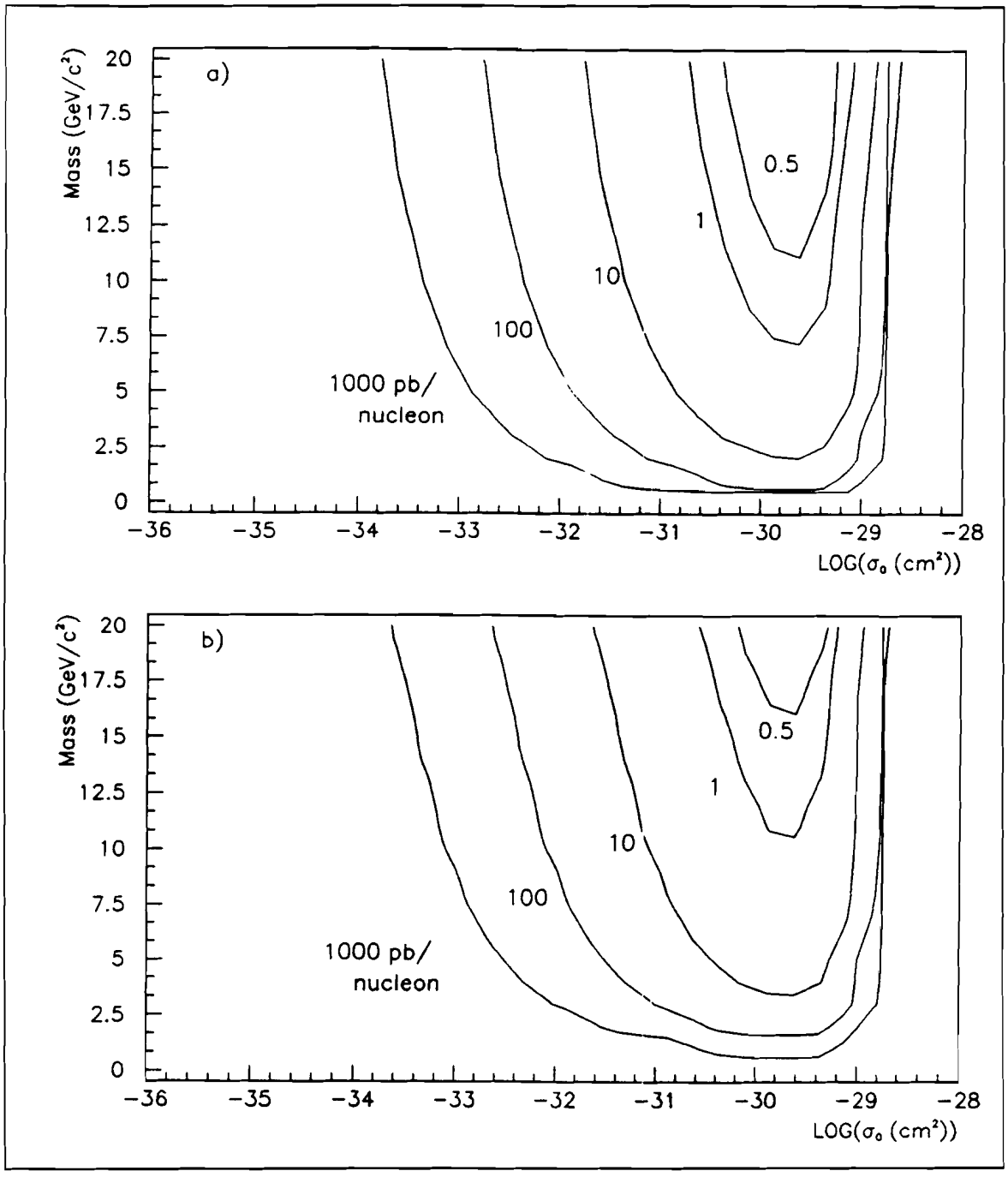

Figure 6.10: For stable particles with a constant interaction cross section: the solid contours indicate equal 90% CL upper limits on production cross section times branching ratio (pb/nucleon) as indicated as a function of mass and interaction cross section σ_0 for final states a) with a muon b) without a muon. A dependence is assumed to be the same as the total inelastic cross section ($A^{0.72}$). If a linear dependence is assumed, the σB sensitivity ***increases*** by a factor of > 2.2.

Interaction Cross Section Proportional to Energy

We have also considered the case where the interaction cross section σ_{int} is proportional to the energy of the WIMP, ie

$$\sigma_{int} = \sigma_0 \times E \tag{6.12}$$

where E is the WIMP energy and σ_0 is a constant. Such is the case in neutrino interactions for scattering from pointlike objects in the nucleus. For this general WIMP model, $W^{\pm}$ or Z_0 bosons or some unknown particle may be exchanged. We leave the mechanism unspecified.

The first three independent parameters are the same as in the last case: the production cross section σ, the mass M, and the branching ratio B producing the indicated final state. The last parameter is the constant of proportionality σ_0 in Equation 6.12.

Shown in Figure 6.11 are contours of equal 90% CL upper limits on production cross section times branching ratio (pb/nucleon) as a function of mass and interaction constant $\sigma_0 = \sigma_{int}/E$ for final states a) including a muon and b) not including a muon. The difference between the two models producing the results in Figures 6.10 and 6.11 is that in the latter figure the probability of interaction varies over the energy spectrum. The region of highest interaction cross section sensitivity is the same in both models.

In summary, the present experiment excludes stable weakly interacting particles produced directly in 800 GeV/c pN interactions with

- mass between 2 and 20 GeV/c^2 and
- interaction cross section in the range from 10^{-31} to $10^{-29} cm^2$ and
- production cross sections greater than a few picobarns.

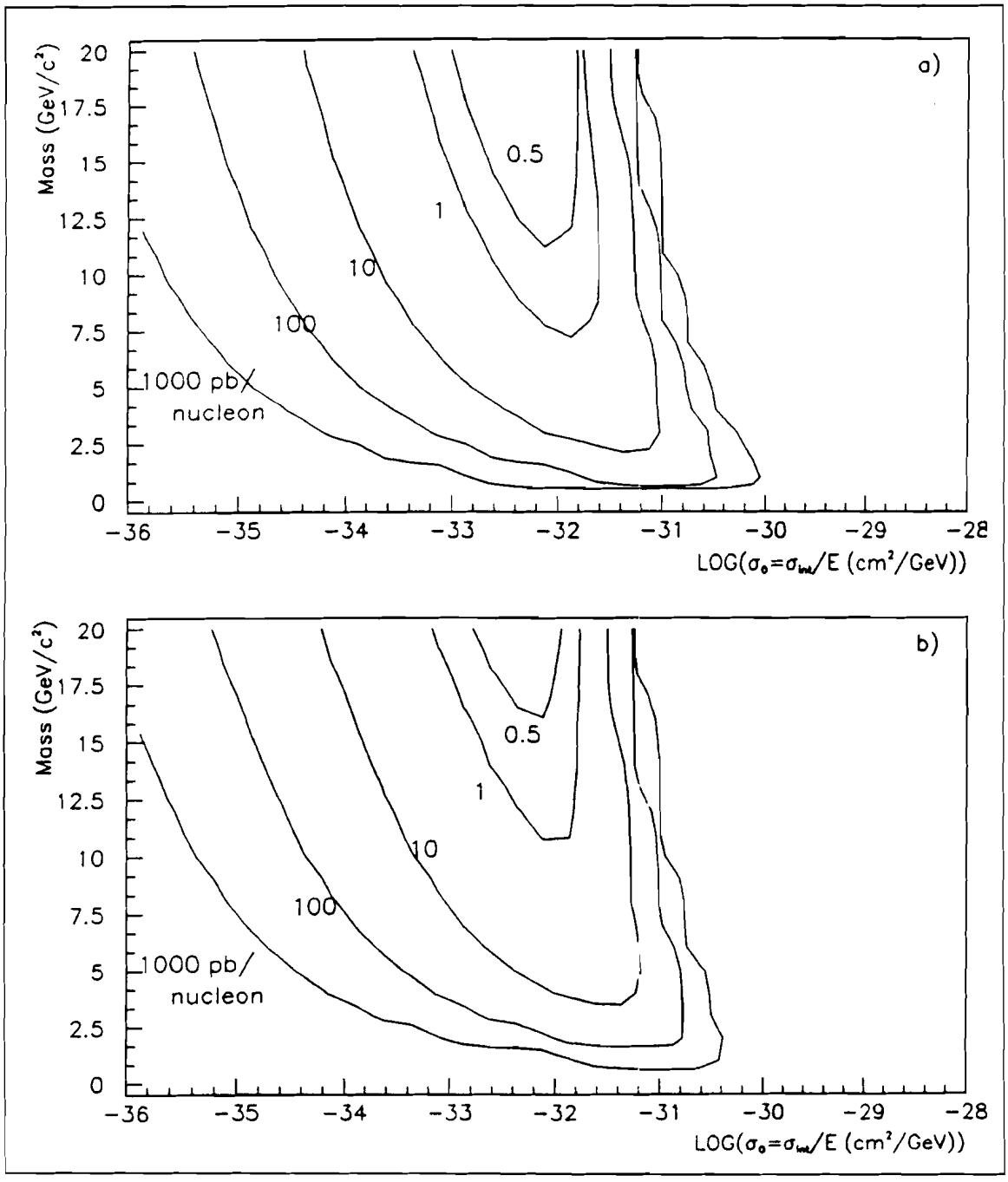

Figure 6.11: For stable particles with interaction cross section proportional to the WIMP energy: the solid contours indicate equal 90% CL upper limits on production cross section times branching ratio (pb/nucleon) as indicated as a function of mass and interaction constant $\sigma_0 = \sigma_{int}/E$ for final states a) with a muon b) without a muon. A dependence is assumed to be the same as the total inelastic cross section ($A^{0.72}$) in pN interactions. If a linear dependence is assumed, the σB sensitivity ***increases*** by a factor of > 2.2.

Chapter 7

Limits on Heavy Neutrino Production

In the last chapter, we considered the possibility that a WIMP could be produced directly in 800 GeV/c pN interactions. In these next two chapters, we consider the possibility that a WIMP is produced as the product of a decay of some other particle produced in the beamline.

In this chapter, we presuppose that a massive neutrino is produced in the decay of a heavy quark state. In summary, the following sequence of processes results in a signal in the E733 detector:

- Heavy quarks are produced at the target or the beam dump from primary or secondary beam particles.
- These states decay promptly with a massive neutral lepton as one of the decay products.
- The massive neutrino is relatively long lived and weakly interacting, so it survives the traversal of the beam dump.
- The particle decays in the E733 detector with a muon in the final state.

Ultimately, we will predict the number of events expected to be seen in the detector over the course of the run, which, as in the last chapter, is the sum over the product of a number of terms. The total number of expected events is given by

$$N_{EE} = \sum_{i=sourcesof}^{heavyquarks} N_q^i \times B_q^i \times \varepsilon^i \times P^i \times B_H. \tag{7.1}$$

Again, each of the terms is the product of a number of terms. The sum over i indicates a sum over all beam particle types that produce the heavy quark states. For each source, production parameterization constants, cross sections, acceptances and efficiencies are different, so each source contribution is calculated separately, and then summed to get the final result. The term N_q^i represents the number of heavy quarks produced from source i and B_q^i is the branching ratio for the heavy quark state to decay to a massive neutrino. Just as in the last chapter, ε^i is a product of acceptances and efficiencies:

$$\varepsilon = \varepsilon_{geo}\varepsilon_{TOF}\varepsilon_{trig}\varepsilon_{timing}, \tag{7.2}$$

each term of which is dependent on the spectrum of particles produced. P^i is the probability that an accepted massive neutrino decays in the detector fiducial volume, and the term B_H represents the branching ratio for the massive neutrino to decay to a final state that satisfies the detector trigger requirements. This chapter describes a model for heavy neutrino production, quantifies each of the terms in Equation 7.1 within the context of the model and presents the resulting limits.

7.1 A Massive Neutrino Model

It has long been recognized that it is possible to extend the Minimal Standard Model to include additional neutrino mass eigenstates [47]. Such particles may arise in new generation weak eigenstates (in a 4th, 5th ... generation isodoublets) or as additional mass eigenstates which mix with the conventionally known light neutrinos.

Combined studies in LEP experiments measuring Z^0 parameters in e^+e^- collisions have shown that the number of light neutrino generations is $N_\nu = 3.00 \pm 0.05 \pm 0.02$ based on measurements in 650,000 Z^0 decays [48]. Further studies [49, 50] exclude the existence of a more general class of massive neutral lepton that mixes with the light neutrinos (as is presented in this chapter). These results apply to any such neutral lepton with masses below 45 GeV/c^2 assuming that these new particles couple to the Z^0 in the same way as the light neutrinos.

In this experiment, the mass sensitivity to neutral leptons is limited to the range $0.5 < M < 1.8\text{GeV/c}^2$, a range much lower and narrower in mass than in these recent LEP experiments. However, we are sensitive to the coupling of neutral leptons to the $W^\pm$ boson rather than to the Z^0 boson, in other words, we look for the same particles produced in a different way.

Consider an extension of the Standard Model in which each weak neutrino flavor eigenstate [1] χ_i is a superposition of a conventional light neutrino mass eigenstate ν_i and $a = 1, 2, ...n$ new heavy neutrino mass eigenstates ν_a^H. Then

$$\chi_i = \nu_i \left[1 - \sum_{a=1}^{n} |U_{ia}|^2\right]^{1/2} + \nu_a^H \sum_{a=1}^{n} |U_{ia}|. \tag{7.3}$$

where i is either e, μ, or τ and the sum over a indicates a sum over the number of heavy lepton species.

In this notation, the neutral and charged currents in the lepton sector are of the form

$$J^{NC} = \sum_{i=e,\mu,\tau} \overline{\chi_i}\gamma^\mu(1-\gamma^5)\chi_i \tag{7.4}$$

and

$$J^{CC} = \sum_{i=e,\mu,\tau} \overline{\chi_i}\gamma^\mu(1-\gamma^5)l_i^\pm. \tag{7.5}$$

The mixing matrix ($|U_{ia}|$), a set of experimentally determined coefficients, express the strength of the mixing between the different mass eigenstates. It must be unitary

[1]The weak eigenstates are defined as those states which couple with unit strength to their respective charged lepton of the same flavor.

to conserve probability, and the values within it are constrained by weak universality [51]. The present limits on mixing between flavors indicate that each weak eigenstate is dominated by a single light (or massless) mass eigenstate. Other non-zero matrix terms may result in mixing between flavors and/or mixing between heavy and light states of the same flavor.

We do not consider mixing between two of the conventional mass eigenstates that couple dominantly to ν_e, ν_μ, or ν_τ; We are considering mixing between one of these light states and a mass eigenstate yet unknown with a mass greater than 0.5 GeV/c^2.

This study is complimentary to the more traditional searches for neutrino oscillations [52] between the light eigenstates (for mixing angles > 0.01 at smaller mass differences). We are searching for states with large mass differences at very small mixing angles ($< 10^{-2}$). In the case of a large mass difference between the species (over 0.5 GeV/c^2), mixing leads to neutrino oscillations of undetectably short wavelength. Mixing occurs instantaneously at the point of production. The massive state manifests itself by arriving at the detector delayed in time relative to the neutrinos in the same bunch.

We assume that mixing occurs between the light and heavy neutrinos of the same flavor as suggested in References [53] and [54]. In this experiment, we are most sensitive to decays into muons, thus the remainder of this chapter will focus on the possibility of a single heavy neutrino mixing with the conventional light muon neutrino.

7.2 Heavy Neutrino Production from the Decay of Heavy Quarks

If a single heavy neutrino eigenstate N_H exists, it couples with strength $|U_{\mu H}|^2$ to $\mu^\pm$. As a consequence, these heavy eigenstates would appear in the semileptonic and leptonic decays of quark states provided the kinematic threshold is satisfied. For

example, a heavy neutrino with mass less than 0.140 GeV/c^2 or 0.5 GeV/c^2 would be produced in the decay of pions or kaons, respectively. A variety of experiments have looked for massive neutrinos from decays such as $\pi \rightarrow \nu\mu$ [55], $K \rightarrow \nu\mu$ [56], $K \rightarrow \nu\nu\bar{\nu}\mu$ [57]. Results of these studies, along with others, will be compared to our results later in the chapter.

The higher energy of the Tevatron makes it possible to extend the region of mass sensitivity beyond the $K^{\pm}$ mass. Heavy quark states such as the D mesons $D^+(c,\bar{d})$, $D^-(\bar{c},d)$, $D_S^+(c,\bar{s})$ and $D_S^-(\bar{c},s)$ are expected to be copiously produced via gluon fusion in both the target and the beam dump. These states have muonic decay modes. The decays of these states to heavy neutrinos will occur in proportion to the mixing parameter squared ($|U_{i\alpha}|^2$).

The Feynman diagram for the two-body decay of a D^+ producing a heavy neutrino is shown in Figure 7.1 a). These heavier states can decay to heavy leptons

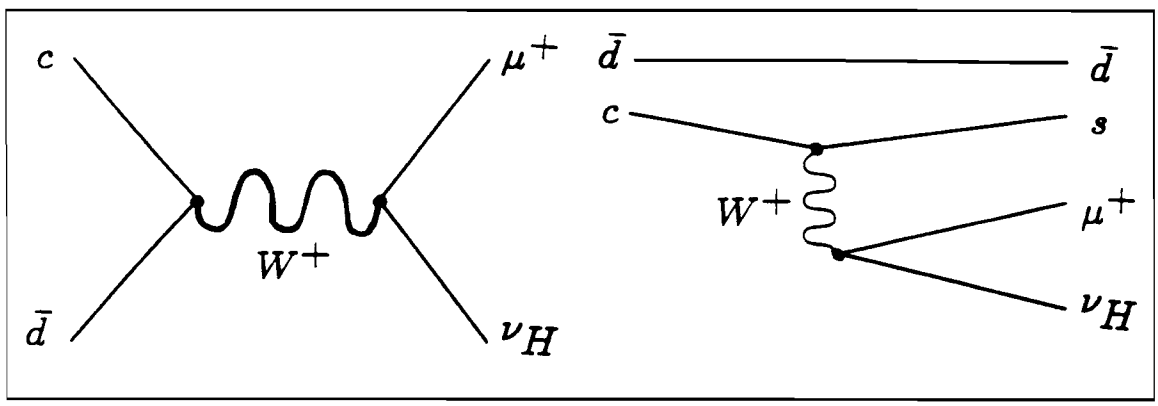

Figure 7.1: Feynman Diagrams demonstrating the a) 2 body and b) 3 body decay of a charged D meson into a final state with a massive neutrino.

up to masses of about 1.7GeV/c^2. A three body decay is also possible as shown in Figure 7.1b), again assuming that the kinematic threshold is satisfied. The hadron in the 3 body decay is most likely a kaon (Cabibbo favored) rather than a pion (Cabibbo suppressed). We will see later that the acceptance for this 3 body decay mode makes this decay channel unimportant for this analysis.

The branching ratios for the 2 body decay modes are predicted theoretically [51]

$$B_q(D^{\pm} \rightarrow \nu_H \mu^{\pm}) = \left(1.57 \times 10^{-2}\right) |U_{\mu H}|^2 \left(\frac{M}{1\mathrm{GeV/c^2}}\right)^2 \left(1 - \frac{M^2}{M_D^2}\right)^2 \tag{7.6}$$

and

$$B_q(D_S^{\pm} \rightarrow \nu_H \mu^{\pm}) = \left(1. \times 10^{-1}\right) |U_{\mu H}|^2 \left(\frac{M}{1\mathrm{GeV/c^2}}\right)^2 \left(1 - \frac{M^2}{M_{D_S}^2}\right)^2 \tag{7.7}$$

where M, M_D, and M_{D_S} are the masses of the heavy neutrino, $D^{\pm}$ meson and $D_S^{\pm}$ meson (sometimes called the $F^{\pm}$ meson), respectively. These branching ratios are the B_q^i in Equation 7.1. Note that they are dependent on the mixing parameter $|U_{\mu H}|^2$ and the heavy neutrino mass M, which are the free parameters of this model. The branching ratio of Equation 7.6 is plotted as a function of $|U_{\mu H}|^2$ in Figure 7.2 for 3 ν_H masses. The curve drops steeply with decreasing $|U_{\mu H}|^2$ for all ν_H masses.

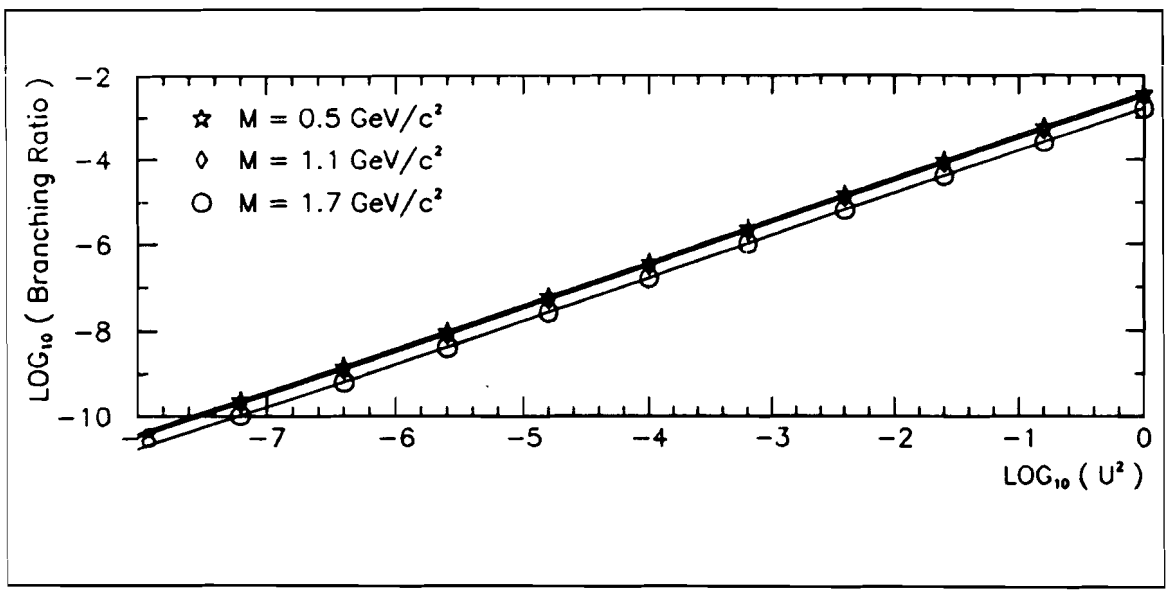

Figure 7.2: The branching ratio for a $D^{\pm}$ meson to decay to a massive neutrino as a function of $|U_{\mu H}|^2$ for ν_H masses of a) 0.5, b) 1.1 and c) 1.7 GeV/c^2 .

It is about 3 times greater for the lowest mass ν_H compared to the highest mass regardless of $|U_{\mu H}|^2$.

The lifetimes [15] of the $D^{\pm}$ and the $D_S^{\pm}$ mesons have been measured to be $(10.66 \pm 0.23) \times 10^{-13}$ s and $(4.45^{+0.30}_{-0.26}) \times 10^{-13}$ s respectively. As a result of these

relatively short lifetimes, decay occurs virtually at the point of production so that secondary interactions in the target or dump are negligible.

7.2.1 Charmed Particle Production and Decay

There are a number of sources of charmed mesons in the neutrino beamline. They include 800 GeV/c protons on the primary target and the beam dump, and secondary beam particles on the beam dump such as $\pi^{\pm}$, $K^{\pm}$ and $p^{\pm}$.

The hadroproduction of D mesons has been measured by experiments at both FNAL and CERN for a number of beam particle types and a range in beam energies. These experiments measure total cross sections and/or constants that express the production in the center of mass such as n and b in the parameterization

$$\frac{d^3\sigma}{dp_T^2 dx_F} \propto (1 - x_F)^n \, exp\left(-bp_T^2\right) \tag{7.8}$$

Measurements of the constant b in Equation 7.8 (indicating the p_T^2 dependence of the production) indicate that b is relatively independent of beam type, beam energy and target type as pointed out in Reference [43]. Therefore, an average value of $b = 1.0$ was used in the simulation of all $D^{\pm}$ and $D_S^{\pm}$ production for all beam types and energies in this analysis. Measurements of the x_F dependence (the constant n in Equation 7.8) vary with beam energy. Higher n values are typically measured at higher beam energies.

Experimentally measured cross sections typically agree within stated uncertainties, though the variation in the central values vary widely [12]. Of the plethora of experimental results available, a few were chosen as representative of charm hadroproduction on the basis of beam energy, statistical weight of the data sample, final state particle identification ability, and sensitivity range in x_F over which production was measured. The effects of the variation in these production parameters will be discussed later.

The D^- and D^+ mesons are *leading* and *non-leading* particles, respectively (as described in Chapter 1). Therefore global fits for both charge states covering low and high x_F were used, rather than using separate production parameterizations for the D^- and D^+.

It should also be noted that some fraction [2] of the charged D mesons produced in pN interactions are not produced directly, but are decay products of higher mass states. Since we expect similar effects in the neutrino beamline, this point is inconsequential.

To parameterize charm production in the neutrino beamline, we have used the results of the following experiments:

FNAL E743 This experiment [58] utilizes a precision vertex detector LEBC (LExan Bubble Chamber) followed by a multiparticle spectrometer (MPS) to study charm production in 800 GeV/c pp interactions. They have measured a total charged D meson production cross section of $\sigma_{tot}(D^+/D^-) = 26 \pm 4\mu b$, and constants n and b in Equation 7.8 of 8.6 ± 2.0 and $0.8 \pm 0.2(\mathrm{GeV/c})^{-2}$ respectively. These results are used to parameterize $D^\pm$ production from 800 GeV/c protons on the target and the beam dump.

CERN NA16[59], NA27[60] These experiments utilize the same precision vertex detector LEBC (LExan Bubble Chamber) followed by a multiparticle spectrometer (EHS - European Hybrid Spectrometer) to study charm production in 360 GeV/c π^-p interactions.

- The NA16 experiment measures $\sigma(D^\pm) = 4.5 \pm^{2.2}_{1.4} \mu b(x_F > 0)$, $n = 2.8 \pm 0.8$, and $a = 1.1 \pm 0.3(\mathrm{GeV/c})^2$.

[2] Estimates of this fraction run as high as 50%.

- The NA27 experiment measures $\sigma(D^{\pm}) = 5.7 \pm 1.5 \mu b(x_F > 0)$, $n = 3.8 \pm 0.6$, and $a = 1.18 \pm^{0.18}_{0.16}$ (GeV/c)^2.

Averaging these results, the cross section for $D^{\pm}$ production in 360 GeV/cπ^-p interactions is $\sigma(D^{\pm}) = 5.1 \pm 2\mu b(x_F > 0)$. The scaling of this cross section over the spectrum of secondary energies will be described later.

The average value of the constant n in Equation 7.8 from these experiments is 3.3. Since the average secondary pion energy in the beamline is less than 250 GeV, a slightly more conservative value of $n = 3.0$ was used in the simulation.

A very limited amount of data are available for $D^{\pm}$ production in $K^{\pm}$N interactions [45]. In this analysis, we assume that this production is the same as that measured in $\pi^{\pm}$N interactions at the same energy.

FNAL E769 Using the TPS detector (a silicon microstrip vertex detector followed by an open-geometry spectrometer) in a Fermilab beamline, the $D_S^{\pm}$ production cross section in 250 GeV/c pN interactions was measured to be $1.5\mu b$ (preliminary) [61].

Shown in Figure 7.3 is a theoretical prediction from Quigg and Ellis [62] of the energy dependence of the charm production cross section in pN and πN interactions. Note that the *shape* of the energy dependence is relatively independent of the charm quark mass. This energy dependence combined with the measurements listed above, are used to predict the $D^{\pm}$ production cross section for the beam particle energies at which measurements are not available. These predicted cross sections are shown in Figure 7.4.

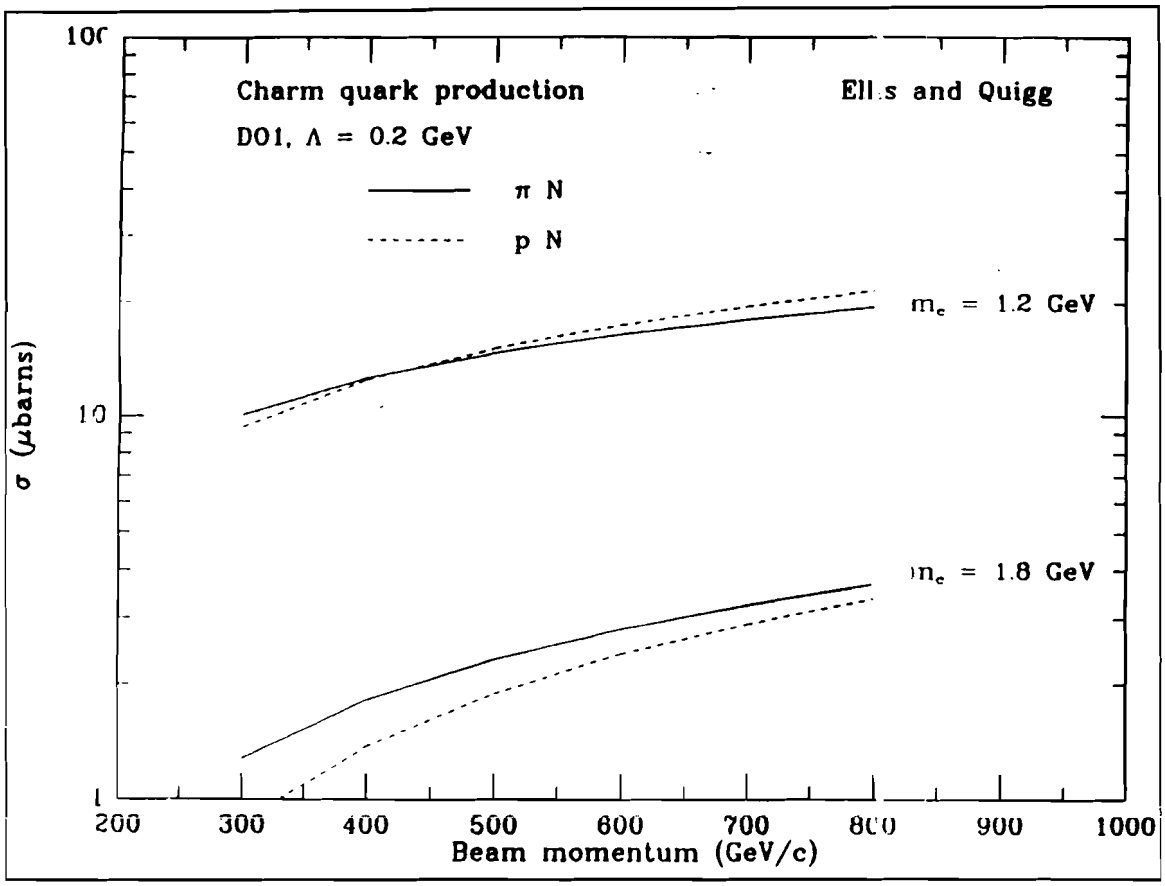

Figure 7.3: Integrated cross sections for the production of charmed quarks in πN (solid lines) and pN (dashed lines) collisions extracted from a paper by Ellis and Quigg.

For example, a measurement of the $D_S^{\pm}$ production cross section in 800 GeV/c pN collisions is not available, so extrapolating the measured cross section of $1.5\mu b$ at 250 GeV/c pN according to the solid curve in Figure 7.3, we obtain $\sigma(D_S^{\pm}) \approx 5.5\mu b$ at 800 GeV/c.

The energy spectra of secondary $\pi^{\pm}$, $K^{\pm}$ and $p^{\pm}$ on the beam dump are shown in Figure 2.2. For secondary protons and antiprotons, the E743 cross section measurement at 800 GeV/c is used to predict $\sigma(D^{\pm})$ at lower proton energies. Similarly, the NA16 and NA27 results are scaled to obtain $\sigma(D^{\pm})$ for the spectrum of energies of secondary pions and kaons.

As we will see later, the secondary flux production of $D^{\pm}$ at the beam dump is

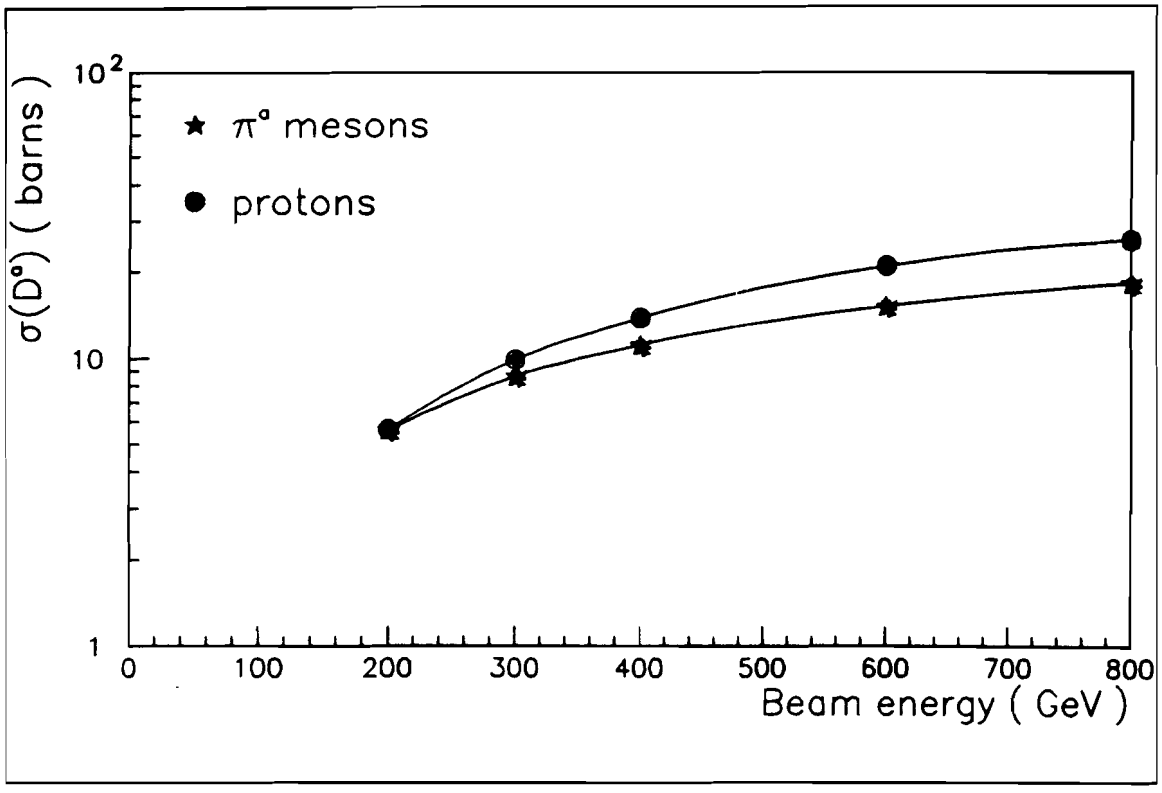

Figure 7.4: Expected $D^{\pm}$ cross section as a function of beam energy in πN (solid lines) and pN (dashed lines) interactions.

not a significant source of ν_H at the detector. We therefore did not simulate $D_S^{\pm}$ production by secondary particles, as we expect this source to contribute equally insignificantly.

In Equation 7.1, the sum over i indicates a sum over all beam particle types. The sources considered are listed explicitly in Table 7.1 by index i.

The production assumptions above can be combined to estimate the term N_q^i in Equation 7.1:

$$N_q^i = POT \times X_{model}^i \times E_{train}^i \times \frac{\sigma_D^i}{\sigma_{total}}, \tag{7.9}$$

where the product of the first 3 terms ($POT \times X_{model}^i \times E_{train}^i$) is the total number of integrated interacting particles of type i, and $\sigma_D^i/\sigma_{total}$ is the fraction of those interacting particles that are expected to produce $D^{\pm}$. To elaborate on each term:

POT is the number of integrated live protons on target as given in Equation 2.7,

Table 7.1: Sources of $D^{\pm}$ and $D_S^{\pm}$ in the neutrino beamline.

index i	Source of $D^{\pm}$
1	800 GeV/c p on target
2	800 GeV/c p on beam dump
3	secondary π^- at beam dump
4	secondary π^+ at beam dump
5	secondary K^- at beam dump
6	secondary K^+ at beam dump
7	secondary p^- at beam dump
8	secondary p^+ at beam dump
index i	Source of $D_S^{\pm}$
1	800 GeV/c p on target
2	800 GeV/c p on beam dump

X^i_{model} is the number of interacting particles per proton on target. For primary protons on the target and the beam dump, $X^1_{model} = 0.6321$ and $X^2_{model} = 0.3679$ respectively as in Chapter 6. For secondary particles, it is given in Table 2.1.

E^i_{train} is the train acceptance, the fraction of particles that make it through the aperatures of the magnet train. The primary proton beam is highly collimated so $E_{train} = 1$ for 800 GeV/c protons on the primary target and the beam dump. For secondary particles, E^i_{train} is given in Table 2.1.

σ^i_D is the measured production cross section for D mesons for each beam particle type i. For primary sources, it is constant. For secondaries, it varies with energy as described earlier in this section.

σ^i_{tot} is the total inelastic interaction cross section for each beam pa le type. It is about $40mb$ for protons, $23mb$ for pions, $23mb$ for kaons, d $42mb$ for antiprotons [15].

Shown in Figure 7.5 is the number of $D^{\pm}$ and $D_S^{\pm}$ mesons expected to be produced

in the beamline as a function of beam type. The beam types i considered are as listed in Table 7.1. The principle sources of $D^{\pm}$ mesons are the primary protons on

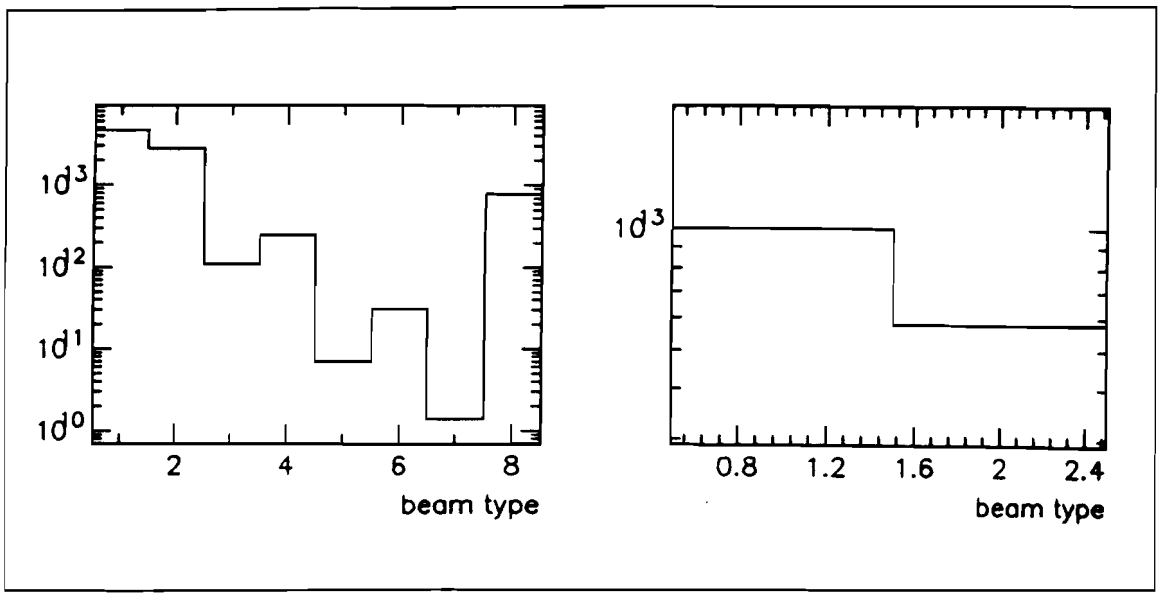

Figure 7.5: The number of a) $D^{\pm}$ and b) $D_S^{\pm}$ particles produced in the beamline as a function of beam type i.

the target and the beam dump, followed by secondary protons and secondary $\pi^{\pm}$ on the beam dump. The $D_S^{\pm}$ mesons are not as copiously produced (as the $D^{\pm}$), but higher branching ratios to heavy neutrinos (in Equation 7.7 relative to Equation 7.6) provide the compensating factor that makes the D_S contribution to the ν_H production significant.

Cross section uncertainty and A dependence

The major source of uncertainty in calculating the number of D mesons produced is the production cross section. A variation in cross section effects the number of produced particles proportionally. If the true production cross section is 20% higher, then 20% more D particles are produced, and 20% more ν_H would be expected in the detector over the course of the run.

The atomic weight dependence (A dependence) of the charm production cross

section has been studied extensively as described in Chapter 1. The total inelastic cross section has been measured to have an $A^{0.72}$ dependence [14] for protons on a nuclear target. Results from experiments studying the hadroproduction of charm indicate charm cross sections with a linear A dependence. See Reference [12] for a good summary of such results. Assuming this is the case, then N_q, the number of heavy quarks produced in the beamline, is enhanced by a factor of ($\frac{A^{1.0}}{A^{0.72}}$ =)2.2 at the target (where $A = 17$) and a factor of 2.5 at the beam dump (where $A = 27$).

7.2.2 Acceptance and Efficiency

Using the production assumptions described, acceptances and efficiencies can be obtained. We have used a computer simulation to accomplish this, taking the following steps:

- D meson production is simulated in the center of mass for each beam source type according to Equation 7.8 with production constants n and b as described in the last section.

- These mesons are allowed to decay as in the Feynman diagrams of Figure 7.1, assuming that the massive neutrino is produced isotropically in the center of mass for both the 2 and 3-body decay modes.

- The trajectories of the heavy neutrinos produced in such decays are projected into space. The fraction of those particles that pass through the detector fiducial volume is the geometric acceptance, ε_{geo}, in Equation 7.2.

- The fraction of those geometrically accepted particles that enter the detector in the time-of-flight search window is the time-of-flight acceptance, ε_{TOF}, in Equation 7.2.

- The trigger acceptance, ε_{TOF}, in Equation 7.2 is the fraction of those geometrically and time-of-flight accepted particles that have a total energy above

5 GeV

- In addition to obtaining the acceptances described above, this simulation produces the expected energy spectrum of accepted particles which will be used in a later section to generate the timing efficiency and the probability of decay in the detector.

Acceptances are described graphically in the following sections. For completeness, geometric, time-of-flight, and trigger acceptances for a number of heavy neutrino masses can be found in the tables of Appendix E as follows:

Table 7.2: Guide to location of acceptance tables for ν_H production.

Table	contains acceptances for this source of ν_H
E.3	ν_H production from 2-body decay of $D_S^{\pm}$ produced by 800 GeV/c protons at the target and beam dump
E.4	ν_H production from 2-body decay of $D^{\pm}$ produced by 800 GeV/c protons at the target and beam dump
E.5	ν_H production from 2-body decay of $D^{\pm}$ produced by the secondary $\pi^{\pm}$ flux at the beam dump
E.6	ν_H production from 2-body decay of $D^{\pm}$ produced by the secondary $K^{\pm}$ flux at the beam dump
E.7	ν_H production from 2-body decay of $D^{\pm}$ produced by the secondary $p^{\pm}$ flux at the beam dump

The geometric acceptance as a function of beam type i and heavy neutrino mass M is shown in Figure 7.6 for heavy neutrinos produced in the 2-body decay of the a) $D^{\pm}$ and b) $D_S^{\pm}$. The acceptance is higher for beam sources closer to the detector with a harder energy spectrum. Thus, the monoenergetic 800 GeV/c protons on the beam dump ($i = 2$) and the secondary protons on the beam dump ($i = 8$) have the best geometric acceptance. Acceptance for protons on the target ($i = 1$) is slightly lower because the target is about 500 meters upstream of the dump.

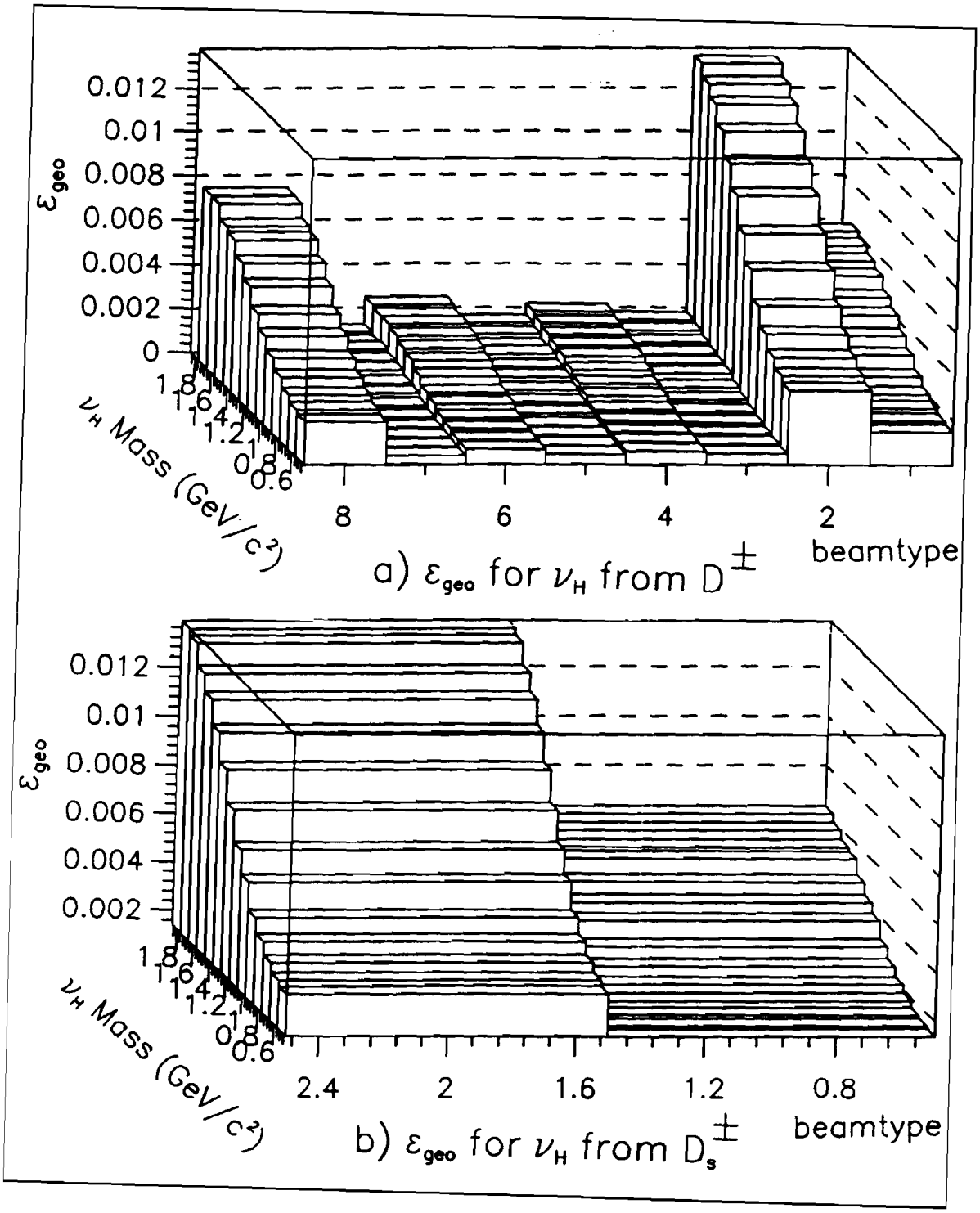

Figure 7.6: The geometric acceptance for heavy neutrinos produced in the 2 body decay of a) $D^{\pm}$ and b) $D_S^{\pm}$ as a function of heavy neutrino mass and beam particle type.

The nature of the decay kinematics results in higher geometric acceptances for higher ν_H mass. The decay introduces more angular dispersion in the beam. This dispersion is less severe as the mass of the heavy neutrino approaches the mass of the parent D meson.

The time-of-flight acceptance as a function of beam type i and heavy neutrino mass M is shown in Figure 7.7 for geometrically accepted heavy neutrinos produced in the 2-body decay of the a) $D^{\pm}$ and b) $D_S^{\pm}$. Recall that this acceptance requirement is roughly equivalent to a high energy cutoff as described in the last chapter (see Figure 6.4). Therefore, higher TOF acceptance occurs for particles with a softer energy spectrum, for example for ν_H produced from the softer secondary particles. In this case, the requirement is much more severe because heavy neutrino masses considered are constrained to be below the D mass (1.8 GeV/c^2). At these low masses, the cutoff energy is low, resulting in low TOF acceptance.

The total acceptance as a function of beam type i and ν_H mass is plotted in Figure 7.8 for ν_H produced from the 2 body decay of a) $D^{\pm}$ and b) $D_S^{\pm}$ mesons. This overall acceptance is the combined geometric, time-of-flight and trigger acceptance. [3] In comparison to direct production acceptances of the last chapter (for the following itemized list, compare Tables E.1 and E.2 to Table E.5):

- The geometric acceptances are up to a factor of 4 smaller than for the direct production of particles of comparable masses. This is because a decay will always tend to increase the angular dispersion of the beam relative to the beam axis.

- For comparable masses, the time-of-flight acceptances are better for the 2 body decay production case (compared to the direct production case) because the energy spectrum is softer. However, in the decay case, the daughter mass is

[3]The trigger acceptance is greater than 88% for the lowest ν_H masses, and quickly rises to over 99% for $\nu_H > 1.0$ GeV/c^2.

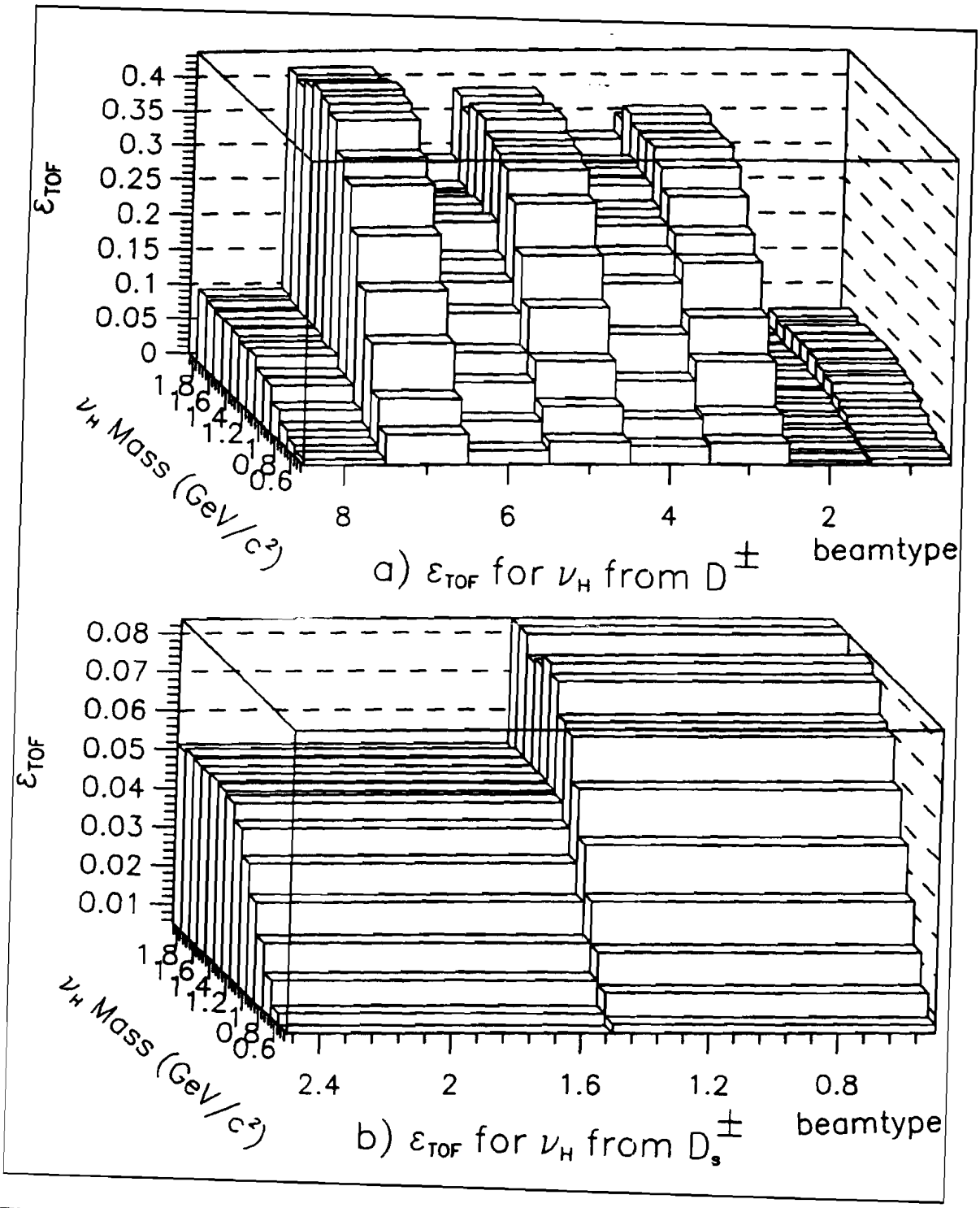

Figure 7.7: The time-of-flight acceptance for geometrically accepted heavy neutrinos produced in the 2 body decay of a) $D^{\pm}$ and b) $D_S^{\pm}$ as a function of heavy neutrino mass and beam particle type.

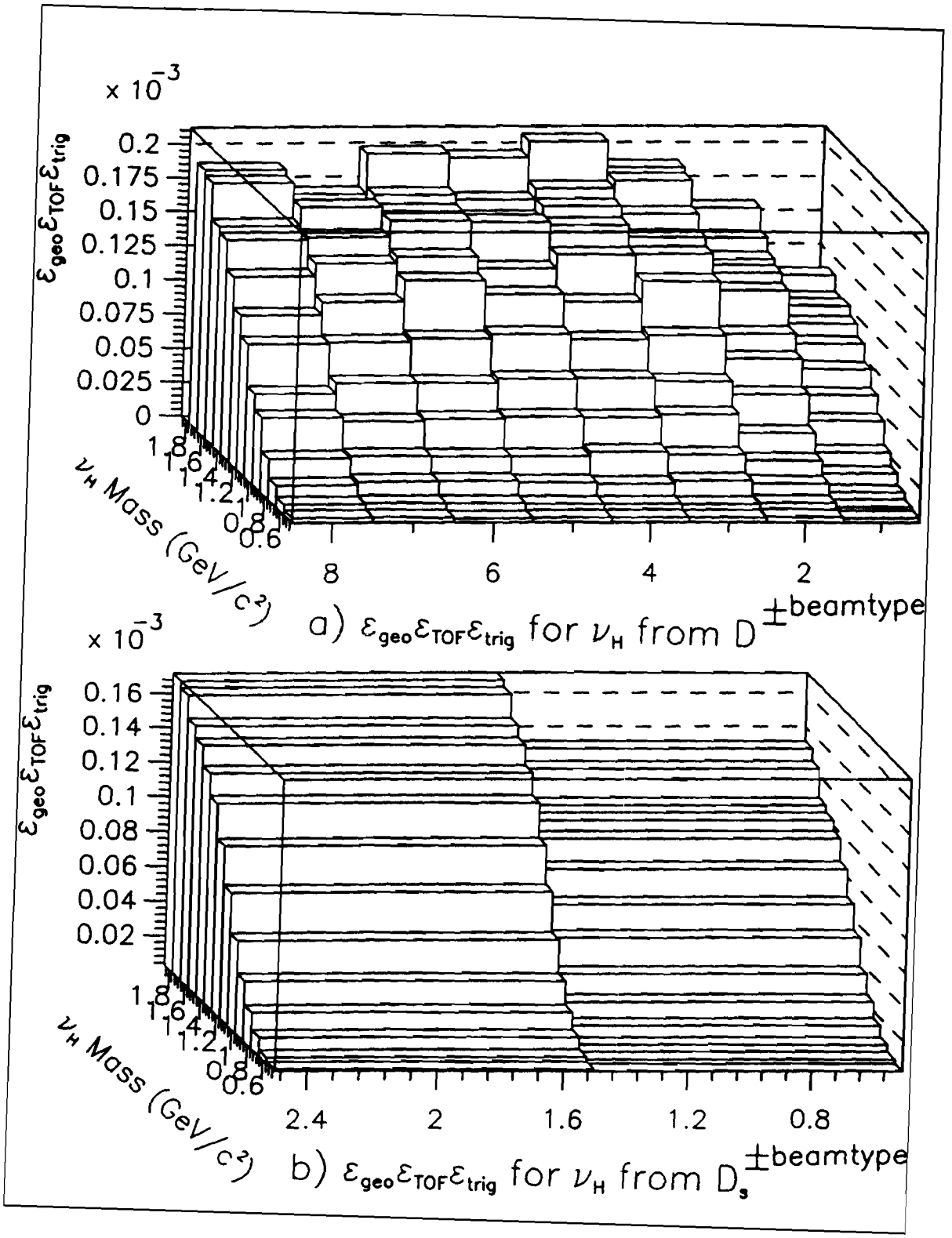

Figure 7.8: The acceptance (combined geometric,time-of-flight and trigger acceptance) for heavy neutrinos produced in the 2 body decay of a) $D^{\pm}$ and b) $D_S^{\pm}$ as a function of heavy neutrino mass and beam particle type.

constrained to be less than the parent mass (in this case $M_D \approx 1.8$ GeV/c^2). Considerably higher TOF acceptances (over an order of magnitude higher) are obtained in the direct production case for higher masses.

- The total acceptance for particles with mass < 1.8 GeV/c^2 is similar for WIMPs produced directly or via decay. Acceptances over an order of magnitude greater are expected for more massive directly produced particles because more massive (> 2 GeV/c^2) particles have higher geometric *and* time-of-flight acceptances.

The geometric and TOF acceptances were also evaluated for the ν_H produced in the 3 body decay of D mesons of Figure 7.1 b). The resulting efficiencies are shown in Table 7.3. These geometric acceptances are typically an order of magnitude lower

Table 7.3: Geometric and time-of-flight acceptances for ν_H produced in the 3 body decay of the $D^{\pm}$ meson produced at the target

ν_H Mass (GeV/c^2)	ε_{geo}	ε_{TOF}	$\varepsilon_{geo}\varepsilon_{TOF}\varepsilon_{trig}$
0.5	0.0000227	0.0043616	0.0000001
0.6	0.0000289	0.0028077	0.0000001
0.7	0.0000372	0.0024210	0.0000001
0.8	0.0000510	0.0031873	0.0000002
0.9	0.0000722	0.0035772	0.0000003
1.0	0.0001148	0.0028007	0.0000003
1.1	0.0002070	0.0045434	0.0000009
1.2	0.0005314	0.0068752	0.0000037

than their two body counterparts because it is even less likely that the product of a 3 body decay is projected into the very forward direction. Time-of-flight acceptances are another factor of $2 - 10$ lower because the geometrically accepted ν_H from the 3 body decay have a harder energy spectrum than their two body counterparts. In conclusion, ν_H produced from the 2 body decay of D mesons do not contribute significantly to the ν_H flux at the detector.

It is prudent to ask how much these acceptances change as the production constants n and b vary (in Equation 7.8). The following figures demonstrate the changes in these efficiencies as a function of changing n and b for ν_H from the decay of $D^{\pm}$ produced by 800 GeV/c protons on the primary target. The values $n = 8.6$ and $b = 1.0$ were used to get the acceptances already shown. The uncertainty in the values of n and b measured in experiment E743 was 2.0 and $0.2(\mathrm{GeV/c})^{-2}$ respectively.

Figure 7.9 a) shows the geometric acceptance as a function of mass assuming a fixed $n = 8.6$ for three values of b: 0.8, 1.0 and 1.2, the first and third values being the value of b at $\pm 1\sigma$ of its central value, respectively. The p_T^2 distribution has a higher mean p_T for lower values of b. Therefore, as expected, the geometric acceptance decreases for lower values of b. As b varies by $\pm 1\sigma$, the geometric acceptance varies by at most 20% for the highest mass, and by less than 13% for low masses.

Figure 7.9 b) shows the geometric acceptance as a function of mass for a fixed $b = 1.0$ and three values of n: 6.6, 8.6 and 10.6, the first and third values being the value of n at $\pm 1\sigma$ of its central value, respectively. The x_F distribution peaks more sharply (at $x_F = 0$) for higher values of n. Geometrically accepted particles are those that are projected into a forward cone with a very small opening angle. Those with a higher x_F are more likely to satisfy this criteria, therefore, particles produced with lower n have a higher geometric acceptance. As n varies by $\pm 1\sigma$, the geometric acceptance varies by about 20 to 30% over the mass range.

Figure 7.10 a) shows the combined geometric and time-of-flight acceptance as a function of mass for n and b as in Figure 7.9 a). The behavior of this combined acceptance mimics that the the geometric acceptance, with higher acceptances for higher values of b.

Figure 7.10 b) shows the combined geometric and time-of-flight acceptance as a function of mass for n and b as in 7.9 b). The behavior of this combined acceptance

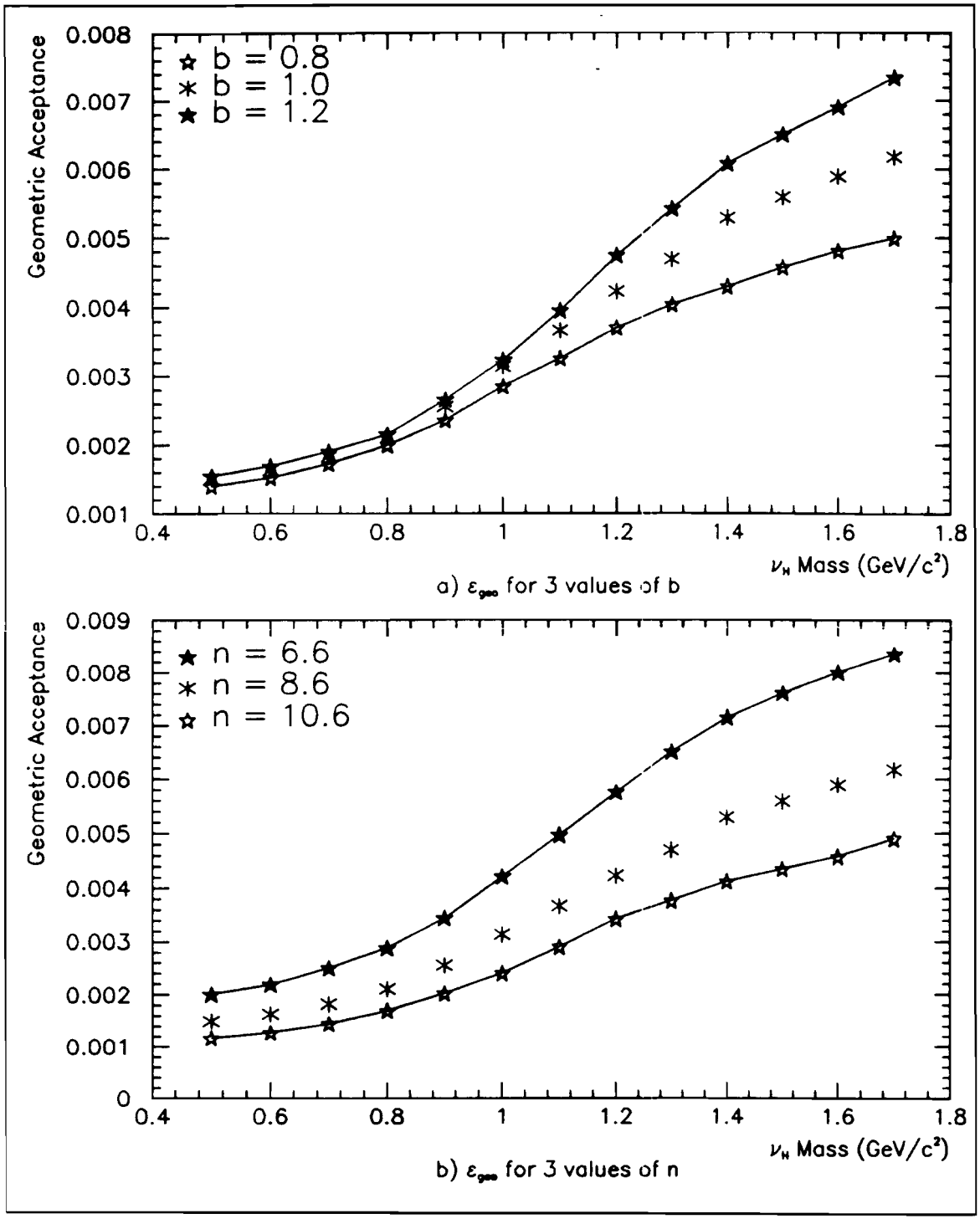

Figure 7.9: Value of the geometric acceptance as a function of ν_H mass for a) a fixed value of n and b varying by $\pm 1\sigma$ of the measured value and b) a fixed value of b and n varying by $\pm 1\sigma$ of the measured value in E743.

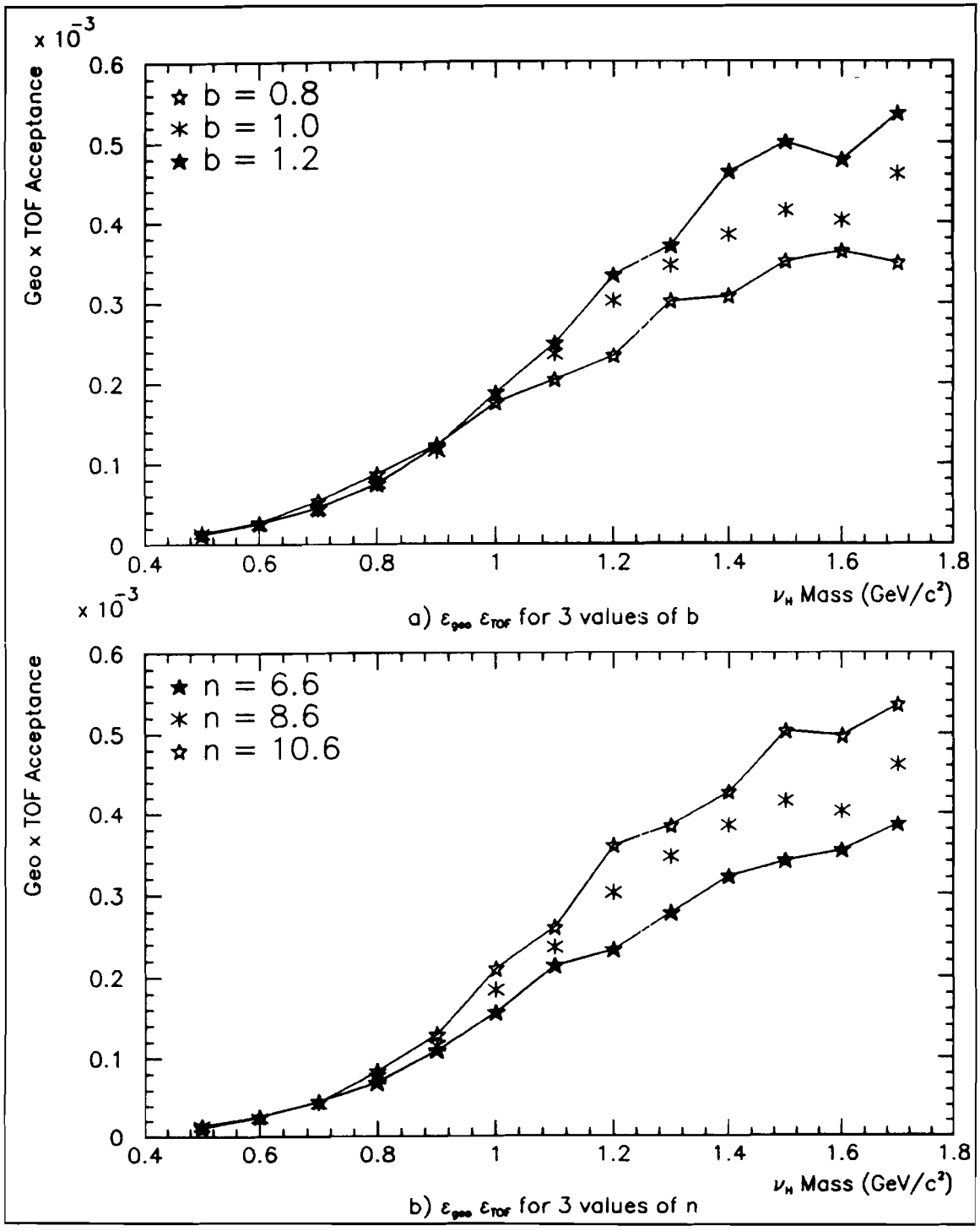

Figure 7.10: Value of the combination of geometric and time-of-flight acceptance as a function of ν_H mass for a) a fixed value of n and b varying by $\pm 1\sigma$ of the measured value and b) a fixed value of b and n varying by $\pm 1\sigma$ of the measured value in E743.

is contrary to that which is seen for the geometric acceptance. This is a result of the maximum energy cutoff of the time-of-flight acceptance requirement. Those high x_F particles that more easily satisfy the geometric acceptance requirement have too high an energy to satisfy the time-of-flight criteria. Thus, particles produced with a higher n are more likely to be geometrically *and* time-of-flight accepted. As n varies by $\pm 1\sigma$, the combined acceptance varies by at most 20% for the highest mass, to less than 5% for the lowest mass.

These variations scale proportionally into the final calculation of expected number of events seen in the detector. If the acceptance is believed to be 20% less, then the number of expected events scales similarly.

7.2.3 ν_H Detection

The last term in Equation 7.2 is the timing efficiency (ε_{timing}), the fraction of ν_H decay events expected to have a reliable event time measurement. This depends on how the heavy neutrino is expected to deposit energy in the detector when it decays. To continue the discussion of this efficiency determination, we first need to consider the expected decay topology.

The expected final state branching ratios have been predicted theoretically [51]. These ratios are summarized in Table 7.4 for 3 heavy lepton masses mixing primarily with ν_μ. The E733 event timing resolution is best for final states that include a muon. Summing appropriate channels in the table (rows 1, 3, and 5), we expect $\approx 60\%$ of all ν_H decays to include a muon. Note that this sum is relatively independent of the ν_H mass in this mass range ($.5 - 2$ GeV/c^2). We assume that all final states that include a muon in the table satisfy the trigger energy requirement.

About 20% of the additional decays may also satisfy the trigger energy requirement (final state of row 2 and 6), having a NC-like final state topology. The corresponding timing resolution is not good enough to improve the final limit result, so

Table 7.4: Branching ratios into specific final states for low-mass neutral heavy leptons, in percent for ν_H mixing primarily with ν_μ.

	Mass(ν_H) (GeV/c^2)	0.5	1.0	2.0
	final state			
1)	$\mu^- e^+ \nu$	13.6	13.8	13.8
2)	$e^- e^+ \nu$	2.4	1.9	1.8
3)	$\mu^- \mu^+ \nu$	5.5	7.3	7.7
4)	$\nu\nu\bar{\nu}$	19.0	15.0	14.1
5)	$l^- + hadrons$	40.5	41.2	41.3
6)	$\nu + hadrons$	18.9	20.8	21.3

it is not discussed further.

To summarize this discussion, we set $B_H = 0.60$ in Equation 7.1.

As stated in the beginning of this section, the timing efficiency (ε_{timing} of Equation 7.2) depends on the final state topology of the ν_H decay in the detector. For charged current-like final states, the timing efficiency decreases slightly with muon angle for single counter timed charged current events (Figure 5.13 a)). It decreases more rapidly with muon angle in multiple counter timed CC-like events (Figure 5.13 b)).

To calculate the timing efficiency for ν_H decays, the measured timing efficiency as a function of muon angle must be folded into the distribution that describes the decay rate per unit muon angle ($d\Gamma/d\theta_\mu$) in ν_H decays. To simplify the simulation, we assume the heavy neutrino undergoes a 2 body isotropic decay producing a muon and a pion [4] in the final state. Note that the final states (that include a muon) used in Table 7.4 are all 3 body decay modes. We make this 2 body decay assumption to simplify the decay simulation and note that this assumption provides a conservative estimate of the timing efficiency for the 3 body decay. [5] The results indicate an

[4] a pion is the lightest possible hadron

[5] The decay products in a 3 body decay mode have on average smaller angles relative to the parent direction than the 2 body decay products. The timing efficiency is higher for smaller angles.

average timing efficiency, ε_{timing}, of between 20 and 25%. The actual results are folded into the final calculation of the number of expected events used to get the limit result for this model.

P (the final term in Equation 7.1), is a probability of ν_H decay in the detector. Just as in the last chapter, for a single particle P is the product of P_s, the probability that the particle survives from the point of production to the detector (a distance D), and P_d, the probability that the WIMP decays within the detector fiducial volume (with a depth $\Delta = 10$ meters). If the heavy neutrino has energy E, momentum P, mass M, and lifetime τ, the probability of decay in the detector is given by

$$P = P_s \times P_d \tag{7.10}$$

$$= exp\left(\frac{-D}{\gamma\beta c\tau}\right) \times \left[1 - exp\left(\frac{-\Delta}{\gamma\beta c\tau}\right)\right], \tag{7.11}$$

where α and β are the standard relativistic boost parameters ($= E/M$ and P/E respectively). This probability is plotted in Figure 6.6 as a function of lifetime τ for a particle with a fixed energy and momentum.

The lifetime has been predicted by Gronau, Leung and Rosner [51] to be

$$\tau = (4.49 \times 10^{-12}) \left(\frac{M}{1\text{GeV/c}}\right)^{-5.17} |U_{\mu H}|^{-2}. \tag{7.12}$$

The lifetime depends on M (the heavy lepton mass) and $|U_{\mu H}|^2$ (the mixing parameter squared). Figure 7.11 shows the lifetime as a function of mixing parameter squared for 3 ν_H masses. Recall a general result of Chapter 6: the region of lifetime sensitivity for the E733 beamline and detector configuration is in the range from about 10^{-8} to 10^{-5} seconds. [6] Figure 7.11 shows that this lifetime range corresponds to a region in $|U_{\mu H}|^2$ that depends on the ν_H mass: The region of $|U_{\mu H}|^2$ sensitivity for ν_H masses 0.5, 1.1 and 1.7 GeV/c^2 is $10^{-7.6} < |U_{\mu H}|^2$ $10^{-4.5}$, $10^{-6.6} < |U_{\mu H}|^2 < 10^{-3.6}$, and $10^{-4.8} < |U_{\mu H}|^2 < 10^{-1.8}$, respectively.

[6] Figure 6.6 shows that the probability P is maximised in this lifetime range.

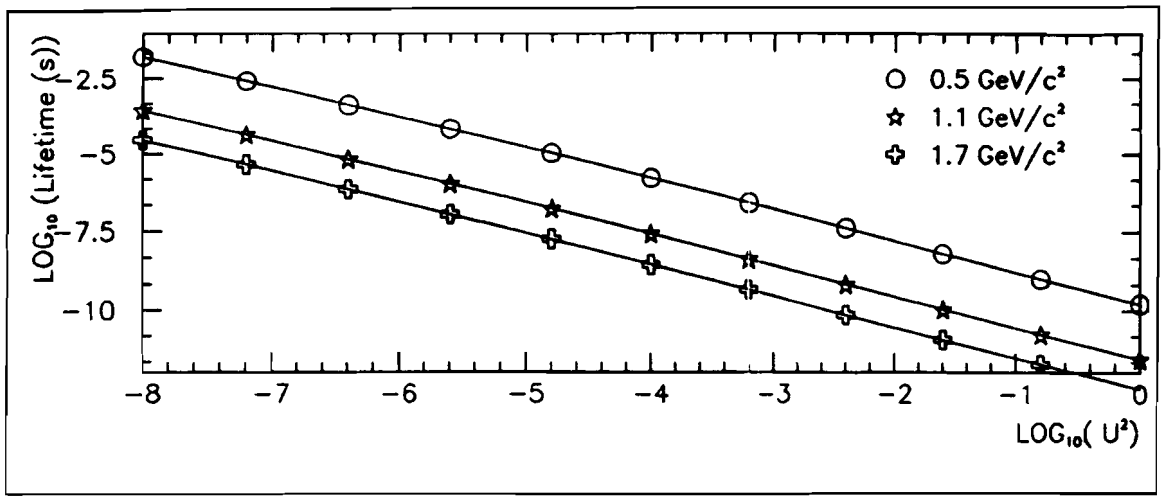

Figure 7.11: The ν_H lifetime as a function of $|U_{\mu H}|^2$ for heavy lepton masses 0.5, 1.1 and 1.7 GeV/c^2 .

The term P depends to a smaller extent on the energy spectrum of the WIMPs. Figure 7.12 shows the probability P as a function of $|U_{\mu H}|^2$ for a ν_H mass = 1.1 GeV/c^2 for two different energies, 10 and 30 GeV/c^2.

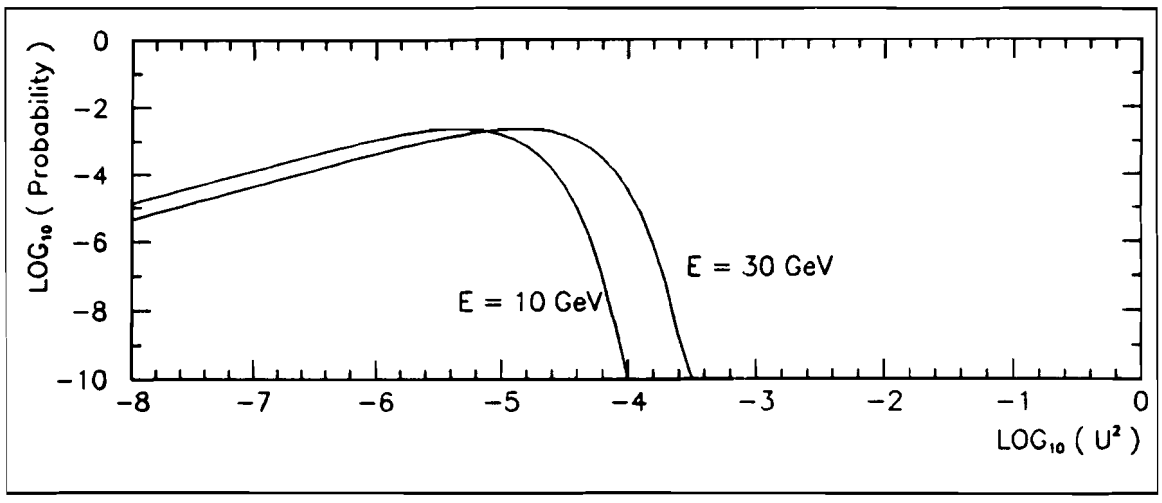

Figure 7.12: Two curves show the probability of decay in the detector as a function of mixing parameter $|U_{\mu H}|^2$ for a heavy lepton with energy 10 and 30 GeV/c^2 , respectively. The hypothetical ν_H was produced from a heavy quark decay at the target (D = 1599 m) with a mass of 1.1 GeV/c^2 .

The shape of the curve in Figure 7.12 combined with the shape of the curve in Figure 7.2 are what dominates the shape of the expected number of events as a

function of $|U_{\mu H}|^2$ for a particular ν_H mass.

Figure 7.13 shows the number of ν_H events expected from each beam source as a function of the mixing parameter $|U_{\mu H}|^2$ for a ν_H mass of 0.9 GeV/c^2 produced via decay of the $D^{\pm}$ meson. These estimates are obtained by calculating the product of all terms in Equation 7.1 for a particular ν_H mass and $|U_{\mu H}|^2$ using the accepted ν_H energy distribution predicted by the simulation described in Section 7.2.2. The uppermost curve indicates the sum of expected events from all beam sources of $D^{\pm}$ assuming an $A^{0.72}$ dependence of the production cross section. The most significant sources of heavy neutrinos are the primary protons on the beam dump and primary target, followed by secondary protons on the beam dump. If a linear $A^{1.0}$ dependence is desired, multiply the contents of each bin by 2.2 or 2.7 for production at the target or dump respectively.

Figure 7.14 is a plot showing the total expected ν_H events from the decay of $D^{\pm}$ mesons from all sources as a function of ν_H mass and mixing parameter squared. The expected linear A dependence of the $D^{\pm}$ production cross section has been factored into this result. Figure 7.13 is one slice of the entire phase space shown in this figure without the A dependence factored in.

Similarly, Figure 7.15 shows the total expected ν_H events from the decay of $D_S^{\pm}$ mesons as a function of ν_H mass and mixing parameter squared. Again, the expected linear A dependence of the production cross section has been factored into this result.

To summarize, the total number of ν_H events expected in the detector over the course of the run is the sum of the product of terms in Equation 7.1 over all beam sources i listed in Table 7.1.

The results of Figures 7.14 (total events from $D^{\pm}$) and 7.15 (total events from $D_S^{\pm}$) can be added to obtain the total number of expected ν_H events as a function of heavy neutrino mass and mixing parameter squared. The regions of ν_H mass versus $|U_{\mu H}|^2$ space with a statistically significant number of events as described in Chapter

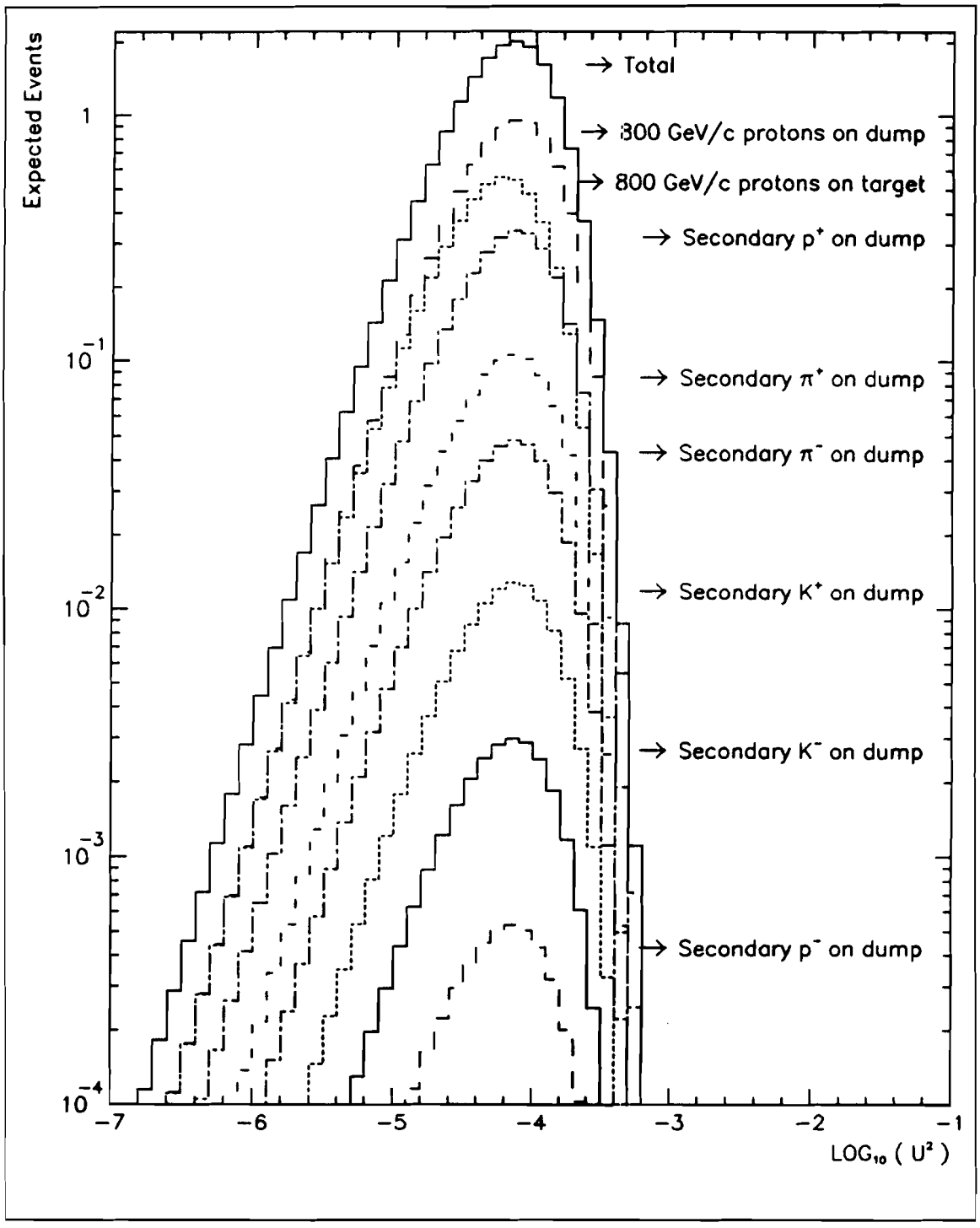

Figure 7.13: For massive neutrinos produced from the decay of the $D^{\pm}$ meson with a mass of 0.9 GeV/c^2 , the expected total number of events (top curve) and the contribution to the total from each beam source (as annotated) is shown as a function of the mixing parameter squared.

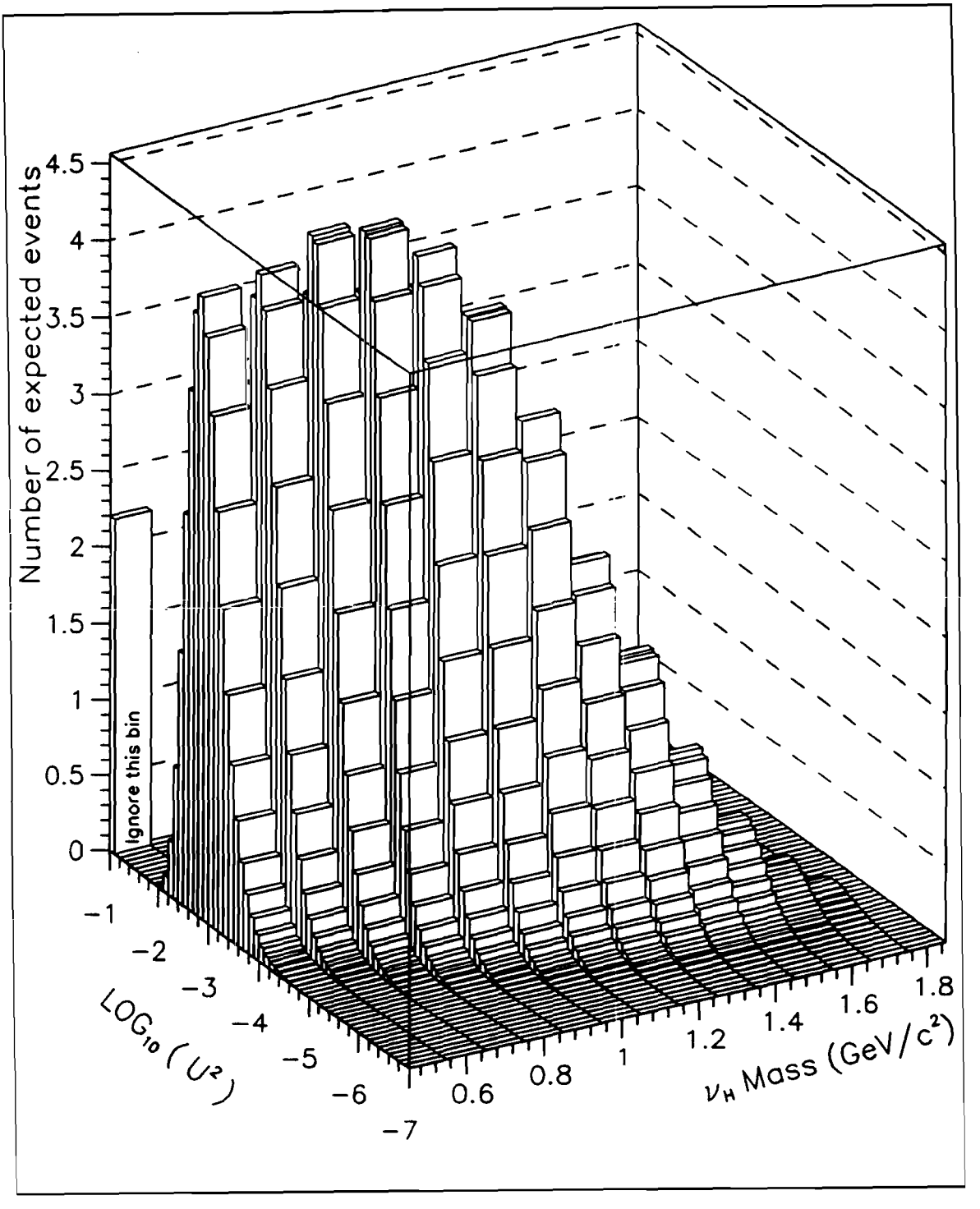

Figure 7.14: Expected ν_H events as a function of heavy neutrino mass and mixing parameter squared from the decay of the $D^{\pm}$ meson.

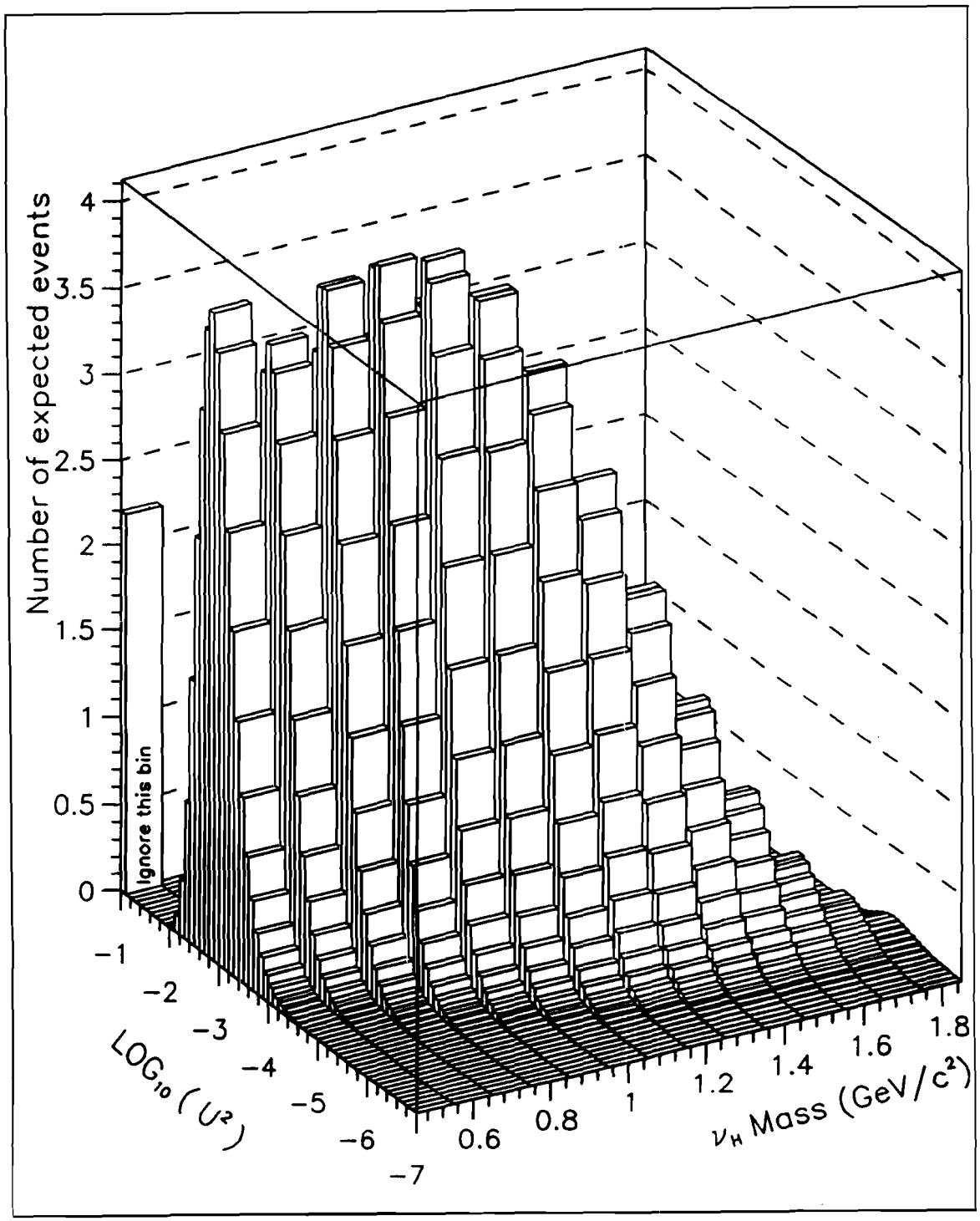

Figure 7.15: Expected ν_H events as a function of heavy neutrino mass and mixing parameter squared from the decay of the $D_S^{\pm}$ meson.

5 can be ruled out: The region excluded at the 90% confidence level (any region with > 2.3 expected events) is shown in Figure 7.16. The current experiment can rule out the existence of massive neutrinos in a region where the mass ranges from 0.5 to 1.4 GeV/c^2 and the coupling strength $|U_{\mu H}|^2$ to $\mu^\pm$ is in the range from 10^{-3} to 10^{-5}.

Figure 7.17 shows the results of the current experiment superimposed on a plot showing the results of other experiments (in Reference [63]) searching for massive neutrinos produced via similar mechanisms. [7]

Summarizing the results of the other experiments:

a) The CHARM collaboration [63] searched for heavy neutrinos in a prompt neutrino beam at CERN. This experiment assumed heavy neutrinos were produced via decay of D mesons produced in a beam dump. They looked specifically for the decays $\nu_H \rightarrow e^+e^-\nu_e$, $\nu_H \rightarrow \mu^-e^+\nu_e$, $\nu_H \rightarrow \mu^+e^-\nu_\mu$, and $\nu_H \rightarrow \mu^+\mu^-\nu_\mu$ (and the corresponding antiparticle processes) in an empty decay region parallel to the CDHS [64] and CHARM [65] neutrino detectors. No events were found that were compatible with any of these specific decay topologies.

b) The CHARM collaboration also searched for massive neutrinos in their wide-band neutrino beam using the CHARM neutrino detector. In this analysis, massive neutrinos were presumed to be produced via the neutrino-nucleon neutral-current interaction $\nu N \rightarrow \nu_i X$ where the ν_H then decays promptly to a muon plus hadrons.

c) At SIN [8] [55], limits on massive neutrino production were obtained by studying the energy spectrum of the μ^+ in $\pi \rightarrow \nu\mu$ decay using a plastic scintillation counter.

[7] The MARK II experiment searches for massive neutrinos in e^+e^- interactions rather than from the decay of hadronic states.

[8] SIN - Schweizerisches Institut für Nuklearforschung

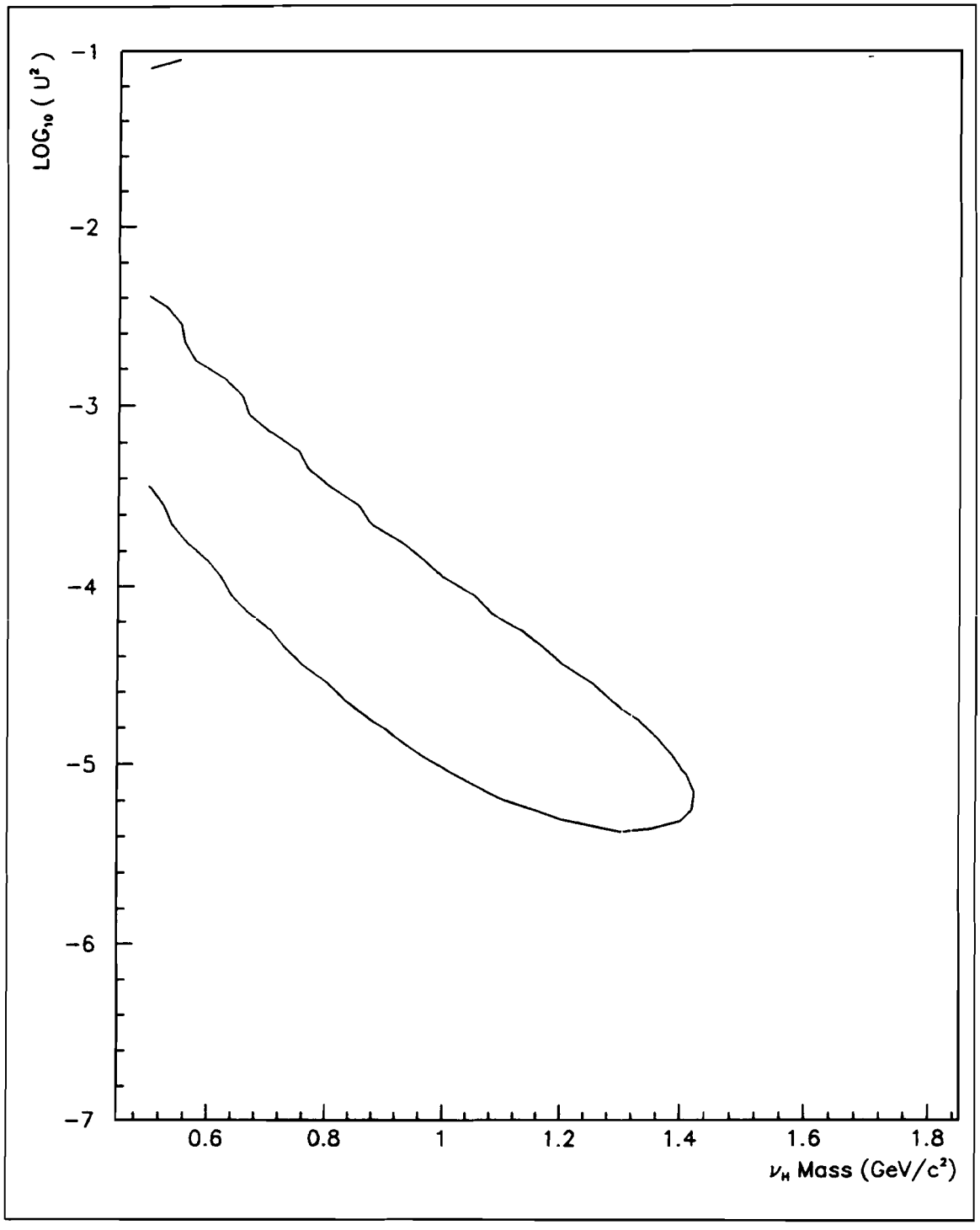

Figure 7.16: The region excluded at the 90% confidence level by the present experiment as a function of heavy neutrino mass and mixing parameter squared.

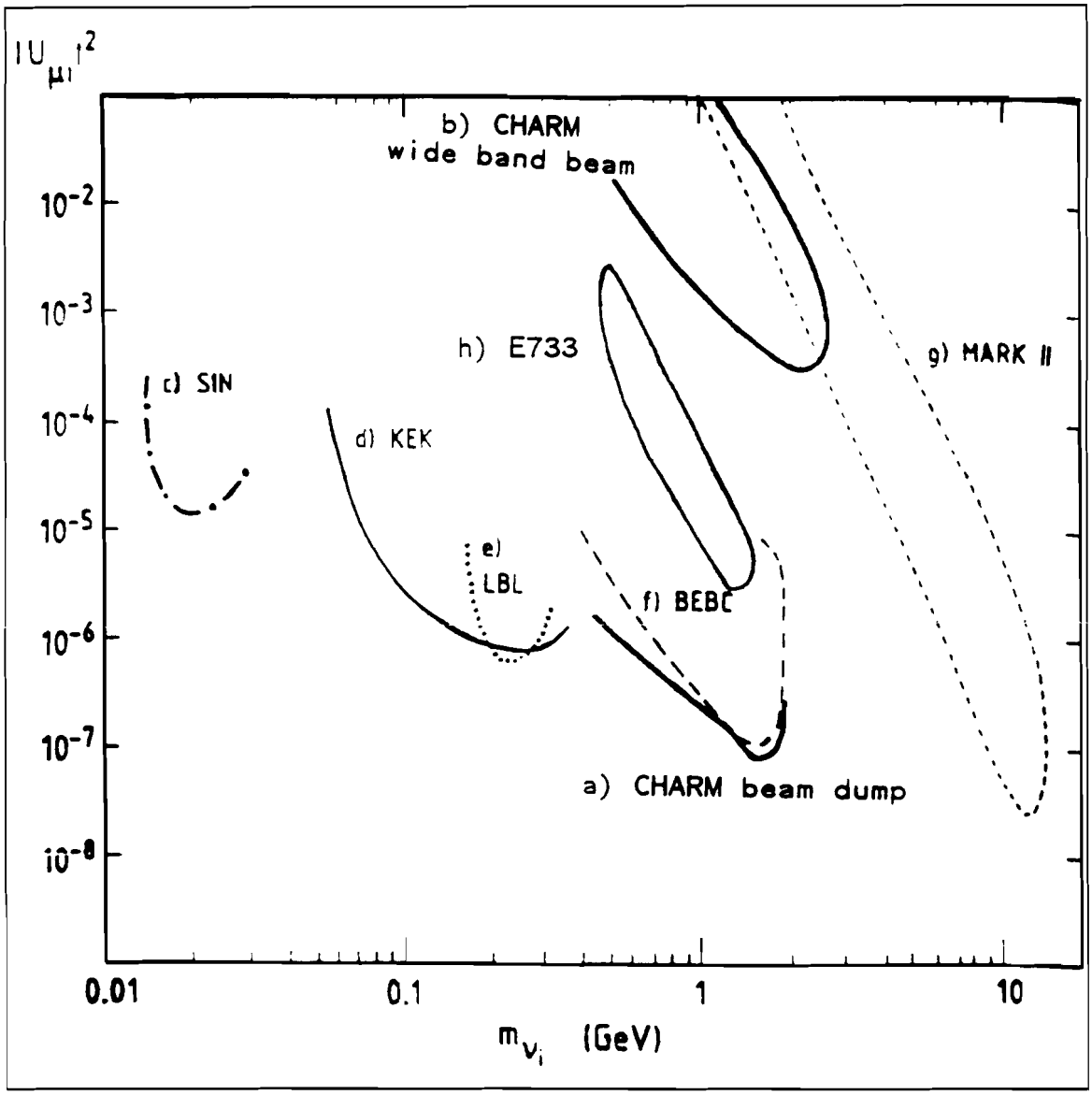

Figure 7.17: Limits at the 90% confidence level on $|U_{\mu H}|^2$ as a function of the neutrino mass: a) limits obtained in the CHARM beam dump experiment; b) limits obtained in the CHARM wide-band neutrino beam; c) limits obtained studying the decay $\pi \to \nu\mu$ at SIN; d) limits from the study of the decay $K \to \nu\mu$ at KEK; e) limits from the study of the decay $K \to \nu\mu\nu^*$ at LBL; f) limits obtained in the BEBC beam dump g) limits obtained from the MARK II experiment

d) An experiment at the KEK [9] Laboratory in Japan [56] was able to set limits on heavy neutrinos by studying the momentum spectrum of muons in the decay $K \rightarrow \nu\mu$.

e) A counter experiment in the LBL [10] Bevatron [57] found no evidence for the decay $K^+ \rightarrow \mu^+\nu\bar{\nu}\nu^*$ and was able to set limits on ν_H as a result.

f) The BEBC [66] beam dump experiment makes the same production assumptions as the CHARM beam dump experiment (described above). They looked specifically for the final states $\mu^-e^+\nu_e$, $\mu^-\mu^+\nu_\mu$, or $\mu^-\pi^+$ consistent kinematically with the decay of a heavy neutrino in a bubble chamber downstream of a proton beam dump Their limit is obtained after a background subtraction.

g) The MARK II [67] experiment found no evidence for heavy neutrinos in looking for secondary vertices consistent with the production of massive neutrinos via the interaction $e^+e^- \rightarrow \nu_i\bar{\nu}_i$.

The BEBC and CHARM beam dump results (curves g) and a) respectively of Figure 7.17) represent their upper limits on the coupling strength $|U_{\mu H}|^2$ as a function of ν_H mass. Therefore, these experiments have ruled out the present experiment's excluded phase space previously. However, it should be emphasized that the method used in the present experiment is completely different from those of the beam dump experiments cited. The integrity of the BEBC results and CHARM beam dump results rely entirely on the pattern recognition and kinematic reconstruction of very specific expected ν_H decay topologies, while the current experiment requires *only* that a muon be present in the final state without regard for other final state particles. Therefore, the present experiment is sensitive to other unanticipated decay

[9] KEK - National Laboratory for High Energy Physics in Oho, Tsukuba-shi, Ibaraki-ken, Japan

[10] LBL - Lawrence Berkeley Laboratory

topologies. Also, since there are no muon class events with an event time outside of the time-of-flight window, no background subtraction is involved in this analysis.

Recent results from LEP have also ruled out such states, unless some mechanism is invoked that suppresses their coupling to the Z^0 boson.

Chapter 8

Supersymmetry

Supersymmetric theories exist which include supersymmetric particles with masses within the kinematic accessibility of the current experiment. Specifically, some regions of the "light gluino window" [68] ($1 < Mass(\tilde{g}) < 5$ GeV/c^2) have not been unambiguously excluded by any experiment to date [15]. In this chapter, we evaluate the sensitivity of the E733 detector to a supersymmetric model that includes low energy gluinos, squarks and photinos. We do not consider the interaction of supersymmetric W, Z and Higgs bosons or supersymmetric leptons.

The processes that lead to a signal in the detector of supersymmetric particle production are as follows:

- Gluinos ($\tilde{g}$) are produced in 800 GeV/c p-N interactions.
- $\tilde{g}$'s decay promptly ($\tau \leq 10^{-12}$ sec) producing massive photinos ($\tilde{\gamma}$) amongst its decay products.
- We assume that the $\tilde{\gamma}$ is the LSP (lightest superpartner) and that R-parity is conserved (the $\tilde{\gamma}$ does not decay). It interacts weakly with matter. It survives traversal of the shielding but interacts in the detector. Because it is massive, it arrives at the detector later than it's respective neutrino bunch.

The number of events expected to be seen in the detector during the course of the run due to supersymmetric particle production is given by

$$E_x = \sum_{beamtypes} (N_{\tilde{g}})\,(BR_{\tilde{g}})\,(\varepsilon)\,(P_{int}). \tag{8.1}$$

The beamtypes considered for SUSY particle production are the primary protons on the primary target and the beam dump. Secondary particles in the beamline are not considered to be significant sources of SUSY particles. Summarizing the terms in the above expression:

- $N_{\tilde{g}}$ represents the total number of $\tilde{g}$'s produced in the beamline from each beamtype.
- $BR_{\tilde{g}}\ (\tilde{g} \rightarrow \tilde{\gamma} + X)$ is the branching ratio for a $\tilde{g}$ to decay to a $\tilde{\gamma}$ inclusively (X indicates any other decay products).
- ε is a product of acceptances and efficiencies as in the last two chapters:

$$\varepsilon = \varepsilon_{geo}\varepsilon_{tof}\varepsilon_{trig}\varepsilon_{timing} \tag{8.2}$$

- P_{int} is the probability that the $\tilde{\gamma}$ survives traversal of the shielding and then interacts in the detector.

The independent parameters of the model are the $\tilde{g}$ mass and the $\tilde{q}$ mass. Other necessary parameters can be inferred from these quantities within the framework of the supersymmetric model.

8.1 Gluino Production and Decay

Gluinos are produced by primary (800 GeV/c) protons on the target or beam dump. Leading order Feynman diagrams for gluino production in *pp* interactions are shown in Figure 8.1. The dominant production mechanism is expected to be gluon fusion

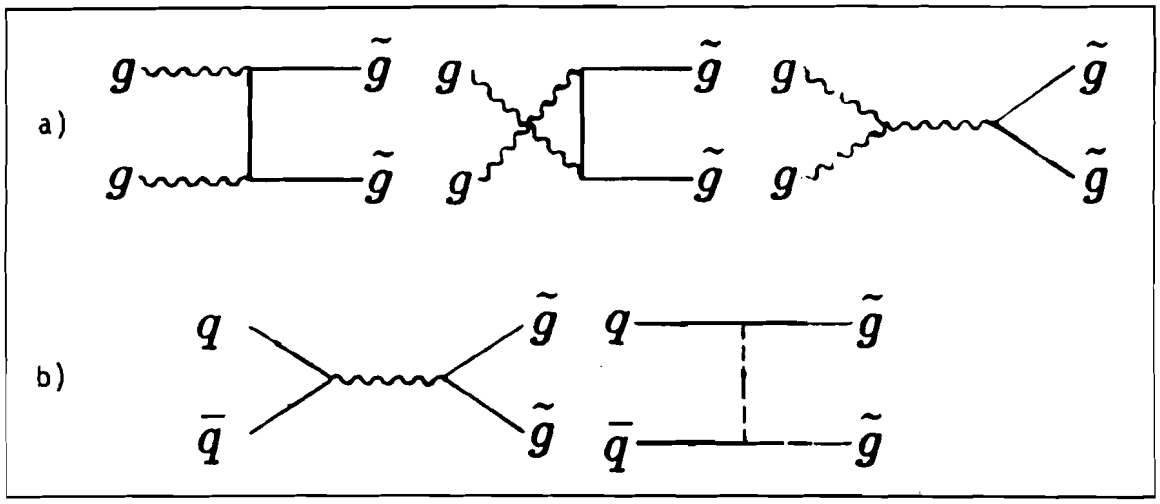

Figure 8.1: The leading order Feynman diagrams for gluino production in pp interactions via a) gluon fusion and b) $q\bar{q}$ annihilations.

(Figure 8.1a)). Drell-Yan (quark-antiquark annihilation) processes (Figure 8.1b)) may also contribute, but at a less significant rate.

In Equation 8.1, the number of gluinos produced, $N_{\tilde{g}}$, with production cross section $\sigma_{\tilde{g}}$ in 800 GeV/c pp interactions, is

$$N^i_{\tilde{g}} = POT \times X^i_{model} \times \frac{\sigma_{\tilde{g}}}{\sigma_{tot}}. \tag{8.3}$$

Just as in Equation 6.2, POT is the number of integrated live protons on target as given in Equation 2.7 and $X^i_{model} = 0.6321$ and 0.3679 at the primary target ($i = 1$) and the beam dump ($i = 2$) respectively. Again, σ_{tot} is the total cross section for 800 GeV/c protons ($40mb$). We assume the atomic weight dependence of the gluino production cross section is the same as that of the total cross section. Then the ratio $\frac{\sigma_{\tilde{g}}}{\sigma_{tot}}$ is the fraction of interacting protons that are expected to produce gluinos.

The $\tilde{g}$ production cross section as a function of $\tilde{g}$ mass for a number of different center-of-mass energies has been estimated [69] as shown in Figure 8.2. For this analysis, the curve indicating $\sqrt{s} = 25$ GeV was utilized [1]. At lower gluino masses, the production cross section is comparable to that of charm production. $\sigma_{\tilde{g}}$ decreases

[1]The analogous curve for $\sqrt{s} = 39$ GeV is not expected to be significantly different based on the position of the curve for $\sqrt{s} = 540$ GeV.

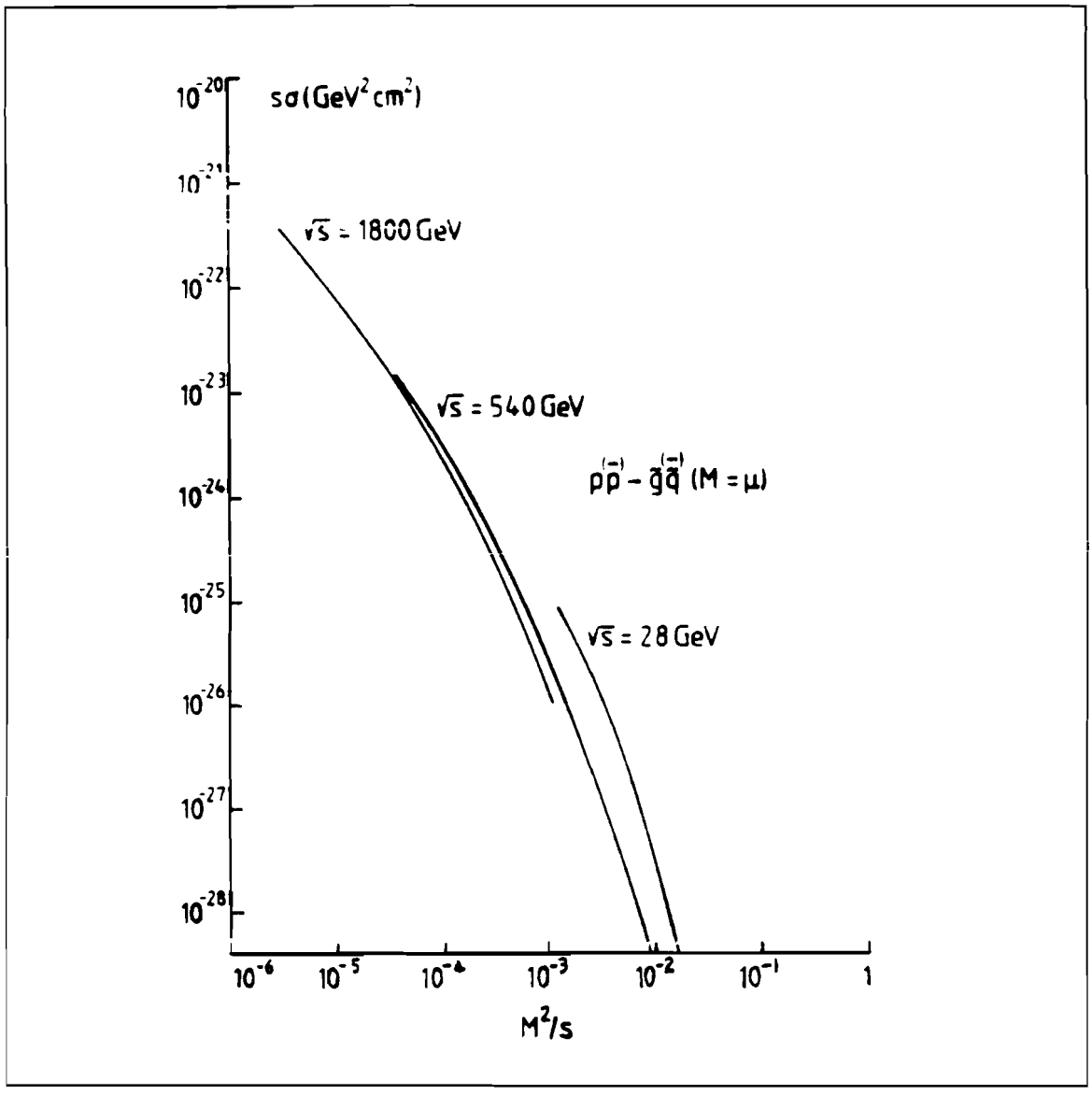

Figure 8.2: The predicted cross section for pp (or $p\bar{p}$) $\rightarrow \tilde{g} + \tilde{q}(\bar{\tilde{q}})$ for a number of center-of-mass energies from P.R.Harrison and C.H.Llewellyn Smith.

drastically as gluino mass increases, falling below $\sigma_{\tilde{g}} = 10^{-8}$ barns for masses greater than 5 GeV/c^2.

The squark mass is expected to be greater than 13.7 GeV/c^2 based on direct squark searches in e^+e^- interactions [70].[2] We assume the squark mass is greater than the gluino mass. As a result, decaying gluinos produce photinos 100% of the time ($BR_{\tilde{g}} = 1.00$ in Equation 8.1) via the decay mode

$$\tilde{g} \rightarrow \tilde{\gamma} + q\bar{q}$$

In the absence of this assumption, additional decay channels open up that are not considered in this analysis.

The $\tilde{g}$ lifetime, estimated by Dawson, Eichten and Quigg [17], is given by

$$\tau = \frac{48\pi M_{\tilde{q}}^4}{\alpha\alpha_s e_q^2 M_{\tilde{g}}^5}, \tag{8.4}$$

where $M_{\tilde{g}}$ and $M_{\tilde{q}}$ are the gluino and squark masses, respectively, and e_q is the quark electric charge. The lifetime is proportional to the squark mass, reflecting the fact that a gluino decay proceeds via squark exchange. The higher the squark mass, the longer the gluino lifetime.

Long lived gluinos ($\tau > 10^{-8}$) may be unconfined or may be bound within charged or neutral hadrons. The current experiment is insensitive to such states because their interaction cross section is expected to be similar to that of Standard Model strongly interacting particles and therefore they would be absorbed in the shielding upstream of the detector. If such neutral states are not strongly interacting, limits for long lived gluinos can be obtained using the results of Chapter 6.

In this chapter, we consider only gluinos with lifetimes shorter than 10^{-13} seconds. So gluinos decay essentially at the point of production before a secondary interaction in the target or dump is probable. Contours indicating lines of constant τ are drawn for reference on the $(M_{\tilde{g}}, M_{\tilde{q}})$ phase space plot at the end of this chapter.

[2]This is their most conservative estimate.

A computer simulation was used to study $\tilde{g}$ production and decay characteristics (described in the remainder of this section) as well as determine acceptances for $\tilde{\gamma}$ detection (described in the next section). Gluino masses up to 11 GeV/c^2 were simulated. Negligible sensitivity to higher mass gluinos is expected due to production cross sections less than 10^{-11} barns.

The differential production cross section for gluinos is parameterized as in a similar analysis [42]:

$$\frac{d^3\sigma}{dp^3} \propto (1 - x_F)^5 \times exp(-3.45\sqrt{p_T^2 + M_{\tilde{g}}^2}). \tag{8.5}$$

$\tilde{g}$'s are expected to produce $\tilde{\gamma}$'s isotropically in the center-of-mass frame. The distribution of $\tilde{\gamma}$ energies in the $\tilde{g}$ rest frame is predicted [71] to be

$$\frac{d\Gamma}{d\xi} \propto \sqrt{\xi^2 - \eta^2}\left[\xi(1 - 4\xi/3) + \eta(1 - 2\xi) - (\frac{2}{3} - \xi)\eta^2 + \eta^3\right], \tag{8.6}$$

where $\xi = E_{\tilde{\gamma}}/M_{\tilde{g}}$ and $\eta = M_{\tilde{\gamma}}/M_{\tilde{g}}$ ($M_{\tilde{\gamma}}$ and $E_{\tilde{\gamma}}$ are the $\tilde{\gamma}$ mass and energy). It is generally assumed that the photino mass is $\approx 1/6$ of the gluino mass based on an argument using the ratio of strong and electromagnetic coupling constants [18].

The photino energy distribution (in the gluino center of mass) produced using Equation 8.6 is shown in Figure 8.3 for a gluino mass of 6 GeV/c^2($M_{\tilde{\gamma}}$ = 1 GeV/c^2). After the boost to the lab frame, $\tilde{\gamma}$'s have, on average, a harder energy spectrum than the conventional ν beam as shown in Figure 8.4. Figure 8.4 a) shows the expected geometrically accepted $\tilde{\gamma}$ energy distribution in the lab frame for three $\tilde{g}$ masses. Figure 8.4 b) shows the expected neutrino energy distribution entering the fiducial volume.

8.2 Acceptance and Efficiency

A computer simulation, using the production and decay assumptions stated in the last section, is used to obtain the photino acceptances and efficiencies and determine

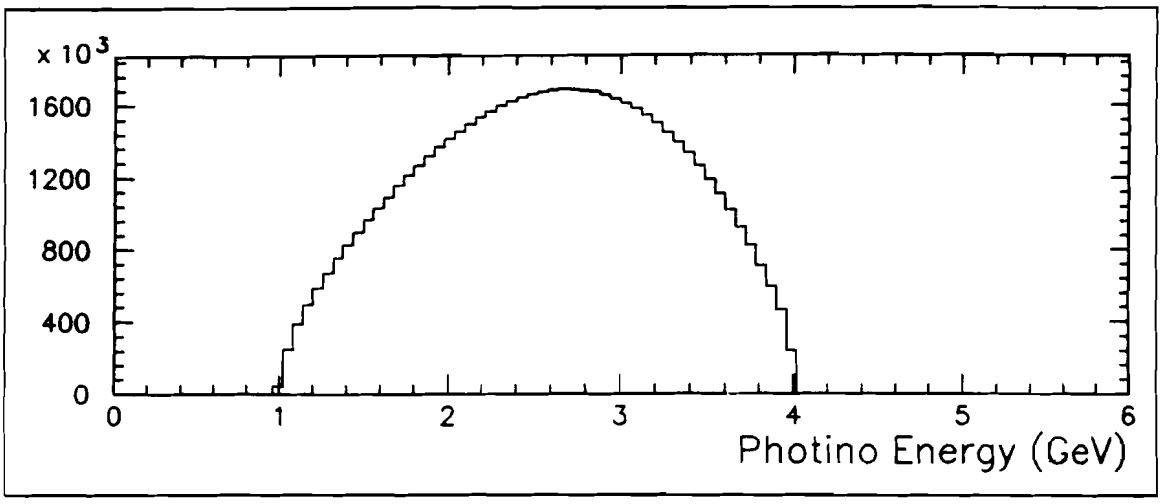

Figure 8.3: The predicted photino energy distribution in the center of mass of the decaying gluino for a gluino mass of 6 GeV/c^2 ($M_{\tilde{\gamma}} = 1$ GeV/c^2).

the energy spectrum of accepted photinos (the spectrum of geometrically accepted photinos is shown in Figure 8.4 a)). The values of all acceptances (geometric, time-of-flight and trigger acceptances) described in this section are listed in Tables E.8 in Appendix E.

The geometric acceptance as a function of gluino mass is shown in Figure 8.5a). The solid and dashed curves indicate the acceptance for gluino production at the target and dump respectively. Geometric acceptance is highest at low mass because lower masses have a smaller average p_T as a result of the mass dependence in the exponent of Equation 8.5. This acceptance does not rise with mass, as it rises with increasing heavy neutrino mass in Chapter 7 because the photino mass is a fixed fraction of the gluino mass. The heavy neutrino mass is allowed to approach the parent mass; as it does so, the neutrino tends to be more aligned with the direction of the parent.

The time-of-flight acceptance as a function of gluino mass is shown in Figure 8.5b). As discussed below, the interaction of photinos in the detector is not expected to produce muons in the final state. Therefore, the final state is classified as neutral current-like and the shower timing TOF search window applies. Note that

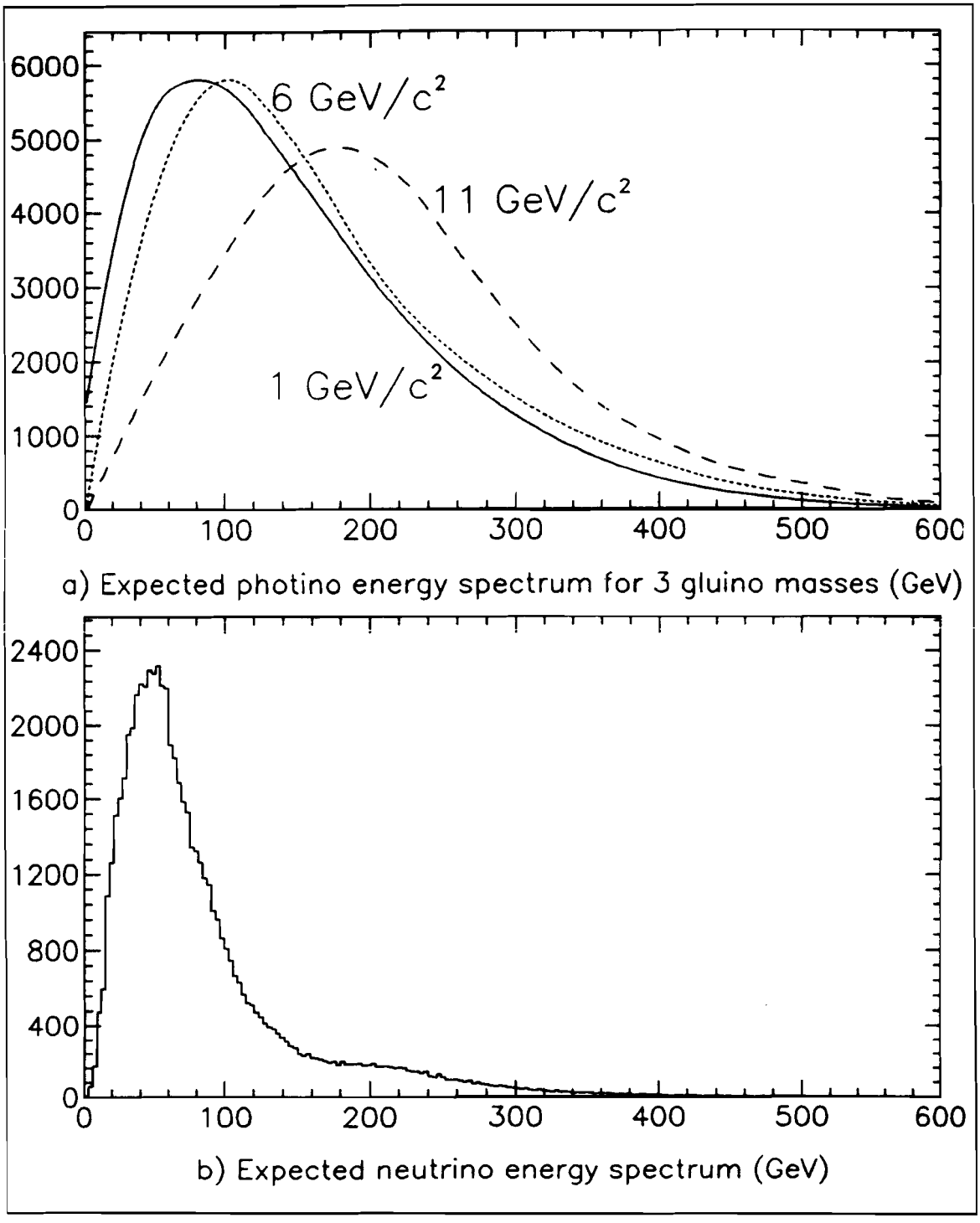

Figure 8.4: Expected energy distributions for geometrically accepted a) photinos and b) neutrinos. Each of the three curves in a) represent the photino spectrum corresponding to gluino masses of 1, 6, and 11 GeV/c² ($M_{\tilde{\gamma}} = M_{\tilde{g}}$).

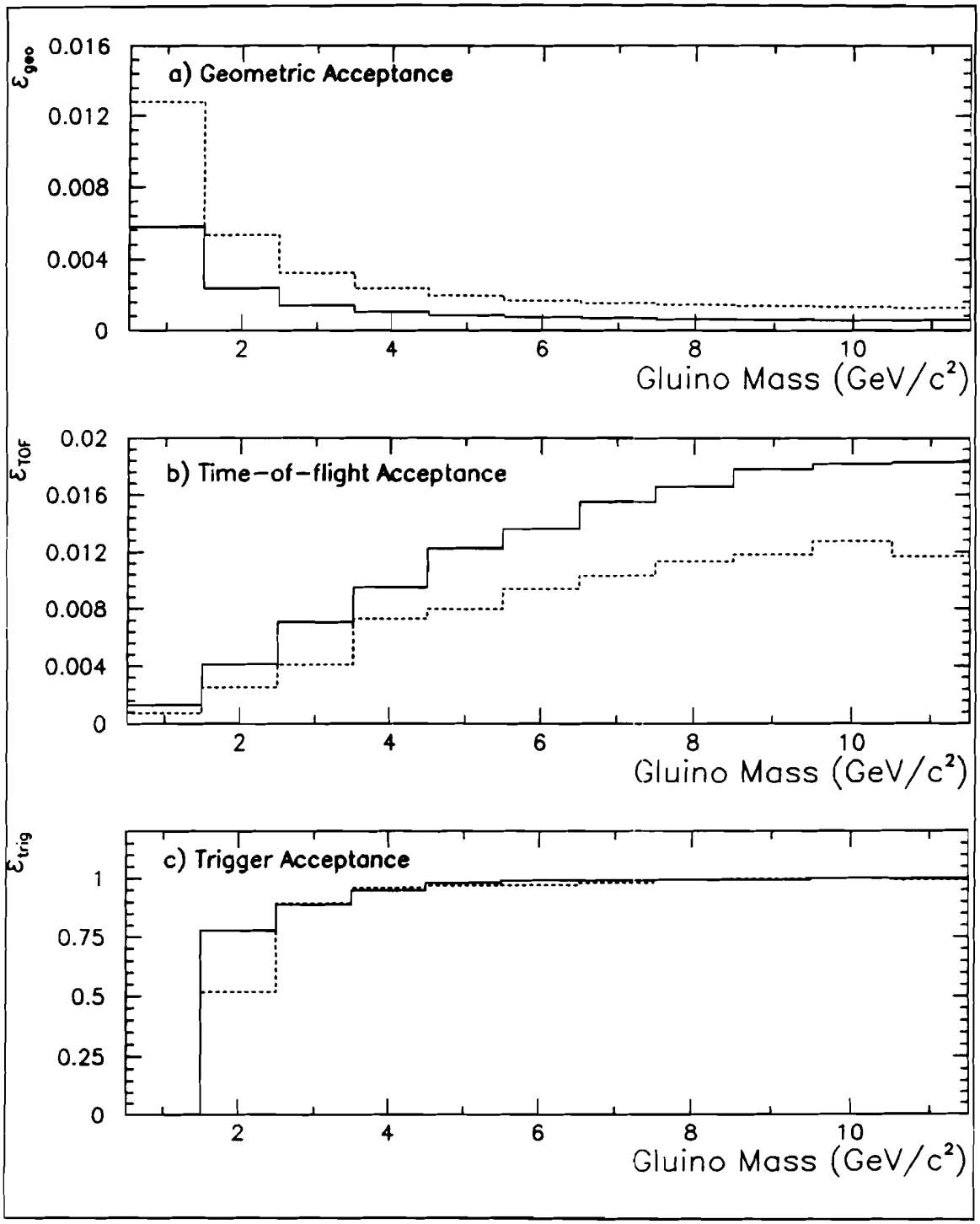

Figure 8.5: The a) geometric b) time-of-flight and c) trigger acceptance as a function of gluino mass for production at the primary target (solid line) and beam dump (dashed line).

photinos produced from gluinos (with $1 < M_{\tilde{g}} < 11$ GeV/c^2) all have masses less than 2 GeV/c^2, and as a result, time-of-flight acceptances for these photinos is low overall. This is due to the low maximum energy cutoff for low masses described in Chapter 6.

The trigger acceptance, plotted as a function of gluino mass in Figure 8.5c), is the fraction of geometrically and time-of-flight accepted particles that have at least 5 GeV/c^2 of energy to deposit in the detector. Due to the time-of-flight acceptance, very low mass photinos have a low maximum energy cutoff that may be close to or below the trigger threshold. Therefore, the trigger acceptance is zero for a gluino mass of 1 GeV/c^2, but it rises rapidly to nearly 1.0 for masses above 4 GeV/c^2.

The overall acceptance (product of $\varepsilon_{geo}\varepsilon_{TOF}\varepsilon_{trig}$ in Equation 8.2) as a function of gluino mass is shown in Figure 8.6. The acceptance is relatively flat for gluino

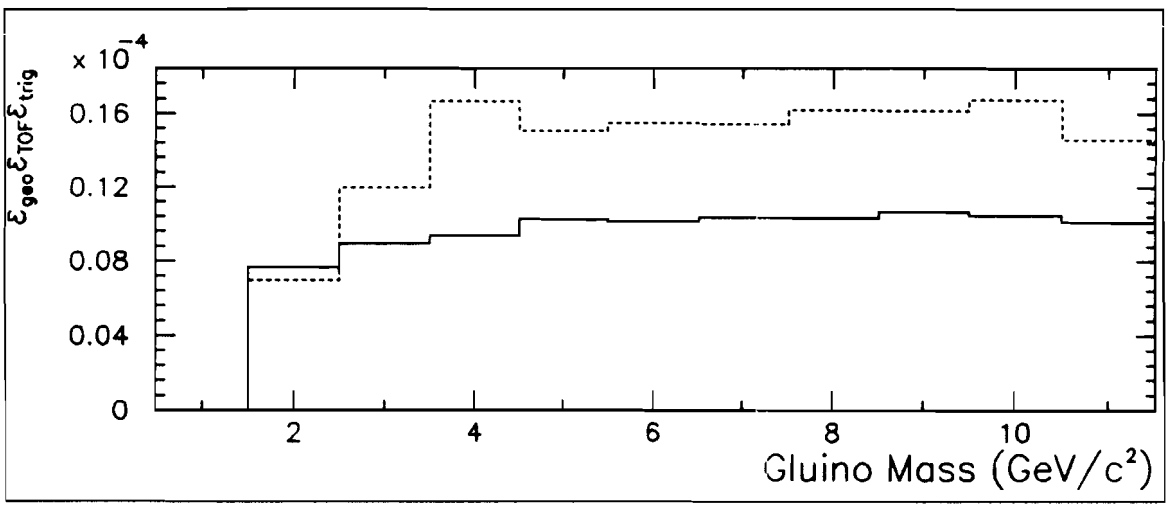

Figure 8.6: The overall acceptance (the combined geometric, time-of-flight and trigger acceptance) as a function of gluino mass for production at the primary target (solid line) and beam dump (dashed line).

masses from 2 to 11 GeV/c^2 (around 0.000010 and 0.000015 for production at the target and beam dump, respectively as listed in Table E.8).

Figure 8.7 shows the leading order Feynman diagrams for a photino interacting with quarks and gluons in normal matter. Figure 8.7 a) demonstrates photino inter-

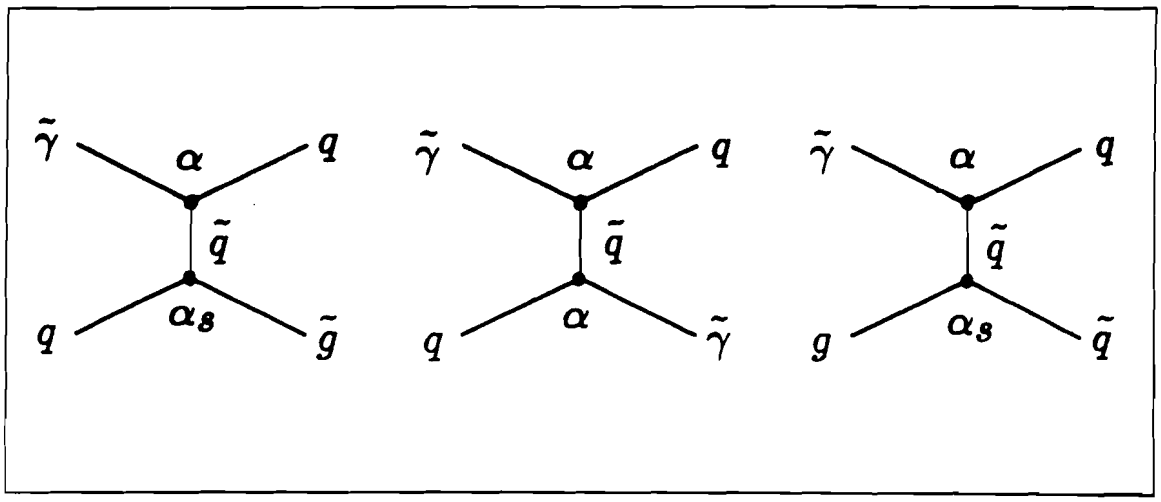

Figure 8.7: Feynman diagrams for photino interaction in normal matter.

action proceeding via inverse gluino decay, expected to be the dominant interaction process. The electromagnetic scattering process of Figure 8.7 b) $\tilde{\gamma} + q \rightarrow \tilde{\gamma} + q$ is also possible, but the cross section is two orders of magnitude smaller (amplitude of this process is proportional to α^2 rather than $\alpha\alpha_S$ as in Figures 8.7 a) and c)). The process in Figure 8.7 c) is restricted by phase space because the on-shell squark mass is expected to be higher than 15 GeV/c^2.

Assuming the gluino decay diagram of Figure 8.7 a) dominates, the final state develops in the detector as follows :

$$\begin{array}{ccccc} \tilde{\gamma} + q & \longrightarrow & \tilde{g} & + q & \\ & & \downarrow & & \\ & & \tilde{g} & \rightarrow \tilde{\gamma} & + q\bar{q} \end{array}$$

From assumptions made previously, the gluino produced in the photino interaction decays promptly to a photino and two additional quarks. Therefore the final state photino interaction contains three quark jets and one photino which escapes the detector. This photino is not expected to carry with it a large fraction of the initial photino energy. Therefore, when a $\tilde{\gamma}$ interacts in the detector, we assume it deposits

all of its energy therein.

The timing efficiency, the last term in Equation 8.2, is the fraction of events seen that are expected to have a reliable event time measurement. For neutral current-like events, the timing efficiency depends on the final state energy as shown in Figure 5.27. Time-of-flight accepted particles are those with low energy (10 – 50 GeV) where the timing efficiency varies from about 13 to 43%. The energy dependence (of Figure 5.27) is folded into the final limit result.

8.3 Photino Interactions in the Detector

The last term in Equation 8.1 is P_{int}, the probability that an accepted photino will interact in the detector. As seen previously, it is the product of two terms:

$$P_{int} = P_s \times P_i \tag{8.7}$$

$$= exp(-\sigma N_{dump}) \times [1 - exp(-\sigma N_{det})]. \tag{8.8}$$

P_s is the probability that the photino survives from the point of production to the detector (traverses the shielding) [3]. P_i is the probability that the WIMP interacts within the fiducial volume [4]. Both terms depend on the interaction cross section σ.

The $\tilde{\gamma}$ interaction cross section, corresponding to the diagram of Figure 8.7 a), is parameterized as in a similar analysis [72]:

$$\sigma = \frac{32}{9}\left(\frac{\pi\alpha\alpha_s}{M_{\tilde{q}}^4}\right) s \int \sum_{i=quarks} Q_i^2 \left(1 - \frac{M_{\tilde{g}}^2}{xs}\right)^2 \left(1 + \frac{1}{8}\frac{M_{\tilde{g}}^2}{xs}\right) x q_i(x) dx, \tag{8.9}$$

where s is the $\tilde{\gamma}p$ center-of-mass energy squared. The sum is over all quarks and antiquarks found in the target nuclei with fractional electric charge Q_i and quark distribution function $q_i(x)$.

The variable of integration, x, is the the scaling variable *Bjorken x*, the fractional momentum carried away by the inclusively observed particle. It varies from 0 to

[3]The shielding contains $N_{dump} = 5.0 \times 10^{29}$ target nucleons $/cm^2$

[4]There are $N_{det} = 8.1 \times 10^{26}$ target nucleons $/cm^2$ within the detector fiducial volume.

1. Standard (HMRS) quark distribution functions [73] were used to calculate the integral numerically [5].

Equation 8.9 includes a gluino mass threshold term $(1 - \frac{M_{\tilde{g}}^2}{xs})$, reflecting the requirement that an interacting photino must have enough energy to produce an on-shell gluino in the final state. Plotted in Figure 8.8 is effectively [6] the minimum photino energy required to produce a gluino as a function of gluino mass. This mini-

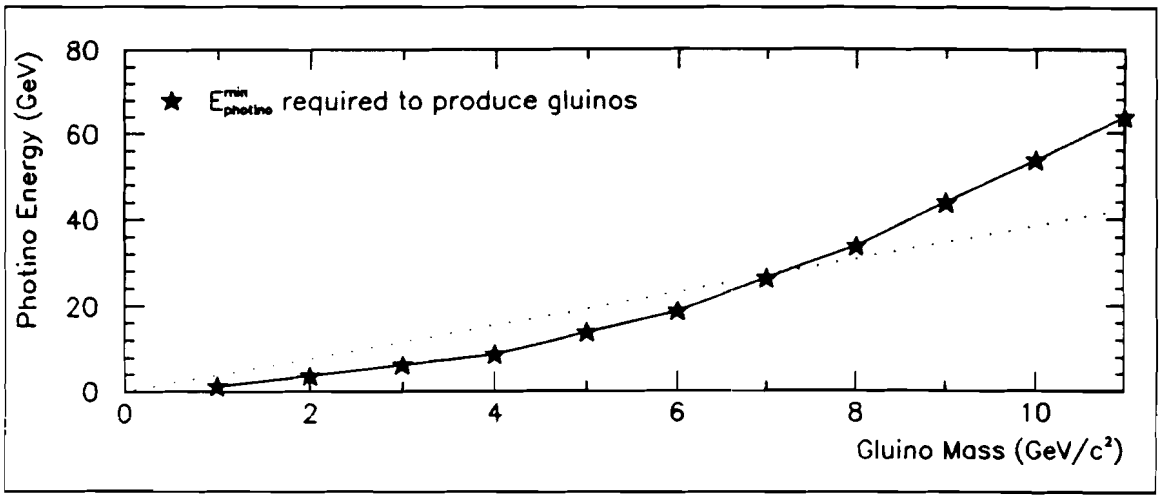

Figure 8.8: The minimum photino energy required to produce a gluino as a function of the gluino mass (solid curve). Also shown is the maximum energy for time-of-flight acceptance for production at the primary target (dotted line).

mum energy required is higher than the minimum energy required by the trigger for gluino masses larger than 2 GeV/c^2. Overlaid on this plot is the maximum energy that a photino can have such that it is time-of-flight accepted within the shower timing search window for production at the primary target.

These curves cross at $M_{\tilde{g}} \approx 7$ GeV/c^2. Therefore events in the detector due to gluinos with masses higher than 7 GeV/c^2 would not occur in the TOF search window. For gluino masses less than 7 GeV/c^2, photino interactions occurring in the detector in the TOF search window have an energy in the narrow region between the two curves.

[5] An average Q^2 (momentum transfer squared) of 15(GeV/c)^2 was assumed.
[6] The minimum energy plotted is the energy at which $\sigma M_{\tilde{g}}^4$ rises above $10^{-42} cm^2$.

After the integration and summation are carried through, the cross section of Equation 8.9 is found to be dependent on the $\tilde{\gamma}$ energy in addition to the squark and gluino masses. Figure 8.9a) shows how the cross section varies with photino energy for a squark mass of 1 GeV/c^2 and 3 different photino (gluino) masses: The solid, dotted and dashed curves correspond to $M_{\tilde{g}} = 1, 6$ and 11 GeV/c^2 respectively ($M_{\tilde{\gamma}} = M_{\tilde{g}}/6$). Figures 8.9 b) and 8.9 c) are the same curves for $M_{\tilde{q}} = 10$ and 100 GeV/c^2 respectively. We see that the interaction cross section:

- can vary by orders of magnitude in the low energy region where time-of-flight acceptance is nonzero,

- but asymptotically approaches a constant at high energies.

The expected geometrically accepted photino energy spectrum ranges from a few GeV to hundreds of GeV as shown in Figure 8.4 a). Although the time-of-flight acceptance is zero in the high energy region, high energy photinos with cross sections in the appropriate range would be recorded with event times consistent with that of a normal neutrino event, contaminating the neutrino neutral current event sample. The regions of phase space where this is probable at a measurable level are shown in the next section.

In summary, there are a number of factors that limit the sensitivity of the present experiment to this particular model of supersymmetric particle production. The various minimum and maximum energy thresholds as well as the energy dependence of the timing efficiency and the cross section are folded into the final limit result. The following section reviews the results of other experiments sensitive to supersymmetric particles in the light gluino window and summarizes the final results of this analysis.

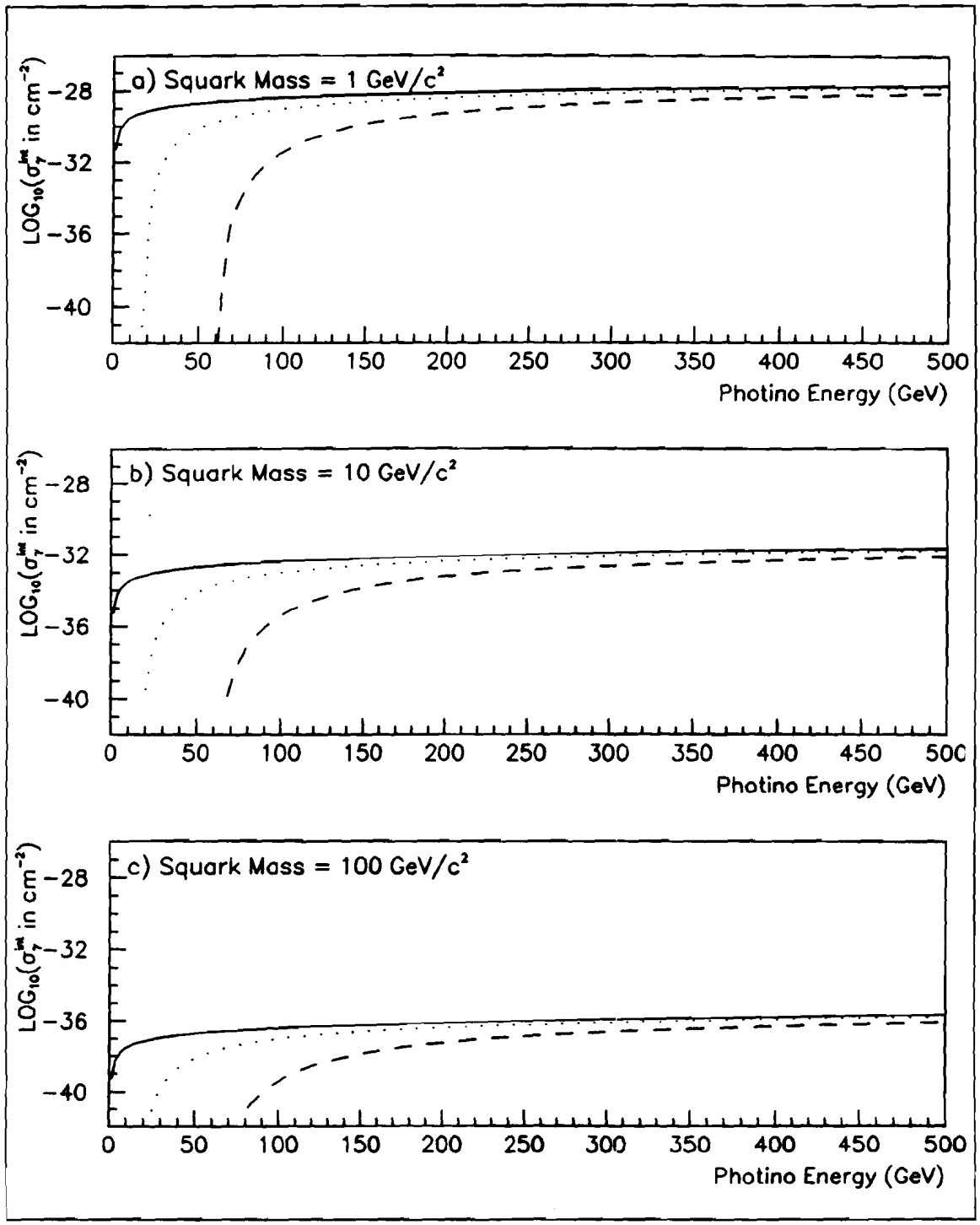

Figure 8.9: For $M_{\tilde{q}}$ of a) 1, b) 10 and c) 100 GeV/c^2 , the photino interaction cross section as a function of photino energy for three photino (gluino) masses (solid, dotted and dashed curves correspond to $M_{\tilde{g}} = 1, 6$ and 11 GeV/c^2 respectively).

8.4 Results

Figure 8.10, adapted from reference [74], shows the regions of the light gluino window excluded at the 90% confidence level by a number of experiments. The two curves extending roughly from the lower left to the upper right corner of the plot indicate lines of constant gluino lifetime of 10^{-8} and 10^{-10} s for reference. They separate experiments searching for gluinos in the stable and unstable gluino regions. The methods used by the various experiments vary widely. They are summarized below.

SPS [7] Long lived gluinos may be unconfined or may be bound within charged or neutral hadrons. If gluinos are combined with quark antiquark pairs to form hadrons, the MIT-bag model suggests [75] that the hadron mass should approach that of the gluino mass if the gluino is massive. A number of different experiments, referred to collectively as Stable Particle Searches (SPS), have excluded charged [76, 77] and neutral [21] states with lifetimes longer than 10^{-8} seconds using time-of-flight techniques.

HELIOS [8] The HELIOS experiment searched for evidence of SUSY production in 450 GeV proton nucleus interactions [78]. The 4π calorimeter utilized makes it possible to measure the missing energy in events. Such missing energy is used as a signature of long lived gluinos escaping the detector. This method does not rely on either the photino interaction cross section, or the gluino decay characteristics, but it does assume that gluino is only weakly interacting. Antoniadis et al. [74] have interpreted the HELIOS result to exclude the entire region indicated by I in Figure 8.10.

[7] Stable Particle Searches
[8] High Energy Lepton and Ion Spectrometer

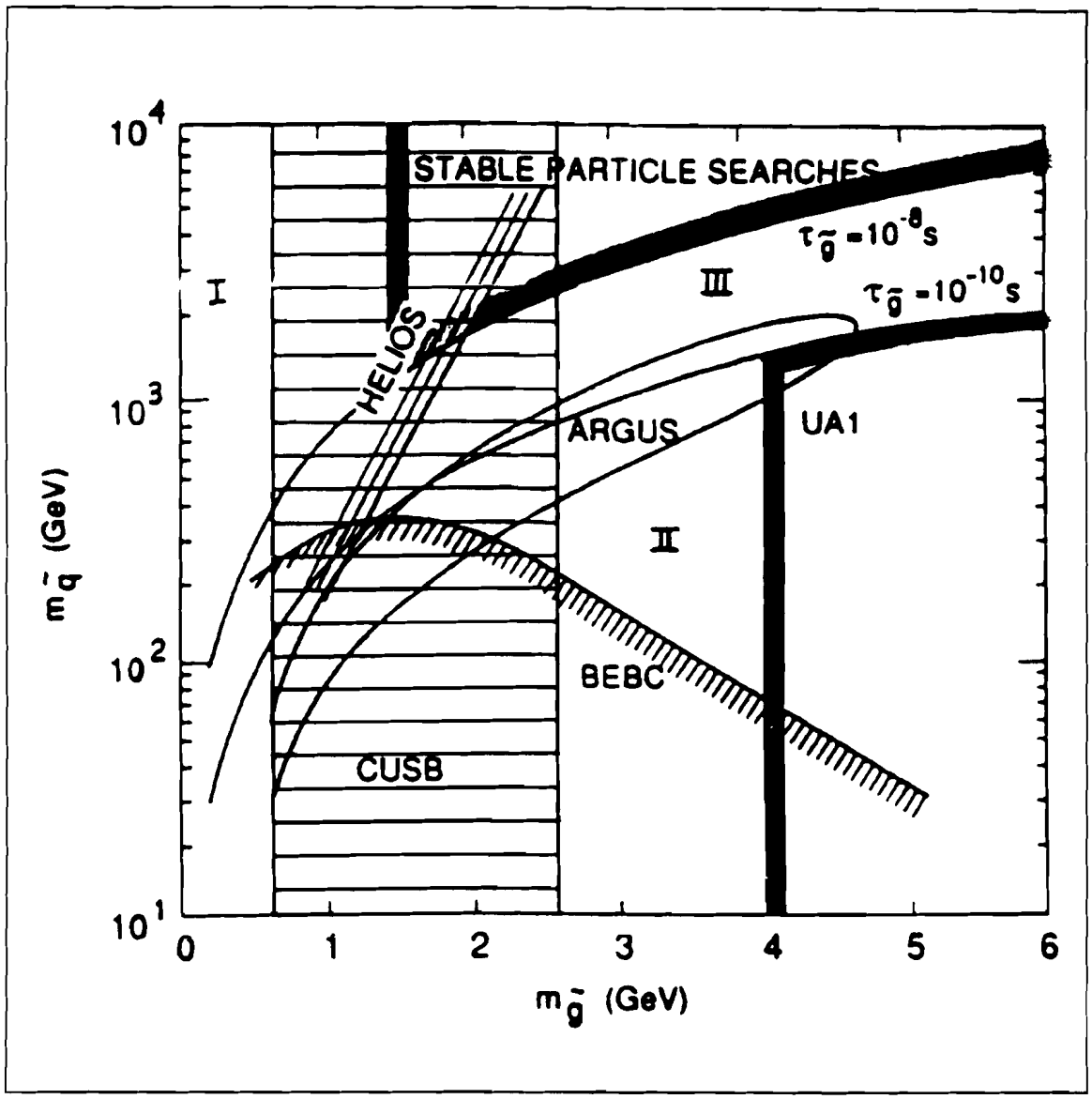

Figure 8.10: Regions of the light gluino window excluded by other experiments at the 90% confidence level adapted from Antoniadis et al.

CUSB [9] Bound $\tilde{g}\tilde{g}$ states are expected to have properties similar to Υ and J/ψ mesons, and therefore might appear in radiative decays of the excited states of these vector mesons. Using the CUSB electromagnetic calorimeter in a run of CESR [10] operating at the $\Upsilon(9460)$ peak, 400,000 radiative decays of the $\Upsilon(9460)$ were studied. No evidence of gluino production was found [79].

ARGUS Using the ARGUS detector at the DORIS II e^+e^- storage ring, $\chi_b(1^3P_1)$ mesons are expected to decay to gluinos if the gluino mass is less than 5 GeV/c^2. In the absence of secondary vertices consistent with the decay of gluinos to a photino and quarks, the ARGUS collaboration [80] sets limits on gluino production for intermediate gluino lifetimes ($10^{-11} < \tau_{\tilde{g}} < 10^{-9}$ seconds).

BEBC This experiment [42] looked for an excess of neutral current-type neutrino events in a large bubble chamber sitting downstream of a proton beam dump. Candidate photino induced events (events having no identified final state charged lepton) are distinguishable from neutrino neutral current events because:

- photinos are expected to have, on average, a harder energy spectrum than neutrinos and
- photino induced events are expected to have less missing transverse energy (and p_T) than a neutrino neutral current event.

Other beam dump experiments, such as E613 [81] at Fermilab and CHARM [72] at CERN, use a similar method to exclude a similar region of the light gluino phase space.

[9] CUSB - Columbia University and SUNY at Stony Brook
[10] CESR - Cornell Electron Storage Ring

Similar limits were also set by an experiment looking for gluino decays in nuclear emulsion [82], a technique independent of the photino cross section.

UA1 The UA1 limit [83] was obtained by searching for events with four quark jets with large missing transverse energy (but no high energy charged lepton) in proton-antiproton collisions. Sensitivity decreases for $M_{\tilde{g}} < 4$ GeV/c^2 because as photino masses become lighter, missing E_t becomes smaller such that events appear indistinguishable from Standard Model quark jets. Long lived gluinos ($\tau > 10^{-10}$ s) escape the apparatus undetected. The UA1 group also sets a limit of $M_{\tilde{q}} > 45$ GeV/c^2 independent of the gluino mass.

Shown in Figure 8.11 is the previous figure expanded to show the region of phase space in which the E733 detector is sensitive. At the outset, it should be emphasized that by expanding this phase space to include squark masses less than 10 GeV/c^2, we have violated our initial assumptions, namely that the squark mass is greater than the gluino mass. In this region of low squark mass, other decay modes open up which we have not considered.

In other words, we have taken the model into a region of phase space in which it was not intended. The purpose of this exercise is merely to make a point about how the various production and acceptance energy requirements, along with an extreme variation in interaction cross section with energy have conspired to cause insensitivity to this particular type of production in the time-of-flight search window.

Recall three previous results:

1. From Figure 8.8, no events are expected in the detector in the TOF search window if the gluino has a mass higher than 7 GeV/c^2.

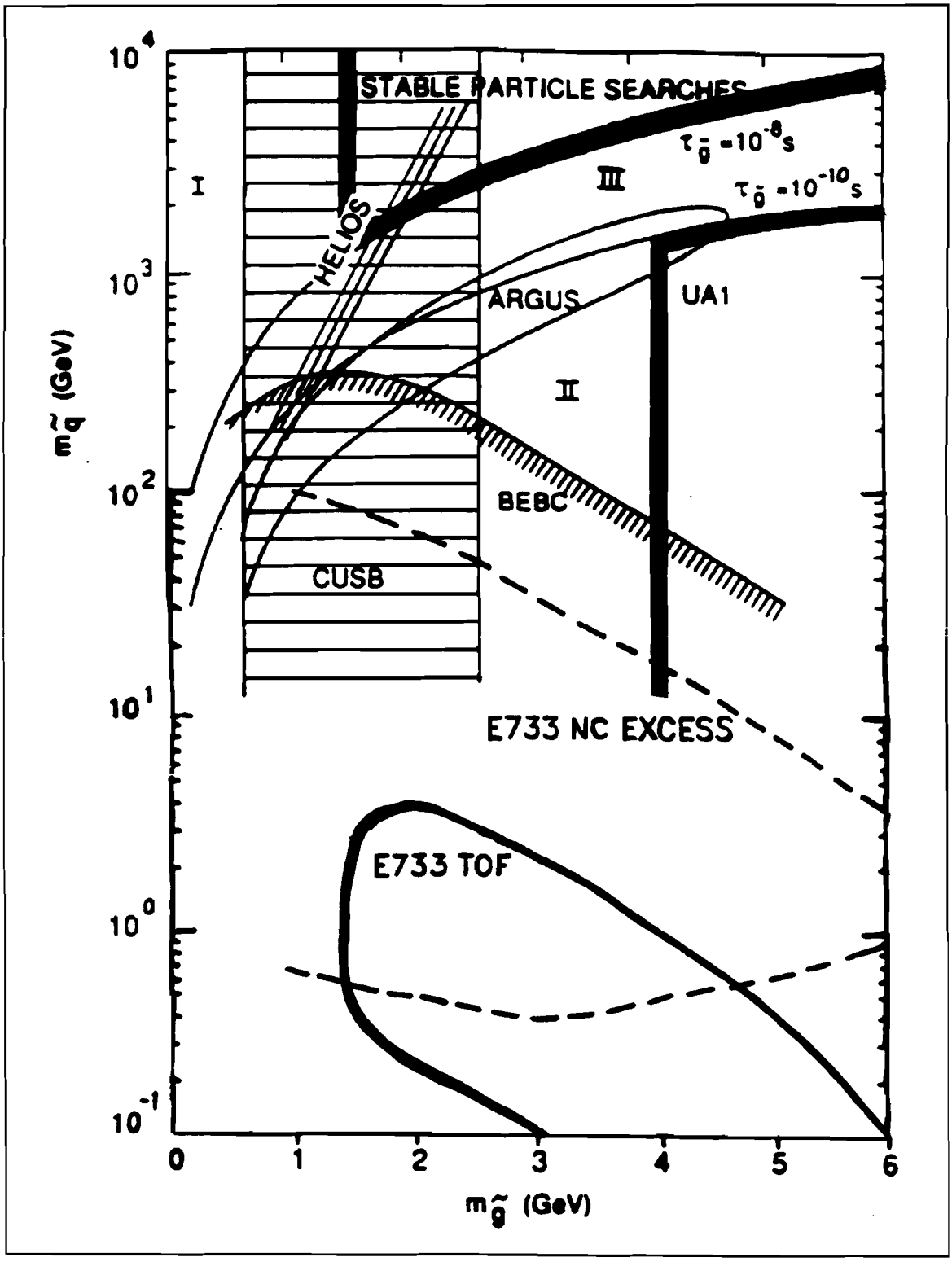

Figure 8.11: The previous figure, adapted from Antoniadis et al., is expanded here to show the region of sensitivity of the present experiment.

2. For gluino masses lower than 7 GeV/c^2, the time-of-flight acceptance requires photinos in a low energy range (5 – 30 GeV/c^2)

3. A general result of Chapter 6: the E733 detector is most sensitive to particles with an interaction cross section in the range from 10^{-31} to $10^{-29} cm^2$.

Looking at Figure 8.9, we see that for low energy photinos, the interaction cross section is in the $10^{-30} cm^2$ range only when the squark mass is very low. Therefore, the region of sensitivity is for gluino masses between 2 and 7 GeV/c^2 and very low squark mass: The solid curve, labeled ''E733 TOF'', indicates the region of phase space in which a statistically significant number of events (≥ 3.5) is expected in the shower timing TOF search window.

Geometrically accepted photinos are predicted to have energies up to a few hundred GeV. Though only low energy photinos are time-of-flight accepted, high energy photino interactions may also occur in the detector, contaminating the neutrino neutral current event sample. At high energy, photinos have an interaction cross section within a few orders of magnitude of $10^{-30} cm^2$ over a wide range in energy for squark masses between 1.0 and 20 GeV/c^2. The frequency of expected high energy photino interactions as a function of squark and gluino mass has been calculated via computer simulation. The dashed curve, denoted ''E733 NC EXCESS'' indicates the region of phase space where the total number of expected events (inside *and* outside of the TOF search window) is expected to exceed 3% of the total neutrino neutral current event sample [11]. The beam dump experiments mentioned above use such an excess combined with an additional analysis of event topology, to exclude the region denoted by BEBC in Figure 8.10.

[11] Three percent of 31,000 NC events is 930 events. A 3% increase in the NC event sample would result in roughly a 3% change in R_ν, where $R_\nu = \sigma^{NC}(\nu N)/\sigma^{CC}(\nu N)$. The measured value of R_ν in the present experiment [32] is 0.3075$\pm$.0041 (statistical) $\pm$0.0043 (systematic) above 10 GeV, which is within 1% of the value measured in comparable deep inelastic scattering experiments [84, 85]. The uncertainties added in quadrature are less than 2% of the measured value.

The E733 NC EXCESS contour is by no means an attempt to set a limit using this method. Rather it is simply to emphasize that when all factors are considered, unexpected manifestations of the model being considered can arise that turn out to be more significant than originally anticipated.

8.5 Conclusions

We have attempted to set limits on low energy supersymmetric particle production. No statistically significant improvement in comparison to existing results was obtained using the time-of-flight method.

CONCLUSION

The combination of the high luminosity typical in high energy neutrino production beamlines, the minimum bias trigger configuration and the event timing ability of the FMMF detector make the present experiment uniquely sensitive to neutral massive particles with lifetimes longer than 10^{-8} s and interaction cross sections less than 10^{-29} $cm^2/nucleon$.

The present experiment excludes (at the 90% confidence level)

- heavy neutrinos ν_H (produced from the decay of heavy quark states) which decay to a final state that includes a muon with
  - mixing strength $|U_{\mu H}|^2$ between 10^{-3} and 10^{-5} and
  - ν_H mass between 0.5 and 1.2 GeV/c^2,
- noninteracting unstable objects produced directly in 800 GeV/c pN interactions with
  - mass between 1 and 20 GeV/c^2,
  - mean lifetime between 10^{-8} to 10^{-4} seconds and
  - production cross section greater than a few picobarns/nucleon,
- stable weakly interacting objects produced directly in 800 GeV/c pN interactions with
  - mass between 1 and 20 GeV/c^2,
  - interaction cross section between 10^{-29} and 10^{-31} $cm^2/nucleon$ and
  - production cross section greater than a few picobarns/nucleon.

Appendix A

The FMMF Collaboration

Tevatron Wide Band Neutrino Experiment E733

M.Abolins, R.Brock, W.G.Cobau[1], E.Gallas, R.W.Hatcher, D.Owen, G.J.Perkins, M.Tartaglia[2], and H.Weerts
Michigan State University
East Lansing, Michigan

D.Bogert, S.Fuess, G.Koizumi, and L.Stutte
Fermi National Accelerator Laboratory
Batavia, Illinois

J.I.Friedman, H.W.Kendall, V.Kistiakowsky, T.Lyons, L.S.Osborne, R.Pitt, L.Rosenson, U.Schneekloth, B.Strongin, F.E.Taylor, and R.Verdier
Massachusetts Institute of Technology
Cambridge, Massachusetts

J.K.Walker, A.White[3], and W.J.Womersley[4]
University of Florida
Gainsville, Florida

[1] University of Maryland
[2] Fermi National Accelerator Laboratory
[3] University of Texas at Arlington
[4] SSC Laboratory

Appendix B

Time of Flight Calculation

The time-of-flight t_{TOF} is not the time required for an object to traverse a given distance. Rather, it is defined as the time required for a massive particle to travel a given distance minus the time that a massless particle would require to travel that same distance.

Let D be the distance (in meters) from the point of production to the point of interaction or decay in the laboratory frame, and let c be the speed of light ($c = 0.3m/ns$). A particle with rest mass M, lab energy E and momentum P, will have a velocity $v = \beta c$ in the laboratory frame (where $\beta = P/E$). Then

$$\begin{aligned} t_{tof} &= t - t_0 \\ &= \frac{D}{c}\left[\frac{1}{\beta} - 1\right] \\ &= \frac{D}{c}\left[\frac{E}{P} - 1\right] \\ &= \frac{D}{c}\left[\sqrt{\frac{P^2 + M^2}{P^2}} - 1\right] \\ &= \frac{D}{c}\left[\sqrt{1 + \frac{M^2}{P^2}} - 1\right]. \end{aligned}$$

Using the binomial expansion $(1+x)^n = 1 + nx + \frac{n(n-1)x^2}{2!} + \ldots$ for the quantity under the square root

$$t_{tof} = \frac{D}{c}\left[\left(1 + \frac{1}{2}\frac{M^2}{P^2} + \ldots\right) - 1\right]$$

which reduces to

$$t_{tof} = \frac{D}{2c}\left(\frac{M^2}{P^2}\right) \tag{B.1}$$

in all kinematic regions in which we are concerned.

Appendix C

Calculations from Time-of-Flight Counters

The following sections describe how time measurements are made using time-of-flight counter output when the counter is struck by a single minimum ionizing particle (a muon, for example). A schematic of a TOF counter traversed by a single isolated track is shown in Figure C.1. For all of the following calculations, we assume that

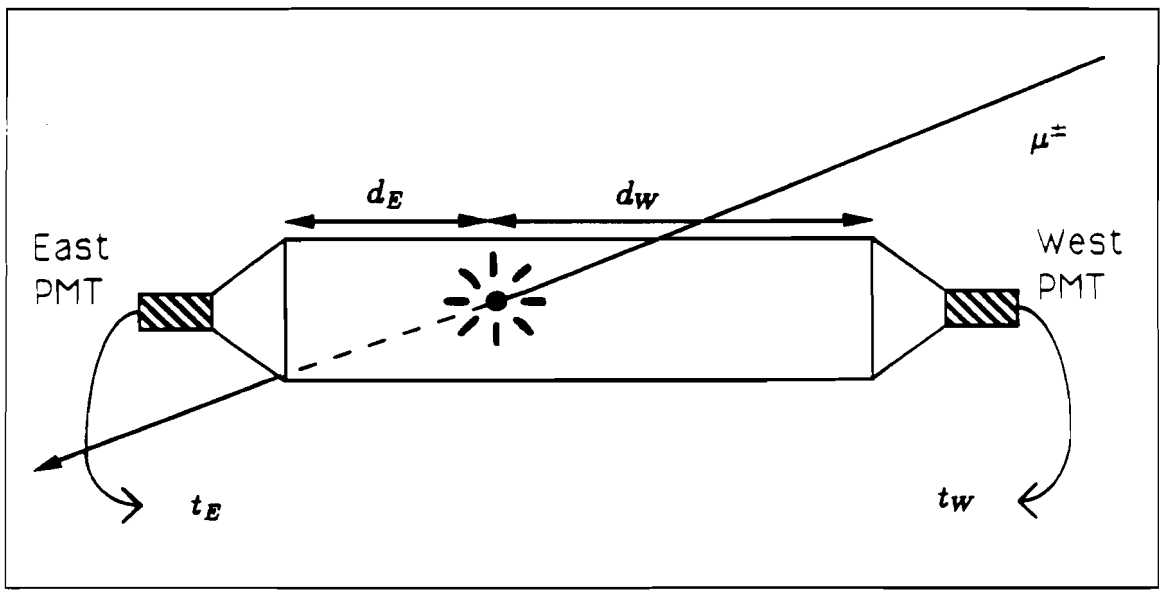

Figure C.1: A Schematic of a time-of-flight counter struck by a single minimum ionizing particle.

a charged particle strikes the counter at time $t_0 = 0$ at a point that is distance d_e from the east counter edge and d_w from the west counter edge. The total length of

the counter is

$$D = d_e + d_w. \tag{C.1}$$

The east and west photomultiplier tubes (PMTs) at each end of the counter detect scintillation light produced by the charged particle traversal. Their discriminated output measures the times t_e and t_w, the time of arrival of the light at the east and west photocathodes, respectively, relative to time $t_0 = 0$.

The following calculations are meant to illustrate how the event times are obtained from the PMT measurements. They use simplified assumptions for clarity of presentation. In the true calculation of event times:

- Two times are measured per PMT corresponding to the time the output PMT pulse cross a low (L) and high (H) threshold.
- The measured times are relative to the phase of the RF clock (rather than to the idealized $t_0 = 0$).
- Measured times are corrected for cable delays, RF clock shifts, etc.

Also, the time measurements described below have ideal timing resolution. In reality, the timing resolution of a counter is known to be about 0.8 ns.

C.1 The Speed of Light in Scintillator

The total length of a TOF counter is known and the times t_E and t_W are measured. Let v be the speed of light in the scintillator. Then

$$d_E = vt_E \quad and \quad d_W = vt_W. \tag{C.2}$$

Using the length of the counter as a constraint (Equation C.1), the velocity of light in the scintillator is

$$v = \frac{D}{t_E + t_W}, \tag{C.3}$$

which is independent of the hit position in the scintillator.

C.2 Timing Events with Isolated Tracks

If we want to calculate the time that a track hit the counter based on measurements t_E and t_W, we must correct these times for the time that the scintillator light requires to travel from the point of energy deposition to the photocathode. We assume v, the velocity of light in the scintillator, is known. The east and west corrected times are:

$$t'_E = t_E - \frac{d_E}{v} \qquad and \qquad t'_W = t_W - \frac{d_W}{v}. \tag{C.4}$$

The average of these corrected times is the best measured event time:

$$\begin{aligned} T &= \frac{t'_E + t'_W}{2} \\ &= \frac{1}{2}\left[t_E + t_W - \frac{D}{v}\right], \end{aligned} \tag{C.5}$$

which also is independent of the hit position in the scintillator.

Appendix D

Trigger, Timing, and RF Electronics

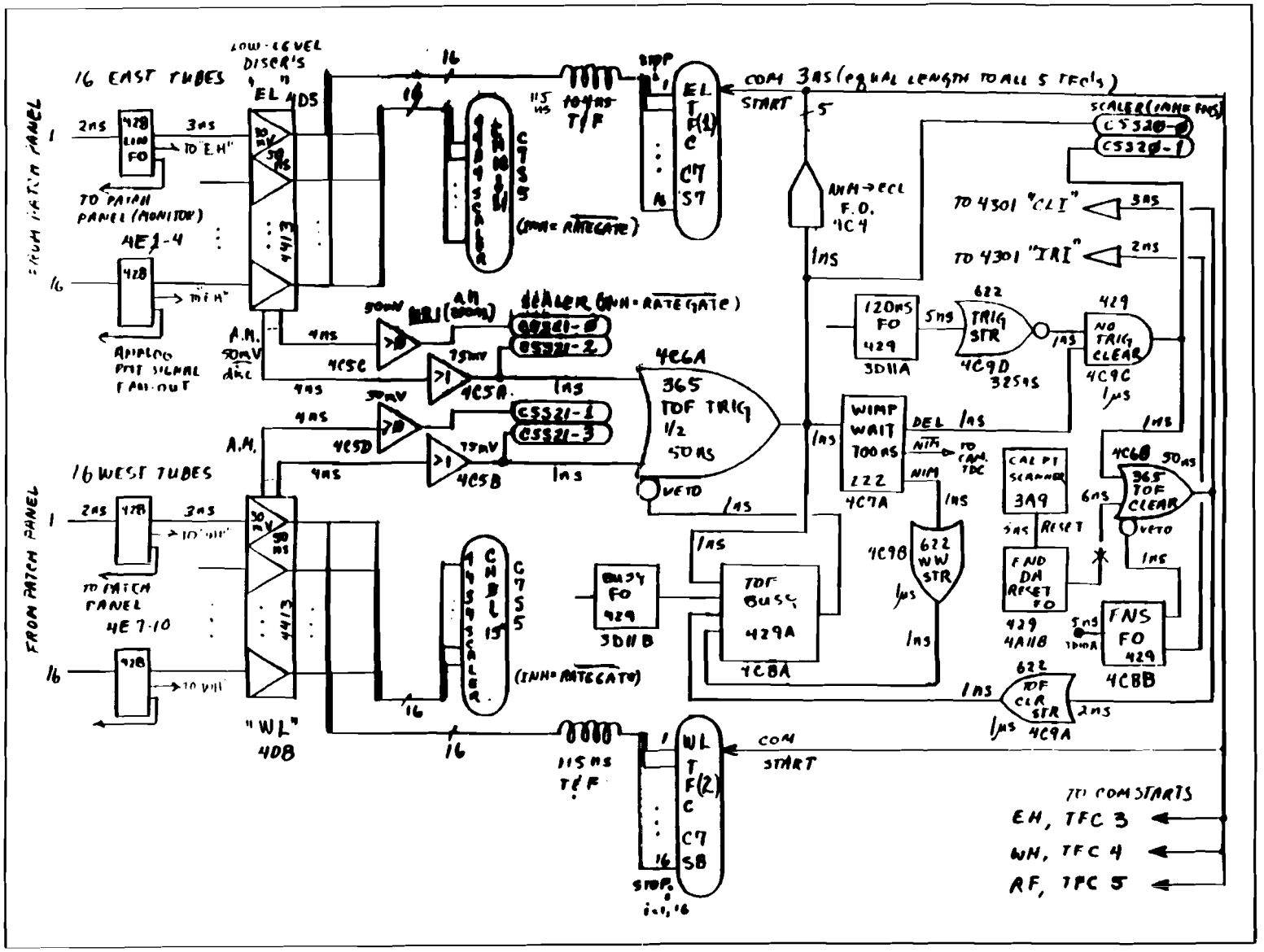

Figure D.1: Time-of-flight trigger and timing logic circuitry.

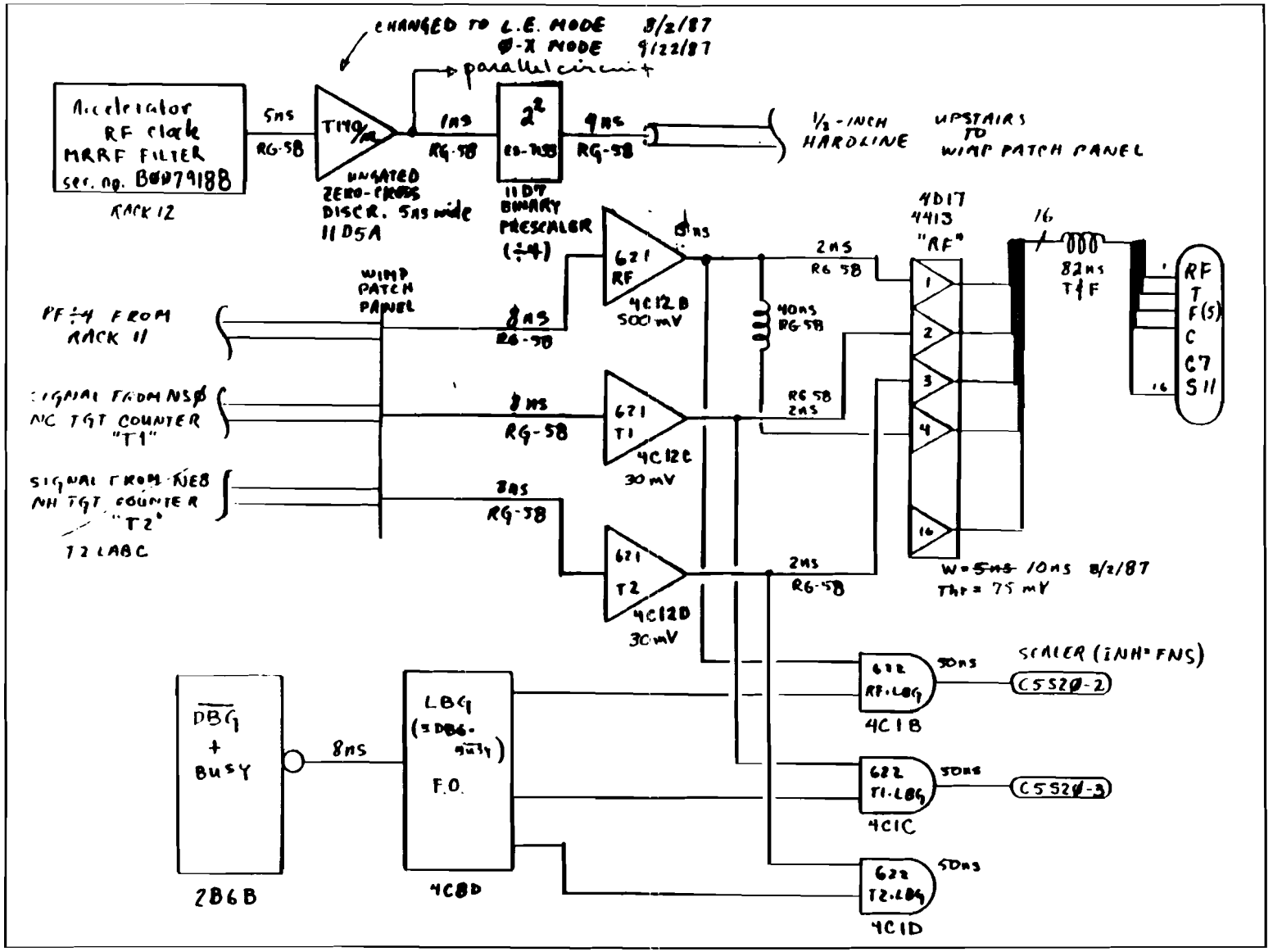

Figure D.2: Time-of-flight RF clock electronics.

Appendix E

Acceptance Tables

Table E.1: Geometric, time-of-flight and trigger acceptances for particles directly produced by 800 GeV/c protons at the primary target. The muon track timing TOF window is used to obtain these time-of-flight acceptances.

Acceptances for WIMPs directly produced by 800 GeV/c protons on the primary target				
WIMP Mass (GeV/c^2)	ε_{geo}	ε_{TOF}	ε_{trig}	$\varepsilon_{geo}\varepsilon_{TOF}\varepsilon_{trig}$
1.	0.14E-01	0.50E-02	0.97E+00	0.67E-04
2.	0.90E-02	0.32E-01	0.10E+01	0.28E-03
3.	0.74E-02	0.86E-01	0.10E+01	0.63E-03
4.	0.67E-02	0.16E+00	0.10E+01	0.11E-02
5.	0.66E-02	0.24E+00	0.10E+01	0.16E-02
6.	0.68E-02	0.32E+00	0.10E+01	0.22E-02
7.	0.71E-02	0.40E+00	0.10E+01	0.28E-02
8.	0.75E-02	0.47E+00	0.10E+01	0.35E-02
9.	0.79E-02	0.53E+00	0.10E+01	0.42E-02
10.	0.84E-02	0.59E+00	0.10E+01	0.50E-02
11.	0.90E-02	0.65E+00	0.10E+01	0.58E-02
12.	0.95E-02	0.69E+00	0.10E+01	0.66E-02
13.	0.10E-01	0.73E+00	0.10E+01	0.74E-02
14.	0.11E-01	0.77E+00	0.10E+01	0.82E-02
15.	0.11E-01	0.80E+00	0.10E+01	0.90E-02
16.	0.12E-01	0.83E+00	0.10E+01	0.99E-02
17.	0.13E-01	0.85E+00	0.10E+01	0.11E-01
18.	0.13E-01	0.88E+00	0.10E+01	0.11E-01
19.	0.14E-01	0.90E+00	0.10E+01	0.12E-01
20.	0.14E-01	0.91E+00	0.10E+01	0.13E-01

Table E.2: Geometric, time-of-flight and trigger acceptances for particles directly produced by 800 GeV/c protons at the beam dump. The muon track timing TOF window is used to obtain these time-of-flight acceptances.

Acceptances for WIMPs directly produced by 800 GeV/c protons on the beam dump				
WIMP Mass (GeV/c^2)	ε_{geo}	ε_{TOF}	ε_{trig}	$\varepsilon_{geo}\varepsilon_{TOF}\varepsilon_{trig}$
1.	0.30E-01	0.39E-02	0.98E+00	0.11E-03
2.	0.20E-01	0.22E-01	0.10E+01	0.44E-03
3.	0.16E-01	0.56E-01	0.10E+01	0.92E-03
4.	0.15E-01	0.10E+00	0.10E+01	0.16E-02
5.	0.15E-01	0.16E+00	0.10E+01	0.24E-02
6.	0.16E-01	0.21E+00	0.10E+01	0.32E-02
7.	0.16E-01	0.26E+00	0.10E+01	0.42E-02
8.	0.17E-01	0.31E+00	0.10E+01	0.52E-02
9.	0.18E-01	0.35E+00	0.10E+01	0.64E-02
10.	0.19E-01	0.39E+00	0.10E+01	0.75E-02
11.	0.20E-01	0.43E+00	0.10E+01	0.86E-02
12.	0.22E-01	0.46E+00	0.10E+01	0.10E-01
13.	0.23E-01	0.49E+00	0.10E+01	0.11E-01
14.	0.24E-01	0.53E+00	0.10E+01	0.13E-01
15.	0.26E-01	0.55E+00	0.10E+01	0.14E-01
16.	0.27E-01	0.57E+00	0.10E+01	0.16E-01
17.	0.28E-01	0.60E+00	0.10E+01	0.17E-01
18.	0.30E-01	0.62E+00	0.10E+01	0.18E-01
19.	0.31E-01	0.64E+00	0.10E+01	0.20E-01
20.	0.33E-01	0.66E+00	0.10E+01	0.22E-01

Table E.3: Geometric, time-of-flight and trigger acceptances for heavy neutrinos produced from the decay of $D_S^{\pm}$ produced by 800 GeV/c protons at the primary target and the beam dump. The muon track timing TOF window is used to obtain these time-of-flight acceptances.

Acceptances for ν^H from $D_S^{\pm}$ produced by 800 GeV/c protons on the primary target				
ν^H Mass (GeV/c^2)	ε_{geo}	ε_{TOF}	ε_{trig}	$\varepsilon_{geo}\varepsilon_{TOF}\varepsilon_{trig}$
0.50	0.14E-02	0.74E-02	0.92E+00	0.93E-05
0.60	0.15E-02	0.14E-01	0.95E+00	0.19E-04
0.70	0.16E-02	0.22E-01	0.98E+00	0.35E-04
0.80	0.19E-02	0.33E-01	0.98E+00	0.62E-04
0.90	0.22E-02	0.46E-01	0.10E+01	0.10E-03
1.00	0.26E-02	0.58E-01	0.10E+01	0.15E-03
1.10	0.31E-02	0.70E-01	0.99E+00	0.22E-03
1.20	0.39E-02	0.71E-01	0.10E+01	0.27E-03
1.30	0.43E-02	0.79E-01	0.10E+01	0.34E-03
1.40	0.48E-02	0.82E-01	0.10E+01	0.39E-03
1.50	0.54E-02	0.79E-01	0.10E+01	0.43E-03
1.60	0.56E-02	0.78E-01	0.10E+01	0.44E-03
1.70	0.60E-02	0.84E-01	0.10E+01	0.50E-03
1.80	0.63E-02	0.83E-01	0.10E+01	0.53E-03

Acceptances for ν^H from $D_S^{\pm}$ produced by 800 GeV/c protons on the beam dump				
ν^H Mass (GeV/c^2)	ε_{geo}	ε_{TOF}	ε_{trig}	$\varepsilon_{geo}\varepsilon_{TOF}\varepsilon_{trig}$
0.50	0.31E-02	0.51E-02	0.89E+00	0.14E-04
0.60	0.34E-02	0.83E-02	0.92E+00	0.26E-04
0.70	0.38E-02	0.15E-01	0.96E+00	0.54E-04
0.80	0.43E-02	0.23E-01	0.98E+00	0.95E-04
0.90	0.50E-02	0.31E-01	0.99E+00	0.15E-03
1.00	0.61E-02	0.39E-01	0.99E+00	0.24E-03
1.10	0.71E-02	0.46E-01	0.10E+01	0.33E-03
1.20	0.84E-02	0.51E-01	0.99E+00	0.42E-03
1.30	0.98E-02	0.52E-01	0.10E+01	0.50E-03
1.40	0.11E-01	0.52E-01	0.10E+01	0.57E-03
1.50	0.12E-01	0.52E-01	0.10E+01	0.62E-03
1.60	0.13E-01	0.52E-01	0.10E+01	0.66E-03
1.70	0.14E-01	0.52E-01	0.10E+01	0.71E-03
1.80	0.14E-01	0.51E-01	0.10E+01	0.71E-03

Table E.4: Geometric, time-of-flight and trigger acceptances for heavy neutrinos produced from the decay of $D^{\pm}$ produced by 800 GeV/c protons at the primary target and the beam dump. The muon track timing TOF window is used to obtain these time-of-flight acceptances.

Acceptances for ν^H from $D^{\pm}$ produced by 800 GeV/c protons on the primary target

ν^H Mass (GeV/c^2)	ε_{geo}	ε_{TOF}	ε_{trig}	$\varepsilon_{geo}\varepsilon_{TOF}\varepsilon_{trig}$
0.50	0.15E-02	0.91E-02	0.94E+00	0.13E-04
0.60	0.16E-02	0.15E-01	0.93E+00	0.23E-04
0.70	0.18E-02	0.24E-01	0.98E+00	0.43E-04
0.80	0.21E-02	0.36E-01	0.99E+00	0.75E-04
0.90	0.25E-02	0.45E-01	0.10E+01	0.11E-03
1.00	0.31E-02	0.59E-01	0.99E+00	0.18E-03
1.10	0.37E-02	0.65E-01	0.10E+01	0.24E-03
1.20	0.42E-02	0.72E-01	0.10E+01	0.30E-03
1.30	0.47E-02	0.74E-01	0.10E+01	0.34E-03
1.40	0.53E-02	0.73E-01	0.10E+01	0.38E-03
1.50	0.56E-02	0.74E-01	0.10E+01	0.41E-03
1.60	0.59E-02	0.68E-01	0.10E+01	0.40E-03
1.70	0.62E-02	0.74E-01	0.10E+01	0.46E-03

Acceptances for ν^H from $D^{\pm}$ produced by 800 GeV/c protons on the beam dump

ν^H Mass (GeV/c^2)	ε_{geo}	ε_{TOF}	ε_{trig}	$\varepsilon_{geo}\varepsilon_{TOF}\varepsilon_{trig}$
0.50	0.34E-02	0.54E-02	0.88E+00	0.16E-04
0.60	0.37E-02	0.10E-01	0.92E+00	0.35E-04
0.70	0.41E-02	0.17E-01	0.97E+00	0.70E-04
0.80	0.48E-02	0.24E-01	0.99E+00	0.11E-03
0.90	0.57E-02	0.31E-01	0.99E+00	0.18E-03
1.00	0.70E-02	0.39E-01	0.10E+01	0.27E-03
1.10	0.82E-02	0.43E-01	0.99E+00	0.35E-03
1.20	0.96E-02	0.43E-01	0.10E+01	0.41E-03
1.30	0.11E-01	0.50E-01	0.10E+01	0.54E-03
1.40	0.12E-01	0.47E-01	0.10E+01	0.56E-03
1.50	0.13E-01	0.46E-01	0.10E+01	0.58E-03
1.60	0.13E-01	0.48E-01	0.10E+01	0.63E-03
1.70	0.14E-01	0.51E-01	0.10E+01	0.71E-03

Table E.5: Geometric, time-of-flight and trigger acceptances for heavy neutrinos produced from the decay of $D^{\pm}$ produced by the secondary π^- and π^+ flux on the beam dump. The muon track timing TOF window is used to obtain these time-of-flight acceptances.

Acceptances for ν^H from $D^{\pm}$ produced by secondary π^- on the beam dump				
ν^H Mass (GeV/c^2)	ε_{geo}	ε_{TOF}	ε_{trig}	$\varepsilon_{geo}\varepsilon_{TOF}\varepsilon_{trig}$
0.50	0.53E-03	0.31E-01	0.91E+00	0.15E-04
0.60	0.59E-03	0.60E-01	0.92E+00	0.33E-04
0.70	0.68E-03	0.12E+00	0.95E+00	0.81E-04
0.80	0.81E-03	0.18E+00	0.95E+00	0.14E-03
0.90	0.95E-03	0.24E+00	0.98E+00	0.23E-03
1.00	0.11E-02	0.27E+00	0.99E+00	0.30E-03
1.10	0.13E-02	0.31E+00	0.10E+01	0.41E-03
1.20	0.16E-02	0.34E+00	0.10E+01	0.54E-03
1.30	0.17E-02	0.36E+00	0.10E+01	0.61E-03
1.40	0.17E-02	0.36E+00	0.10E+01	0.62E-03
1.50	0.19E-02	0.36E+00	0.10E+01	0.68E-03
1.60	0.21E-02	0.37E+00	0.10E+01	0.77E-03
1.70	0.22E-02	0.36E+00	0.10E+01	0.77E-03

Acceptances for ν^H from $D^{\pm}$ produced by secondary π^+ on the beam dump				
ν^H Mass (GeV/c^2)	ε_{geo}	ε_{TOF}	ε_{trig}	$\varepsilon_{geo}\varepsilon_{TOF}\varepsilon_{trig}$
0.50	0.63E-03	0.26E-01	0.91E+00	0.15E-04
0.60	0.68E-03	0.54E-01	0.94E+00	0.35E-04
0.70	0.75E-03	0.96E-01	0.98E+00	0.70E-04
0.80	0.90E-03	0.15E+00	0.97E+00	0.13E-03
0.90	0.10E-02	0.21E+00	0.98E+00	0.22E-03
1.00	0.13E-02	0.24E+00	0.99E+00	0.31E-03
1.10	0.15E-02	0.27E+00	0.99E+00	0.40E-03
1.20	0.17E-02	0.29E+00	0.10E+01	0.49E-03
1.30	0.20E-02	0.31E+00	0.10E+01	0.61E-03
1.40	0.21E-02	0.31E+00	0.10E+01	0.65E-03
1.50	0.22E-02	0.32E+00	0.10E+01	0.70E-03
1.60	0.24E-02	0.30E+00	0.10E+01	0.72E-03
1.70	0.26E-02	0.33E+00	0.10E+01	0.84E-03

Table E.6: Geometric, time-of-flight and trigger acceptances for heavy neutrinos produced from the decay of $D^{\pm}$ produced by the secondary K^- and K^+ flux on the beam dump. The muon track timing TOF window is used to obtain these time-of-flight acceptances.

Acceptances for ν^H from $D^{\pm}$ produced by secondary K^- on the beam dump				
ν^H Mass (GeV/c^2)	ε_{geo}	ε_{TOF}	ε_{trig}	$\varepsilon_{geo}\varepsilon_{TOF}\varepsilon_{trig}$
0.50	0.50E-03	0.33E-01	0.91E+00	0.15E-04
0.60	0.54E-03	0.72E-01	0.92E+00	0.35E-04
0.70	0.62E-03	0.12E+00	0.95E+00	0.73E-04
0.80	0.71E-03	0.19E+00	0.95E+00	0.13E-03
0.90	0.88E-03	0.25E+00	0.98E+00	0.22E-03
1.00	0.10E-02	0.32E+00	0.99E+00	0.32E-03
1.10	0.12E-02	0.35E+00	0.99E+00	0.42E-03
1.20	0.14E-02	0.37E+00	0.99E+00	0.51E-03
1.30	0.15E-02	0.37E+00	0.10E+01	0.56E-03
1.40	0.17E-02	0.39E+00	0.10E+01	0.68E-03
1.50	0.17E-02	0.39E+00	0.10E+01	0.66E-03
1.60	0.19E-02	0.37E+00	0.10E+01	0.71E-03
1.70	0.20E-02	0.39E+00	0.10E+01	0.80E-03

Acceptances for ν^H from $D^{\pm}$ produced by secondary K^+ on the beam dump				
ν^H Mass (GeV/c^2)	ε_{geo}	ε_{TOF}	ε_{trig}	$\varepsilon_{geo}\varepsilon_{TOF}\varepsilon_{trig}$
0.50	0.73E-03	0.20E-01	0.88E+00	0.13E-04
0.60	0.77E-03	0.51E-01	0.93E+00	0.37E-04
0.70	0.90E-03	0.95E-01	0.96E+00	0.82E-04
0.80	0.10E-02	0.13E+00	0.97E+00	0.13E-03
0.90	0.13E-02	0.17E+00	0.98E+00	0.22E-03
1.00	0.14E-02	0.21E+00	0.99E+00	0.29E-03
1.10	0.18E-02	0.23E+00	0.99E+00	0.41E-03
1.20	0.22E-02	0.27E+00	0.10E+01	0.57E-03
1.30	0.23E-02	0.26E+00	0.10E+01	0.60E-03
1.40	0.26E-02	0.27E+00	0.10E+01	0.69E-03
1.50	0.27E-02	0.26E+00	0.10E+01	0.72E-03
1.60	0.27E-02	0.27E+00	0.10E+01	0.73E-03
1.70	0.29E-02	0.30E+00	0.10E+01	0.85E-03

Table E.7: Geometric, time-of-flight and trigger acceptances for heavy neutrinos produced from the decay of $D^{\pm}$ produced by the secondary p^- and p^+ flux on the beam dump. The muon track timing TOF window is used to obtain these time-of-flight acceptances.

Acceptances for ν^H from $D^{\pm}$ produced by secondary p^- on the beam dump				
ν^H Mass (GeV/c^2)	ε_{geo}	ε_{TOF}	ε_{trig}	$\varepsilon_{geo}\varepsilon_{TOF}\varepsilon_{trig}$
0.50	0.43E-03	0.43E-01	0.90E+00	0.17E-04
0.60	0.48E-03	0.83E-01	0.93E+00	0.37E-04
0.70	0.53E-03	0.15E+00	0.95E+00	0.77E-04
0.80	0.60E-03	0.21E+00	0.95E+00	0.12E-03
0.90	0.73E-03	0.28E+00	0.98E+00	0.20E-03
1.00	0.86E-03	0.34E+00	0.99E+00	0.29E-03
1.10	0.11E-02	0.37E+00	0.10E+01	0.39E-03
1.20	0.11E-02	0.41E+00	0.10E+01	0.47E-03
1.30	0.14E-02	0.43E+00	0.10E+01	0.58E-03
1.40	0.14E-02	0.43E+00	0.10E+01	0.63E-03
1.50	0.16E-02	0.43E+00	0.10E+01	0.68E-03
1.60	0.15E-02	0.42E+00	0.10E+01	0.63E-03
1.70	0.16E-02	0.42E+00	0.10E+01	0.69E-03

Acceptances for ν^H from $D^{\pm}$ produced by secondary p^+ on the beam dump				
ν^H Mass (GeV/c^2)	ε_{geo}	ε_{TOF}	ε_{trig}	$\varepsilon_{geo}\varepsilon_{TOF}\varepsilon_{trig}$
0.50	0.20E-02	0.82E-02	0.89E+00	0.14E-04
0.60	0.21E-02	0.17E-01	0.90E+00	0.32E-04
0.70	0.24E-02	0.28E-01	0.97E+00	0.66E-04
0.80	0.29E-02	0.44E-01	0.97E+00	0.12E-03
0.90	0.34E-02	0.68E-01	0.98E+00	0.22E-03
1.00	0.40E-02	0.69E-01	0.99E+00	0.28E-03
1.10	0.47E-02	0.86E-01	0.10E+01	0.40E-03
1.20	0.56E-02	0.85E-01	0.99E+00	0.47E-03
1.30	0.62E-02	0.93E-01	0.10E+01	0.58E-03
1.40	0.69E-02	0.95E-01	0.10E+01	0.66E-03
1.50	0.72E-02	0.95E-01	0.10E+01	0.68E-03
1.60	0.78E-02	0.99E-01	0.10E+01	0.77E-03
1.70	0.78E-02	0.10E+00	0.10E+01	0.81E-03

Table E.8: Geometric, time-of-flight and trigger acceptances for photinos produced from the decay of gluinos produced by 800 GeV/c protons on the primary target and the beam dump. The shower timing TOF window is used to obtain the time-of-flight acceptances.

Acceptances for $\tilde{\gamma}$ from $\tilde{g}$ decay produced by 800 GeV/c protons on the primary target

$\tilde{g}$ Mass (GeV/c^2)	$\tilde{\gamma}$ Mass (GeV/c^2)	ε_{geo}	ε_{TOF}	ε_{trig}	$\varepsilon_{geo}\varepsilon_{TOF}\varepsilon_{trig}$
1.00	0.17	0.58E-02	0.13E-02	0.00E+00	0.00E+00
2.00	0.33	0.24E-02	0.41E-02	0.78E+00	0.76E-05
3.00	0.50	0.14E-02	0.70E-02	0.89E+00	0.89E-05
4.00	0.67	0.10E-02	0.95E-02	0.95E+00	0.93E-05
5.00	0.83	0.85E-03	0.12E-01	0.98E+00	0.10E-04
6.00	1.00	0.75E-03	0.14E-01	0.10E+01	0.10E-04
7.00	1.17	0.67E-03	0.16E-01	0.99E+00	0.10E-04
8.00	1.33	0.62E-03	0.17E-01	0.10E+01	0.10E-04
9.00	1.50	0.60E-03	0.18E-01	0.10E+01	0.11E-04
10.00	1.67	0.57E-03	0.18E-01	0.10E+01	0.11E-04
11.00	1.83	0.55E-03	0.18E-01	0.10E+01	0.10E-04

Acceptances for $\tilde{\gamma}$ from $\tilde{g}$ decay produced by 800 GeV/c protons on the beam dump

$\tilde{g}$ Mass (GeV/c^2)	$\tilde{\gamma}$ Mass (GeV/c^2)	ε_{geo}	ε_{TOF}	ε_{trig}	$\varepsilon_{geo}\varepsilon_{TOF}\varepsilon_{trig}$
1.00	0.17	0.13E-01	0.74E-03	0.00E+00	0.00E+00
2.00	0.33	0.53E-02	0.25E-02	0.52E+00	0.70E-05
3.00	0.50	0.32E-02	0.41E-02	0.89E+00	0.12E-04
4.00	0.67	0.24E-02	0.73E-02	0.96E+00	0.17E-04
5.00	0.83	0.19E-02	0.80E-02	0.97E+00	0.15E-04
6.00	1.00	0.17E-02	0.94E-02	0.97E+00	0.15E-04
7.00	1.17	0.15E-02	0.10E-01	0.98E+00	0.15E-04
8.00	1.33	0.14E-02	0.11E-01	0.99E+00	0.16E-04
9.00	1.50	0.14E-02	0.12E-01	0.10E+01	0.16E-04
10.00	1.67	0.13E-02	0.13E-01	0.10E+01	0.17E-04
11.00	1.83	0.13E-02	0.12E-01	0.99E+00	0.15E-04

Bibliography

[1] David O. Caldwell . Status of the 17-keV Neutrino . *UCSB-HEP-92-08*, page 5pp, 1992. (also in Proceedings of the 7th Meeting of the Division of Particles and Fields of the APS (DPF 92), Batavia, IL, 10-14 Nov 1992).

[2] Michael S. Turner . Probing the structure of the galactic halo with gamma rays produced by annihilations of weakly interacting massive particles . *Phys.Rev.D*, 34(6):1921–1924, 1986.

[3] David O. Caldwell . The Search for Dark Matter . *UCSB-HEP-90-09*, page 21pp, 1990.

[4] Lawrence M. Krauss . Z Decay and the Search for Dark Matter . *Phys.Rev.Lett*, 64(9):999–1002, 1990.

[5] Gordon Kane . *Modern Elementary Particle Physics* . Addison-Wesley Publishing Company, Inc., 1987. page 151.

[6] M.Kobayashi and T.Maskawa . CP VIOLATION IN THE RENORMALIZABLE THEORY OF WEAK INTERACTION. . *Prog.Theor.Phys.*, 49:652–657, 1973. (In Lichtenberg, D. B. (Ed.), Rosen, S. P. (Ed.): Developments In The Quark Theory Of Hadrons, Vol. 1*, 218-223.).

[7] N.Cabibbo . Unitary Symmetry and Leptonic Decays . *Phys.Rev.Lett*, 10:531, 1963.

[8] S.Weinberg . A Model of Leptons . *Phys.Rev.Lett*, 19:1264, 1967.

[9] A.Salam . *Elementary Particle Theory* . Almquist and Wiksells, Stockholm, 1969. ed. N.Svartholm.

[10] S.L.Glashow,J.Illiopoulos,L.Maiani . Weak Interactions with Lepton-Hadron Symmetry . *Phys.Rev.D*, 2:1285, 1970.

[11] G.t'Hooft . Renormalization of Massless Yang-Mills Fields . *Nucl.Phys.B*, 33:173, 1971. (also G.t'Hooft, Nucl.Phys.B35 (1971) 167).

[12] S.P.K.Tavernier . Charmed and Bottom Flavoured Particle Production in Hadronic Interactions . *Rep.Prog.Phys.*, 50:1439–1489, 1987.

[13] J.F.Gunion . Short Distance Counting Rules for Low p_T Fragmentation . *Phys.Lett.B*, 88:150–156, 1979.

[14] A. S. Carroll et al . Absorption Cross Sections of $\pi^{\pm}$, $K^{\pm}$, p and $\bar{p}$ on Nuclei Between 60 and 280 GeV/c . *Phys.Lett.B*, 80:319–22, 1979.

[15] J.J.Hernandez et al (Particle Data Group) . *Review of Particle Properties* , volume 45. The American Physical Society, 1992.

[16] Xerxes Tata . An Introduction to Supersymmetry and Supersymmetry Phenomenology . *University of Hawaii at Manoa Preprint*, UH-511-713-90:76pp, 1990.

[17] Sally Dawson, E.Eichten, and C.Quigg . Search for Supersymmetric Particles in Hadron-hadron Collisions . *Phys.Rev.D*, 31(7):1581–1637, 1985.

[18] H.P.Nilles . Supersymmetry, Supergravity and Particle Physics . *Phys.Rep.*, 110:1–162, 1984.

[19] J.Ellis, J.S.Hagelin, D.V.Nanopoulos, K.Olive, and M.Srednicki . Supersymmetric Relics from the Big Bang . *Nucl.Phys.B*, 238:453, 1984.

[20] R.E.Shrock . Test for the Existence of Effectively Stable Neutral Heavy Leptons . *Phys.Rev.Lett.*, 26:1688–1691, 1978.

[21] H. Richard Gustafson et al . Search for New Massive Long-Lived Neutral Particles. *Phys.Rev.Lett.*, 37(8):474–477, 1976.

[22] A. J. Malensek . Empirical Formula for Thick Target Production . *Fermilab Preprint*, FN-0341:10pp, 1981.

[23] H. W. Atherton et al . Precise Measurements of Particle Production by 400 GeV/c Protons on Beryllium Targets . *CERN*, 80-07:25pp, 1980.

[24] L. Stutte. N-Center Wide Band Neutrino Beam . *Fermilab Preprint*, TM-1305:27pp, 1985.

[25] David C.Carey, Karl L. Brown and F.C.Iselin . DECAY TURTLE (Trace Unlimited Rays Through Lumped Elements): A Computer Program for Simulating Charged Particle Beam Transport Systems, Including Decay Calculations . *Fermilab Computing Report*, PM-31:71pp, 1982. (also SLAC-0246, Mar 1982).

[26] E.Gallas. Neutrinos from K_L^0 Decay . *E733 note*, 90-01:8pp, 1990.

[27] Thomas Stewart Mattison . *Comparison of Charged and Neutral Current Structure Functions*. PhD thesis, Massachusetts Institute of Technology, 1978.

[28] William Gilbert Cobau . *Nucleon Structure Functions from Deep Inelastic Charged Current Neutrino Scattering*. PhD thesis, Michigan State University, 1992.

[29] Anthony Malensek and Linda Stutte . Update on the Tevatron Muon Shield . *Fermilab Preprint*, TM-1422(2271.000):29pp, 1986.

[30] B.Strongin . *Opposite Sign Dimuon Production in High Energy Neutrino-Nucleon Interactions*. PhD thesis, Massachusetts Institute of Technology, 1989.

[31] Stu Fuess. 1987/88 Beam Center . *E733 note*, 88-2, 1988.

[32] George J. Perkins . *A Measurement of the Ratio of Neutral Current to Charged Current Deep Inelastic ν_μ Scattering Interactions in a Fine Grain Detector at FNAL*. PhD thesis, Michigan State University, 1992.

[33] Michael Tartaglia, et al . Hadron Calorimetry with Proportional Tubes in E-733 at Fermilab . *Proceedings of the Gas Sampling Calorimetry Workshop II*, Fermilab:259–290, 1985.

[34] R.Hatcher. *Multimuon Final States in Neutrino-Nucleon Scattering.* PhD thesis, Michigan State University, 1993.

[35] Michael Albert Tartaglia . *A Measurement of the Elastic Scattering Cross Section,* $\nu_\mu + e^- \rightarrow \nu_\mu + e^-$. PhD thesis, Massachusetts Institute of Technology, 1984.

[36] W.J. Womersley, et al . Hadron Showers in a Low Density Fine Grained Flash Chamber Calorimeter . *NIM*, A267:49–68, 1988. (ERRATUM-ibid.A278:447-451,1989).

[37] Michael Tartaglia . Prototype TOF Counter Timing Tests , 1986. Unpublished E733 note.

[38] Michael Tartaglia . THE E733 TIME-OF-FLIGHT SYSTEM , 1988. Unpublished E733 note.

[39] Michael A. Tartaglia . A Search for Neutral Penetrating Particles . *New Directions in Neutrino Physics at Fermilab*, I:43–56, 1988.

[40] F.James and M.Roos . MINUIT Function Minimization and Error Analysis . CERN Program Library entry D506 , 1989. Copyright CERN, Geneva.

[41] S.G.Naculich and C.P.Yuan . Can the Electroweak Symmetry Breaking Sector be Hidden ? . *Phys.Lett.B*, 293:395–399, 1992.

[42] A.M.Cooper-Sarkar et al . Bounds on Light Gluinos from the BEBC Beam Dump Experiment. *Phys.Lett.B*, 160:212–216, 1983.

[43] Steven Reucroft . Heavy Flavor Hadroproduction . *CERN Preprint*, CERN-EP-83-155:20pp, 1983. (Published in Tahoe Multipart.Dyn.1983:638 (QCD161:C49:1983)).

[44] Ai Gia Nguyen . Characteristics of Charm Particles Produced by 800 GeV P-P Collisions . *PhD Thesis*, 1988.

[45] S.Barlag et al . Production of D, D^* and D_s mesons in 200 GeV/cπ^-, K$^-$ and $p-Si$ interactions . *Z.Phys.C-Particles and Fields*, 39:451–460, 1988.

[46] J.Badier et al . Mass and Lifetime Limits on New Long-Lived Particles in 300 GeV/cπ^- Interactions . *Z.Phys.C*, 31:21–32, 1986. (The NA3 Collaboration).

[47] R.N.Mohapatra and P.B.Pal . *Massive Neutrinos in Physics and Astrophysics* . World Scientific, 1991.

[48] ALEPH, DELPHI, L3 and OPAL (The LEP Collaborations). Electroweak parameters of the Z^0 resonance and the standard model . *Phys. Lett. B*, 276:247–253, 1992.

[49] L3 Collaboration . A search for heavy charged and neutral leptons from Z^0 decays . *Phys. Lett. B*, 251-2:321–330, 1990.

[50] D.Decamp et al . Searches for new particles in Z decays using the ALEPH detector. *Phys. Rept.*, 216:253–340, 1992.

[51] M.Gronau, C.N.Leung and J.L.Rosner . Extending Limits on Neutral Heavy Leptons . *Phys.Rev.D*, 29:2539–2558, 1984.

[52] S.M.Bilenky and S.T.Petcov . Massive Neutrinos and Neutrino Oscillations . *Rev.Mod.Phys.*, 59:671, 1987. (ERRATUM-ibid.61,169,1989).

[53] Rabindra N.Mohapatra and Goran Senjanovic . Neutrino Mass and Spontaneous Parity Nonconservation . *Phys.Rev.Lett.*, 44(14):912–915, 1980.

[54] Rabindra N.Mohapatra and Goran Senjanovic . Neutrino masses and mixings in gauge models with spontaneous parity violation . *Phys.Rev.D*, 23(1):165–180, 1981.

[55] R. Abela et al . Search for an Admixture of Heavy Neutrino States in Pion Decay . *Phys.Lett*, 105B(4):263–266, 1981.

[56] T.Yamazaki et al . Search for Heavy Neutrinos in Kaon Decay . *LEIPZIG*, 1:262, 1984. (Proc.XXII Intern.Conf. on High Energy Physics).

[57] C.Y.Pang et al . Search for Rare K^+ Decays. I. $K^+ \to \mu^+\nu\bar{\nu}\nu^*$. *Phys.Rev.D*, 8:1989, 1973.

[58] R.Ammar et al . D Meson Production in 800 GeV/c pp Interactions . *Phys.Rev.Lett*, 61:2185, 1988. (also NUB-2944(1988)).

[59] M.Aguilar-Benitez et al . D Meson Branching Ratios and Hadronic Charm Production Cross Sections . *Phys.Lett*, 135:237–242, 1984. (The LEBC-EHS Collaboration).

[60] M.Aguilar-Benitez et al . Charm Hadron Properties in 360 GeV/cπ^-p Interactions . *Z.Phys.C*, 31:491–511, 1986. (The LEBC-EHS Collaboration).

[61] R.Jedicke . private communication.

[62] R.K.Ellis and C.Quigg . A Pinacoteca of Cross Sections for Hadroproduction of Heavy Quarks . *FNAL*, FN-445(2013.000):70pp, 1987.

[63] J.Dorenbosch et al . A Search for Decays of Heavy Neutrinos in the Mass Range 0.5 – 2.8 GeV . *Phys.Lett.B*, 166:473–478, 1986. (The CHARM Collaboration).

[64] M.Holder et al . A Detector for High-Energy Neutrino Interactions . *NIM*, 148:235, 1978. (CDHS - CERN-Dortmund-Heidelberg-Saclay Collaboration).

[65] A.N.Diddens et al . A Detector for Neutral Current Interactions of High-Energy Neutrinos. . *NIM*, 178:27, 1980. (CHARM - CERN-Hamburg-Amsterdam-Rome-Moscow Collaboration).

[66] A.M.Cooper-Sarkar et al . Search for Heavy Neutrino Decays in the BEBC Beam Dump Experiment . *Phys.Lett.B*, 160:207–211, 1985. (The WA66 Collaboration).

[67] G.J.Feldman . Search for Heavy Neutrino Production at PEP . *SLAC*, PUB-3822:7pp, 1985.

[68] Glennys R. Farrar . Light Gluinos . *Phys.Rev.Lett.*, 53(11):1029–1032, 1984.

[69] P.R.Harrison and C.H.Llewellyn Smith . Hadroproduction of Supersymmetric Particles . *Nuclear Physics B*, 213:223–240, 1983.

[70] H.-J.Behrend et al . Searches for Supersymmetric Particles with the CELLO Detector at PETRA . *Z.Phys.C*, 35:181–199, 1987.

[71] Howard E. Haber and Gordon L. Kane . Gluino Decays and Experimental Signatures . *Nuclear Physics B*, 232:333–348, 1984.

[72] F. Bergsma et al . Bounds on Supersymmetric Particles from a Proton Beam-Dump Experiment . *Phys.Lett.B*, 121:429–432, 1983.

[73] P.N.Harriman, A.D.Martin, W.J.Stirling, and R.G.Roberts . Parton Distributions Extracted from Data on Deep Inelastic Lepton Scattering, Prompt Photon Production and the Drell-Yan Process . *Phys.Rev.D*, 42:798–810, 1990. (HMRS).

[74] I.Antoniadia, John Ellis and D.V.Nanopoulos . LEP Data and the Light Gluino Window . *Phys.Lett.B*, 262(1):109–112, 1991.

[75] M.Chanowitz and S.Sharpe . Spectrum of Gluino Bound States . *Phys.Lett.B*, 126(3,4):225–230, 1983.

[76] B.Alper et al . Large Angle Production of Stable Particles Heavier than the Proton and a Search for Quarks at the CERN Intersecting Storage Rings . *Phys.Lett.B*, 46(2):265, 1973.

[77] D.Cutts et al . Search for Long-Lived Heavy Particles . *Phys.Rev.Lett*, 41(6):363, 1978.

[78] T.Akesson et al . A Search for Weakly Interacting Neutral Particles in Missing Energy Events in 450 GeV/c pN Collisions . *Z.Phys.C*, 52:219–225, 1991.

[79] P.M.Tuts et al . Search for Light Gluinos . *Phys.Lett.B*, 186:233–236, 1987.

[80] H.Albrecht et al . Search for Gluinos in Decays of the $\chi_b(1^3P_1)$ Meson . *Phys.Lett.B*, 167(3):360–364, 1986. (The ARGUS Collaboration).

[81] R.C.Ball et al . Mass and Lifetime Limits on Supersymmetric Particles from a Proton Beam-Dump Experiment . *Phys.Rev.Lett*, 53(14):1314–1317, 1984. (The Fermilab E613 Collaboration).

[82] R.Arnold et al . Experimental Search for Associated Gluino Production and Decay in 350 GeV/cπ^- Emulsion Interactions . *Phys.Lett.B*, 186(2):435–439, 1987.

[83] C.Albajar et al . Events with Large Missing Transverse Energy at the CERN Collider: III. Mass Limits on Supersymmetric Particles . *Phys.Lett.B*, 198(2):261–270, 1987. (The UA1 Collaboration).

[84] H.Abramowicz et al . A Precision Measurement of $\sin^2(\theta_W)$ from Semileptonic Neutrino Scattering . *Phys.Rev.Lett.*, 57:298, 1986. (The CDHSL Collaboration).

[85] J.V.Allaby et al . A Precise Determination of the Electroweak Mixing Angle from Semileptonic Neutrino Scattering . *Z.Phys.C*, 36:611, 1987. (The CHARM Collaboration).